

# 博士論文

Investigation of plasma mode-transition  
by two-photon absorption laser-induced fluorescence and  
particle simulation in microwave discharge ion thruster  
(2光子レーザ誘起蛍光法と粒子計算によるマイクロ波放電型イオン  
スラスターのプラズマモード遷移の研究)

by

山下 裕介

Yusuke Yamashita

A Dissertation Submitted in Partial Fulfillment of the  
Requirements for the Degree of  
Doctor of Philosophy

Department of Aeronautics and Astronautics  
Graduate School of Engineering  
The University of Tokyo, Japan

# ABSTRACT

The  $\mu 10$  microwave discharge ion thruster was used in various space missions, e.g., the Japanese asteroid sample return missions Hayabusa and Hayabusa2 and will be used in Phaeton flyby mission DESTINY<sup>+</sup>. This thruster utilizes electron cyclotron resonance (ECR) and a mirror magnetic field. By continuously heating electrons in the mirror magnetic field, plasma is generated. However, the laser absorption spectroscopy of excited neutral particles inside the thruster revealed that plasma is also generated outside the mirror magnetic field as flow rate increases. Previous Electrooptic (EO) measurement revealed that after generating plasma, microwaves cannot propagate, i.e., cut-off occurs. This phenomenon restricts the maximum thrust performance. Similar phenomena are also observed in other ECR plasma sources, but the physical mechanisms are not revealed yet. Therefore, one very important question needs to be answered; *why plasma is generated except for mirror magnetic field.*

To answer this question, experimental evaluation of the local excitation and ionization rates is very effective; however, this measurement remains a challenge. Generally, the ionization and excitation rates can be expressed as;  $k_{i,j} = \langle \sigma_{i,j} v_e \rangle n_e n_j$ , where  $k_{i,j}$  is  $i$ -th production rate from lower state  $j$  (e.g., ground-state),  $\langle \sigma_{i,j} v_e \rangle$  is the rate coefficient from state  $i$  to state  $j$ ,  $n_e$  is the electron density, and  $n_j$  is the number density at lower state  $j$ . To evaluate  $\langle \sigma_{i,j} v_e \rangle$ , the cross-section  $\sigma_{i,j}$  and electron velocity distribution function (EVDF) are necessary. Even though EVDF can be theoretically evaluated by Langmuir probe and LTS, it is very difficult to measure non-Maxwellian electrons because of the low signal ratio, and the electrons are very sensitive to  $k_{i,j}$ . Additionally, in low-temperature plasmas, not only direct reactions from the ground state, but also reactions from metastable neutral particles, i.e., stepwise ionization, can be important, because relatively low-energy electrons can induce the ionization.

To overcome this problem, the measurement of ground-state neutral density and spontaneous emission intensity using two-photon a two-photon absorption laser-induced fluorescence spectroscopy (TALIF) experimental setup is proposed. This idea is based on the characteristic that

the wavelength of spontaneous emission by electron impact excitation is the same as that of fluorescence by two-photon excitation. Because of this characteristic, the ground-state neutral density and then the spontaneous emission intensity can be measured using the same experimental setup of TALIF. The two-photon excitation process from  $1s_0$  to  $2p_3$  were selected. The excitation process emits fluorescence from  $2p_3$  to  $1s_2$  at 834.68 nm. The difference in the excitation and ionization energy is only 1 eV; thus, from information about excitation process, the ionization process can be estimated. From the experiments, it was revealed that the spontaneous emission intensity sharply increases according to flow rate around the optimal flow rate. This sharp increase could be caused by three factors; stepwise excitation, stepwise ionization, and increase of the electron temperature. Therefore, each cause was evaluated based on previous data, the metastable neutral density, and electron temperature. As a result, it was found that stepwise excitation and ionization from the metastable state  $1s_5$  is the main cause of the sharp increase. Because relatively low energy electrons can induce stepwise ionization, the stepwise ionization is main cause of plasma generation outside the mirror magnetic field.

Though the proposed experimental approach can suggest the insight that the stepwise ionization can induce the plasma mode-transition, the transition in the ionization and excitation rate distributions, and relationship between each measurement parameter, e.g., various neutral densities and electric field of microwaves cannot be revealed. Hence, to overcome this problem, three numerical approaches were employed. First, to estimate the total ionization rate distribution including direct and stepwise ionization, particle simulation of ground-state was performed. Second, to estimate the excitation rate distribution in the metastable state, particle simulation of metastable state was performed. Last, to clear the contribution of stepwise ionization against the plasma density, quasi-1D simulation of plasma and the electric field of microwave was performed. From the three simulation results, spatial structure of plasma mode-transition was revealed. At low flow-rate, direct ionization and excitation is occurred in the magnetic confinement region. Then, the generated metastable neutral particles transport to the

exit of the waveguide and inside the waveguide. As flow rate increases, the stepwise ionization from the transported metastable neutral particles is occurred and then more metastable neutral particles are transported to inside the waveguide. When the plasma density inside the waveguide was high enough to prevent the propagation of microwaves, a plasma mode-transition occurred. The spatial structure can explain the mechanism of previous thruster improvement, e.g., gas injection, and can provide clues for thruster designs able to achieve additional thrust improvement.

# Nomenclature

$A$ : Einstein's A coefficient	$n$ : Density
$A_\theta$ : Vector potential in azimuthal direction	$N$ : Number
$B$ : Einstein's B coefficient	$P$ : Pressure
$c$ : Light speed	$p$ : Absorbed power per Volume
$D$ : Diameter	$P_{de}$ : Possibility of de-excitation
$D_r$ : Diffusion coefficient in radial direction	$Q$ : Quenching effect
$E$ : Energy	$R$ : Ratio of ionization rate between waveguide and magnetic confinement region
$F$ : Thrust	$r$ : Radial
$f$ : Distribution function	$R_p$ : Plasma radius
$F$ : Factor	$S_F$ : Fluorescence signal intensity
$f(\vec{x})$ : Normalized function	$T$ : Temperature
$f_{sc}$ : Sensitivity coefficient	$t$ : Time
$h$ : Planck constant	$U$ : Bulk velocity
$I$ : Spontaneous emission	$U$ : Bulk velocity
$I_{2+}$ : Ion beam current due to doubly charged ion	$v$ : velocity
$I_{3+}$ : Ion beam current due to triply charged ion	$V$ : Volume
$I_{sp}$ : Specific impulse	$v$ : Individual velocity
$I_+$ : Ion beam current due to singly charged ion	$z$ : Axial position
$I_b$ : Ion beam current	$\alpha_{E,C}$ : Ratio of absorbed power between ECR and Collision
$j$ : Current density	$\alpha_{th}$ : Thermal accommodation coefficient
$k$ : Rate coefficient	$\alpha_m$ : Correction factor due to multiple charged ion
$K_{ex}$ : Total excitation rate at metastable state	$\bar{\alpha}_p$ : Matrix of individual velocity update
$k_B$ : Boltzmann coefficient	$\Delta$ : Difference
$K_c$ : Clausius's factor	$\eta_{ex}$ : Ion extracted efficiency
$k_q$ : Quenching rate constant	$\eta_i$ : Ratio of ion recombination at grid
$I_L$ : Laser power	$\eta_u$ : Propellant utilization efficiency
$L_w$ : Length of waveguide	$\eta_w$ : Ratio of excitation rate between waveguide and magnetic confinement region
$m$ : Mass	$\gamma$ : Dispersion
$\dot{m}$ : mass flow rate per volume	
$\dot{M}$ : Total mass flow rate	

$\Gamma$ : Ion extracted efficiency	<i>confined</i> : Magnetic confinement region
$\Gamma_B$ : Bohm flux	<i>conv</i> : Convolution
$v_{\hat{e}x}$ : effective exhaust velocity	<i>cut</i> : Cut-off
$\kappa_p$ : Plasma conductivity	<i>de</i> : De-excitation
$\lambda$ : Wavelength	<i>Do</i> : Doppler
$\mu_0$ : Vacuum Permeability	<i>e</i> : Electron
$\nabla^2$ : Laplacian in transverse direction	<i>ECR</i> : Electron cyclotron resonance
$\nu$ : Collision frequency	<i>eq</i> : Equilibrium
$\Omega$ : Hall parameter	<i>excite</i> : Excited
$\omega$ : Angular frequency	<i>g</i> : Ground state
$\Omega_1$ : Region inside magnetic confinement region	<i>G</i> : Gaussian
$\Omega_2$ : Region outside magnetic confinement region	<i>h</i> : Higher excited state
$\phi$ : Electrostatic potential	<i>i</i> : ion
$\psi_{escape}$ : Escape factor	<i>in</i> : Injection
$\rho$ : Charged density	<i>ioni</i> : Ionization
$\sigma$ : Cross section	<i>L</i> : Lorentz
$\tau$ : Lifetime (Mean free time)	<i>l</i> : Laser
$\tau_{depth}$ : Optical depth	<i>l</i> : Lower excited state
$\vec{B}$ : Magnetic field	<i>L</i> : Left
$\vec{E}$ : Electric field	<i>m</i> : microwave
$\vec{S}$ : Poynting vector	<i>me</i> : Metastable state
$\varepsilon$ : Permittivity	<i>n</i> : Neutral
$\xi_{m,n}$ : n-th positive root of derivative n-th Bessel function in radial direction	<i>p</i> : Plasma
	<i>r</i> : Resonance state

## Subscript

$\perp$ : Perpendicular	<i>recom</i> : Ion recombination
$\parallel$ : Parallel	<i>s</i> : Screen grid
<i>A</i> : Accelerator	<i>spo</i> : Spontaneous emission
<i>ce</i> : Electron cyclotron	<i>th</i> : Thermal
<i>ch</i> : Child-Langmuir limit	<i>tho</i> : Theoretical
<i>Coll</i> : Collision	<i>w</i> : Waveguide
	<i>wall</i> : Wall

## ACKNOWLEDGEMENT

私の博士課程の5年間は、多くの人に支えられました。この5年間で得た経験は、これから研究者として歩いていくための糧となりました。

まず初めに、修士前半の指導教官である國中先生、修士課程後半、博士課程の指導教官である西山先生に感謝を申し上げます。國中先生には、パイオニアのマインドを教えてくださいました。これは、私の博士研究のテーマを決定する上で大変参考になりました。西山先生には、イオンスラストを制作する上で、制作しやすいような設計を都度教えてくださいました。また、査読論文執筆の際は、毎回添削のお時間をいただきありがとうございました。

月崎先生には、修士課程1年の時にレーザ実験の研究をご指導いただきました。特に、修士課程前半では、アメリカで研究されているにも関わらず、毎週進捗報告の時間を取っていただきありがとうございました。また、研究費の面でも、数千万円クラスのレーザ系、光学系に特化したチャンバーの作成を行っていただきありがとうございました。このレーザ系、チャンバーなしには、私の博士課程は完遂できなかったと思います。

Stanford大学の原先生には、数値計算で大変お世話になりました。独学での数値計算技術の発展に限界を感じていたところ、博士1年の時に留学のお誘いをいただきました。留学中は、毎日のように議論してくださり、先生の研究に対する姿勢、進め方全てにおいて参考となり、今後数値計算の研究を進めるための礎となりました。今後ともよろしくお祈りします。

次に、博士審査での副査を担当していただいた、小紫先生、小泉先生、杵淵先生、鷹尾先生に感謝申し上げます。小紫先生には、光学厚さの指摘、レーザ計測系に指摘をいただき、論文を充実させることができました。小泉先生には、科学用語の使い方の指摘から博士論文の構成の指摘を行っていただきました。杵淵先生には、本審査のみならず、2光子吸収LIF法の実験の立ち上げで大変お世話になりました。鷹尾先生にも、本審査のみならず、ことあるごとに数値計算の議論をしてください大変ありがとうございました。

研究室の先輩である神田さん、谷さん、吉川さん、井出さん、ジュリオ、森田さんには後輩として指導していただきありがとうございました。特に、シミュレーションの研究出身である私にとってはいきなり実験の研究とは、ハードルが高く、一つ一つを乗り越えるために、先輩方には色々教えてくださいました。後輩の白川君、宮君、濃野君、服部さん、小磯君、高木君にもお世話になりました。突然晩御飯を誘っても、みんな来てくれて、たわいのない会話によって、リラックスすることができました。船田さんには、修士1年の時から大変お世話になりました。特に、レーザの購入の際には、入札について右も左もわからない私に丁寧にやり方を教えてくださいました。研究室で私が疲れているときも、美味しい紅茶を入れていただきありがとうございました。

美佑には博士3年の間、大変お世話になりました。研究で疲れている中、元気をもらえました。日々刺激のある毎日で、英語の添削並びに日常生活をサポートしていただきました。波瀾万丈の人生だと思いますが、これからも一緒に楽しく歩いていけたらと思います。

最後にここまで育ててくれた両親と兄に対して深く感謝申し上げます。

## TABLE OF CONTENTS

<b>ACKNOWLEDGEMENT</b> . . . . .	6
<b>LIST OF FIGURES</b> . . . . .	10
<b>LIST OF TABLES</b> . . . . .	15
<b>LIST OF TERMS AND ABBREVIATIONS</b> . . . . .	16
<b>1 Introduction</b> . . . . .	<b>1</b>
1.1 Development of Electric Propulsion . . . . .	1
1.2 Gridded Ion thruster . . . . .	2
1.2.1 DC gridded ion thruster . . . . .	4
1.2.2 RF gridded ion thruster . . . . .	7
1.2.3 Gridded Microwave discharge ion thruster . . . . .	9
1.3 Plasma physics of EP devices . . . . .	13
1.3.1 Low-temperature magnetized plasma . . . . .	13
1.3.2 Plasma chemistry . . . . .	14
1.3.3 Plasma diagnostics . . . . .	16
1.3.4 Plasma mode-transition . . . . .	17
1.4 Problem statement . . . . .	17
1.4.1 Development of $\mu 10$ ion thruster . . . . .	18
1.4.2 Review of internal plasma diagnostics . . . . .	22
1.5 Challenge . . . . .	28
1.5.1 Plasma mode-transition hypothesis . . . . .	28
1.5.2 Measurement of excitation and ionization processes . . . . .	28
1.5.3 Numerical estimation of ionization and excitation rate distributions . . . . .	31
1.5.4 Thesis outline . . . . .	33
<b>2 Experimental evaluation of ionization and excitation processes by measuring ground-state neutral density and spontaneous emission intensity</b> . . . . .	<b>34</b>
2.1 Outline of TALIF measurement . . . . .	34
2.2 Theory . . . . .	38
2.2.1 Two-photon excitation . . . . .	38
2.2.2 Spontaneous emission . . . . .	39
2.2.3 Determination of the wavelength . . . . .	40
2.2.4 Rate equation . . . . .	44
2.3 Experimental devices . . . . .	47
2.3.1 $\mu 10$ ion thruster system . . . . .	47
2.3.2 Ground test facility . . . . .	52
2.3.3 Vacuum Facility . . . . .	52
2.3.4 Laser and Optical Devices . . . . .	56
2.4 Experimental setup . . . . .	61
2.4.1 Ground-state neutral density measurement . . . . .	61
2.4.2 Spontaneous emission intensity measurement . . . . .	63
2.4.3 Measurement point . . . . .	63
2.5 Validity of TALIF measurement . . . . .	67
2.5.1 Temporal function of fluorescence signal . . . . .	67
2.5.2 Calibration of TALIF signal . . . . .	72
2.5.3 Laser power effect . . . . .	75
2.5.4 Optical window effect . . . . .	77
2.5.5 Broadening of fluorescence signal . . . . .	78
2.5.6 Experimental error . . . . .	83

2.6	Experimental result . . . . .	86
2.6.1	Effect of gas injection . . . . .	86
2.6.2	Electron heating inside the waveguide . . . . .	94
2.7	Evaluation of excitation and ionization processes . . . . .	102
2.7.1	I. Stepwise excitation . . . . .	104
2.7.2	II. Increase of electron density . . . . .	106
2.7.3	III. Increase of electron temperature . . . . .	109
2.8	Possible mechanism of plasma mode-transition . . . . .	113
2.9	Short conclusion and achievement . . . . .	113
<b>3</b>	<b>Numerical estimation of ionization and excitation rate distributions</b>	<b>118</b>
3.1	Objective . . . . .	118
3.1.1	Ground-state neutral particles . . . . .	119
3.1.2	Metastable neutral particles . . . . .	119
3.1.3	Electric field of microwaves . . . . .	119
3.2	Ground-state neutral particles . . . . .	120
3.2.1	Modeling ground-state neutral particles including ionization and recombination . . . . .	120
3.2.2	Gas injection . . . . .	124
3.2.3	Boundary condition . . . . .	124
3.2.4	Simulation flow . . . . .	125
3.2.5	Simulation results . . . . .	127
3.3	Metastable neutral particles . . . . .	137
3.3.1	Modeling of metastable neutral particles . . . . .	137
3.3.2	Numerical result . . . . .	140
3.4	Effect of stepwise ionization from metastable neutral particles . . . . .	145
3.4.1	Modeling of plasma diffusion equation and microwave propagation . . . . .	145
3.4.2	Numerical aspect . . . . .	149
3.4.3	Simulation result . . . . .	149
3.5	Spatial structure of plasma mode-transition . . . . .	155
3.6	Short conclusion . . . . .	158
<b>4</b>	<b>Conclusion</b>	<b>161</b>
<b>Appendices</b>		
<b>Appendix A</b>	<b>Thruster Performance in various grid and magnetic field configuration</b>	<b>166</b>
A.1	Outline . . . . .	166
A.2	Grid parameter . . . . .	166
A.2.1	Grid design . . . . .	166
A.2.2	Experimental results . . . . .	167
A.2.3	Discussion of grid parameter . . . . .	169
A.3	Magnetic field geometry and height of discharge chamber . . . . .	171
A.3.1	Hypothesis . . . . .	171
A.3.2	Experimental results . . . . .	173
A.3.3	Discussion of magnetic field geometry and height of discharge chamber . . . . .	175
A.4	Other possible improvements . . . . .	178
A.4.1	Short conclusion . . . . .	179
<b>Appendix B</b>	<b>Plasma hysteresis caused by high-voltage breakdown</b>	<b>180</b>
B.1	Objective . . . . .	180
B.2	Plasma hysteresis of the microwave discharge ion thruster . . . . .	181
B.3	Proposed recovery method . . . . .	183
B.3.1	Concept . . . . .	183
B.3.2	Demonstration . . . . .	183
B.4	Characteristics of plasma hysteresis . . . . .	184
B.4.1	Grid parameter . . . . .	184
B.4.2	Plasma conditions inside waveguide . . . . .	185
B.4.3	Short conclusion . . . . .	185

<b>Appendix C</b>	<b>Development of full kinetic particles in cell simulation</b>	<b>187</b>
C.1	Outline . . . . .	187
C.2	Super Computer facility . . . . .	190
C.3	Explicit ES-full-PIC simulation . . . . .	190
	C.3.1 Numerical model . . . . .	190
	C.3.2 Electrostatic field . . . . .	191
	C.3.3 Numerical procedure . . . . .	193
	C.3.4 Macroscopic quantities . . . . .	194
	C.3.5 Electron-scale phenomena . . . . .	195
	C.3.6 Ion-scale phenomena . . . . .	200
C.4	Implicit EM full-PIC simulation . . . . .	203
	C.4.1 Review of ECSIM . . . . .	203
	C.4.2 Electromagnetic field update . . . . .	204
C.5	Satisfying Gauss-law . . . . .	205
	C.5.1 Proposed improvement for LTPs . . . . .	205
	C.5.2 Benchmark problem . . . . .	211
	C.5.3 Macroscopic conservation . . . . .	213
	C.5.4 Momentum conservation . . . . .	213
	C.5.5 Application of conservation-law to benchmark problem . . . . .	216
	C.5.6 Application to ECR plasma source . . . . .	218
	C.5.7 Demonstration of sub-cycle method . . . . .	223
C.6	Short conclusion . . . . .	227
<b>Appendix D</b>	<b>Simulated ion extraction in the absence of ion extraction</b>	<b>229</b>
D.1	Objective . . . . .	229
	D.1.1 Proposed methods to reproduce the neutral density under ion extraction . . . . .	230
	D.1.2 Validity of ‘simulated experiment without ion extraction’ and ‘decoupled numerical simulation’ . . . . .	232
D.2	Short conclusion . . . . .	236
	<b>REFERENCES</b> . . . . .	<b>236</b>

## LIST OF FIGURES

1.1	Schematics of DC discharge ion thruster. . . . .	5
1.2	The NASA's asteroid explorer Deep Space 1 [1]. . . . .	5
1.3	NASA's asteroid explorer DAWN [2]. . . . .	6
1.4	ESA/JAXA Mercury orbiter BepiColombo [3, 4]. . . . .	6
1.5	Schematics of ratio frequency discharge ion thruster. . . . .	7
1.6	The ESA's communication satellite Artemis [5]. . . . .	8
1.7	Schematics of microwave discharge ion thruster. . . . .	10
1.8	Japanese asteroid explorer Hayabusa and Hayabusa2. Phaeton fly by mission DESTINY+ [6, 7].	11
1.9	The small Space Probe PROCYON [8]. . . . .	12
1.10	Performance development of microwave discharge ion thruster $\mu 10$ . Ion beam current versus propellant flow rate. Blue: Hayabusa, green: Hayabusa2, red: Enhanced model 1, black: Enhanced model 2. . . . .	19
1.11	Grid optics system of ion thrusters. The extracted ion beam current is limited by the Child-Langmuir law given by Eq.(1.4) . . . . .	20
1.12	Photograph of major 10 cm class ion thrusters. (a) XIPS-13, (b) T5, (c) RIT-10, (d) $\mu 10$ . Detailed thruster performances data are summarized in Tab. 1.2 . . . . .	21
1.13	Transition of photographs outside thruster as a function of propellant flow rate. These photographs are taken under the same conditions, e.g, exposure time. . . . .	22
1.14	Luminescence measurements using an optical fiber probe. Net input microwave power 34 W [9]. . . . .	24
1.15	Metastable state $1s_5$ neutral density distribution. Top: distribution when the propellant was injected only from the waveguide inlet (WG), Bottom : distribution from the discharge chamber inlets (DC). At propellant flow rates of 1.00 sccm from the waveguide inlet and 2.00 sccm from the discharge chamber inlet, it was not possible to detect absorbance [10]. . . . .	25
1.16	Resonance state $1s_4$ neutral density distribution. Top: distribution when the propellant was injected only from the waveguide inlet (WG), Bottom : distribution from the discharge chamber inlets (DC). At propellant flow rates of 1.00 sccm from the waveguide inlet and 2.00 sccm from the discharge chamber inlets, it was not possible to detect absorbance [11]. . . . .	26
1.17	Electric field distribution oscillating parallel to the dipole antenna along the center line of the plasma source in the accelerated plasma at mass flow rates of 0, 1, 2, 3, 4 sccm [12]. The input microwave power is 34 W. The measurement error is 10 % on the amplitude of the electric field. . . . .	27
1.18	Correlation between ground-state neutral density and spontaneous emission intensity. If the step-wise excitation and ionization cannot be neglected compared to direct excitation, the spontaneous emission intensity sharply increases. . . . .	30
2.1	Difference of photon excitation process between LIF and TALIF. In TALIF, two times wavelength can excite compared to LIF. . . . .	39
2.2	Principle of measuring (a) ground-state neutral density and (b) spontaneous emission intensity by electron-impact excitation. . . . .	42
2.3	Spectrum diagram of a $\mu 10$ thruster at a mass flow rate of 2.00 sccm and an ion beam current of 137 mA. The inlet of propellant is the discharge chamber. . . . .	43
2.4	Two photon excitation process. Ground state $1s_0$ is excited by a wavelength of 224.29 nm and emits fluorescence with 834.7 nm from $2p_3$ to $1s_2$ . . . . .	46
2.5	A schematic of the $\mu 10$ microwave discharge ion thruster . . . . .	48
2.6	Thruster configurations to investigate the physical aspects against plasma mode transition, I.effect of gas injection, II. effect of electron heating inside the waveguide. (a) Hayabusa model, WG injection, (b) Hayabusa model, DC injection, (c) Enhanced model 2 , with WG ECR, (d) Enhanced model 2, without WG ECR. . . . .	50
2.7	Schematic diagram of power supply and vacuum facility. . . . .	53
2.8	Photograph of power supply unit and feed-through unit at vacuum chamber. . . . .	53

2.9	Photograph of controller unit of vacuum pumps and vacuum gauge. Pirani gauge measured in range of $0.1 \sim 10^5$ Pa, and hot cathode gauge measured less than 0.1 Pa. . . . .	54
2.10	Photograph of vacuum chamber. Two Cryogenic pumps are equipped at the top, and one Turbomolecular pump and one rotary pump were equipped at the bottom. At left-side, ion thruster was operated. . . . .	55
2.11	Front view of thruster. Laser was injected from the bottom window. . . . .	55
2.12	Power supply of Nd:yag laser. In this thesis, two times harmonic wavelength of 1064 nm, i.e., 532 nm, was used. . . . .	57
2.13	Nd:yag Laser system. The laser beam is introduced to dye laser by using two mirrors. . . . .	58
2.14	Dye laser system. This dye laser converted to the wavelength from 532 nm to $650 \sim 700$ nm by using dye, and the three harmonic light was extracted. A laptop can operate dye laser system, for example, the changing wavelength. . . . .	58
2.15	The circulation system of dye laser. There are two kinds of aqueous solutions. The concentration is described in catalog. The concentration of one aqueous solution is 10 times denser than that of another. . . . .	59
2.16	Example of fluorescence in TALIF measurement. This pressure of xenon gas cell is 10 Torr. . . . .	59
2.17	Schematics of detector. To collect fluorescence signal, two convex lens are used. In addition, to remove noise of plasma emission, a band-pass filter was used. . . . .	60
2.18	Photograph of Oscilloscope. . . . .	61
2.19	Experimental setup for the TALIF spectroscopy measurements. Left: view of detection, right: view of laser injection. When measuring the ground-state neutral density, a fluorescence of $834.7 \pm 2$ with laser injection is detected. When measuring the spontaneous emission, the signal of $834.7 \pm 2$ without laser injection is detected. Here, we measured three measurement points from the screen grid, 7.0-, 11.5-, and 16.0-cm. . . . .	64
2.20	Averaging technique of TALIF signal. Because TALIF signal is low-signal ratio, signal of laser scattering used by detecting time of laser. . . . .	65
2.21	Transition of TALIF signal with respect to the number of average. Green line: laser signal detected by PMT2, red line: fluorescence signal detected by PMT1 in Fig. 2.19 . . . . .	66
2.22	Typical fluorescence signal in TALIF measurement at optimal flow rate respectively. Experimental condition: DC injection at 2.9 sccm, WG injection at 1.8 sccm. Measurement point is 11.5 cm from screen grid. There are three kinds of signal: (a) cold gas, (b) without ion extraction, and (c) with ion extraction. . . . .	70
2.23	Fluctuation of spontaneous emission intensity in case of DC 1 sccm. The fluctuation is approximately 0.15% at Maximum. . . . .	71
2.24	Two cases of temporal fluorescence signals in case of DC 1 sccm. In case 2, the ground-state neutral density becomes negative due to fluctuation of spontaneous emission. . . . .	71
2.25	Confirmation of Sensitivity coefficient about hot cathode gauge. In this experiment, 0.5 sccm of xenon gas is continuously injected and increase of pressure measured by hot cathode gauge was measured. First: before data obtained after TALIF measurement, second: data obtained after TALIF measurement . . . . .	73
2.26	The ground-state neutral densities without thruster operation as function of flow rate. Here, the absolute value of ground-state neutral density is obtained by calibration. . . . .	74
2.27	Intensity of the fluorescence signal with respect to laser power. Experimental condition is cold gas at the flow rate is 2 sccm of DC injection. . . . .	75
2.28	Intensity of the fluorescence signal with respect to pressure in two kinds of laser power. Red: 1.2 mJ, Blue: 0.6 mJ. Experimental condition is cold gas at the flow rate is 2 sccm of DC injection. . . . .	76
2.29	A comparison of ion beam currents with and without optical windows. Legend: DC = data from the discharge chamber propellant injection inlets, WG = data from the waveguide. . . . .	77
2.30	The fluorescence spectra obtained from cold gas, ionized state and beam extraction measurements. The spectra were recorded at 2.0 sccm from DC injection. . . . .	81
2.31	The fluorescence spectra obtained from cold gas, ionized state and beam extraction measurements. The data was normalized the experimental results (Fig. 2.30). The spectra were recorded at 2.0 sccm from DC injection. . . . .	82
2.32	The fluorescence spectra obtained from cold gas, ionized state and beam extraction measurements. Voigt functions fitted the normalized experimental data (Fig. 2.31). The spectra were recorded at 2.0 sccm from DC injection. . . . .	82
2.33	Ion beam currents with respect to propellant flow rate. Left: WG injection, right: DC injection. Red plot: optimal flow rate. . . . .	84

2.34	Reproducibility of TALIF measurement. Top: ground-state neutral density. Bottom: Spontaneous emission intensity. Red: measured by December 2020, Black: measured by September 2020. . . .	85
2.35	The ground state neutral densities of the cold gas with respect to propellant flow rate. Legend: WG = data from the waveguide inlet, DC = data from the discharge chamber injection. . . . .	87
2.36	Axial distribution of ground-state neutral density using TALIF measurement in case of 'WG injection'. Blue line: without ion extraction, red line: with ion extraction. (a) before optimal flow rate (1.0 sccm), (b) optimal flow rate (1.8 sccm), (c) after optimal flow rate (3.0 sccm). . . . .	88
2.37	Axial distribution of ground-state neutral density using TALIF measurement in case of 'DC injection'. Blue line: without ion extraction, red line: with ion extraction. (a) before optimal flow rate (2.0 sccm), (b) optimal flow rate (2.9 sccm), (c) after optimal flow rate (3.5 sccm). . . . .	89
2.38	Comparison of neutral densities between estimation and TALIF measurement. Estimated neutral density was calculated by Eq.(2.28). . . . .	92
2.39	Spontaneous emission with respect to ground-state neutral density. Top: WG injection, bottom: DC injection. Each value represents a propellant flow rate in units of standard cubic centimetres per minute (sccm). Red plot: optimal flow rate.. . . . .	93
2.40	Ion beam current versus flow rate. In these thrusters, configurations are common and shown in Fig. 2.6 . . . . .	95
2.41	Photograph before and after plasma mode-transition. The ion beam current is shown in Fig. 2.40. Configurations are summarized in Fig. 2.6. The black dashed circle is the diameter of the waveguide. (a): 'w WG ECR', (b): 'w/o WG plasma', and 'w/o WG ECR'. . . . .	96
2.42	Beam current, ground-state neutral density, and excited emission intensity with respect to propellant flow rate. In this paper, there are three measurement points at $z = -7.0, -11.5, -16.0$ cm from the screen grid. Estimated neutral density was calculated by using Eq. (2.28) . . . . .	98
2.43	Beam current with respect to ground-state neutral density. The ground-state neutral density and the beam current are obtained by the arithmetic mean of three measurement points. Each value means the propellant flow rate in sccm unit. . . . .	100
2.44	Spontaneous emission intensity with respect to ground-state neutral density. The ground-state neutral density and the excited emission are obtained by the arithmetic mean of three measurement points. Each value means the propellant flow rate in sccm unit. . . . .	101
2.45	Excitation process of neutral species. Each density is the result after mode-transition. The excited density is measured by LAS and quoted from reference [10, 11]. . . . .	104
2.46	Ratio of rate coefficient between direct and stepwise excitation. The cross-section uses by RDW approach [13, 14]. . . . .	107
2.47	Ratio of the rate coefficient between direct and stepwise for excitation and ionization. The cross-section of ionization from metastable state $1s_5$ is quoted from Ton-That and Flannery work [15]. . . . .	108
2.48	Magnetic field strength $ \vec{B} $ and gradient of magnetic field in the direction of magnetic field line $ \partial  \vec{B}  / \partial s $ . $ \vec{B} $ and $ \partial  \vec{B}  / \partial s $ are related to evaluation of collisionless and collisional heating in Eq. (2.40) and (2.41). . . . .	112
2.49	Hypothesis of plasma mode-transition based on experimental results. . . . .	113
3.1	Schematics of neutral flow with and without ion extraction. Without ion extraction, additional ion recombination is generated at the accelerator grid. . . . .	121
3.2	Ion current ratio measured by planar probe [16, 17]. These results are utilized as ion recombination distribution $f_{recom}(\vec{x}_{recom})$ in various flow rate condition in WG and DC injection. These data are utilized data as the distribution function of ion recombination. Each location is illustrated in [18]. . . . .	122
3.3	Model of ionization rate by using two driven parameters: $R$ and $L_w$ . $R$ is the ratio of the ionization rates in the waveguide and the discharge chamber. $L_w$ is the distance of the ionization area from the screen grid. . . . .	123
3.4	Simulation flow of DSMC model. . . . .	126
3.5	Comparison of neutral density distributions (a) without ion extraction, (b) with ion extraction. Left: WG injection, right: DC injection. Arrow shows the gas injection. $R$ and $L_w$ are defined in Eq. (3.7) and Fig. 3.3. In both WG and DC injections, the simulation condition is (ii) optimal flow rate . . . . .	128
3.6	Comparison of time-averaged axial velocity along central axis. Top: WG injection, bottom: DC injection. Blue line: without ion extraction, red line: with ion extraction. The velocity is calculated by Eq. (3.10). $R$ and $L_w$ are defined in Eq. (3.7) and Fig. 3.3. . . . .	132

3.7	Comparison of neutral density distribution between TALIF spectroscopy and DSMC simulation in the presence of ion extraction at WG injection. The explanation of $R$ and $L_w$ are written in section 3.2.1. . . . .	135
3.8	Comparison of neutral density distribution between TALIF spectroscopy and DSMC simulation in the presence of ion extraction at WG injection. The explanation of $R$ and $L_w$ are written in section 3.2.1. . . . .	135
3.9	Spatial structure of ionization from estimation of ground-state neutral particles. . . . .	136
3.10	De-excitation process of metastable neutral particles. (1): Excitation to higher excited state and transition to resonance state ( $1s_4$ ), (2): excitation to higher excited state and reproduces metastable state ( $1s_5$ ), (3): stepwise ionization including singly, multiply charged ions, (4) wall diffusion inside thruster. . . . .	138
3.11	Model of metastable generation by using two driven parameters: $\eta_w$ and $L_w$ . $\eta_w$ is the ratio of the ionization rates in the waveguide and the discharge chamber. $L_w$ is the distance of the ionization area from the screen grid. . . . .	139
3.12	Sensitivity of de-excitation time against metastable neutral density distribution. (a) $\nu_{coll} = 0$ Hz, (b) $\nu_{coll} = 10^3$ Hz, (c) $\nu_{coll} = 10^4$ Hz, (d) $\nu_{coll} = 10^5$ Hz. The source term of metastable neutral particles shows two cases. $\eta_w = 0\%$ . . . . .	141
3.13	Sensitivity of de-excitation time against metastable neutral density distribution. (a) $\nu_{coll} = 0$ Hz, (b) $\nu_{coll} = 10^3$ Hz, (c) $\nu_{coll} = 10^4$ Hz, (d) $\nu_{coll} = 10^5$ Hz. The source term of metastable neutral particles shows two cases. $\eta_w = 100\%$ , $L_w = 10$ cm . . . . .	141
3.14	Comparison of metastable neutral density distributions. Black line: LAS experiment results quoted from ref. [19], red and blue line: simulation results considering the plasma mode-transition. Simulation results include the minimum and maximum value due to variation of $\nu_{coll} = 0 \sim 10^5$ Hz. 143	
3.15	Spatial structure of generation and diffusion on metastable neutral particles $1s_5$ . . . . .	144
3.16	Electric field of microwaves parallel component $E_y$ in central line. Results of 3D FDTD simulation and EO probe are quoted by [12]. . . . .	148
3.17	Correlation between the location of plasma inside the waveguide and microwave propagation. Three case on $L_w$ ; $L_w = 5, 7, 10$ cm are simulated. The experimental results are quoted by EO probe measurement. . . . .	150
3.18	Correlation between the plasma density and microwave propagation under $L_w = 7$ cm. The experimental results are quoted by EO probe measurement [12]. . . . .	151
3.19	Correction between stepwise ionization from metastable neutral particles, plasma density, and electric field of microwave density and electromagnetic field of microwaves. . . . .	154
3.20	Spatial structure of plasma mode-transition. (i) At low flow rates, direct ionization and excitation is occurred in the magnetic confined region, and then the generated metastable neutral particles transport to the exit of the waveguide and inside the waveguide. (ii) From the transported metastable neutral particles, indirect excitation and ionization is occurred the exit of the waveguide and inside the waveguide, and the particles are more transported to inside the waveguide. When the plasma density inside the waveguide is high enough to prevent the propagation of microwaves, the plasma mode-transition occurs. . . . .	157
A.1	Ion beam current with respect to propellant flow rate. For each experimental result, the maximum error was $\pm 0.1$ sccm for propellant flow and $\pm 5$ mA for ion beam current. . . . .	168
A.2	Estimated neutral density versus propellant flow rate. The grid configurations are summarized in Tab. A.1. The neutral density is estimated using Eq. (2.28). The error bars show the uncertainty due to the current ratio of the doubly and triply charged ions. . . . .	170
A.3	Case of ECR layer splitting. . . . .	172
A.4	Screen current in the combination of Samarium cobalt magnet (Sm) and Neodymium magnet (Nd). 173	
A.5	Screen current in case of ECR layer splitting. . . . .	174
A.6	The relationship between the height of discharge chamber and volume ratio of magnetic confined region. Here, the relative height of discharge chamber $H = 0$ means the height of the Hayabusa 2 model. In: inner magnet, out: outer magnet. . . . .	177
A.7	The relationship between the height of discharge chamber and volume ratio of magnetic confined region. Here, the relative height of discharge chamber $H = 0$ means the height of the Hayabusa 2 model. In: inner magnet, out: outer magnet. . . . .	177
B.1	Schematic diagrams of ion beam current versus propellant flow rate (a) without and (b) with hysteresis. The arrows show the directions along which the propellant flow rate can be changed . .	182
B.2	Flow chart of recovery method. . . . .	183
C.1	Schematics of microwave ion thruster $\mu 10$ in physical view . . . . .	194

C.2	Macroscopic quantities of the numerical simulation. (a) Electron temperature, (b) electron density, (c) ionization rate, and (d) plasma potential in the $r$ - $z$ plane. . . . .	196
C.3	Single electron motion using the plasma parameters from the simulation results to study the effects of electromagnetic fields. The figure shows the time function of the electron energy in three cases; (a) $\vec{B}_s$ , (b) $\vec{E}_m + \vec{B}_s$ , and (c) $\vec{E}_m + \vec{E}_s + \vec{B}_s$ . . . . .	197
C.4	Single electron motion using the plasma parameters from the simulation results to study the effects of electromagnetic fields. The figure shows each trajectory in three cases; (a) $\vec{B}_s$ , (b) $\vec{E}_m + \vec{B}_s$ , and (c) $\vec{E}_m + \vec{E}_s + \vec{B}_s$ . . . . .	198
C.5	Time averaged electron energy distribution function of the discharge chamber. . . . .	199
C.6	Single ion motion using the plasma parameters from the simulation results to study the effects of electromagnetic fields. The figure shows each trajectory in two cases; (a) $\vec{B}_s$ , (b) $\vec{E}_s + \vec{B}_s$ . . . . .	201
C.7	Macroscopic azimuthal ion velocity distribution in two cases; (a) $\vec{B}_s$ , (b) $\vec{E}_s + \vec{B}_s$ . . . . .	202
C.8	Current percentage distribution of ions and electrons and surface area percentage. Electron (simulation) and ion (simulation) show the numerical results of the current ratio of ion and electron. Ion (experiment) is the results of measurement using the electrostatic probe in the Hayabusa mode and quoted from Ref. 11. The surface area represents the area at each wall. . . . .	202
C.9	Sub-cycle method that maintains ECSIM. During a sub-cycle, particle interpolation for the current density is not necessary. . . . .	209
C.10	Time development of growth rate in Weibel instability [20]. GL refers to Gauss's law satisfying ECSIM proposed by Chen [21]. EG refers to the exact-gyro scheme proposed in subsection C.5.1. . . . .	212
C.11	Discrete difference of macroscopic conservation obtained at $\omega_{pe}\Delta t = 100$ . (a) Charge, (b) momentum, and (c) energy. $\partial\vec{Q}/\partial t$ and $\partial\vec{F}/\partial x$ are the time variable and flux defined in Eq. (C.56). . . . .	217
C.12	Comparison of electron cyclotron motion between conventional and high-accurate Boris solver. Top: conventional, and bottom: high-accurate. . . . .	218
C.13	Comparison of conventional and exact-gyro (EG) Boris push in ECR heating process. Here, $T_m$ is one cycle of microwaves. . . . .	219
C.14	Numerical dispersion relation for extraordinary waves. The dispersion relation can be calculated using the discrete Fourier transform (Eq. (C.60)). Red: EG-ECSIM, blue: ECSIM, black: theory. EG refers to the exact-gyro scheme proposed in subsection C.5.1. Top: $T_m/40$ , center: $T_m/20$ , bottom: $T_m/10$ . In the high-frequency region ( $\omega^* > \omega_{Re}^*$ ), the EG scheme can suppress the dispersion error compared to that for the conventional ECSIM scheme. . . . .	222
C.15	Numerical proof of sub-cycle method. Residual error is the difference between macroscopic and particle interpolation. This figure shows that the explicit current densities calculated using macroscopic and particle interpolation are exactly the same during a sub-cycle. . . . .	225
C.16	Electric field with respect to the number of sub-cycle time step. $L$ is the number of sub-cycles. . . . .	225
C.17	Simulation time and numerical error versus number of sub-cycles. Note that the simulation was performed on a single processor. Here, the numerical error is that defined in Eq. (C.64). . . . .	226
D.1	Two-dimensional neutral density distribution in case of WG injection. The simulation cases are summarized in Tab D.2. For comparison, simulation results in the case with ion extraction (Fig. 3.5) are also shown. . . . .	235
D.2	Two-dimensional neutral density distribution in case of DC injection. The simulation cases are summarized in Tab. D.2. For comparison, simulation results in the case with ion extraction (Fig. 3.5) are also shown. . . . .	235

## LIST OF TABLES

1.1	Major electron-impact reactions for xenon . . . . .	16
1.2	Comparison of 10 cm class ion thruster. Photographs are shown in Fig. 1.12 [22, 16, 23, 24]. . . . .	20
1.3	Summary of purpose and targets in numerical simulation . . . . .	33
2.1	Major application of TALIF measurements for EP devices . . . . .	37
2.2	Wavelength of TALIF measurement for major application of EP devices [25]. . . . .	42
2.3	Experimental condition of thruster operation . . . . .	48
2.4	Abbreviation of thrusters that uses in this chapter. Detailed configurations are shown in Fig.2.6 . . . . .	51
2.5	Detail of Model number and company in optical devices . . . . .	56
2.6	Comparison of FWHM obtained by TALIF signal in case of (a) cold gas, (b) w/o ion ext, and (c) w ion ext... These experiment results are fitted by Voight function to evaluate Lorentz and Gaussian broadening. . . . .	79
2.7	Beam current for photograph for four cases. The photograph is shown in Fig. 2.41. . . . .	95
2.8	Evaluation of stepwise excitation against direct excitation. These rate coefficients are calculated using Eq. (2.35) assuming that the electron velocity distribution function is an isotropic Maxwellian distribution with an electron temperature of 3–5 eV [26]. The density is quoted from the result after the mode-transition. . . . .	107
3.1	Comparison of the maximum, minimum, average neutral densities for WG and DC injection. Results of this table are obtained from Fig. 3.5. . . . .	129
A.1	configuration of screen and accelerator grids. . . . .	167
B.1	Relationship between the hysteresis region and the neutral density. Grid parameters are summarized in Tab. A.1. The densities were estimated using Eq. (2.28). $n_{n,h}$ and $n_{n,l}$ show the neutral densities in case of high-current and low-current mode respectively. The densities are calculated from the ion beam current at the reference propellant flow rate. $\Delta n_n = n_{n,l} - n_{n,h}$ shows the difference of the neutral density between high- and low-current modes. . . . .	184
D.1	Summary of simulation cases to reproduce the neutral density distribution under the condition without ion extraction. (A) ~ (C) is explained in subsection D.1.1. . . . .	234
D.2	Comparison of the maximum, minimum, average neutral densities for WG and DC injection. Results of this table are obtained from Fig. D.1 and D.2. The simulation cases are summarized in Table D.1. . . . .	236



# Chapter 1

## Introduction

### 1.1 Development of Electric Propulsion

Generally, thrust  $F$  and specific impulse  $I_{sp}$  are given by

$$F = \dot{M} \hat{v}_{ex}, \quad (1.1)$$

$$I_{sp} = \frac{\hat{v}_{ex}}{g}. \quad (1.2)$$

Here,  $\dot{M}$ ,  $\hat{v}_{ex}$  are total mass flow rate, and effective exhaust velocity respectively. The equation (1.1) shows that to increase thrust,  $\dot{m}_{ex}$  or  $\hat{v}_{ex}$  must be enhanced. However, the propellant flow rate is limited to the capacity of spacecraft. Hence, to increase the thrust and specific impulse with the same amount of propellant, a high exhaust velocity is required.

In the case of thrusters that uses chemical reaction (Chemical propulsion), the thermal energy of the chemical reaction restricts the specific impulse. Typically, the maximum specific thrust is 500 s theoretically, and about 300 ~ 400 s in practice considering loss of nozzle divergence and thermal loss.

Therefore, to remove this limitation on specific impulse, electric propulsion (EP) devices have been developed [27, 28]. EP devices utilizes electromagnetic forces to enhance exhaust velocity. The concept of EP devices firstly mentioned on the notebook of the US scientist R. H. Goddard in September 1906. Additionally, the Russian scientist Tsiolkovskiy independently considered the concept in 1911. In 1945, an engineering student, Herbert Radd described the propulsion system including solar power and ion propulsion [28].

During the period 1945-56, the concept of EP devices was further developed with detailed analysis. For instance, in 1954, Stuhlinger published an ion propulsion system (in 1964, he later devoted a whole chapter '*Ion Propulsion*'). In 1951, United States of America (USA)

astrophysicist, Lyman Spitzer, published an account of the development of *gridded* ion thrusters [27]. After 1960, EP devices began to be used in space. In 1964, the Scout (code A) EP system was launched for the first time by the US. In this mission, two electron-bombardment ion thrusters [27] were mounted. Though one thruster did not work, the other one operated for 31 minutes. This thrust performance was good agreement with that obtained in a ground test. In 1964, Zond-2 was launched by the Union of Soviet Socialist Republics (USSR). It demonstrated a Teflon propellant Plasma Pulsed Thruster (PPT). In 1965, GGSE-2 was the first successful space operation of the Resist jet thruster by the US. In 1971, the USSR first successfully achieved space operation of the Hall effect thruster (HET). In 1975, the Kren-1 (Kosmos-728) magnetoplasmadynamic (MPD) thruster was first demonstrated by the USSR. After these first space operations, EP devices were used in space operations mainly by the USA and USSR. In Japan, the Institute of Space and Astronautical Science (ISAS) launched an MPD thruster (MS-T4 Tansei-4) in 1980.

In space missions that used EP devices during the period 1962-1980, most of the orbit types were Low Earth orbit (LEO), sub-LEO, and Geostationary orbit (GEO). Some of the most important and attractive EP devices are high specific impulse devices, which can reduce the consumption of propellant. By using this advantage, deep space mission have been developed. In 1998, the US mission Deep Space 1 for the first time flew by an asteroid (Braille) and a comet (Borrelly). In this mission, NSTAR ion thruster was used. In 2003, the first sample return mission from an asteroid (Itokawa) firstly launched by Japan. In this mission,  $\mu$  10 ion thruster was used. In Japan, successive mission (Hayabusa2) was also launched in 2014. In 2018, the BepiColombo mission was launched, using a T-6 ion thruster. The above missions could not be achieved using lower specific impulse thruster, and thus advantage of EP devices was demonstrated. Entering the 21st century, small spacecraft, e.g., mini-satellites, microsatellites, and cubesat are rapidly developing by using the electrospray thruster, gridded ion thruster, PPT, and resistojet. A more detailed history of EP devices is given in reference [27, 29, 30].

## 1.2 Gridded Ion thruster

Generally, gridded ion thrusters (GITs) consist of a discharge chamber and a grid system [22]. The process for generating thrust involves following steps.

1. High energy electrons able to ionize the injected gas are generated.

2. The high-energy electrons are confined to suppress wall loss.
3. Ions are extracted from the plasma at the grid system.
4. The ion beam is neutralized by using an electron source (cathode).

In the grid system, ions are extracted from the plasma by applying high voltage at the grid. Depending on the method of plasma generation, gridded ion thrusters can be categorized into direct-current (DC) [1, 2], radio frequency (RF) [5], and microwave discharge types [31, 32, 7]. In this section, schematics of the gridded ion thrusters are introduced with examples of space operations where they are used.

### 1.2.1 DC gridded ion thruster

A schematic of a DC gridded ion thruster is shown in Fig.1.1 [22]. A hollow cathode is utilized as the electron source. The electrons are accelerated by the potential gap between the cathode and plasma potentials. Then, the high energy electrons ionize the neutral particles. Generally, a magnetic field is applied near the wall to enhance the electron confinement. These thrusters are classified into Kaufman type and cusp type according to the shape of the magnetic field. DC gridded ion thrusters can provide uniform and high-density plasma. In contrast, a hollow cathode can restrict the lifetime and the operation of the hollow cathode is complicated.

Major space missions that use DC discharge gridded ion thrusters are shown in Fig.1.2, 1.3, and 1.4. NASA launched the asteroid probe Deep Space 1 with one NASA Solar Electric Propulsion Technology Applications Readiness (NSTAR) ion thruster in 1998 [1]. The weight of DS1 was 486 kg. It was able to generate 2.5 kW of electric power at 1 AU. Most of the power was supplied from the NSTAR ion thruster, which had a throttling level from 0.6 kW (F: 21 mN, Isp: 2000 sec) to 2.5 kW (F: 93 mN, Isp: 3100 s). The total efficiency of the NSTAR ion thruster was 63 % at maximum. Using this thruster, DS1 flew by the asteroid 1992 KD Braille. The DS1 extended its mission until the encounter with the comet Borrelly in September 2001. The NSTAR thruster operated for 16,000 hours. After DS1, NASA launched the asteroid probe DAWN in 2007 shown in Fig. 1.2. NSTAR ion thrusters were also adopted as the main propulsion system. The destinations of DAWN were Vesta and Ceres [2]. By 2012, DAWN had operated three NSTAR ion thrusters for over 31,000 hours, consuming over 300 kg of xenon. The DAWN mission was extended to 2018. ESA's BepiColombo mission is a collaboration with the Japan Aerospace Exploration Agency (JAXA), with the objective to study the planet Mercury and its environment. BepiColombo was launched in Oct 2018 [3, 4]. The weight of BepiColombo was 1080 kg. Four thrusters based on the 22 cm class Kaufman-type thruster, T6, were mounted. The maximum thrust is 125 mN. The thruster will arrive at Mercury in late 2025.

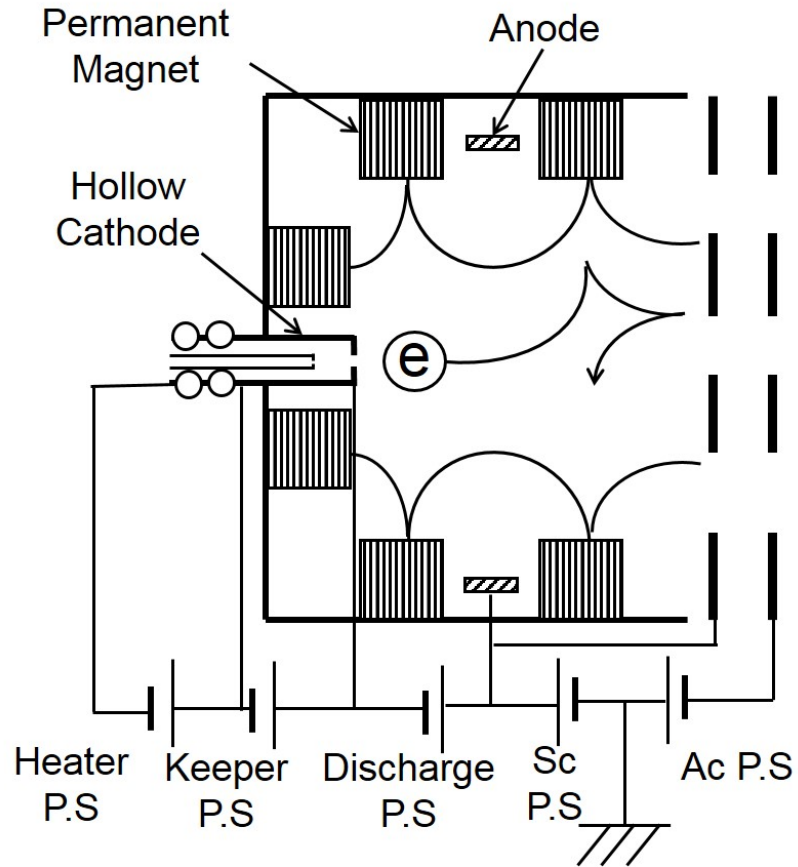


**Fig. 1.1** Schematics of DC discharge ion thruster.



**Fig. 1.2** The NASA's asteroid explorer Deep Space 1 [1].

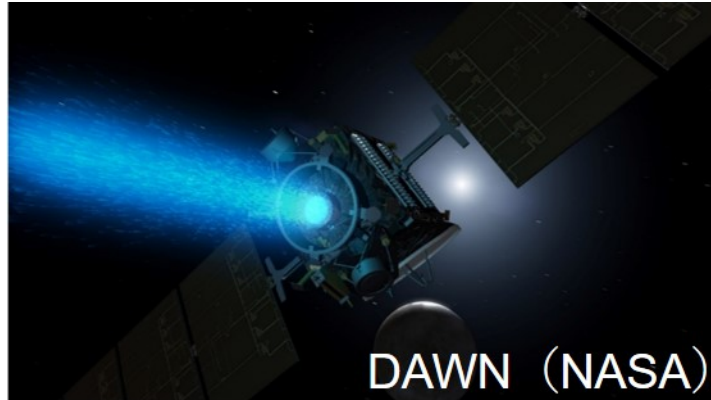


**Fig. 1.3** NASA's asteroid explorer DAWN [2].



**Fig. 1.4** ESA/JAXA Mercury orbiter BepiColombo [3, 4].

### 1.2.2 RF gridded ion thruster

To eliminate potential lifetime restrictions due to a hollow cathode, radio frequency (RF) type thruster have been developed. This type utilizes electromagnetic field at radio frequencies to heat electrons. A simplified schematic of an RF gridded ion thruster is shown in Fig. 1.5. RF voltage is applied to an antenna structure around or in the plasma, and the RF coil is wrapped around a discharge chamber made of a dielectric material. Generally, the RF discharge types are capacitive and inductive (CCP and ICP) coupling types in the RF discharge type, but ICP is often used because ICP can obtain a high ion density [22]. Typically, wide range of frequencies from 0.8 to 10 MHz is utilized. As shown in Fig. 1.6, ESA's communication satellite Artemis employed a German RF ion thruster "RIT-10" and British Kaufmann type "T5" for orbit raising [5].

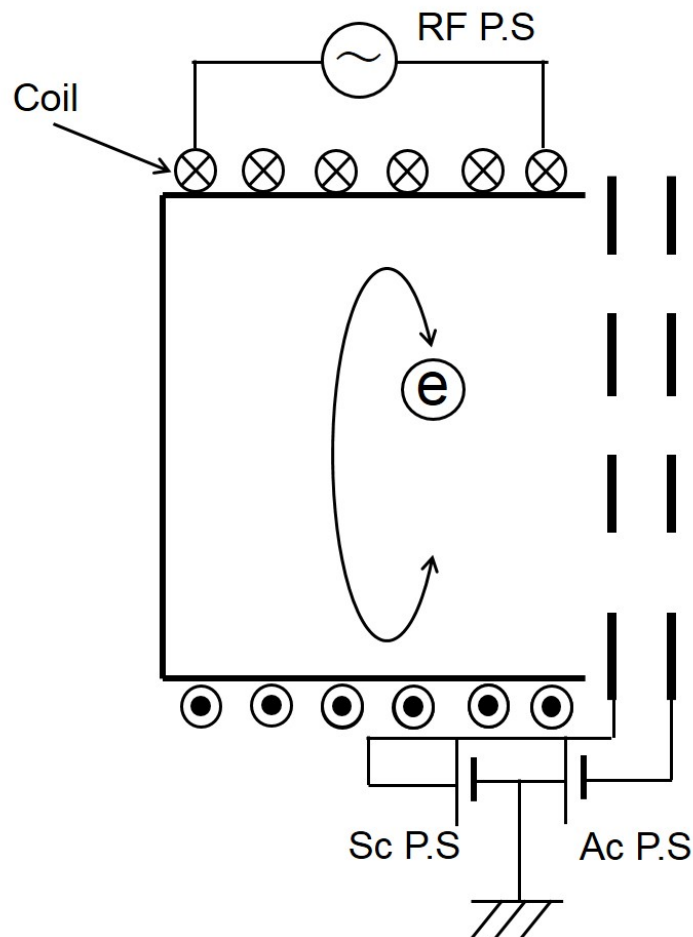


**Fig. 1.5** Schematics of radio frequency discharge ion thruster.



**Fig. 1.6** The ESA's communication satellite Artemis [5].

### 1.2.3 Gridded Microwave discharge ion thruster

Besides RF ion thrusters, microwave discharge is another solution to generate a plasma source without a hollow cathode. A schematic of the microwave discharge ion thruster is shown in Fig. 1.7. To confine electrons inside the discharge chamber, two ring-shaped permanent magnets are arranged. During operation, electrons are heated by electron cyclotron resonance (ECR) continuously during electron confinement. Though the plasma density is lower than that for the DC discharge type, the thruster can be easily operated both in ground-tests and space missions because a hollow cathode is not utilized. To neutralize ion beam, the electron sources also utilize a microwave discharge.

In JAXA, several sizes of microwave thrusters such as the 1-cm class “ $\mu 1$ ” [33], 10-cm class “ $\mu 10$ ”, and 20-cm class “ $\mu 20$  [34]”, have been developed. The  $\mu 10$  thruster was used in the Japanese asteroid explorer missions “Hayabusa” and “Hayabusa 2” as shown in Fig. 1.8. In both missions, 4 thrusters were mounted. In the Hayabusa missions, the accumulated operation was 40,000 hours consuming 45 kg of xenon by the end of the mission [6]. In the Hayabusa2 mission, each thruster reached 5000-6000 hours at 2019 [7]. Additionally, in the University of Tokyo, 1-cm class microwave discharge ion thrusters are utilized in the Small Space Probe ‘PROCYON’ (Fig. 1.9) [8] and nano-satellite HODOYOSHI-4 [35]. PROCYON successfully achieved 223 h operation of on interplanetary orbit. In future mission, Phaethon flyby mission DESTNIY<sup>+</sup> will utilize the  $\mu 10$  thruster [36].

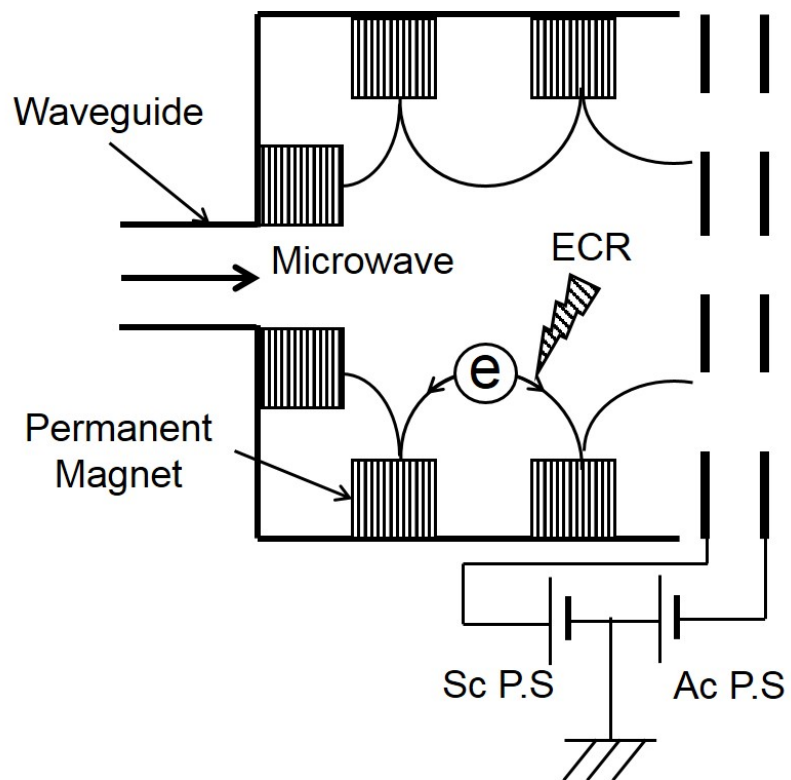


**Fig. 1.7** Schematics of microwave discharge ion thruster.

(a) Hayabusa



(b) Hayabusa 2



(c) Destiny+



**Fig. 1.8** Japanese asteroid explorer Hayabusa and Hayabusa2. Phaeton fly by mission DESTINIY+ [6, 7].

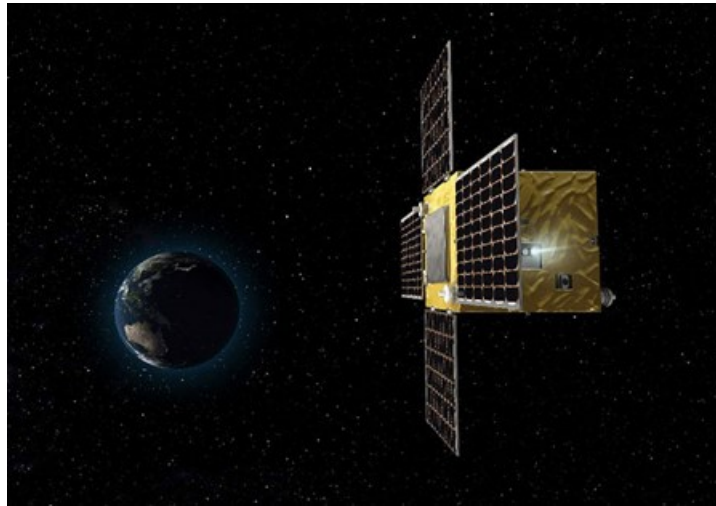


**Fig. 1.9** The small Space Probe PROCYON [8].

### 1.3 Plasma physics of EP devices

In many EP devices, plasma is generated by ionizing the propellant. To make a highly efficient thruster, the design is very important for thrust performance and lifetime; for example, the suppression of wall loss. Because the thrust performance and lifetime strongly involve plasma physics, it is essential background for the development of EP devices. Especially, in many of EP devices, a magnetic field is applied [37, 30]. In this case, the physical phenomena can become very complicated. In this section, the key aspects of plasma physics in EP devices are introduced.

#### 1.3.1 Low-temperature magnetized plasma

In EP devices such as gridded ion thrusters [22], Hall effect thrusters [38], and plasma thrusters (which uses a magnetic nozzle) [39], the plasma can be categorized as low-temperature plasma (LTP). LTPs are very commonly applied to various scientific and technological fields; for example, plasma processing, plasma food sterilization, and environmental applications [40]. Typically, LTPs have characteristic of electron energies of a few eV to 10 eV [40], and the ionization degree is a few % to 10%. LTPs are generated in the plasma sources, and thus the plasma sheath are formed near the wall (surface). Typically, the energy of the plasma sheath is a few to hundreds of eV. Ions sputter the (surface) by the energy of plasma sheath. In many cases, electron energies (temperature) are much higher than the ion or neutral temperatures, i.e., the plasma is in non-thermal equilibrium.

Additionally, in many devices that use LTPs, a magnetic field is applied to suppress the wall loss or to accelerate the plasma [31, 38, 39]. Typically, the magnetic field is a few mT to a few T. In this situation, Hall parameter  $\Omega = \omega_{ce}/\nu_e \approx 10 \sim 10^4$ , where  $\omega_{ce}$  is electron gyro-frequency and  $\nu_e$  is the effective collision frequency of electrons. Because  $\Omega > 1$  means electrons are magnetized, and  $\Omega \approx 10 \sim 10^4$  means the electrons are strongly magnetized. In magnetized cases, the electron mobility parallel to magnetic field is very larger than that perpendicular to magnetic field. To travel across the magnetic field, it is necessary to collide with other particles (neutral particles or ions), which is called classical transport [41]. However, many experimental results indicate that the electron mobility measured by experiments are larger than those predicted by classical transport, which is called anomalous transport. In EP devices, especially HETs, anomalous transport is a critical phenomenon and many researchers

investigate the anomalous transport (heating) using theory, measurement, and numerical simulations [37, 38, 42, 43, 44, 45, 46, 47, 48, 49]. Additionally, because of weak collisions and anomalous heating, electron velocity distribution function (EVDF) cannot be Maxwellian distribution. In fact, non-Maxwellian electrons are observed by many numerical simulation [18, 50, 51, 52, 53] and experimental results [54, 55]. These non-Maxwellian electrons are very sensitive to the ionization rate and play an important role in plasma dynamics.

### 1.3.2 Plasma chemistry

In plasma sources, the reactions between neutral particles, ions, and electrons are utilized for several purposes, e.g, ionization, sputtering, and coating [40, 56]. Generally, the plasma are generated by the electron impact ionization. Additionally, not only ionization but also electronic excitation by electron-impact occur at that time. In molecular gas, e.g, water, dissociative ionization and excitation also occur [57]. In this thesis, xenon is used as a propellant, so these reactions are not discussed.

The electronic configuration is  $1s^2 2s^2 2p^6 3s^2 3p^6 3d^{10} 4s^2 4p^6 5s^2 4d^{10} 5p^6$  in case of xenon in the ground-state. Thus, if excitation occurs, the electrons in  $5p^6$  are transition to another state. In this thesis, electrical configurations are expressed by Paschen notation for simplicity. The correspondence between Paschen notation and excited levels is given in reference [13]. For instance, the ground-state in Paschen notation is  $1s_0$ .

Though there are many kinds of reactions, the important ones are summarized in Tab. 1.1. Generally, ionization and excitation are mainly divided into direct and stepwise (indirect) cases. In direct reactions, e.g., ionization and excitation, electrons react with ground-state neutral particles. On the other hand, in stepwise (indirect) reactions, electrons react with excited state neutral particles. In excitation cases, the lower excited-state particles, e.g,  $1s_4, 1s_5$  can be excited to a higher electrically excited state  $Xe^{**}$  and  $Xe^{***}$  ( $2p_i, 3d_i, 2s_i, 3p_i$ ). In this case, the transition from a higher excited state ( $Xe^{**}, Xe^{***}$ ) to a lower excited state ( $Xe^*$ ) occurs with spontaneous emission. In case of ionization, the excited neutral particles can be ionized to singly, doubly, and triply charged ions. The other reactions are shown. In addition to the stepwise reactions from the lower excited neutral particles, the ionization from the singly-charged ions to doubly-charged ions may be important because the minimum electron energy is very much smaller than that of direction ionization and the ion density can be of the same order as metastable neutral particles. Experimentally, the optical emission was observed near

400 – 500 nm, which indicates that electrically excited ions exist [38]. These ions are used in laser-induced fluorescence spectroscopy (LIF) [58, 59, 60, 61]. Though these interactions between singly and multiply charged ions can be important for EP devices, the effect is outside the scope of this thesis. As mentioned by Pitchford and Boeuf [62], in the case of high-pressure plasma discharge ( $\sim 100$  torr), it was reported that three-body collision is important. However, the pressure in gridded ion thrusters is typically  $10^{-5} - 10^{-4}$  torr, which indicates that the three-body collision can be neglected. For the same reason, Penning ionization can be also neglected [63].

In LTPs, it is generally known that metastable neutral particles, e.g.,  $1s_5$  can be important in the excitation and ionization processes. These metastable particles have very long natural lifetimes ( $\sim 40$  s [64]) compared to resonance states. This is because transitions from metastable states are *forbidden* and are much less probable than *allowed* transitions from other excited states to the ground-state. Direct ionization from the ground-state requires 12.1 eV, whereas stepwise ionization from metastable neutral particles  $1s_5$  requires only 3.8 eV in case of xenon [65], which indicates that relatively low-energy electrons can ionize the particles. Numerical simulation models including the electronically excited states have been proposed by Boeuf [66], Hagelaar [67], and Hara [68]. In addition, recently, theoretical electron-impact cross-sections for xenon ions have been calculated by the Dirac B-spline R-matrix method [69]. Using these theoretical cross-sections in the Collisional-radiative model (CRM), Chaplin et al. pointed out the stepwise ionization from metastable neutral particles is very important for singly-charged ions and doubly-charged ions in Hall effect thrusters [70].

To evaluate the influence of plasma reaction quantitatively, the rate coefficient  $k_{ij}$  are defined as follows.

$$k_{ij} = \int_0^{\infty} \sigma_{ij}(E_e) \sqrt{\frac{2E_e}{m_e}} f(E_e) dE_e, \quad (1.3)$$

where  $\sigma_{ij}$ ,  $E_e$ ,  $m_e$ ,  $f(E_e)$  are the cross-section for excitation from  $i$  to  $j$ , electron energy, electron mass, and electron energy distribution function (EEDF) respectively. Thus, rate coefficient  $k_{ij}$  is determined by the cross-section  $\sigma_{ij}$  and EEDF  $f(E_e)$ . Generally, the cross-section is a function of the electron energy as summarized by LXcat project [71]. If  $f(E_e)$  is stationary isotropic Maxwellian distribution, the rate coefficient is a function of the electron temperature (electron mean energy); this assumption is often used the estimation of rate coefficient.

However, it should be note that non-Maxwellian electrons may not be neglected because the electrons are very sensitive to the rate coefficient.

**Table 1.1** Major electron-impact reactions for xenon

Reaction type	Reaction	Minimum energy,eV	States
Direct Excitation	$\text{Xe} + e^- \rightarrow \text{Xe}^* + e^-$	8.32	Metastable ( $1s_5$ )
Direct Excitation	$\text{Xe} + e^- \rightarrow \text{Xe}^* + e^-$	8.44	Radiative ( $1s_4$ )
Direct Excitation	$\text{Xe} + e^- \rightarrow \text{Xe}^{**}(\text{Xe}^{***}) + e^-$	9.45	Higher excited state
Direct ionization	$\text{Xe} + e^- \rightarrow \text{Xe}^+ + 2e^-$	12.13	Singly-charged ion
Direct ionization	$\text{Xe} + 2e^- \rightarrow \text{Xe}^{++} + 3e^-$	33.11	Doubly-charged ion
Direct ionization	$\text{Xe} + 3e^- \rightarrow \text{Xe}^{+++} + 4e^-$	65.4	Triply-charged ion
Stepwise Excitation	$\text{Xe}^* + e^- \rightarrow \text{Xe}^{**}(\text{Xe}^{***}) + e^-$	-	Higher excited state
Stepwise Ionization	$\text{Xe}^* + e^- \rightarrow \text{Xe}^+ + 2e^-$	3.81	Ground-state ion
Stepwise Ionization	$\text{Xe}^* + 2e^- \rightarrow \text{Xe}^{++} + 3e^-$	24.79	Doubly-charged ion
Stepwise Ionization	$\text{Xe}^* + 3e^- \rightarrow \text{Xe}^{+++} + 4e^-$	57.08	Triply-charged ion

### 1.3.3 Plasma diagnostics

Many kinds of plasma diagnostics have been developed to measure plasma parameters, e.g, density, temperature, and velocity. Plasma diagnostics are mainly divided into electrical measurement and optical measurements. In the EP community, a Langmuir probe [72, 73, 74], emission probe [75, 76, 77, 78], and Faraday cup [79] are often utilized. However, electrical measurements may disturb the plasma environment. To avoid this problem, non-contact methods have been developed, e.g., optical measurements. For instance, passive methods, e.g., optical emission spectroscopy (OES), have been utilized [70, 80, 81, 82]. Because most plasmas in EP devices are in non-thermal equilibrium, Boltzmann equilibrium cannot be satisfied. To consider the effect of non-thermal equilibrium, the CRM approach is often used. Additionally, active optical measurements, i.e., laser spectroscopy, have been utilized. For instance, laser-induced fluorescence (LIF) to measure ion velocity [58, 59, 60, 61], laser-Thomson scattering (LTS) to measure electron density and temperature [55, 83, 84], and two-photon laser induced fluorescence spectroscopy (TALIF) have been developed [25, 85, 86, 87, 88]. Based on the success of plasma diagnostics, the measurement results contribute to the improvement of thruster performance.

However, the measurement of local excitation and ionization rates is still challenging. Generally, the ionization and excitation rates can be written as  $k_{i,j} = \langle \sigma_{i,j} v_e \rangle n_e n_j$ , where  $k_{i,j}$  is the  $i$ -th production rate from a lower state  $j$  (e.g., the ground-state),  $\langle \sigma_{i,j} v_e \rangle$  is the rate coefficient from state  $i$  to state  $j$ ,  $n_e$  is the electron density, and  $n_j$  is the number density at the lower state  $j$ . To evaluate  $\langle \sigma_{i,j} v_e \rangle$ , the cross-section  $\sigma_{i,j}$  and electron velocity distribution function (EVDF) are necessary. Even though the EVDF can be evaluated by the Langmuir probe and LTS methods theoretically. However, it is very difficult to measure of non-Maxwellian electrons because of the low signal to noise ratio, while the electrons are very sensitive to  $k_{i,j}$ .

Additionally, in low-temperature plasma, not only direct ionization and excitation from the ground state, but also stepwise ionization from metastable neutral particles can be important as described in section 1.3.1. Thus, experimental evaluation methods for ionization and excitation are strongly desired.

#### 1.3.4 Plasma mode-transition

A plasma mode transition (i.e., hysteresis) has often been observed for RF and microwave plasma sources such as capacitively coupled plasma, inductively coupled plasma, and electron cyclotron resonance (ECR) plasma [89, 90, 91, 92, 93, 94]. For RF plasma sources, mode transitions are often observed between dominant capacitive coupling (E-mode) dominant and inductive coupling (H-mode) dominant modes [95, 96, 97, 98].

In the case of ECR plasma sources, from the observation of external photographs, it was found that the plasma is concentrated on the magnetic confined region at relatively low pressure or low microwave power. On the other hand, as the microwave power and pressure increases, plasma is also generated outside of the magnetic confined region. A similar mode transition has been observed for the microwave discharge ion thruster ( $\mu 10$ ) [99].

### 1.4 Problem statement

This section, outlines the problem statement for this thesis. First, the author shows the development of thrust performance in the  $\mu 10$  thruster. Second, to understand the layout of this work, the author introduces a brief review of previous measurements inside the thruster. Finally, the challenges of this work are presented.

#### 1.4.1 Development of $\mu 10$ ion thruster

After Hayabusa was launched, improvements were made to the thruster performance. First, based on success of 20 cm class microwave discharge ion thruster [34], the gas injection was additionally equipped between two magnets and thickness of screen grid becomes thin from 1.0 mm to 0.8 mm, which can improve the maximum thrust by 30% compared to Hayabusa mode [7, 9, 32].

Then, the outer magnet was changed to expand the volume of the magnetic confined region and the screen grid was further thinned from 0.8 mm to 0.5 mm, and the maximum thrust was increased by 20% compared to the Hayabusa 2 model [16, 17]. In this thesis, this thruster is called 'Enhanced model 1'. Then, to simplify the magnet shape while maintaining thruster performance as much as possible, the inner magnet was also redesigned [99, 100]. In this paper, this thruster is called 'Enhanced model 2'. The performance improvements are shown in Fig. 1.10. In this thruster, the ion beam current is controlled by changing propellant flow rate, while microwave power is fixed at 34 W. The most important characteristic is that the maximum thrust is limited by the propellant flow rate in any thruster. Here, the flow rate that exhibits the maximum thrust (beam current) is called the optimal flow rate. If the flow rate exceeds the optimal flow rate, the beam current is drastically decreases with increasing propellant flow rate. Performance improvement can be achieved by increasing the optimal flow rate. Thus, *why this optimal flow rate exists, and how the optimal flow rate is determined* are important questions to improve thruster performance. In appendix A, thrust performance in various magnetic strengths and grid configurations was described.

In Enhanced model 1' and 'Enhanced model 2', the ion beam current has two high-current modes. This phenomenon is also important, but will not be discussed in the main body of this thesis, although it is discussed in appendix B.

Generally, Child-Langmuir law represents one of the limitation of thrust (beam current) in gridded ion thrusters (Fig.1.11) [22]. The current density in the Child-Langmuir law is given by,

$$j_{ch} = \frac{4}{9} \epsilon_0 \sqrt{\frac{2\phi}{m}} \frac{V_s^{\frac{3}{2}}}{L_e^2}. \quad (1.4)$$

Here, Then, the maximum ion beam current due to the limitation of Child-Langmuir law is

given by,

$$J_{ch} = j_{ch} F_p A_{eff}. \quad (1.5)$$

Here  $F_p, A_{eff}$  are the flatness parameter and surface area respectively. In  $\mu 10$ , the beam current is not uniform at the grid. Since the space charge limitation limits the maximum current density, it is necessary to evaluate the non-uniformity. This non-uniformity exhibits a flatness parameter, of about 0.7 for  $\mu 10$  [16]. Substituting the typical parameters of  $\mu 10$  into Eq. (1.4) and (1.5), and taking this effect into consideration assuming the extraction area corresponds to the actual opening area,  $J_{ch} \approx 350$  mA. The estimation indicates that the performance limitation of  $\mu 10$  is not derived from Child-Langmuir law, because the maximum current of  $\mu 10$  is about 210 mA. Data for some major 10 cm class ion thruster are shown in Fig.1.12 and Tab.1.2 and these results indicate that ion beam current reach about 240 mA at least [16, 22, 23, 24]. Thus, it is suspected that other limitations exist in microwave discharge ion thrusters.

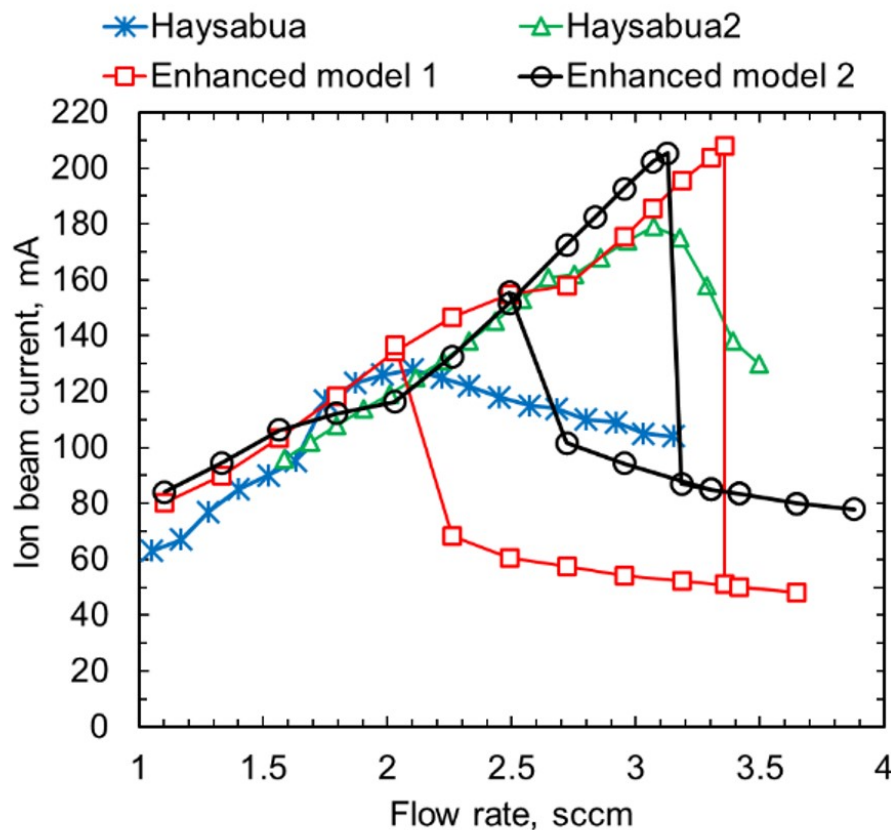


**Fig. 1.10** Performance development of microwave discharge ion thruster  $\mu 10$ . Ion beam current versus propellant flow rate. Blue: Hayabusa, green: Hayabusa2, red: Enhanced model 1, black: Enhanced model 2.

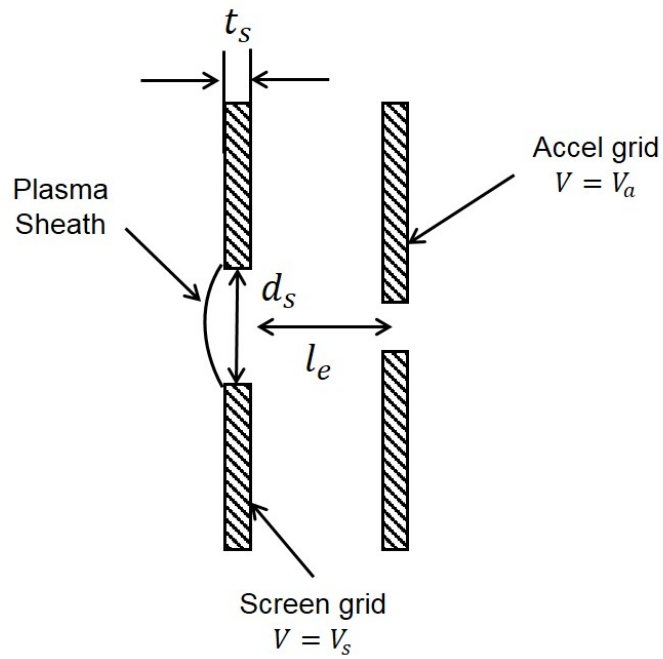


**Fig. 1.11** Grid optics system of ion thrusters. The extracted ion beam current is limited by the Child-Langmuir law given by Eq.(1.4)

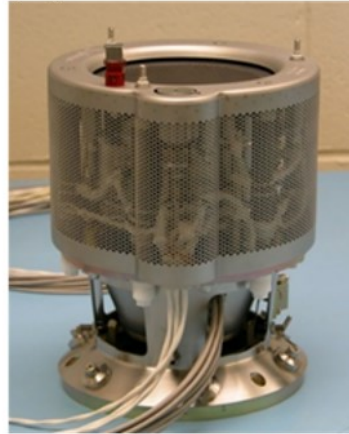
**Table 1.2** Comparison of 10 cm class ion thruster. Photographs are shown in Fig. 1.12 [22, 16, 23, 24].

Thruster	$\mu 10$	RiT-10	T-5	XIPS-13
Diameter, cm	10	10	10	13
Disharge type	Microwave	RF	Kaufman	Cusp
Thrust, mN	12	15	18	17.2
Maximum ion beam current, mA	207	234	329	400
Specific impulse, s	3120	3325	3000	2507
Total power, W	465	459	476	421
Thrust efficiency, %	40	52	55	50

(a) XIPS-13



(b) T5



(c) RIT-10



(d)  $\mu$ 10



**Fig. 1.12** Photograph of major 10 cm class ion thrusters. (a) XIPS-13, (b) T5, (c) RIT-10, (d)  $\mu$  10. Detailed thruster performances data are summarized in Tab. 1.2

## 1.4.2 Review of internal plasma diagnostics

First, Fig. 1.13 shows external photographs of the thruster at various flow rates. The photographs indicate that the luminescence is drastically changes with increasing of the propellant flow rate. Specially, downstream of the waveguide, luminescence cannot be observed at a low flow rate. However, at the optimal flow rate, luminescence starts to be observed downstream of the waveguide. Above the optimal flow rate, the luminescence is concentrated downstream of the waveguide. In the case of xenon, red luminescence shows spontaneous emission due to the transition from higher excited neutral particles to lower excited neutral particles. On the other hand, blue luminescence shows spontaneous emission from the transition from higher-energy excited ions to lower-energy excited ions. Because the luminescence was changed by increasing the propellant flow rate, this indicates that the excitation and ionization processes are also changed. A similar phenomenon is also observed in other ECR plasma sources and is called plasma mode transition. Specifically, in the case of low flow rate, the ionization is concentrated in magnetic confined region. As the flow rate increases, the ionization occurs outside the magnetic confined region. However, only information outside thruster, the detailed mechanism cannot be revealed from information obtained by external observation. In particular, the axial dependence cannot be resolved.

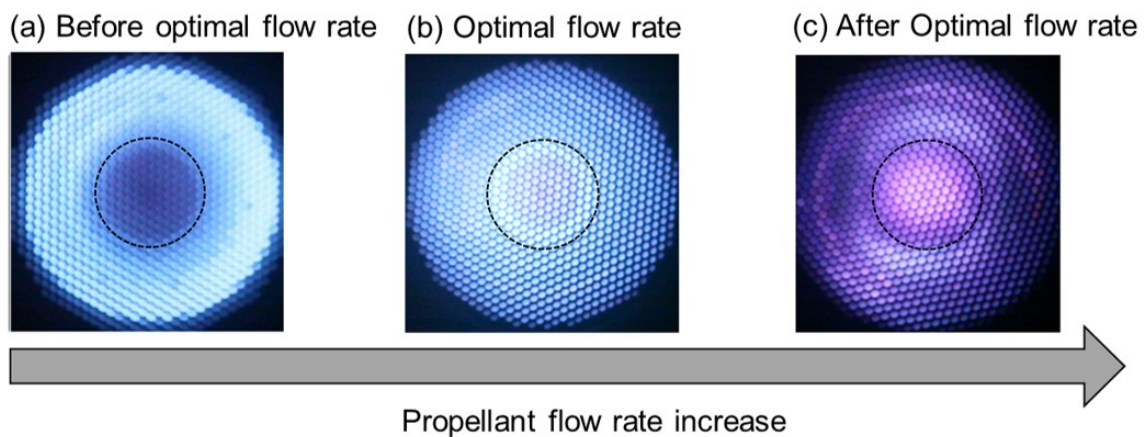


**Fig. 1.13** Transition of photographs outside thruster as a function of propellant flow rate. These photographs are taken under the same conditions, e.g, exposure time.

Thus, to obtain the information about the internal plasma characteristics, optical measurements have been developed. Generally, a Langmuir probe has the disadvantage that the probe can disturb the plasma state. Notably, in microwave plasma sources, Dielectric materiel of the

probe can disturb by the electric field of the microwaves. To avoid this disturbance, internal plasma diagnostics have been performed by using an optical fiber probe. Tsukizaki and Kuni-naka firstly proposed optical fiber measurements [9]. The optical emission distribution inside the thruster at the central axis was measured as shown in Fig.1.14. The results showed that the optical emission inside the waveguide increases according to the propellant flow rate. Because most natural lifetimes are the order of several ten ns at maximum and the velocity have the order of  $10^3$  m/s, the particles can move only the order of  $\mu$  m, which is much smaller than the thruster scale. Thus, this measurement indicates that electrons exist inside the waveguide as the propellant flow rate increases.

Additionally, the excited neutral particle densities in both the resonance state ( $1s_4$ ) [11] and metastable state ( $1s_5$ ) [10] were measured by laser absorption spectroscopy (LAS). Along with the optical emission distribution, metastable neutral density inside the waveguide increased according to the propellant flow rate. The resonance states neutral density could not be detected by the lower propellant flow rate, but the absorption could be detected as the flow rate increases. The absolute value of the metastable and resonance states were calculated from the Boltzmann equilibrium and excited electron temperature  $T_{e,excite}$  measured by the line pair method [19]. The metastable neutral density was on the order of  $10^{17} - 10^{18} \text{ m}^{-3}$ , and the resonance state neutral density is the order of  $10^{15} - 10^{16} \text{ m}^{-3}$  at a flow rate of 3 sccm which is the optimal flow rate in the case of DC injection. Thus, the metastable neutral density is two orders of magnitude larger than that of resonance states.

Finally, an electric-optical (EO) probe was used to measure the electric field of the microwaves [11, 12]. The electric field of microwaves can be measured by the change in polarization of light waves propagating through one round trip in the EO probe. The measurement results are shown in Fig. 1.17. The experimental results revealed that the microwaves cannot propagate sufficiently to the discharge chamber, e.g., cut-off phenomenon after optimal flow rate. In other words, the plasma density inside the waveguide increases according to the flow rate.

Based on the above-mentioned previous works, the plasma is generated inside the waveguide as the propellant flow rate increases. Then, after plasma mode-transition, microwaves cannot propagate to the discharge chamber because of the cut-off phenomenon. However, *why plasma is generated inside the waveguide* was not revealed. Generally, in ECR plasma

sources, the plasma is generated at the magnetic confined region due to continuous ECR heating and the mirror magnetic field. Thus, the plasma generation process cannot be explained. Thus, to reveal the physical mechanism of the ionization process, it is necessary to measure this phenomenon.

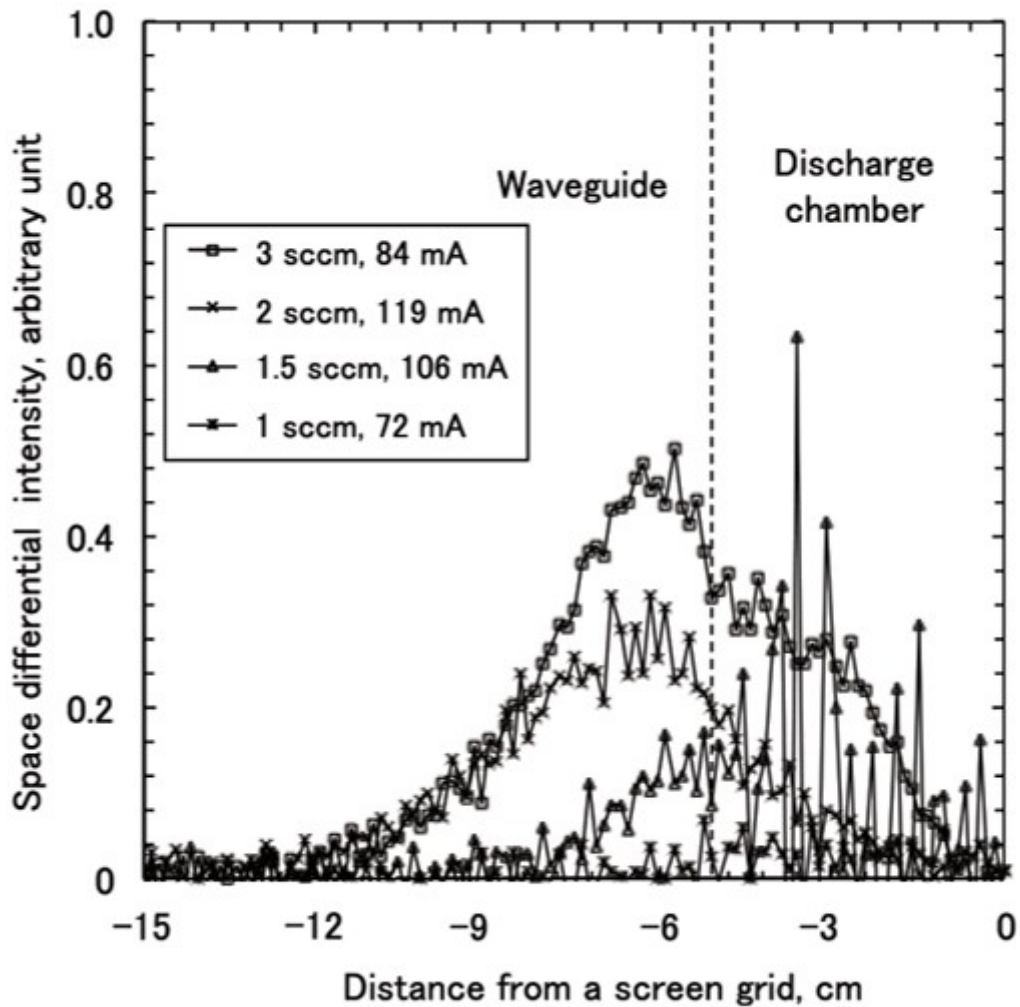
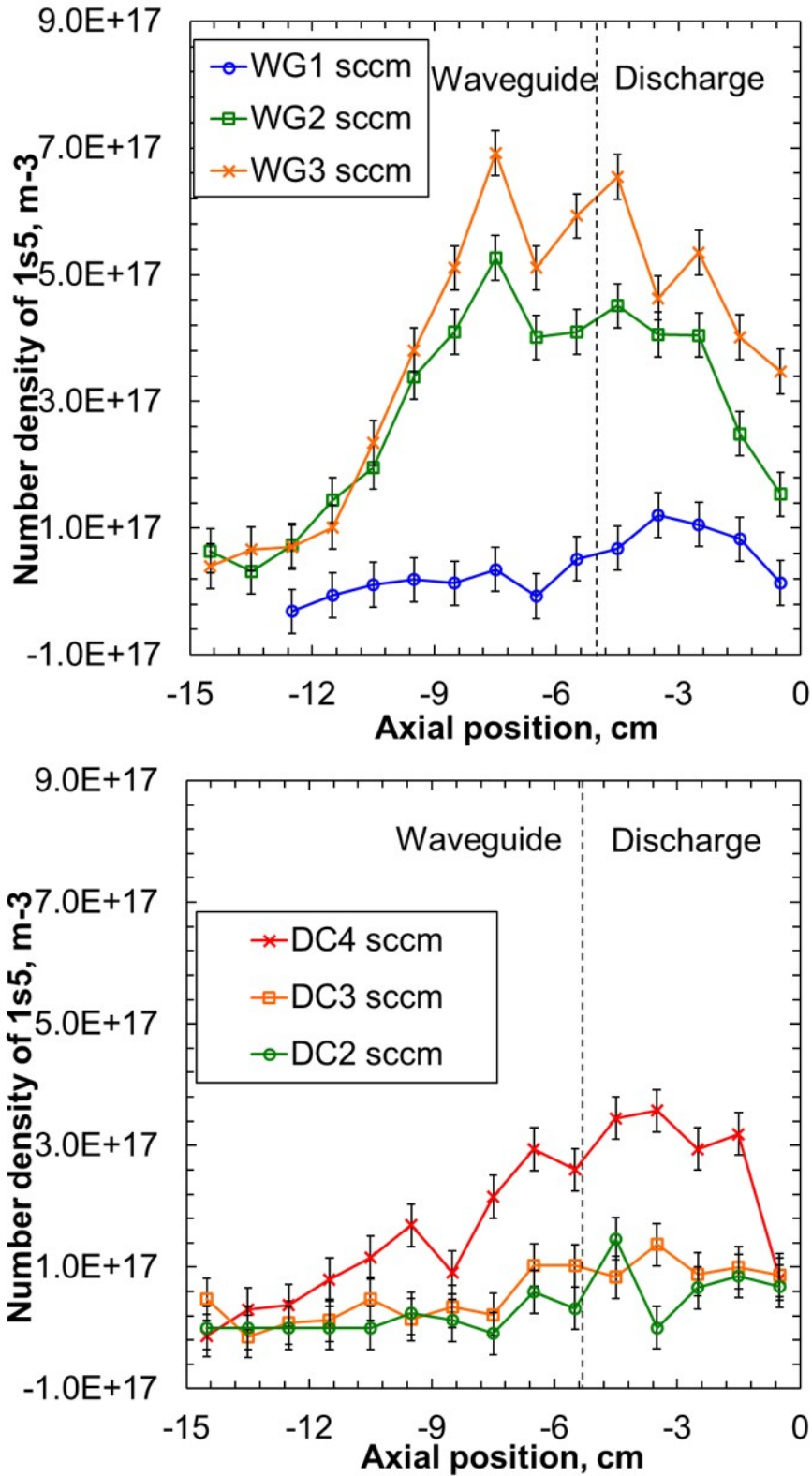
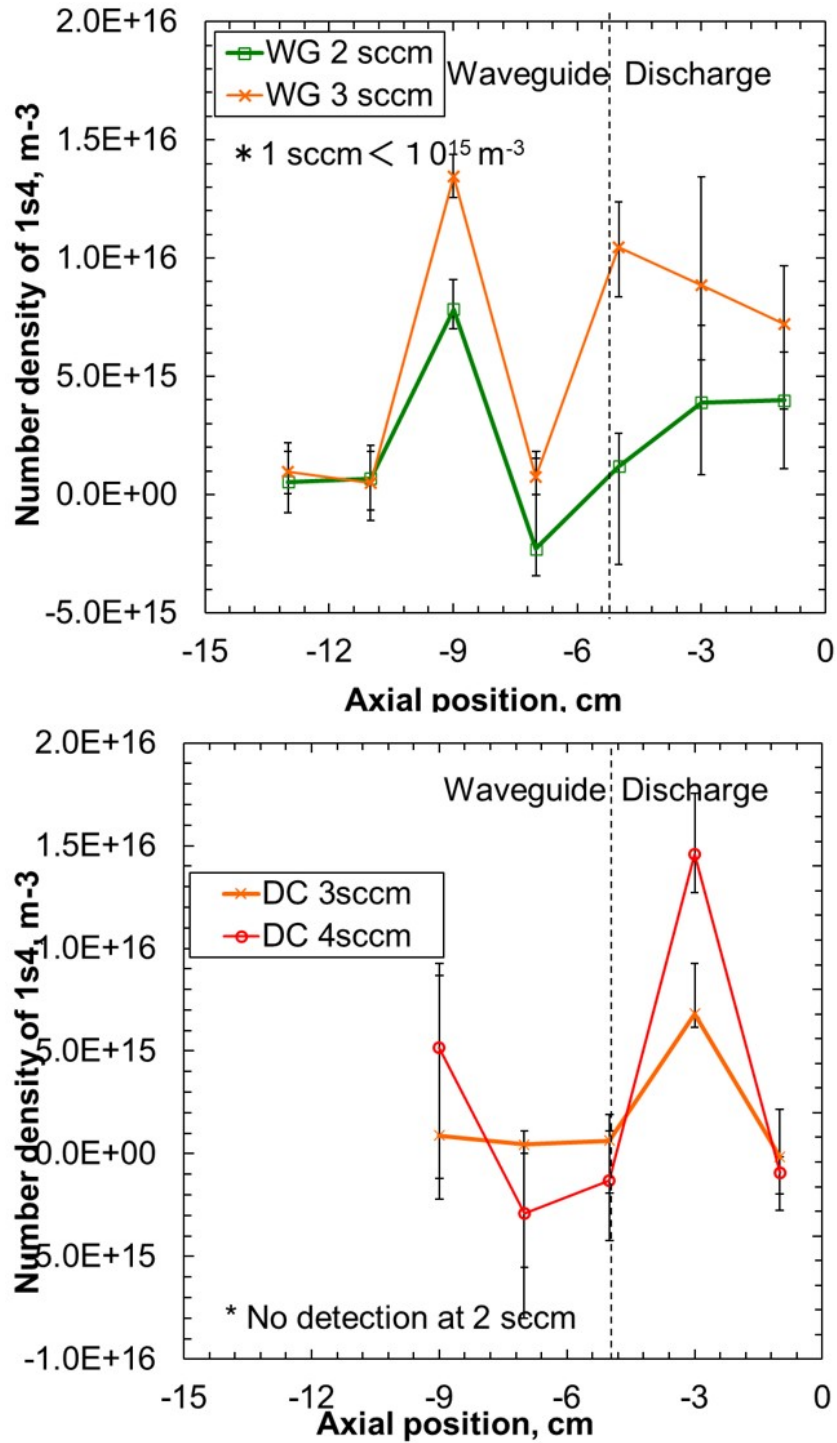


Fig. 1.14 Luminescence measurements using an optical fiber probe. Net input microwave power 34 W [9].



**Fig. 1.15** Metastable state  $1s_5$  neutral density distribution. Top: distribution when the propellant was injected only from the waveguide inlet (WG), Bottom : distribution from the discharge chamber inlets (DC). At propellant flow rates of 1.00 sccm from the waveguide inlet and 2.00 sccm from the discharge chamber inlet, it was not possible to detect absorbance [10].



**Fig. 1.16** Resonance state  $1s_4$  neutral density distribution. Top: distribution when the propellant was injected only from the waveguide inlet (WG), Bottom : distribution from the discharge chamber inlets (DC). At propellant flow rates of 1.00 sccm from the waveguide inlet and 2.00 sccm from the discharge chamber inlets, it was not possible to detect absorbance [11].

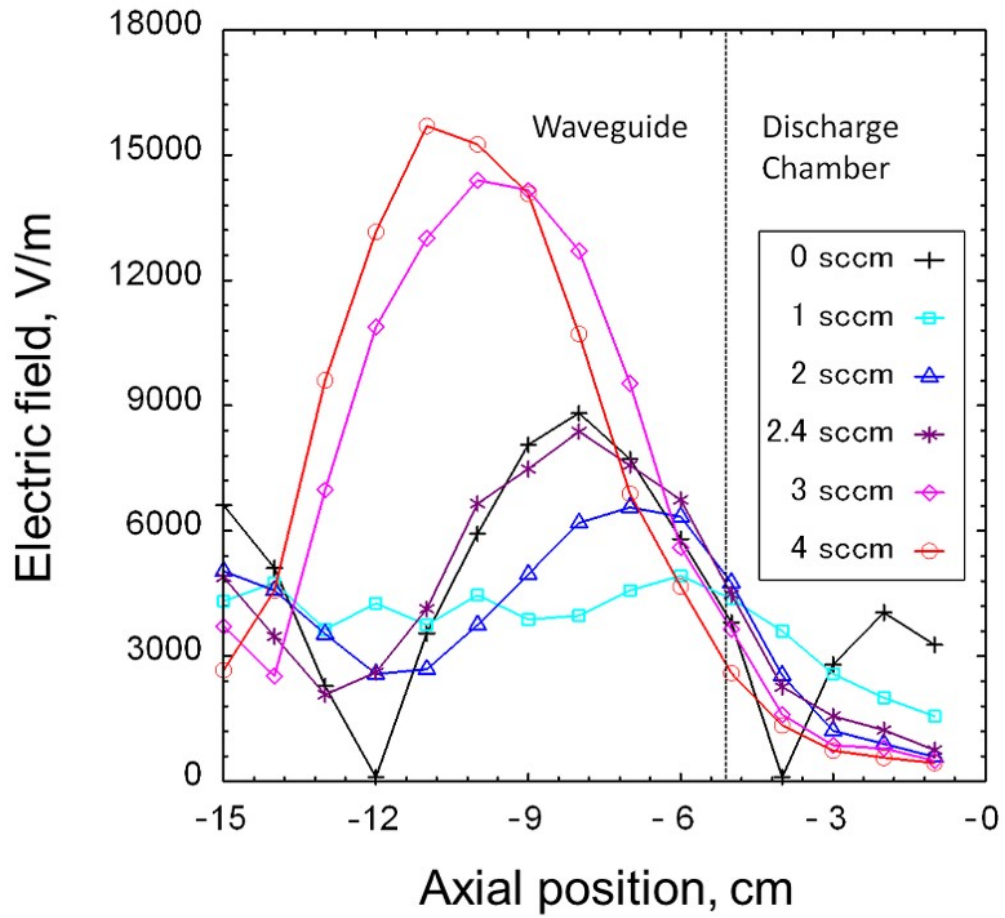


**Fig. 1.17** Electric field distribution oscillating parallel to the dipole antenna along the center line of the plasma source in the accelerated plasma at mass flow rates of 0, 1, 2, 3, 4 sccm [12]. The input microwave power is 34 W. The measurement error is 10 % on the amplitude of the electric field.

## 1.5 Challenge

To understand the physical mechanism of the ionization process inside the waveguide, the author proposes the hypothesis of plasma mode-transition. Then, to prove the hypothesis, both experimental and simulation approaches are utilized. In this section, the purposes of the experiment and simulation are introduced.

1. Measurement of ionization and excitation process
2. Numerical estimation of ionization and excitation rate distributions

### 1.5.1 Plasma mode-transition hypothesis

Based on the characteristic of ECR plasma sources, the plasma is strongly inhomogeneous, including the plasma density and electron temperature, and this characteristics were observed several full-kinetic simulation works [18]. In magnetic confined region, the plasma density is one order of magnitude larger than that of other regions. In this area, electron temperature exceeds 10 eV, which means that the direct ionization can be occurred easily. In contrast, the electron temperature is 3-4 eV outside the magnetic confined region, which indicates that the number of electrons that induce the direct ionization is drastically small. Thus, according to the high plasma density and electron temperature, direct ionization and excitation are also concentrated in the magnetic confined region. Additionally, the Hall parameter  $\Omega \approx 10^3 \sim 10^4$ , which indicates that electrons are strongly magnetized. Therefore, it is difficult for electrons to transport from the discharge chamber to the waveguide.

However, metastable neutral particles can be transported to the discharge chamber and the electron energy generating the stepwise ionization of singly-charged ions requires 3 – 4 eV, which indicates that electrons that are not heated by ECR can generate plasma. Therefore, stepwise ionization can be important for generation of plasma inside the waveguide, which induces a plasma mode-transition. Therefore, the author proposes experimental and numerical approaches that can evaluate the ionization and excitation process of direct and stepwise ionization.

### 1.5.2 Measurement of excitation and ionization processes

Generally, to evaluate local ionization rates including direct and stepwise, it is necessary to measure the electron density, EVDF, and lower state neutral density (e.g., ground-state and

metastable state) at the same location. However, because it is expected that the plasma density is the order of  $10^{16} \sim 10^{17} \text{ m}^{-3}$  [18] and the measurement point is inside the thruster, it is difficult to measure electron density and EVDF accurately. Thus, in this study, the excitation process directly evaluated by measuring ground-state neutral density and spontaneous emission intensity at the same time under the experimental set up of TALIF. If a higher excited state transit to a lower excited state, spontaneous emission is generated, which provide information about the excitation process. Generally, the spontaneous emission intensity can be expressed as follows.

$$I_{spo} = I_0 \left( k_{g,j} n_g + \sum_{i=1}^N k_{i,j} n_i \right) n_e \quad (1.6)$$

Here,  $I_0$  is a constant value,  $k_{g,j}$  and  $k_{m,j}$  are rate coefficients from ground-state  $g$  and lower excited state  $j$  to higher excited state  $j$ . Noted that Eq. (1.6) assumes optically thin, that is, the radiation trapping is neglected because of low plasma density [4]. The validity of optically thin will be discussed in chapter 2. The natural lifetime of the spontaneous emission is on the order of ten ns: thus the neutral particles can move only within 0.01 mm, which indicates that the discrepancy between measurement point and the point of spontaneous emission can be considered negligible.

Figure 1.18 shows the correlation between the ground-state neutral density and spontaneous emission intensity. If the ground-state neutral density can be measured, direct excitation rate can be estimated. Then, if stepwise excitation is not negligible, the intensity of the spontaneous emission is not proportional to the ground-state neutral density. Additionally, in this case, stepwise ionization also cannot be neglected because the ionization energy is close to the excitation energy. In this case, the electron density at the measurement point is enhanced due to the stepwise ionization; thus the spontaneous emission intensity in Eq. (1.6) further increases. Last, increase of the electron temperature can also enhance the spontaneous emission intensity. Thus, to determine the main contributions to the spontaneous emission, experiments were conducted on several kinds of thruster by changing the location gas injection and electron heating process.

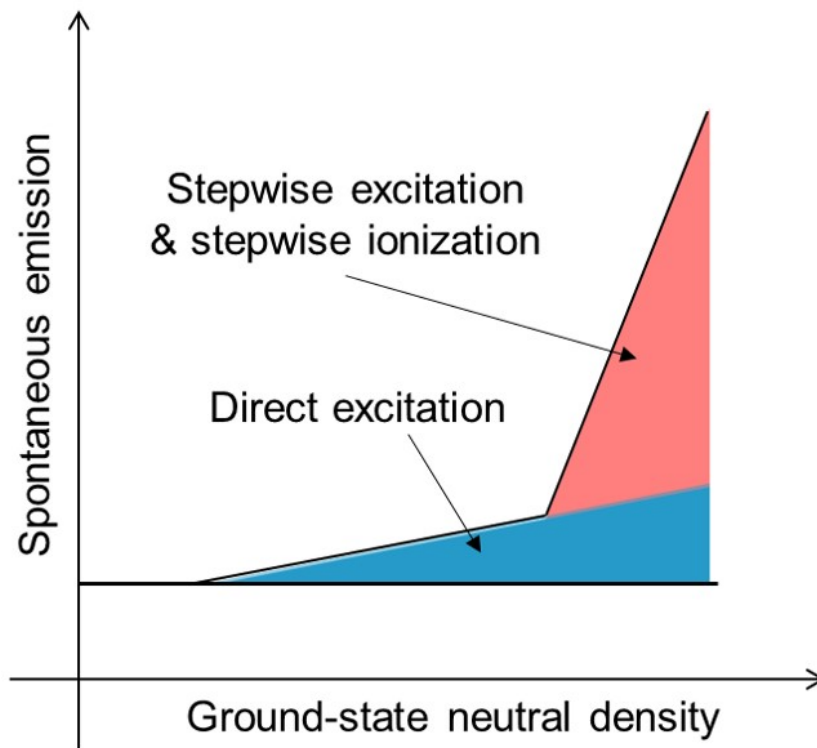


**Fig. 1.18** Correlation between ground-state neutral density and spontaneous emission intensity. If the stepwise excitation and ionization cannot be neglected compared to direct excitation, the spontaneous emission intensity sharply increases.

### 1.5.3 Numerical estimation of ionization and excitation rate distributions

In previous studies, the excited neutral density and electric field of microwaves were measured. In this thesis, the ground-state neutral density and spontaneous emission intensity were measured. These experimental data should show the physical mechanism of plasma mode-transition partly. However, experimental measurement approach generally has following two weaknesses.

1. Observation and location of plasma parameters are limited (Unobserved parameters exist)
2. Correlation between each parameters is unclear

For instance, the unobserved parameters, e.g., electron density, ionization rate, and excitation rate, can be important. Further, the measurement location is limited to the central axis because of the problems of the low signal to noise ratio and disturbance. Additionally, relationship between each measured parameter is not clear.

Numerical simulation techniques are very useful for overcoming these problem. In case of plasma, the most accurate approach is to simulation all phenomena by using kinetic treatment (e.g., full-kinetic simulation), and then to compare with the experimental data. For instance, Takao and Koizumi performed three-dimensional electrostatic (ES) full-PIC simulation for 1cm class microwave discharge and then the simulation results are verified by using metastable neutral density distribution measured by LAS [50, 101]. However, these accurate approaches are limited to relatively small size thruster. In case of  $\mu 10$  thruster, the scale is ten times larger and three dimensional full-PIC simulation is very challenging. Especially, in microwave plasma sources, it is very important whether the wavelength of microwave is larger than the scale of thruster or not. If the wavelength is larger, electromagnetic (EM) treatment is desirable, whereas EM treatment is generally more difficult than ES one in view of computational cost and numerical stability. In appendix C, detailed description about difference between ES and EM PIC simulations, and then the author developed two approaches; two-dimensional explicit ES PIC simulation and one-dimensional semi-implicit EM PIC simulation.

An alternative would be a data assimilation approach. For instance, in HETs, to reproduce anomalous collision frequencies, kinetic treatment is necessary such as ECDCI. However, as described in the previous paragraph, it is very computationally expensive. Hence, 'artificial' anomalous collision frequency is employed in Hybrid-PIC simulation, and then the simulation

results compared with experimental data such as the discharge current, the electron temperature, and the plasma density [102, 103, 104]. By comparing simulation results by using many kinds of '*artificial*' anomalous collision frequency with experimental data, '*true*' anomalous collision frequency is estimated. Additionally, time-resolved parameters are estimated by physics constrained-extended Kalman filter [105].

In this work, by using similar approach, the ionization and excitation rate distributions were estimated. Specifically, the following kinds of numerical simulations were performed. Then, the objective of the numerical simulations and estimation parameters are summarized in Tab. 2.5.

- (a) Particle simulation of ground-state neutral particles
- (b) Particle simulation of metastable neutral particles
- (c) Simulation of electromagnetic field and plasma density

In case (a), the purpose is to estimate the ionization rate, and to clarify the ground-state neutral density distribution due to changes in gas injection. Generally, the characteristic length of this thruster is the order of 0.1 m. The neutral density is the order of  $10^{18} \sim 10^{19} \text{m}^{-3}$ ; thus, the mean free path is about  $1 \sim 10$  m. In other words, Knudsen number is about  $10 \sim 100$ . Generally, if the Knudsen number is larger than 10, the flow can be regarded as free molecular flow [106], which indicates that the kinetic treatment of kinetic effects is necessary. In this thesis, to capture neutral dynamics including kinetic effect, direct simulation via the Monte Carlo method (DSMC) was utilized. In chapter 3, the estimation of ionization rate distribution will be described under nominal thruster operation, i.e., with ion extraction. In appendix D, the difference of neutral density between with and without ion extraction will be discussed.

In case (b), the purpose is to estimate the excitation rate for metastable states. Generally, the metastable neutral particles have natural lifetime on the order of ten seconds, but the actual lifetime can be reduced due to wall diffusion and collision with other particles [80]. Thus, to specify the location where metastable particles are generated, i.e., excitation rate distribution in metastable state, it is necessary to calculate the particle simulation considering the de-excitation of wall diffusion and collision with other particles. In this thesis, Monte Carlo approach was used to simulate the de-excitation [107].

Last, in case (c), the purpose is to estimate the contribution of stepwise ionization. Gen-

erally, the electric field of microwaves is damped in the presence of plasma, i.e., a cut-off phenomenon [41]. The amplitude of the electric field strongly depends on the plasma density. Thus, by the comparison of electromagnetic field obtained by numerical simulation and experiment, the plasma density can be estimated. Further, if plasma diffusion equation [56] is coupled, the contribution of stepwise ionization can be elucidated. Specifically, depending on the ratio of density between ground-state neutral density and the metastable neutral density, stepwise ionization can be comparable to that of direct ionization.

**Table 1.3** Summary of purpose and targets in numerical simulation

Target	Remark	Purpose	Validation
Ground-state neutral particles	Particle simulation (DSMC)	Estimation of ionization rate distribution. Effect of gas injection against neutral density distribution	TALIF
Metastable state neutral particles	Particle simulation and Monte Carlo approach to simulate the de-excitation due to collision with other particles	Estimation of excitation rate distribution at metastable state	LAS
Electromagnetic field of microwaves	Plasma diffusion equation and Helmholtz equation of the electric field	Contribution of stepwise ionization against the plasma density	EO probe

#### 1.5.4 Thesis outline

In chapter 2, the experimental approach to evaluate the excitation and ionization processes by measuring ground-state neutral density and spontaneous emission intensity is proposed. Then, the development of TALIF measurement is also described. Chapter 3 expresses numerical approach to estimate ionization and excitation rate distributions. There are three kinds of simulation; ground-state neutral particles, metastable neutral particles, and electric field of microwaves. In chapter 4, experimental results in chapter 2 and simulation results in chapter 3 are summarized and then describe cause of plasma mode-transition. In appendix A, thrust performance in various magnetic strengths and grid configuration are summarized. Then, possible thrust improvement based on physical mechanism of plasma mode-transition is proposed. In appendix B, detailed explanation of plasma hysteresis and the operation method is mentioned. Appendix C exhibits the development of full-kinetic simulation. Last, in appendix D, difference of neutral densities between with and without ion extraction are discussed by using DSMC and TALIF.

## Chapter 2

# Experimental evaluation of ionization and excitation processes by measuring ground-state neutral density and spontaneous emission intensity

### 2.1 Outline of TALIF measurement

In this thesis, the ground-state neutral density and spontaneous emission intensity were measured under the experimental setup of TALIF. In this section, outline of these measurements will be introduced.

In EP community, Neutral particles can give important information on plasma parameters such as the ionization degree and the charged exchange (CEX). Specifically, the  $\mu 10$  microwave ion thruster developed in Japan exhibits a 40% increase in thrust by changing the propellant inlet from the waveguide to the discharge chamber [7, 32, 9]. Additionally, the microwave cathode lifetime in this unit is improved by increasing the flow rate [7]. Neutral dynamics is also important for low frequency oscillation, e.g., breathing mode, of HETs [38, 49].

Direct simulation Monte Carlo (DSMC) simulations have been performed to analyze the behaviour of neutral particles. However, this simulation requires assuming reflection at the boundary and a neutral temperature [106]. In addition, with plasma, it is necessary to consider the recombination of ions at the wall. Then, the energy of recombined particles needs to assume because the energy depends on the wall material and gas [108]. In addition, ionization collisions and wall neutralization are considered to affect the neutral particle density distribution. Therefore, the measurement of neutral particles will also give useful information for numerical simulations.

There are several methods to measure the neutral density. For instance, Nakayama used a

pressure gauge to measure the neutral density [109]. Although the neutral particles were successfully measured in that work, this technique may not be applied to the plasma environment of EP devices because the metallic probe can disturb this environment. Laser spectroscopy is an attractive measurement in view of non-contact that is less disturbance against plasma. Laser spectroscopy to measure neutral particles can be mainly divided into laser Rayleigh scattering (LRS) and laser induced fluorescence (LIF). Because the wavelength of the scattering signal is the same as that of the laser light, effective stray light removal technology is necessary [110]. In LIF, the wavelength of the fluorescence signal is different from that of the laser and hence LIF does not need highly effective stray light removal technology.

Based on background, LIF methods are commonly utilized in EP community. As described in section 1.3.2, neutral particles can be divided into excited neutral particles or ground state particles. Neutral excited state have been measured by normal LIF and LAS. However, it is difficult to measure ground-state neutral particles by using normal LIF and LAS (will describe the reason in later section 2.2). However, the information about the excited neutral particles is insufficient to capture the neutral density because most neutral particles are in the ground-state in case of non-equilibrium plasma. In non-equilibrium plasma, the relationship between the excited and ground states, i.e., Boltzmann relation, may be inaccurate. Thus, it is difficult to obtain the neutral density from the density of excited neutral particles.

To overcome these limitations, two-photon absorption LIF (TALIF) has been developed [25, 85, 86, 87, 88]. TALIF measurements have been also utilized in many kind of applications except for EP devices. For instance, in application of heated wind tunnel, gas temperature have been measured by TALIF [111]. The temperature corresponds to Doppler broadening of TALIF spectra. In addition, in plasma community, the absolute density measurement of atomic oxygen have been measured [112]. The absolute density is obtained by a calibration of xenon TALIF measurement. TALIF measurements have been applied to measure the density, temperature and velocity of ground-state neutral particles from around 1990. In TALIF measurement, Empirical intensity–density relationships between the fluorescence signal and neutral species in the plume that take into account all states have been studied in detail using the ion gauge [87]. Hence, it does not require model to evaluate the neutral density.

The TALIF measurement against EP devices are summarized in Tab. 2.1. In HETs, M.W. Crofton applied to SPT-140 to investigate the neutral velocity near the plume, and the collision

of ions and neutral particles like CEX [85]. In gridded ion thrusters, C. Eichhorn applied to RIT-10 to measure the relationship between the neutral density and ion beam current at the plume [87]. After K Kinefuchi developed the TALIF measurement system for the first time in Japan [25], the author applied to microwave cathode to investigate the relationship between anode current and ground-state neutral density [88].

However, in above activities, the location of measurement is limited to the plume due to difficulty of access and low signal to noise (S/N) ratio. The measurement inside the thruster has capability of revealing the physical mechanism, e.g., ionization process, which is just the propose of this study. In 2019, C. Eichhorn tried the measurement inside the RIT10 gridded ion thruster [113]; however, he reported that the measurement inside the TALIF was succeeded by detecting the fluorescence from the orifice of grids, but the measurement is limited at the propellant utilization efficiency. To mitigate the issues noted above, the work employed two 4-mm-diameter windows for the purposes of laser beam injection and signal detection. Because these windows are very small, thrust performance can maintain at reasonable level. Additionally, to evaluate the excitation and ionization, the spontaneous emission intensity by electron impact excitation is measured at the same time.

In this work, TALIF measurements are applied to four types of thrusters to reveal the plasma mode-transition. First, to investigate the effect of gas injection, i.e., neutral density distribution, waveguide injection (WG) and Discharge chamber injection (DC) are performed in the magnetic field of Hayabusa model. DSMC works reveled that the location gas injection clearly produces the difference of ground-state neutral density inside the waveguide. Additionally, the thrust performance is clearly different, thus the effect of gas injection against plasma mode-transition can be reveled. In another cases, the TALIF measurement is applied to the 'Enhanced model 2'. Then, 'Enhanced model 2' is changed so that ECR heating does not occur. Because the spontaneous emission intensity is a function of electron temperature, thus the effect of electron heating process against plasma mode-transition was investigated.

**Table 2.1** Major application of TALIF measurements for EP devices

Thruster	Location	Purpose	Reference
HET, SPT-140	Plume	Measure neutral velocity near cathode	[85]
GIT, RIT-10	Plume	Relationship between neutral density and ion beam current	[87, 113]
Cathode, $\mu 10$	Plume	Relationship between anode current and neutral density	[88]
GIT, $\mu 10$	Inside	Measure excitation and ionization processes	this study

## 2.2 Theory

### 2.2.1 Two-photon excitation

Generally, reaction from ground-state by singly photon-excitation is given by

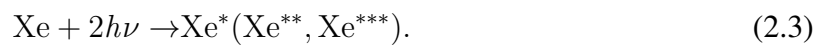


Thus, wavelength of photon (laser) is decided by the difference of higher (excited) state and lower state. Generally, to generate photon-excitation from  $i$  (lower) state to  $j$  (higher) state, the wavelength  $\lambda_1$  is decided by

$$\lambda_1 = \left( \frac{E_i - E_j}{hc} \right)^{-1}. \quad (2.2)$$

Here,  $c$  is light speed,  $h$  is Plank constant.  $E_i$  and  $E_j$  are the energy at  $i$  and  $j$  states respectively. The case of excitation from ground-state, i.e.,  $E_i = 0$  eV is considered. Because the excitation energy in case of xenon is about  $E_j = 8 \sim 11$  eV typically [65], the wavelength can be calculated;  $\lambda_1 \approx 112 \sim 148$  nm. Generally, The range of wavelength that is shorter than 200 nm is generally called Vacuum Ultra Violet (UAVV). In this range, it is difficult to use a laser because the power of a laser with a wavelength shorter than 200 nm is absorbed in the air. Thus, it is difficult to use singly photon ionization, i.e., normal laser-induced fluorescence spectroscopy (LIF) and LIF measurement is limited between both excited states.

To solve these limitation of normal LIF, two-photon excitation is used. Figure 2.1 shows the schematics of single-photon and two-photon excitation respectively. Generally, the reaction of two photon excitation can be expressed as follows.



In this situation, the wavelength  $\lambda_2$  can be calculated by

$$\lambda_2 = \left( \frac{E_i - E_j}{2hc} \right)^{-1}. \quad (2.4)$$

The results indicate that the wavelength of two-photon excitation is two times larger than that of single-photon excitation, i.e.,  $\lambda_2 = 2\lambda_1 \approx 224 \sim 256$  nm, which is larger than 200 nm. Thus, the LIF that use two-photon excitation, i.e., TALIF, can excite the ground state. As

shown in Eq.(2.3), there are many choices of the excitation  $Xe^*$ ,  $Xe^{**}$ ,  $Xe^{***}$ , which means that the excitation process can be selected according to required conditions. These requirement will be described in section 2.2.3.

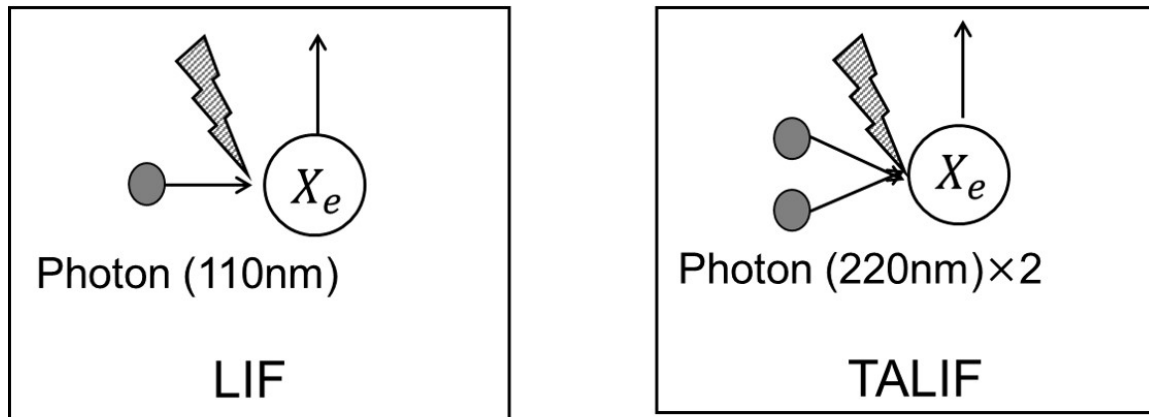


**Fig. 2.1** Difference of photon excitation process between LIF and TALIF. In TALIF, two times wavelength can excite compared to LIF.

## 2.2.2 Spontaneous emission

In this paper, the ground-state neutral density and spontaneous emission intensity are measured at the same time. This measurement is based on a principle that the wavelength of fluorescence and spontaneous emission by electron-impact excitation is the same. For instance, in case of the normal LIF against metastable ions, the wavelength of fluorescence is different that of spontaneous emission by electron-impact excitation [25]. Thus, comparing with the normal LIF with TALIF, in TALIF measurement, the main background noise is the spontaneous emission of same wavelength that cannot be eliminated by optical devices (e.g., band-pass filter, monochromator), whereas can measure the ground-state neutral density and spontaneous emission intensity under the same experimental setup. The spontaneous emission includes the direct excitation from the ground-state neutral density and the stepwise excitation that is excited from lower excited states, e.g., metastable neutral particles. Because the rate coefficient of the direct excitation is proportional to the ground-state neutral density, the stepwise excitation can be evaluated by comparing the ground-state neutral density with the spontaneous emission intensity.

### 2.2.3 Determination of the wavelength

There are many kinds of two-excitation process depending on the excitation energy as summarized in [25]. In this thesis, following four points are considered to select the wavelength.

- (a) Trade-off between the fluorescence signal and spontaneous emission intensity at the same excitation process
- (b) Other spontaneous emission near the fluorescence wavelength
- (c) Resonant state at lower excited state
- (d) Excitation energy

Table. 2.2 shows the wavelength of TALIF for major application of EP devices. As described in previous subsection, TALIF measurement has a characteristic that the wavelength of fluorescence and spontaneous emission are the same. Though this characteristic has a benefit that the ground-state neutral density and spontaneous emission intensity can be measured based on the same optical devices, the spontaneous emission is an inevitable noise against the fluorescence signal. The fluorescence intensity determines branching ratio and cross-section. For instance, the fluorescence intensity is the biggest in case of 823.16 nm. Thus, this wavelength is optimal to measure the density without plasma. Colorado university achieved the novel lower the density of  $10^{14} \text{ m}^{-3}$  by using this wavelength [114]. Additionally, 828.10 nm is also good selection to measure the density without plasma. However, as described in C. Eichhorn, these excitation processes have large spontaneous emission intensities by electron-impact excitation [87]. Hence, these excitation processes may not optimal in case with plasma.

In case with plasma, C. Eichhorn reported that the excitation processes that fluorescence are the wavelength of 834.68 nm and 788.74 nm are good selections. Particularly, C. Eichhorn utilized the wavelength of 788.74 nm to measure the ground-state neutral density in RIT-10 ion thruster because the other spontaneous emissions, 840.9 and 828.0 nm exist near 834.68 nm, i.e., point (b) [87].

The typical spectra of  $\mu 10$  thruster is shown in Fig.2.3. In case of RIT-10, the spontaneous emission intensity of 834.68 nm is 40 ~ 50 times larger than that of 788.74 nm. On the other hand, in case of  $\mu 10$ , the spontaneous emission intensity of 834.68 nm is only two times larger than that of 788.74 nm. Considering the fluorescence intensity of 834.68 nm is 6 ~ 7 times

larger than that of 788.74 nm, the wavelength of 834.68 nm is the best choice in view of point (a). Of course, to remove disadvantage of point (b), a band-pass filter that can remove other kinds of spontaneous emission is essential.

Point (c) is important for evaluating the spontaneous emission intensity and fluorescence intensity. It is possible that the spontaneous emission and the fluorescence are reabsorbed, i.e, radiation trapping [4]. The quantitative effect of radiation trapping can be evaluated by escape factor. In case of xenon, the escape factor that exhibit the effect of optical depth  $F_{escape}$  can be expressed as approximate form [115].

$$\psi_{escape} \approx \frac{2 - \exp(-\tau_{i,j,depth}/1000)}{1 + \tau_{i,j,depth}}, \quad (2.5)$$

where,  $\tau_{i,j,depth}$  is optical depth of the transition from  $i$  th state to  $j$  th state. The optical depth can be expressed in case of the Doppler broadening [4].

$$\tau_{i,j,depth} = \frac{\lambda_{i,j}^3}{8} \frac{g_i}{g_j} A_{i,j} n_i R_p \sqrt{\frac{m_n}{2\pi k_B T_n}}, \quad (2.6)$$

where,  $g$  is multiplicity and  $R_p$  is the radius of plasma. The equation indicates that if the lower excited state density  $n_i$  is large, the validity of optically thin can be violated, which leads to the decrease of the spontaneous emission and fluorescence intensity. Hence, the lower excited state should be resonant state because the density of resonant state is lower than that of metastable state.  $1s_2$  is the resonant state, whereas  $1s_3$  is metastable state. The lower excited state is  $1s_2$  in case of fluorescence of 834.7 nm, whereas that is  $1s_3$  in case of fluorescence of 787.7 nm. Thus, the fluorescence of 834.7 nm is superior to the validity of optically thin. From the estimation of OD rate equation proposed by Hara [38], the ratio of ground-state and the resonance state is approximately  $n_i/n_g \approx 10^{-6} - 10^{-5}$  under the electron density of  $n_e \approx 10^{16} - 10^{17} \text{ m}^{-3}$  [18]. Thus, considering the ground-state neutral density is on the order of  $10^{18} - 10^{19} \text{ m}^{-3}$ , the lower neutral density is on the order of  $10^{12} - 10^{14} \text{ m}^{-3}$ . In this situation, the optical depth is on the order of  $\tau_{i,j,depth} \approx 10^{-4} - 10^{-2}$  and the escape factor is  $0.99 - 0.9999$ . Thus, it can be concluded that the effect of radiation trapping is less than 1% and thus the assumption of optically thin is valid.

Last, point (d) is required so that the difference between ionization and excitation energy is minimized. This requirement means that the difference of electron population that can generate ionization and excitation is minimized. The wavelength of 834.68 nm is also good choice in

view of point (c). In this case, the excitation energy is 11.06 eV, thus the difference between ionization and excitation energy only is about 1 eV. The natural lifetime of the spontaneous emission is 35 ns from NIST database [65], thus the neutral particles can move by only within 0.01 mm, which indicates the discrepancy of measurement point and the spontaneous emission can be negligible.

**Table 2.2** Wavelength of TALIF measurement for major application of EP devices [25].

Laser, nm	Fluorescence, nm	Transition	Excitation energy, eV	Fluorescence intensity
252.49	823.16	$2p_6 \rightarrow 1s_5$	9.82	10,000
249.63	828.10	$2p_5 \rightarrow 1s_4$	9.93	7,000
224.29	834.68	$2p_3 \rightarrow 1s_2$	11.05	2,000
222.57	788.74	$2p_6 \rightarrow 1s_3$	11.07	300

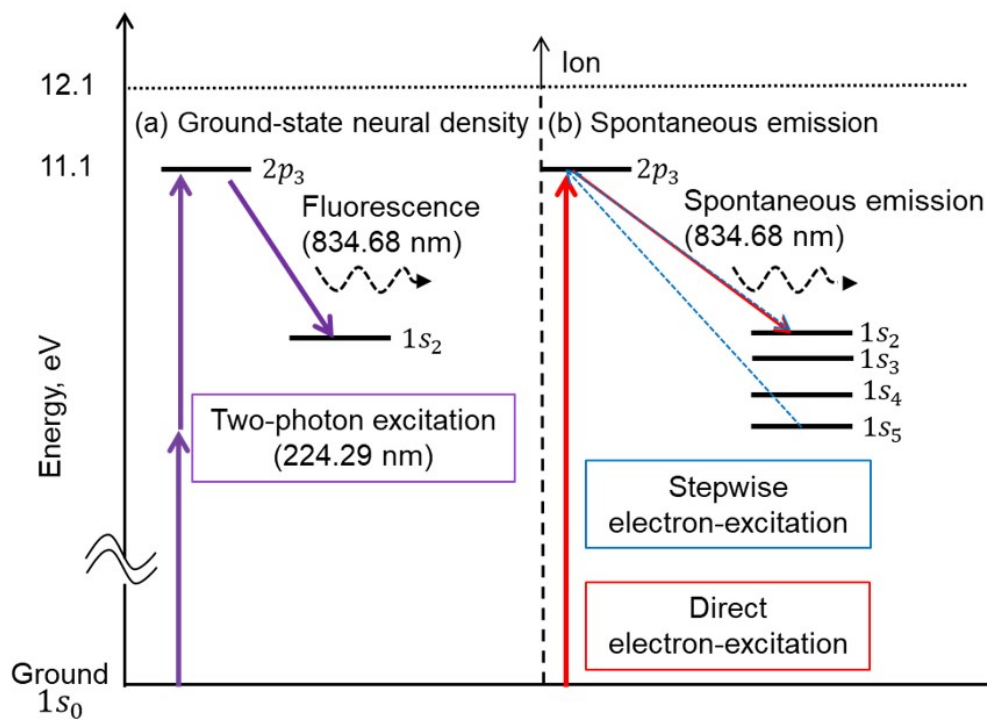


**Fig. 2.2** Principle of measuring (a) ground-state neutral density and (b) spontaneous emission intensity by electron-impact excitation.

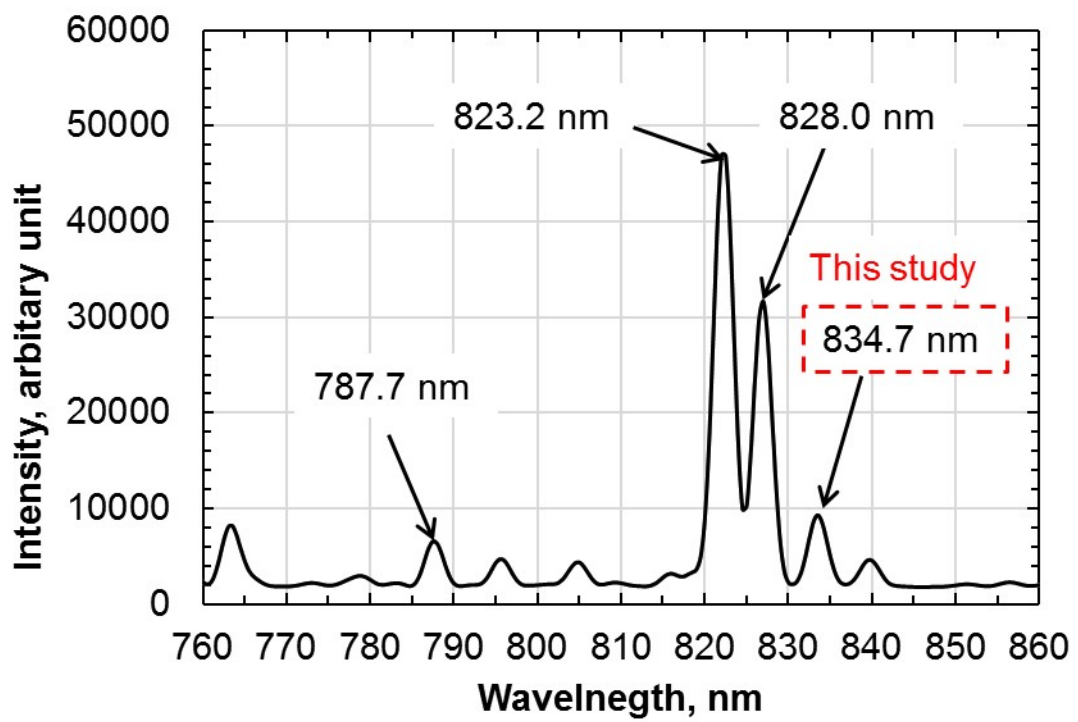


**Fig. 2.3** Spectrum diagram of a  $\mu 10$  thruster at a mass flow rate of 2.00 sccm and an ion beam current of 137 mA. The inlet of propellant is the discharge chamber.

#### 2.2.4 Rate equation

The excitation process of TALIF is shown in Fig. 2.4 [85, 25]. From Fig. 2.4, the rate equation is given by

$$\frac{dn_2}{dt} = B_{02}I_L^2(n_0 - n_2) - B_{20}I_L^2n_2 - (Q + A_{21})n_2. \quad (2.7)$$

where  $n_2$  is the neutral density of the higher excited state,  $n_0$  is the neutral density at the ground state,  $I_L$  is the laser power,  $B$  and  $A$  are Einstein coefficients, and  $Q$  is a quenching term:  $Q = k_q n_0$  and  $k_q$  is a quenching rate constant. By substituting the steady state case:  $dn_2/dt = 0$  into Eq. (2.7), the fluorescence signal  $S_F$  is given by

$$S_F = n_2 A_{21} = \frac{B_{02} I^2 A_{21}}{(B_{20} + B_{02}) I^2 + Q + A_{21}} n_0. \quad (2.8)$$

In this study, the target two-photon excitation is  $1s_0 \rightarrow 2p_3$ , which absorbs at a wavelength of 224.29 nm and emits fluorescence with 834.68 nm. In ref [86],  $A_{21}$  is  $3 \times 10^{-5} s^{-1}$  and  $k_q$  is  $2.5 \times 10^{-7} s^{-1} Pa^{-1}$ . Because the pressure in the microwave cathode is approximately  $n_0 \approx 10^{-2} \sim 10^1 Pa$ ,  $Q = k_q n_0 \approx 10^{-9} - 10^{-6} s^{-1}$  [86]. As a result,  $Q \ll A_{21}$ , and the quenching effect can be neglected. Therefore, the equation can be approximated as

$$S_F = n_2 A_{21} \approx \frac{B_{02} I^2 A_{21}}{(B_{20} + B_{02}) I^2 + A_{21}} n_0. \quad (2.9)$$

Here, two extreme cases are considered. If laser power is very small, i.e.,  $(B_{20} + B_{02}) I^2 \ll A_{21}$ , the fluorescence signal can be further approximated as follows.

$$S_F \approx B_{02} I_L^2 n_0. \quad (2.10)$$

Eq. (2.10) is called weak excitation, and then this fluorescence is proportional to the square of laser power  $I^2$ . On the other hand, if laser power is very large, i.e.,  $(B_{20} + B_{02}) I^2 \gg A_{21}$ , the fluorescence signal can be further approximated as follows.

$$S_F \approx \frac{B_{02} I_L^2 A_{21}}{(B_{20} + B_{02}) I_L^2} n_0 = \frac{B_{02} A_{21}}{(B_{20} + B_{02})} n_0 \quad (2.11)$$

Eq. (2.11) is called saturation, and then this fluorescence does not depend on laser power  $I$ . Thus, it is concluded that sensitivity of the fluorescence signal depends on the laser power.

However, actual fluorescence is not simple. First, in TALIF measurement, laser power has distribution because the laser beam is focused by lens in front of measurement point. In practice, it can be enough that the fluorescence signal is proportional to pressure. In any laser power, Eq. (2.9) shows that the fluorescence signal is proportional to pressure under the laser power is constant. However, if laser power is very strong, photon ionization can be occurred [25], and it makes the ground-state neutral density decreases. Therefore, the relationship between the signal intensity and pressure needs to be investigated to confirm whether Eq. (2.9) is satisfied for the experimental results. This experiment is written in subsection 2.5.3 and 2.5.2.

Finally, temporal function of the fluorescence signal is discussed. To capture decay curve after laser injection cases ( $I_L \approx 0$ ) in Eq. (2.7),

$$\frac{dn_2}{dt} \approx -(Q + A_{21})n_2 \quad (2.12)$$

Solving the above equation, the fluorescence signal exhibits following temporal function.

$$S_F \propto \exp\left(-\frac{t}{Q + A_{21}}\right) \quad (2.13)$$

Thus, the fluorescence is decayed and the temporal constant  $\tau$  is  $\tau = 1/(Q + A_{21})$ . Because  $Q = kn_g$  is proportional to ground-state neutral density, the  $k$  and  $A_{21}$  can be obtained, i.e., Stern–Volmer plot. In limit of low pressure ( $n_g \rightarrow 0$ ),  $\tau \approx 1/A_{21}$ ,  $1/A_{21}$  is the order of several ten ns.

However, PMT also has the time detected signal. To obtain the *true* decay curve of fluorescence, it is necessary to select the PMT that the time constant of PMT can be negligible compared to that of fluorescence. In contrast, in this thesis, PMT that the time constant is the order of 50 ns was used. Thus, natural lifetime and rate time constant cannot be detected accurately. However, in this thesis, because the author focuses on the measuring the ground-state neutral density, this PMT is enough.

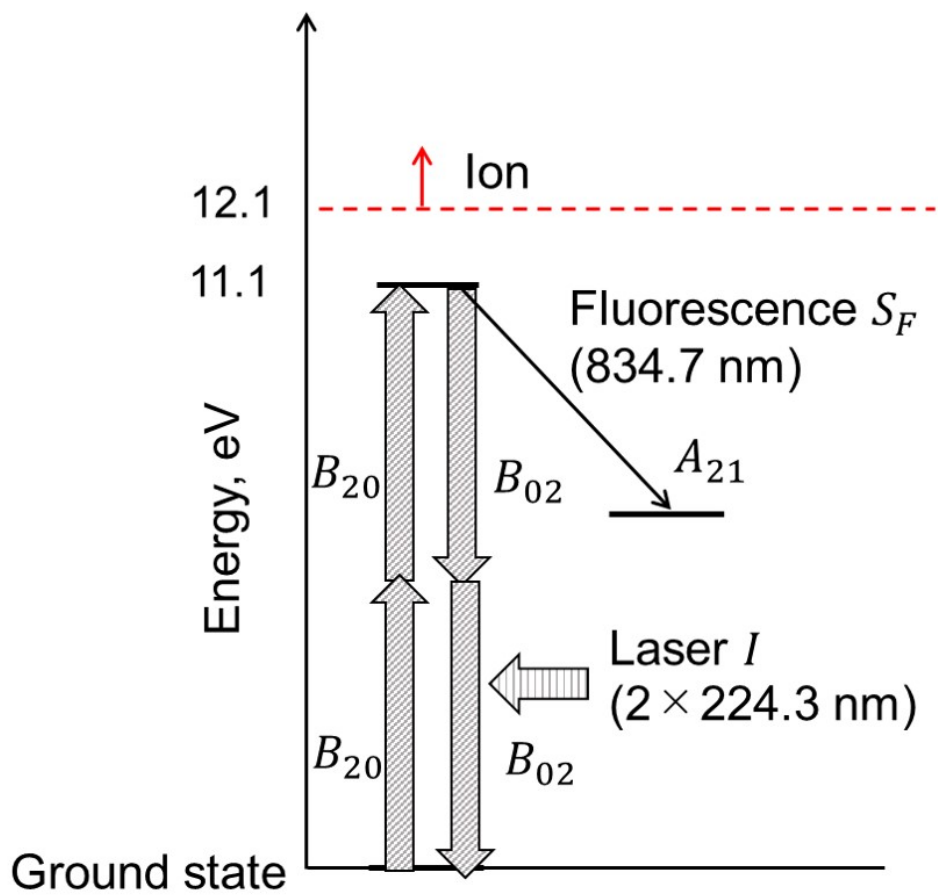


**Fig. 2.4** Two photon excitation process. Ground state  $1s_0$  is excited by a wavelength of 224.29 nm and emits fluorescence with 834.7 nm from  $2p_3$  to  $1s_2$ .

## 2.3 Experimental devices

This section provides the detailed explanations about thruster, laser system, and optical devices.

### 2.3.1 $\mu 10$ ion thruster system

#### 2.3.1.1 Configuration

The configuration of the microwave discharge ion thruster  $\mu 10$  is shown in Fig. 2.5. The thruster consists of a waveguide and a discharge chamber. Inside the waveguide, microwaves are transmitted from an antenna to the discharge chamber. In the discharge chamber, mirror magnetic field is formed to confine electrons by using two magnet rings. Typically, the intensity of magnetic field is 0.01 – 0.5 T, and hall parameter is about  $\Omega \approx 10^3 \sim 10^4$ ; thus electrons are strongly magnetized. At that time, the electrons absorb in the microwave power by ECR heating and they ionize the neutral particles (propellant). It reminds that the region where electrons are confined and continuously heated in the ECR is called the magnetic confined region. The generated ions are transported to a screen grid because the Larmor radius of the ions is larger than that of electrons. The transported ions are accelerated by applying the high-voltage between screen and accelerator grid.

#### 2.3.1.2 Condition of thruster operation

The operation parameters are summarized in Tab. 2.2. The microwaves power is fixed at the 34 W. The previous works show the beam current is not sensitive to the microwave power in both gas injections [9, 34]. On the other hand, the beam current is very sensitive to flow rate and the mode-transitions are observed in some kinds of microwave power [9, 34]. Thus, in this paper, the ground-state neutral density and the spontaneous emission intensity were measured at the microwave power of 34 W and the flow rate varied from 1 sccm to 4 sccm. Additionally, in this thesis, the metastable neutral density by laser-absorption spectroscopy (LAS) will be quoted, and experimental condition is consistent with the measurement of this thesis.

The thickness and diameter of screen grid are 0.5 mm, 3.05 mm respectively. Then, the thickness and diameter of accelerator grid are 1.0 mm, 1.2 mm respectively. The biased the screen and accelerator voltages were fixed at 1500 and -350 V, respectively according to space operation.

**Table 2.3** Experimental condition of thruster operation

Item	Value
Microwave frequency, GHz	4.25
Microwave power, W	34
Thickness of screen grid, mm	0.5
Diameter of screen grid, mm	3.05
Biased voltage at screen grid, V	1,500
Thickness of accelerator grid, mm	1.0
Diameter of accelerator grid, mm	1.2
Biased voltage at accelerator grid, V	-350
Propellant flow rate, sccm	1 ~ 4
Pressure with flow rate of 3 sccm, Pa	$4.0 \times 10^{-3}$

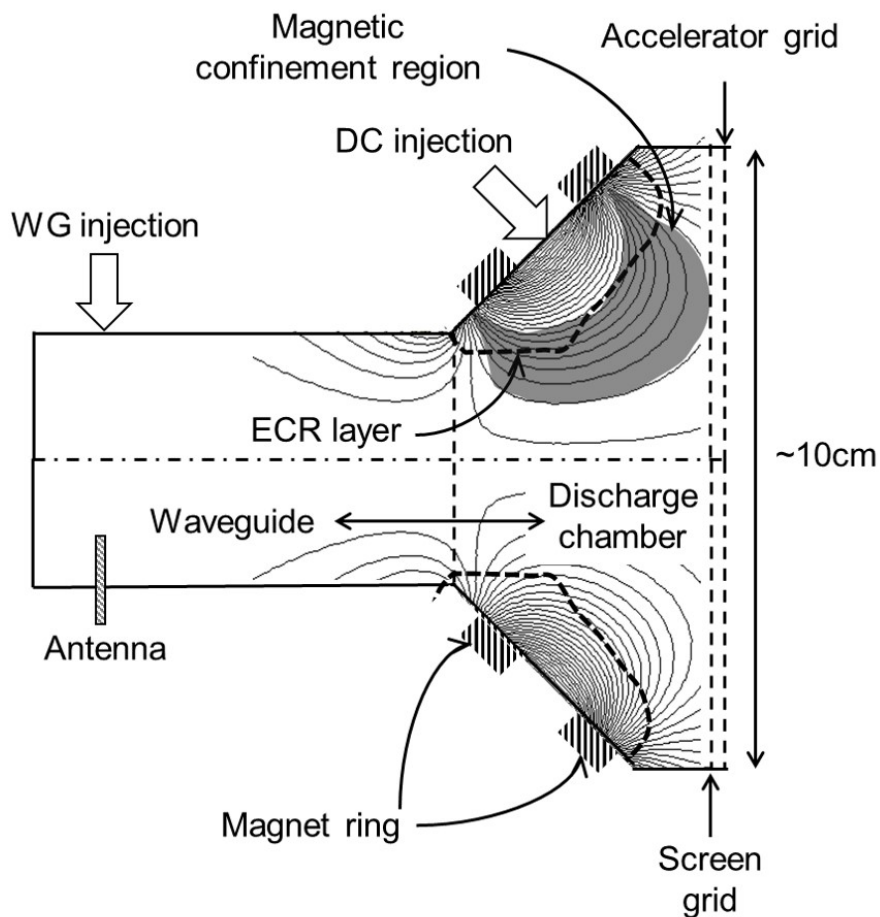


**Fig. 2.5** A schematic of the  $\mu 10$  microwave discharge ion thruster

### 2.3.1.3 Thruster configuration

In this work, TALIF measurements are applied to four types of thrusters to reveal following two physical aspects against plasma mode-transition.

I. Effect of gas injection

II. Effect of electron heating inside the waveguide

To investigate I. and II., five kinds of thrusters were used. The schematics of these configuration are summarized in Fig. 2.6. First, to investigate I., waveguide injection (WG) and Discharge chamber injection (DC) are performed in the magnetic field of Hayabusa model. DSMC works revealed that the location gas injection clearly produces the difference of ground-state neutral density inside the waveguide [116]. Additionally, the thrust performance is clearly different [34, 9], thus the effect of gas injection against plasma mode-transition is very important.

Second, 'Enhanced model 2' was used to investigate II. In nominal version of 'Enhanced model 2', the ECR layer exists inside the waveguide. Here, the line of the ECR layer shows the contour line of magnetic field that is satisfied with ECR condition;  $\omega_{ce} = \omega_m$ . In case of  $\mu 10$ , the magnetic field is 0.15 T. This ECR layer can generates ECR heating, which indicates that electron temperature can be changed. In this thesis, two methods were tried to prevent ECR heating. First, an aluminum ring was attached inside the inner magnet as shown in zoom-up of Fig. 2.6. Second, a quartz plate (thickness: 3 mm) was set parallel to the magnetic field lines. The quartz plate transmits microwaves without attenuation, whereas plasma is not generated inside the waveguide due to the lack of neutral gas. Note that the microwave frequency is slightly increased from 4.25 to 4.29 GHz to modify the matching. However, the position change of the ECR layer caused by this modification is 0.02 mm at maximum, and it is negligibly small [100]. As shown in Tab. 2.4, type (a), (b), (c), (d), and (e) are called 'WG', 'DC', 'w WG ECR', 'w/o WG ECR', and 'w/o WG plasma' respectively.

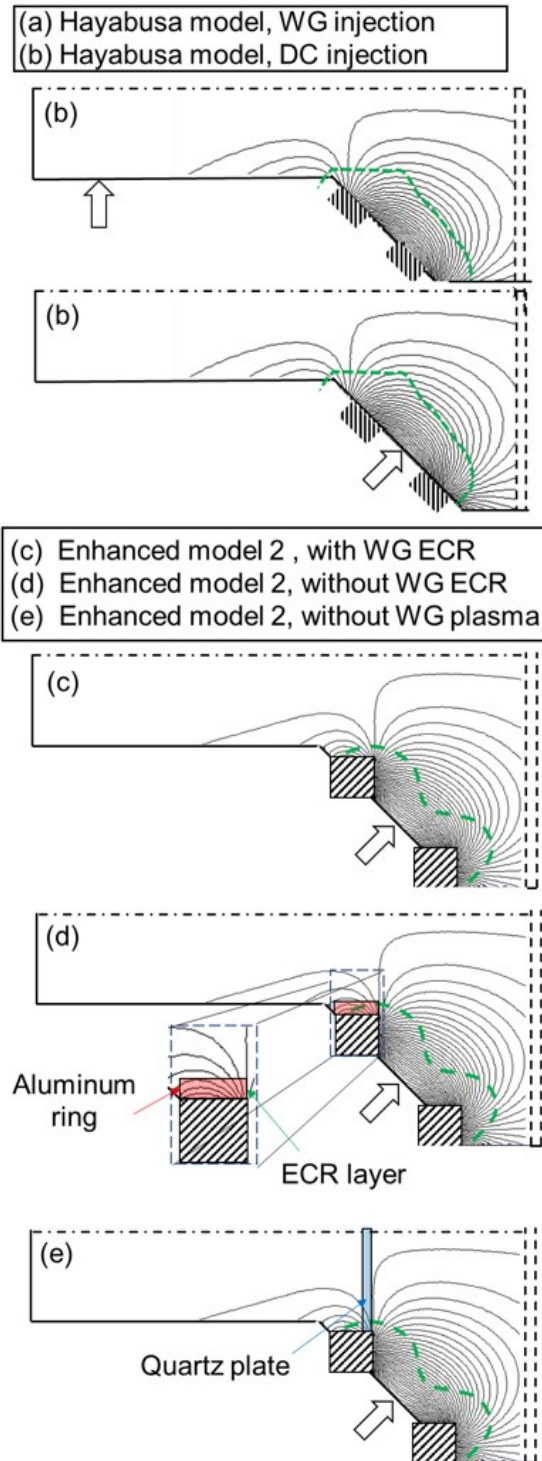


**Fig. 2.6** Thruster configurations to investigate the physical aspects against plasma mode transition, I. effect of gas injection, II. effect of electron heating inside the waveguide. (a) Hayabusa model, WG injection, (b) Hayabusa model, DC injection, (c) Enhanced model 2 , with WG ECR, (d) Enhanced model 2, without WG ECR.

**Table 2.4** Abbreviation of thrusters that uses in this chapter. Detailed configurations are shown in Fig.2.6

Thruster	Abbreviation
(a) Hayabusa model, WG injection	WG
(b) Hayabusa model, DC injection	DC
(c) Enhanced model 2, with WG ECR	w WG ECR
(d) Enhanced model 2, without WG ECR	w/o WG ECR
(e) Enhanced model 2, without WG plasma	w/o WG plasma

## 2.3.2 Ground test facility

### 2.3.2.1 Power and Propellant supply

Figure 2.7 shows the experimental setup of the power supply and the flange to operate the thruster. Operation conditions are summarized in Tab. 2.3. A microwave with 4.25 GHz is excited by an oscillator, the microwave is amplified, and the microwave is introduced into an antenna. The propellant is controlled by mass flow controller, and is injected at the waveguide (WG) and discharge chamber (DC). The voltage of thruster is same as the screen voltage, and the gas system and the microwave system are insulated by the gas isolator and DC block.

Photograph of power supply unit and feed-through unit at vacuum chamber is shown in Fig.2.8. At 100 A flange that locates right-hand side, microwave power is supplied. Then, at top 100 A flange, xenon gas is injected. At bottom 100 A flange, screen and accelerator voltage are introduced into vacuum chamber. 100 A flange at left-side and 200 A flange at center are utilized for PMT voltage of TALIF measurement.

### 2.3.3 Vacuum Facility

The vacuum chamber has a size of 1.8-m-long, 0.8-m-diameter. As shown in Fig. 2.7, the vacuum chamber is equipped with a rotary pump of 500 L/min, a turbo molecular pump of 1400 L/s, and two cryopumps of 5000 L/s. The pressure is  $1 \times 10^{-4}$  Pa without xenon gas, and the pressure is about  $4 \times 10^{-3}$  Pa with xenon gas 3.0 sccm.

Photograph of controller unit on vacuum pumps and vacuum gauges are shown in Fig. 2.9 and Fig. 2.9. This unit can control all valves of vacuum pumps, two cryopumps, a turbo molecular pump, and a rotary pump. Then, in region where pressure is  $10^{-1} \sim 10^5$  Pa, the pressure can be measured by a pirani gauge. Then, where pressure is less than  $10^{-1}$  Pa, the pressure can be measured by a hot cathode gauge. Figure 2.11 shows the front view of thruster. Laser is injected from the bottom window.

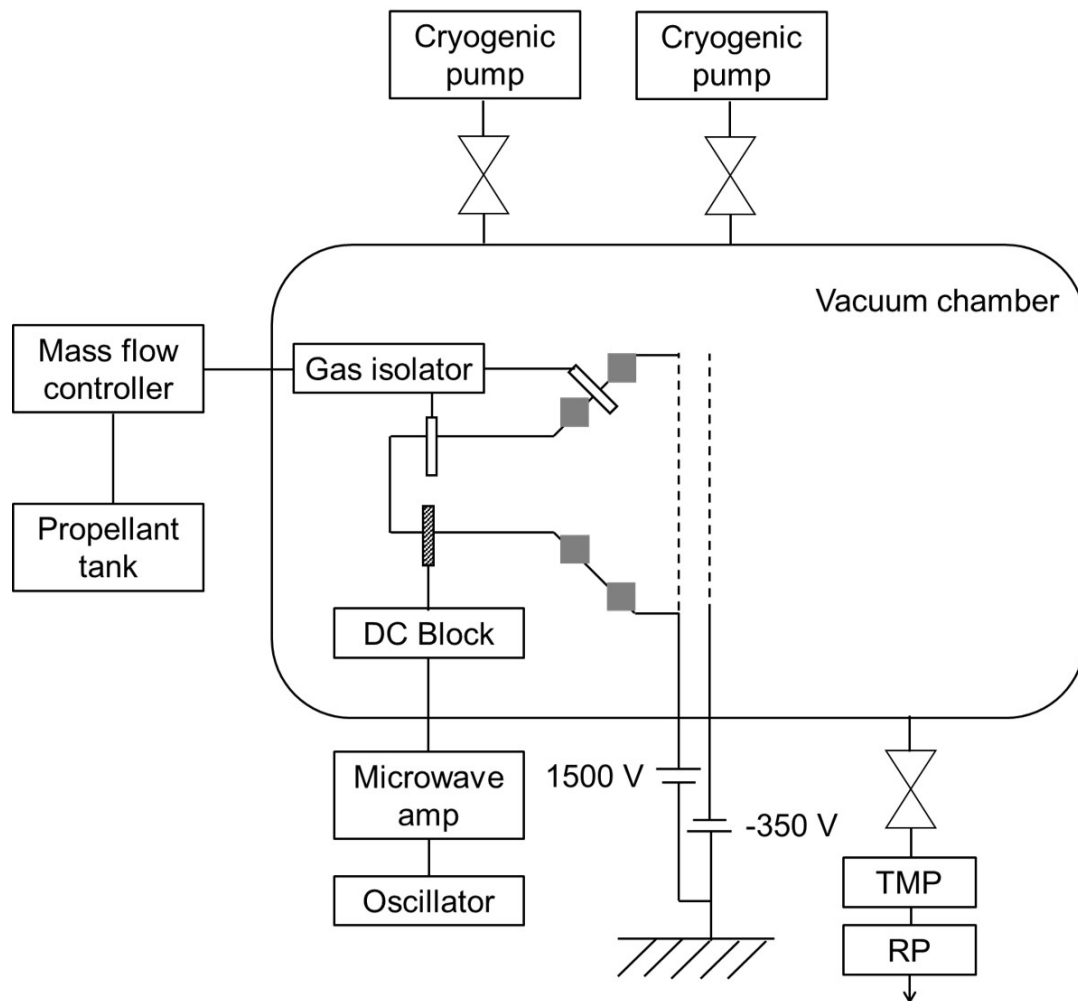


Fig. 2.7 Schematic diagram of power supply and vacuum facility.

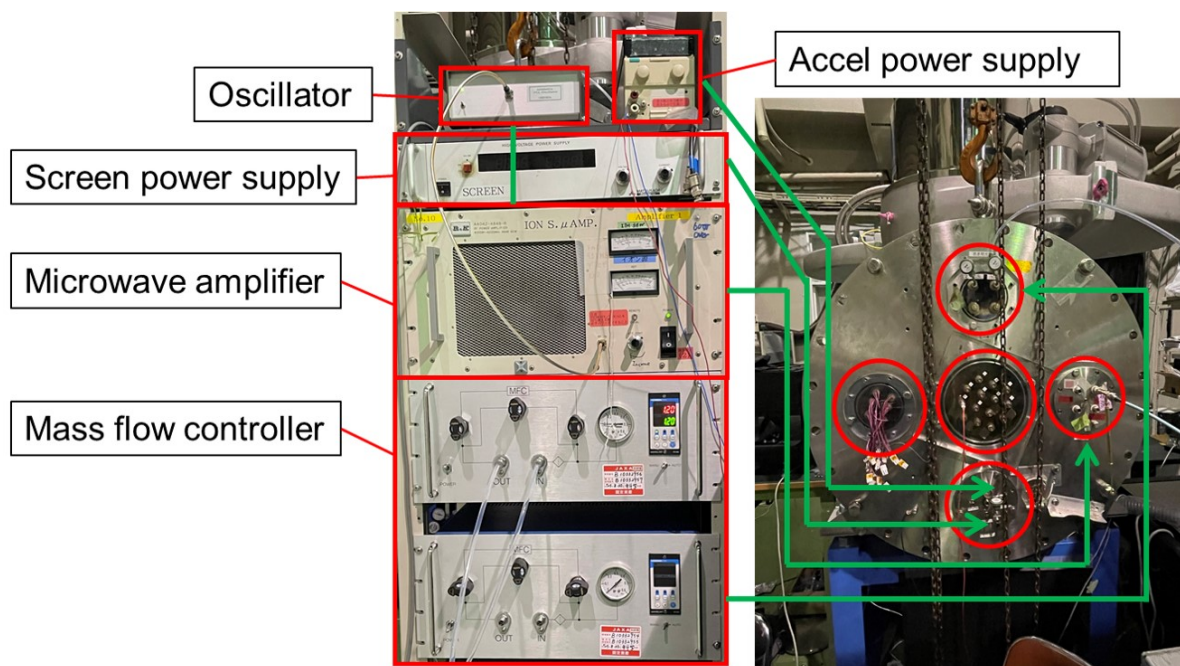
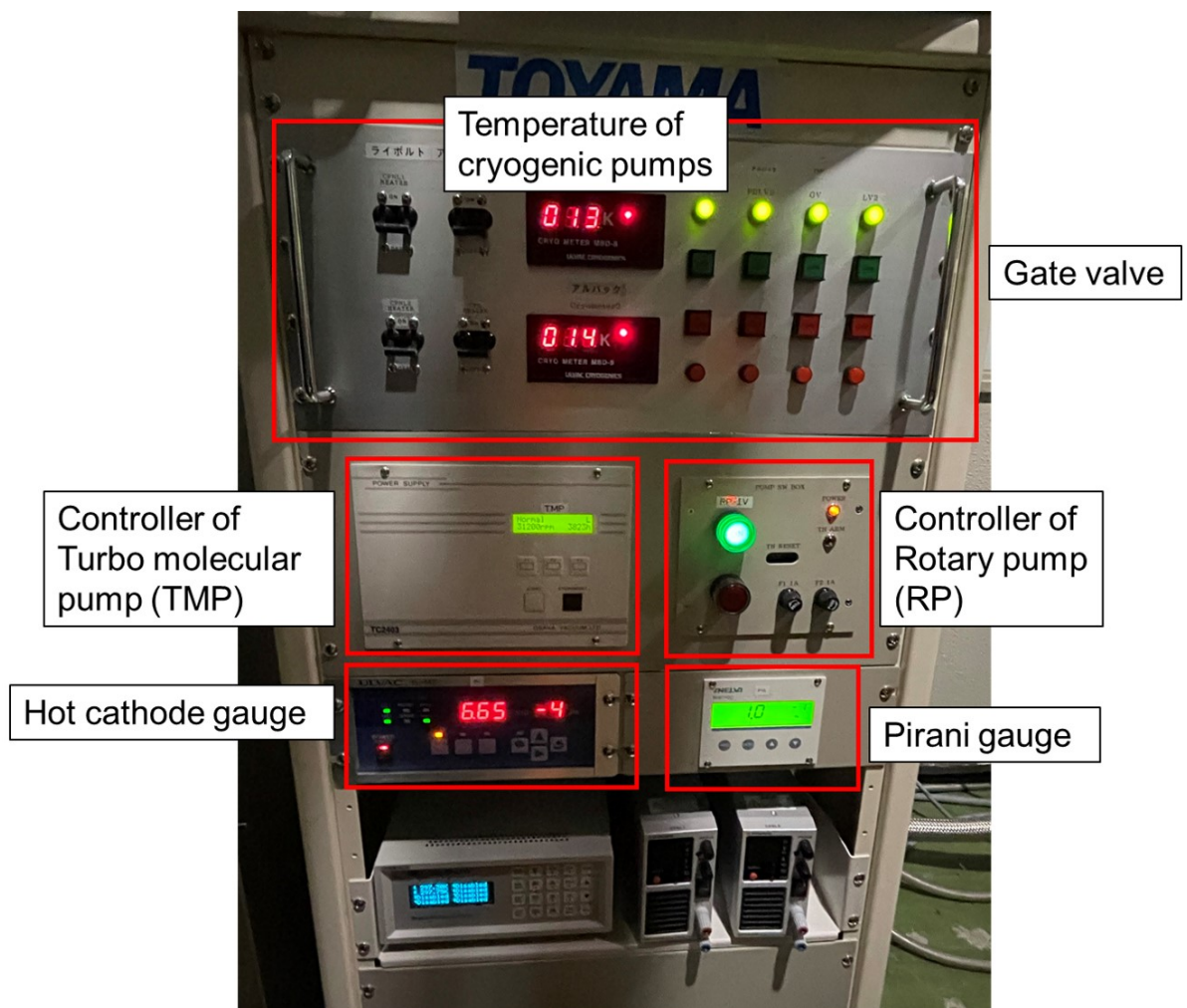
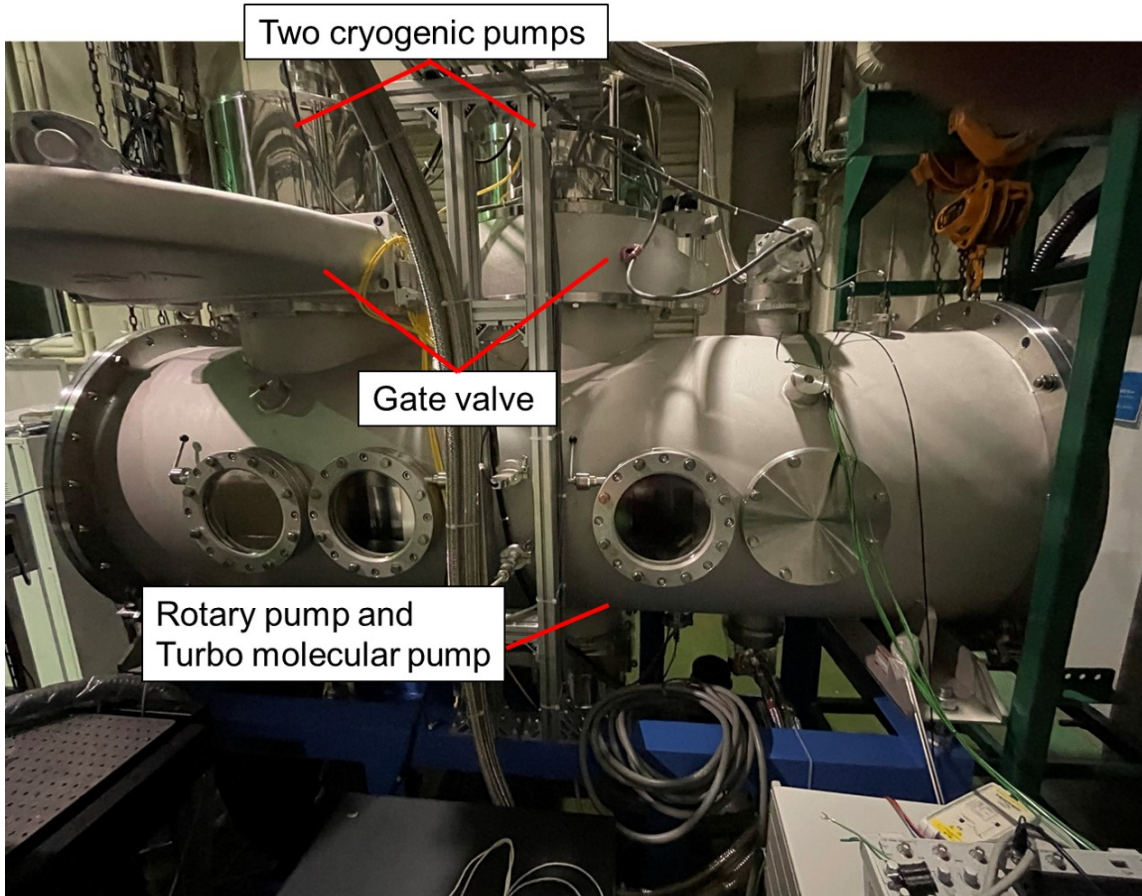


Fig. 2.8 Photograph of power supply unit and feed-through unit at vacuum chamber.



**Fig. 2.9** Photograph of controller unit of vacuum pumps and vacuum gauge. Pirani gauge measured in range of  $0.1 \sim 10^5$  Pa, and hot cathode gauge measured less than 0.1 Pa.



**Fig. 2.10** Photograph of vacuum chamber. Two Cryogenic pumps are equipped at the top, and one Turbomolecular pump and one rotary pump were equipped at the bottom. At left-side, ion thruster was operated.



**Fig. 2.11** Front view of thruster. Laser was injected from the bottom window.

### 2.3.4 Laser and Optical Devices

This section describes the laser and optical devices. The model number and company are summarized in Tab. 2.5.

**Table 2.5** Detail of Model number and company in optical devices

Item	Model number	Company
Nd:Yag laser	NL310	EKSPLA
Dye laser	LiopStar-E-N-D2400	LiopTEC
Oscilloscope	DL9040	Yokogawa
Photomultiplier	H11462-031	Hamamatsu Photonics
Band pass filter	VPF-25C1.5-50-83400	Sigma koki

#### 2.3.4.1 Laser system

The laser system consists of two lasers, a Nd:YAG laser and a dye laser. The Nd:YAG laser plays a role as a laser light source, and the dye laser plays a role of converting the wavelength to the target wavelength. The Nd:YAG laser is a pulse laser of 10 Hz with a pulse energy of 300 mJ, pulse time of 5 ns, and wavelength of 532 nm. The power supply of Nd:yag laser is shown in Fig. 2.12. This system is water-cooled, thus sometimes requires additional water to operate. Fig. 2.13 shows interface between Nd:yag Laser and Dye laser. There are two high efficient reflected mirrors to introduce of the laser power form Nd:YAG laser to the dye laser.

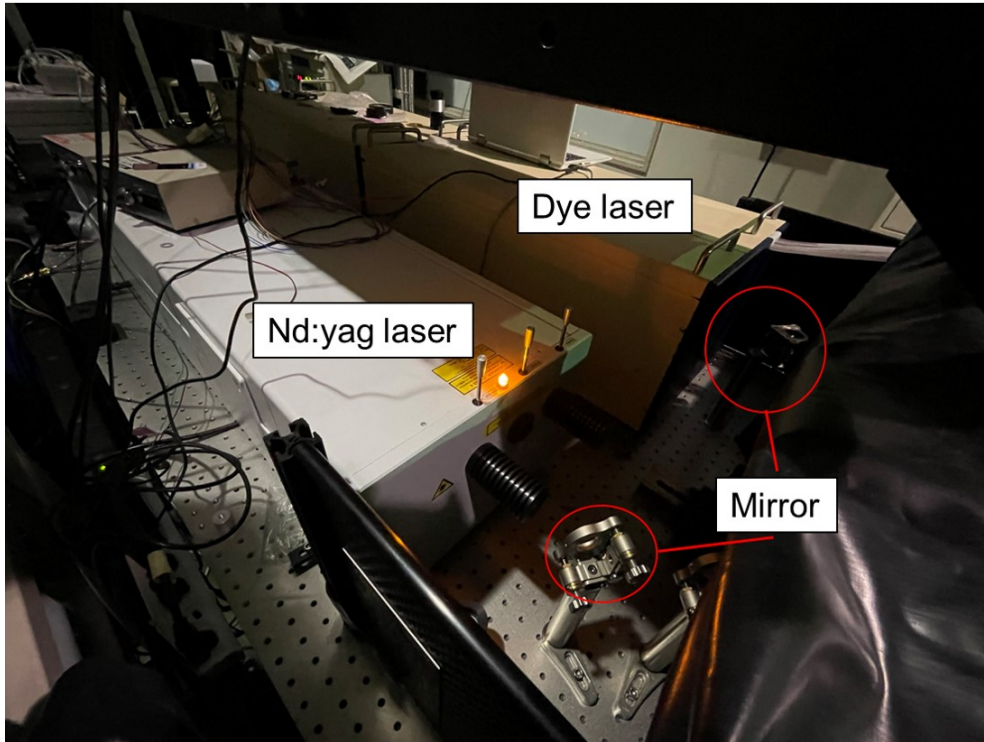
Fig. 2.14 shows the dye laser system. The dye laser converts the wavelength from 532 nm to 224.3 nm with a power of 1.2 mJ. In the dye laser, LDS-698 is used as the dye. For instance, to obtain the laser wavelength of 224.29 nm, the dye converts the wavelength from 532 nm to 672.87 nm. Then, only three harmonic wavelength, i.e.,  $672.87/3=224.29$  nm was extracted from the dye laser. The dye laser system can adjust the wavelength by a laptop. To adjust the wavelength of the dye laser system, xenon gas cell is useful. Fig. 2.16 shows the photograph of fluorescence signal in xenon gas cell at 10 Torr. In this situation, the fluorescence signal can be seen. Thus, the fluorescence signal can provide the wavelength that the fluorescence signal becomes maximum.

Fig. 2.15 shows the circulation system of dye laser. The dye is diluted by ethanol. The concentration of dye is written in catalog. Generally, the concentration is a certain optimal

value. If this is not optimal, the shape of laser beam is not circle. The concentration of one aqueous solution is 10 times denser than that of another, and this density is sensitive to the laser power. The laser goes through the vacuum chamber via a quartz optical window.



**Fig. 2.12** Power supply of Nd:YAG laser. In this thesis, two times harmonic wavelength of 1064 nm, i.e., 532 nm, was used.



**Fig. 2.13** Nd:yag Laser system. The laser beam is introduced to dye laser by using two mirrors.



**Fig. 2.14** Dye laser system. This dye laser converted to the wavelength from 532 nm to 650 ~ 700 nm by using dye, and the three harmonic light was extracted. A laptop can operate dye laser system, for example, the changing wavelength.

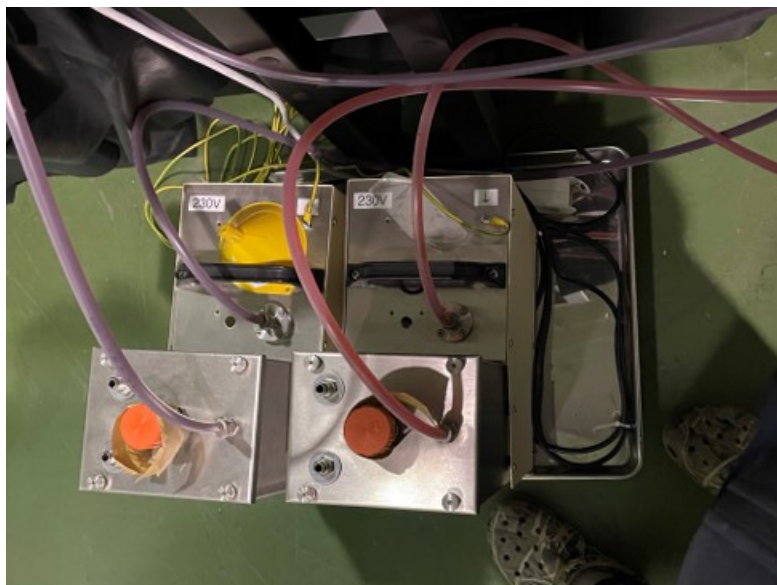


**Fig. 2.15** The circulation system of dye laser. There are two kinds of aqueous solutions. The concentration is described in catalog. The concentration of one aqueous solution is 10 times dancer than that of another.

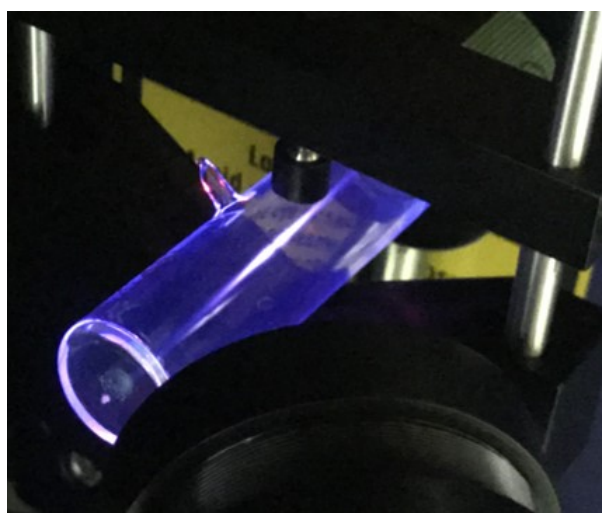


**Fig. 2.16** Example of fluorescence in TALIF measurement. This pressure of xenon gas cell is 10 Torr.

### 2.3.4.2 Detector

Fig. 2.17 shows the detector to obtain the fluorescence and spontaneous emission intensity. In this experiment, a photomultiplier tube (PMT) was used as the detector. Generally, PMT converts the incident light intensity into an electronic signal and amplifies it by using the photoelectric effect. This amplitude depends on the input voltage. When using this detector, There are two points that should be carefully check. First, in this experiment, this is used in a vacuum, but originally it is not a specification to be used in a vacuum. Therefore, if extracting the gas from the vacuum chamber with the active of this PMT, it was broken by Paschen discharge. Second, if the input voltage is increased, the obtained signal is also more amplified. However, if the input voltage is too high, the fluorescence signal is saturated. Typically, when the input voltage exceeds 400 V, the saturation begins. In this thesis, the input voltage of PMT was fixed at the 380 V. Then to remove noise due to plasma emission, the band-pass filter with FWHM of 2 nm was used. Then, to collect signal, two convex lens were equipped.

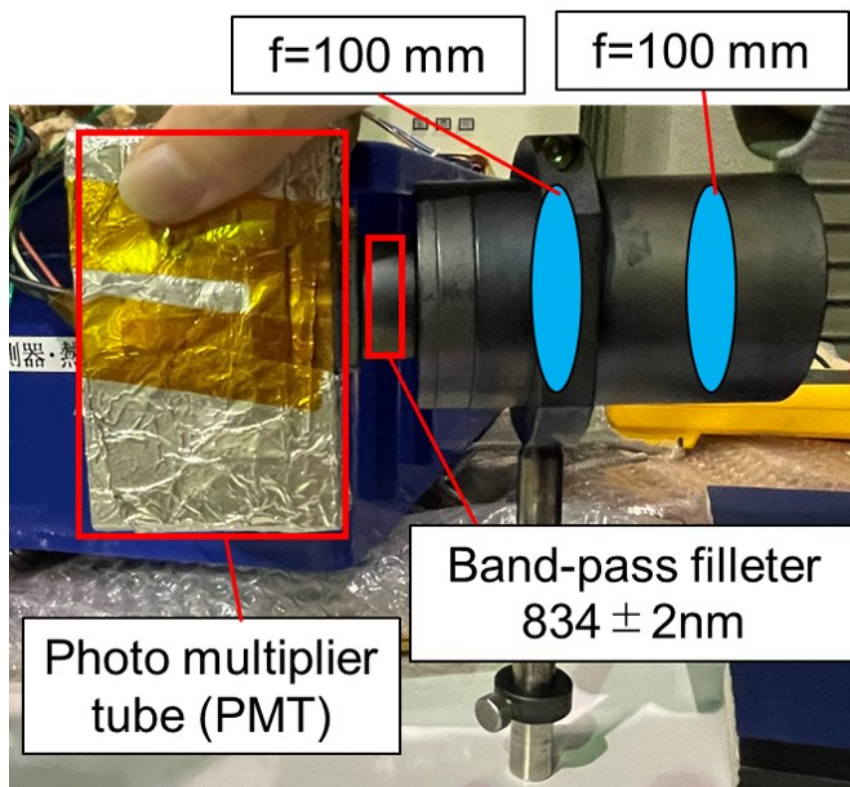


**Fig. 2.17** Schematics of detector. To collect fluorescence signal, two convex lens are used. In addition, to remove noise of plasma emission, a band-pass filter was used.

### 2.3.4.3 Oscilloscope

An oscilloscope was used to detect the fluorescence because the oscilloscope is superior in temporal resolution compared to the omni-ace. Additionally, this oscilloscope can average multiple fluorescence signals by using Trigger mode. Here, Trigger mode is a method to detect the response waveform only when the input signal exceeds a certain set voltage. In this experiment, the averaging function was used to reduce the noise.

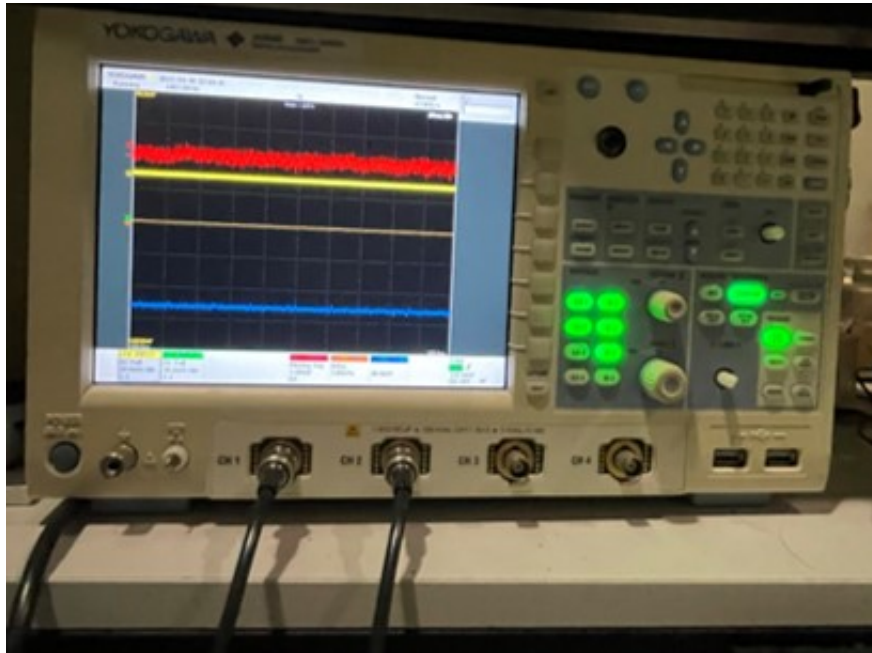


**Fig. 2.18** Photograph of Oscilloscope.

## 2.4 Experimental setup

This section describes the experimental setup for measuring ground-state neutral density and spontaneous emission intensity. Detail explanation about each optical device is described in section 2.3.

### 2.4.1 Ground-state neutral density measurement

Fig. 2.19 shows the experimental setup of the TALIF measurement system that applies to microwave discharge gridded ion thruster. Top figure shows the  $z - y$  plane of the setup for the laser injection. Bottom figure shows the  $z - x$  plane of the setup for the fluorescence detection. Laser power generated from Nd:yag laser and dye laser goes through the vacuum chamber via a quartz optical window. In the vacuum, chamber, there is a lens focusing on the center of the

waveguide. Two 4-mm diameter quartz windows are newly opened for the laser injection and detection. The laser generates two-photon excitation process from ground to state  $1s_0$  to higher excited state  $2p_3$ . The transition from  $2p_3$  to  $1s_4$  immediately occurs, and then the fluorescence of 834.68 nm emits. The fluorescence is obtained by a detector (Fig. 2.17).

In this experiment, the fluorescence signal includes noises, for example, the plasma emission, the pump oscillation, the fluctuation of laser intensity, and electrical noise of PMT. The electrical noise due to PMT can be subtracted by using signal without TALIF measurement. To reduce other noises, two methods are used. First, a band-pass filter that FWHM is 2 nm around 834.7 nm was used to cut the plasma emission except for the spontaneous emission same as the two-photon excitation process. As described in section 2.2, the spontaneous emission is the inevitable noise. To reduce the inevitable noise, fluorescence signal was averaged. The oscilloscope can average multiple fluorescence signals. To detect time of laser, trigger mode was used. However, from the fluorescence signal, the time of laser may not be detected because the fluorescence signal may be hidden due to noise. Thus, another photomultiplier “PMT2” was used to detect the time every-time by measuring the scattering of the pulsed laser. This technique is shown in Fig. 2.20. In this thesis, 3,000 thousand fluorescence signals are totally averaged. Specifically, 500 times fluorescence signals were averaged and then the signal was recorded. This operation was repeated six times. Here, because laser with a frequency of 10 Hz, the averaging takes five minutes ideally. However, in GITs, high-voltage breakdown often occurred between screen grid and accelerator grids. In this case, the fluorescence signal includes spark noise. Typically, a high-voltage breakdown occurs per several minutes, meanwhile this data cannot be used. Hence, to enhance the rate of data-acquisition, the data acquisition is divided into six times. This averaging technique can drastically reduce the fluctuation noises. For instance, Fig. 2.21 shows the transition of averaged fluorescence signal with respect to the number of average. Here, the averaged fluorescence signal and laser scattering signal correspond to red line and green line respectively. Though one fluorescence signal cannot be observed, the fluorescence signal is appeared by increase of number of average.

Above averaging technique can drastically reduce the fluctuation of the spontaneous emission, but cannot remove the off noise, i.e., DC signal due to the spontaneous emission intensity. Of course, this signal can subtracted by detecting the spontaneous emission independently. However, it was found that this subtraction becomes worse on the S/N ratio of fluorescence

signal because the time of spontaneous emission intensity is different from that of ground-state neutral density measurement. Thus, in this thesis, in case of measurement of ground-state neutral density, AC (alternating current) signal was used. By using AC signal, each offset noise can be subtracted in each fluorescence signal, and it is not necessary to subtract the offset noise due to the spontaneous emission.

#### 2.4.2 Spontaneous emission intensity measurement

Spontaneous emission intensity was measured in the same experimental setup as the measurement of ground-state neutral density. In case the measurement of the spontaneous emission intensity, the laser is not injected. As shown in Fig. 2.3, there are two strong excited emissions of 828.0 and 840.9 nm near 834.68 nm [87]. However, these emissions can be removed by the band-pass filter that has FWHM is 2 nm around 834.7 nm. Noted that from NIST database [65], excited emission of xenon ions (Xe II) exists at 834.95 nm and this emission cannot be blocked by the band-pass filter. However, considering the density of neutral species is about ten times larger than that of ions, the excited emission of neutral species is dominant. Actually, from the NIST data base, the relative intensity of Xe I 834.68 nm are twenty times larger than that of Xe II 834.95 nm. Therefore, the observed emission can be regarded as the excited emission of Xe I 834.68 nm. The natural lifetime of Xe I 834.68 nm is 35 ns [65], which indicates that the neutral particles are able to move by about 0.01 mm under the assumption that the thermal velocity is 1000 K, which indicates the discrepancy of location between fluorescence signal and spontaneous emission can be neglected.

#### 2.4.3 Measurement point

The location of measurement focus on the waveguide from following two reasons. One reason is that the phenomena inside the waveguide is important for plasma mode-transition. From the measurement of optical emission indicates that the intensity of optical emission drastically changed between before and after plasma mode-transition. Additionally, DSMC works suggested that the neutral density inside the waveguide clearly changed between DC and WG injection [116], and this optimal flow rate also changed [9]. Thus, these results suggest that the thruster performance strongly depend on the density distribution of the waveguide. Second reason is that it is difficult to measure except for the waveguide because of detection and laser passes. To measure the density inside the discharge chamber, the location of detection is limited

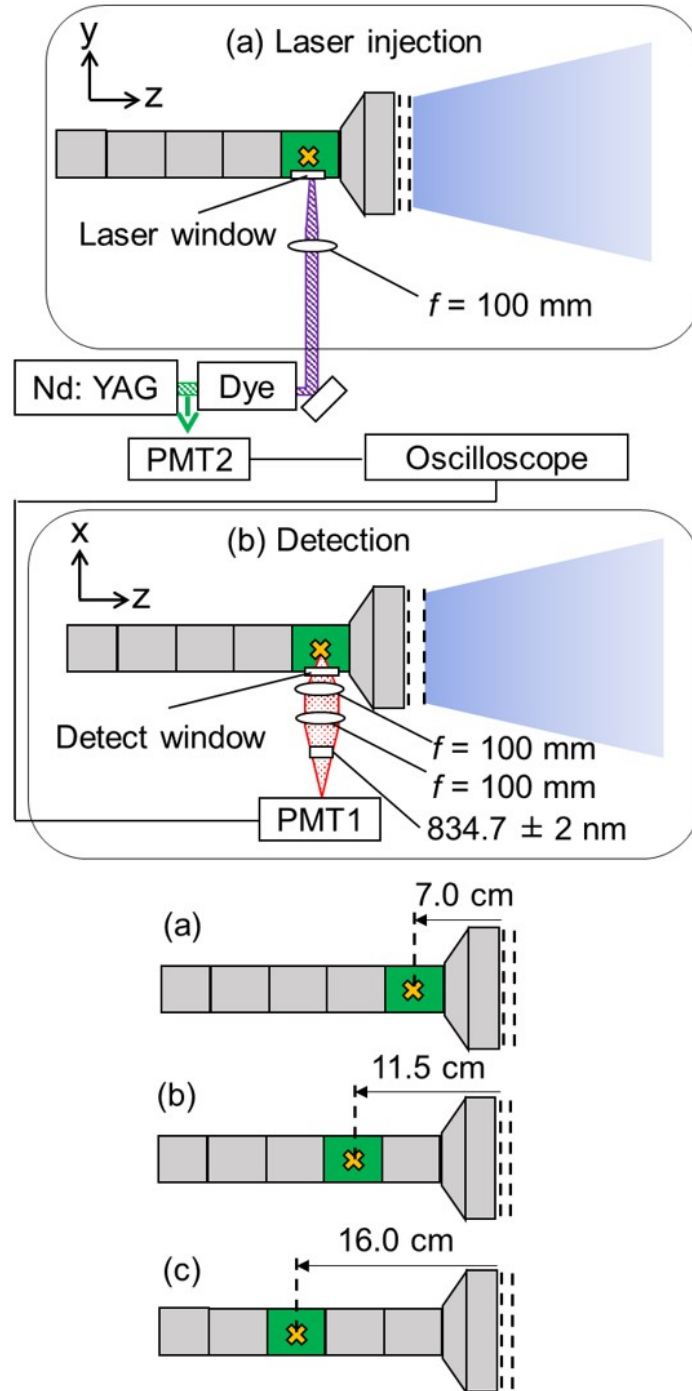


**Fig. 2.19** Experimental setup for the TALIF spectroscopy measurements. Left: view of detection, right: view of laser injection. When measuring the ground-state neutral density, a fluorescence of  $834.7 \pm 2$  with laser injection is detected. When measuring the spontaneous emission, the signal of  $834.7 \pm 2$  without laser injection is detected. Here, we measured three measurement points from the screen grid, 7.0-, 11.5-, and 16.0-cm.

to the orifice at the grid. The author tried to measure the ground-state neutral density inside the discharge chamber from the orifice of grid as suggested by C. Eichhorn [113]. However, this method cannot be measured under nominal thruster operation because of low S/N ratio.



(1) Before average



(2) 5 average



(3) 10 average



(4) 50 times average



(5) 100 times average



(6) 500 times average



**Fig. 2.21** Transition of TALIF signal with respect to the number of average. Green line: laser signal detected by PMT2, red line: fluorescence signal detected by PMT1 in Fig. 2.19

## 2.5 Validity of TALIF measurement

In this section, the validity of TALIF measurement. Specifically, following perspectives will be discussed.

1. Temporal function
2. Calibration method to obtain absolute value of ground-state neutral density
3. Laser power
4. Broadening of fluorescence signal
5. Optical window effect against thruster performance
6. Reproducibility of TALIF measurement

### 2.5.1 Temporal function of fluorescence signal

Figure. 2.22 shows three kinds of fluorescence signals, (a) cold gas, (b) w/o ion ext., (c) w ion ext. Here, 'ext.' means extraction. Top figure shows the result of WG injection, whereas bottom figure shows that of DC injection. As an example, these results were obtained by the by averaging 3,000 laser shots (data acquisition shows subsection. 2.4.1 ), and measurement point is  $z = -11.5$  cm. Experimental condition is optimal flow rate in both WG injection (1.8 sccm) and DC injections (2.9 scccm). Figure. 2.22 indicates that the fluorescence signal increases to a maximum value and decays at about 50 ns after laser injection. Noted that in this experiment, the lifetime of fluorescence seems to be expand because of time constant of PMT. In these plots, the vertical axis is the laser-induced fluorescence signal amplified by the PMT, which had approximately 1 ns resolution in the time domain. The cold gas generated the highest signal intensity together with a stable baseline, since there was no background plasma emission. Once the 34 W microwave power was injected into the thruster, the neutral xenon atoms were ionized, and this decreased the S/N value. The background emission under these conditions introduced a measurement error of approximately 10%.

Comparing (a) with (b), the fluorescence signal is approximately equivalent within 5% including the maximum intensity and the decay rate. Possible cause of decreasing the neutral density is following three reasons.

- I. Ions are leaked from accelerator grid

## II. Other excitation particles

### III. Thermal accommodation effect

First, leakage of ions from the accelerator grid decreases the ground-state neutral density. Second, excitation can decrease the ground-state neutral density. In case of excited state neutral particles at resonant state, they are returned to ground-state after several or several ten ns, whereas metastable state does not transit to ground-state neutral immediately. Thus, metastable density can explain the decrease of ground-state neutral density partly. Thirdly, when ions are lost at the wall, the ions return to neutral particles, and then the velocity and energy are decided by thermal accommodation coefficient  $\alpha_{th}$ . Here,  $\alpha_{th}$  is generally defined as follows [118].

$$T_n = \alpha_{th}T_{wall} + (1 - \alpha_{th})T_i. \quad (2.14)$$

Here, subscription of  $n, wall, i$  mean the reflected, wall, and ions temperatures respectively. Generally,  $\alpha_{th}$  depends on the energy of the ions, scattering angle and surface material [30]. From Ref. [31] and [32], the thermal accommodation coefficient is 0.86 [119] or 0.95 [120] for an aluminum surface and xenon. Then, the coefficient tends to increase as the surface becomes rough [121]. Thus, considering this coefficient is measured on a clean surface and the surface of the thruster is much rougher,  $\alpha_{th}$  is more close to 1.0. If  $\alpha_{th} < 1$ , the high-energy neutral particles exist, resulting in the neutral density decreases because they can rapidly exhaust from the thruster. Though three causes cannot be distinguished, ground-state neutral particles almost account for at least 85%.

In addition, in case (c), the 1500 and -350 V applied to extract an ion beam that provides thrust to the spacecraft in the operational mode. Comparing (b) with (c), the intensity fluorescence signals are reduced. In case of WG injection, the intensity is reduced by approximately 70%, whereas the intensity is reduced by approximately 20%. Generally, considering 0-dimensional continuity equation on ions and neutral particles, the neutral density in case of ion extraction can be expressed as follows [122].

$$n_n = n_{n0}(1 - \eta_u). \quad (2.15)$$

Here,  $n_n, n_{n0}, \eta_u$  are the neutral density without ion extraction, neutral density with ion extraction, and propellant utilization efficiency. In case of optimal flow rate, propellant utilization

efficiency about  $\eta_u \sim 80\%$ , i.e,  $n_n \approx 0.2n_{n0}$ . Thus, Eq. (2.15) can explain the decrease of neutral density in case of DC injection, but it cannot explain that in case of WG injection, which is non 0D effect due to gas injection. This will be discussed in detailed in appendix. D.

In this thesis, the fluorescence intensity was evaluated by integrating from 0 ns to 50 ns in temporal fluorescence signal (Fig. 2.22). Noted that the fluorescence signal contains the fluctuation of spontaneous emission noise. Hence, the case that the intensity of fluctuation is the similar value of that of fluorescence is the lower limit of the ground-state neutral density. For instance, the fluctuation in case of DC 1 sccm is shown in Fig. 2.23. In this case, the spontaneous emission was obtained by averaging 3,000 times and the spontaneous emission was normalized so that the averaged value becomes 1.0. In this case, the intensity of fluctuation is 0.15% at maximum. Figure. 2.24 shows two cases of temporal fluorescence signals in case of DC 1sccm. Because the fluctuation of spontaneous emission is independent on the laser injection, the fluorescence signal of case 2 was buried by the fluctuation. In this case, the integrated value from 0 ns to 50 ns is negative, thus the ground-state neutral density is also negative. In this thesis, the measurement was preformed five times in each thruster operation, and then the dispersion was attached to the density as the error bar.

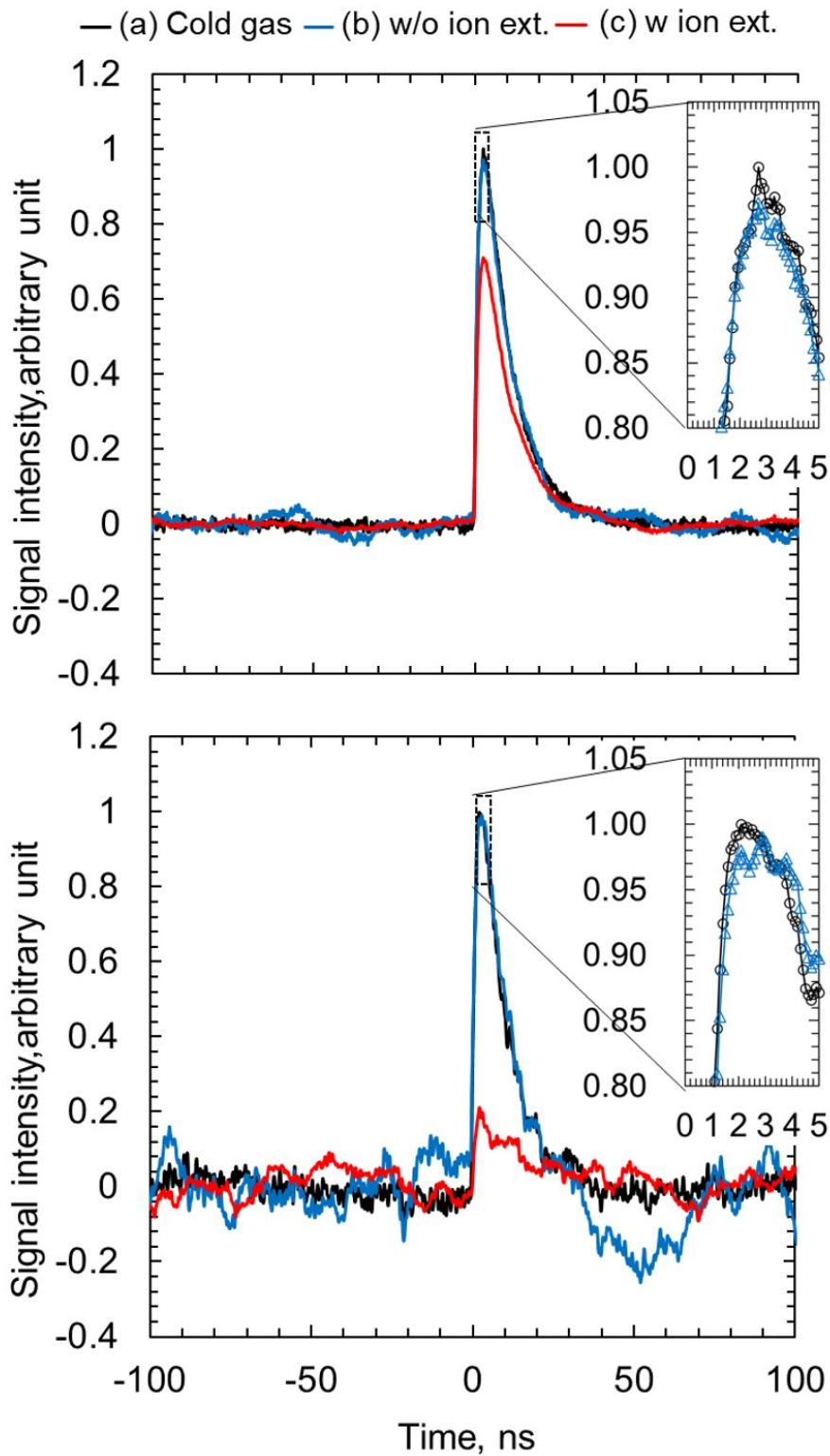


**Fig. 2.22** Typical fluorescence signal in TALIF measurement at optimal flow rate respectively. Experimental condition: DC injection at 2.9 sccm, WG injection at 1.8 sccm. Measurement point is 11.5 cm from screen grid. There are three kinds of signal: (a) cold gas, (b) without ion extraction, and (c) with ion extraction.

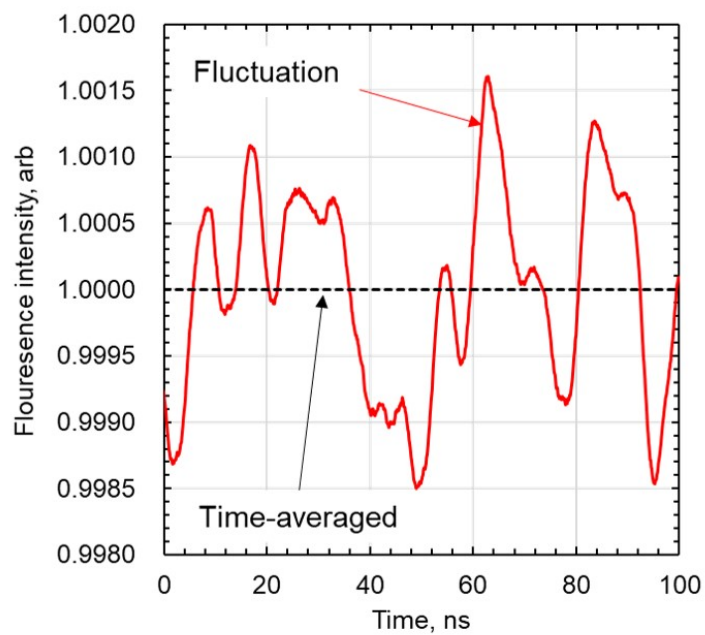


**Fig. 2.23** Fluctuation of spontaneous emission intensity in case of DC 1 sccm. The fluctuation is approximately 0.15% at Maximum.

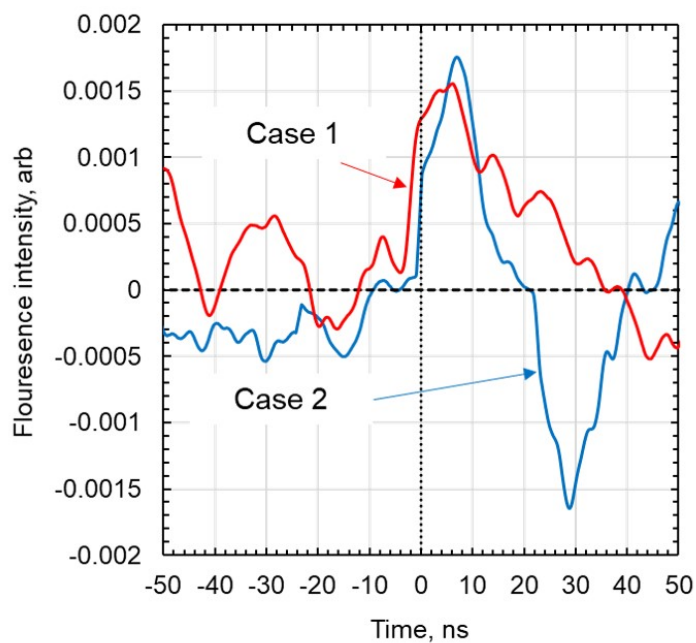


**Fig. 2.24** Two cases of temporal fluorescence signals in case of DC 1sccm. In case 2, the ground-state neutral density becomes negative due to fluctuation of spontaneous emission.

### 2.5.2 Calibration of TALIF signal

To obtain the absolute value of ground-state neutral density, it is necessary to calibration between fluorescence intensity and neutral density. Then, the fluorescence signal was calibrated by the fluorescence signal of known pressure measured by hot cathode gauge. Specifically, following steps were used for this calibration.

- I. Valves of vacuum pumps are closed to maintain the low pressure condition in low-pressure condition (typically,  $1 \times 10^{-5}$  Pa)
- II. Xenon gas is injected, and then the pressure was measured by hot cathode gauge.
- III. Fluorescence signal was obtained at the xenon gas pressure.

Operation II. and III. are repeated as the xenon pressure increases. Noted that this calibration method may include two kinds of uncertainties. First, after closing valves of vacuum pumps, the pressure of vacuum chamber increases due to the output gas and the leakage of air. Thus, this increase of pressure is measured in advance, and then it substrates the measured pressure of xenon. Second, the pressure of hot cathode gauge exhibits the case of Nitrogen gas. Thus, it is necessary to convert from pressure of Nitrogen to that of xenon. The coefficients of the conversion is called sensitivity coefficient. Then, strictly speaking, this coefficient depends on the pressure. Thus, the sensitivity coefficient was obtained experimentally. Specifically, xenon gas injected pressure continuously, and then the increase of pressure was measured. The increase of pressure can be expressed as follows.

$$V_c \frac{dP_c}{dt} = \dot{m}_{in} \quad (2.16)$$

Where,  $V_c$  and  $dP_c/dt$  are the volume of vacuum chamber and the increase of pressure respectively. In this experiment, input flow rate  $\dot{m}_{in}$  was 0.5 sccm. Then, substituting parameters into Eq. 2.16, theoretical  $dP_{c,tho}/dt \approx 8.3 \times 10^{-4}$  Pa/s was obtained. On the other hand, experimental results are shown in Fig. 2.25. 'First' and 'Second' show the data obtained before and after TALIF measurement respectively. The experimental result shows that the pressure linearly increases with respect to time, and then this experimental  $dP_{c,ex}/dt = 2.16 \sim 2.17 \times 10^{-3}$  Pa/s. The difference between  $dP_{c,tho}/dt$  and  $dP_{c,ex}/dt$  exhibits the sensitivity coefficient. Thus, the sensitivity coefficient  $f_{sc}$  can be calculated;  $f_{sc} = \{dP_{c,ex}/dt\}/\{dP_{c,tho}/dt\} \approx 2.6$ . From

catalog, the sensitivity coefficient is  $f_{sc} = 2.5$ , which shows that this experimental result is reasonable, then change of the sensitivity coefficient with respect to pressure can be negligible. Therefore, in this thesis, the sensitivity coefficient is fixed at  $f_{sc} = 2.6$ .

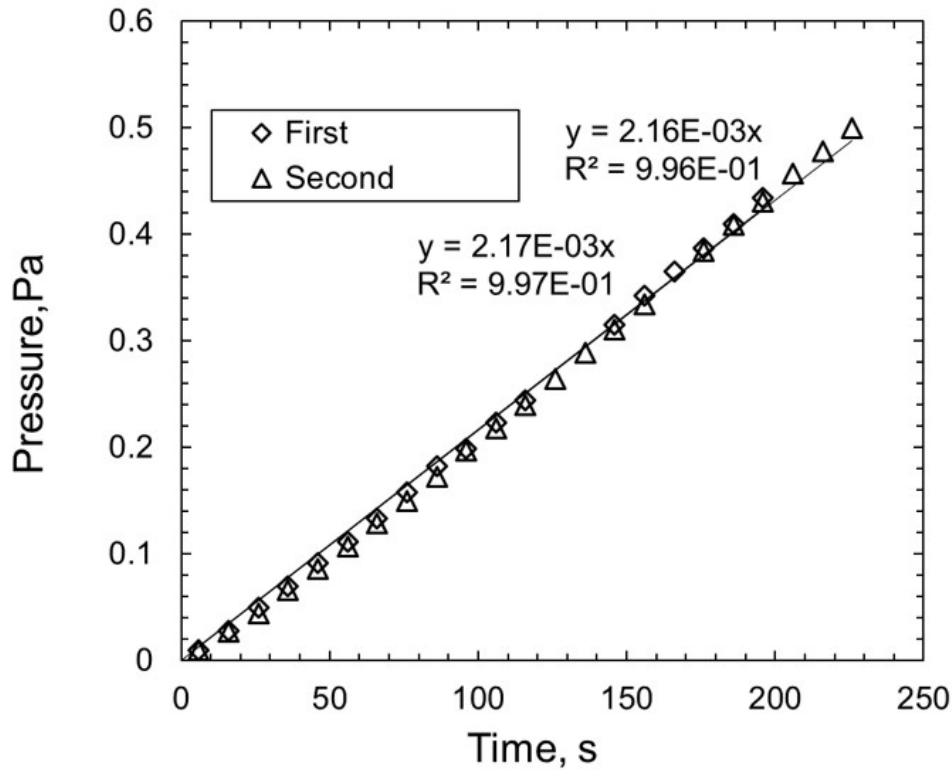


**Fig. 2.25** Confirmation of Sensitivity coefficient about hot cathode gauge. In this experiment, 0.5 sccm of xenon gas is continuously injected and increase of pressure measured by hot cathode gauge was measured. First: before data obtained after TALIF measurement, second: data obtained after TALIF measurement

By using these operations, the calibrated function was obtained as shown in Fig. 2.28. The result indicates that the relationship exhibits the linear function, which means that Eq.(2.9) is satisfied. Then, effect of photo ionization can be neglected in range of pressure.

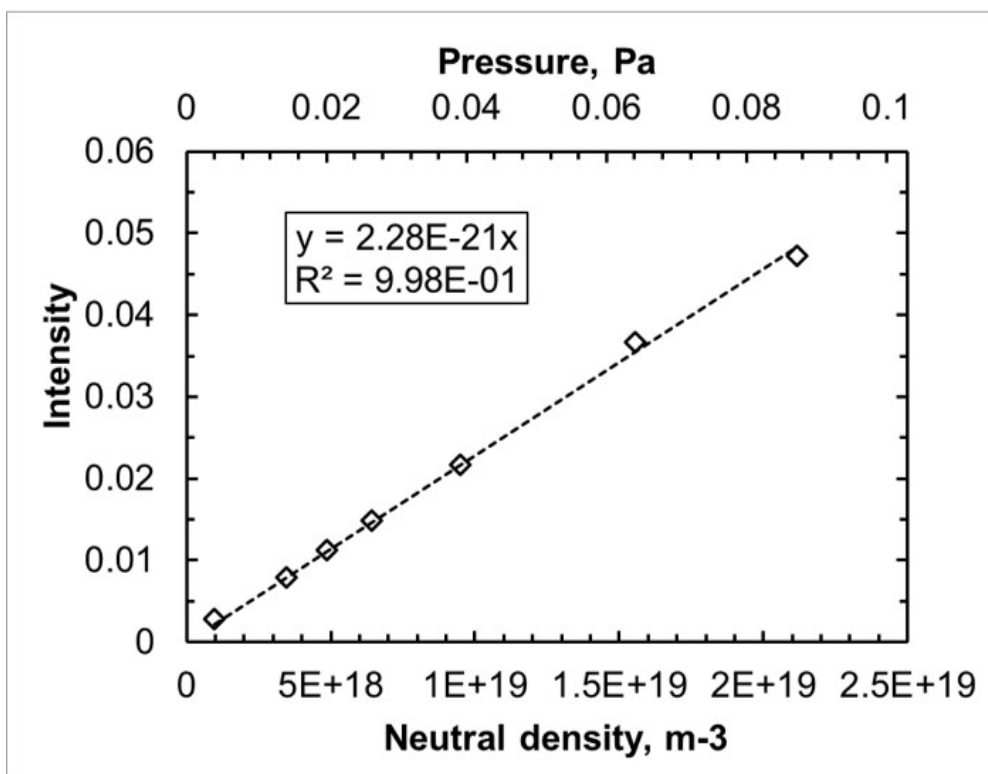


**Fig. 2.26** The ground-state neutral densities without thruster operation as function of flow rate. Here, the absolute value of ground-state neutral density is obtained by calibration.

### 2.5.3 Laser power effect

The sensitivity of the laser power against the fluorescence signal was investigated. First, the intensity of the fluorescence signal with respect to laser power is shown in Fig. 2.27. Here, the case is cold gas at the flow rate is 2 sccm of DC injection. These results show that the fluorescence signal increases corresponding to laser power, but it does not proportional to square of laser power  $I^2$ . Thus, state of excitation is neither saturation nor weak excitation. Kinofuchi also reported that the state of excitation in range of the laser power is neither saturation nor weak excitation [25]. However, the fluorescence signal with respect to flow rate is shown in Fig. 2.28. This experimental result indicates that the fluorescence signal is proportional to flow rate due to low pressure explained by Eq.(2.9). Additionally, as described in the previous subsection, this result can also prove that effect of photo ionization can be neglected in range of pressure.

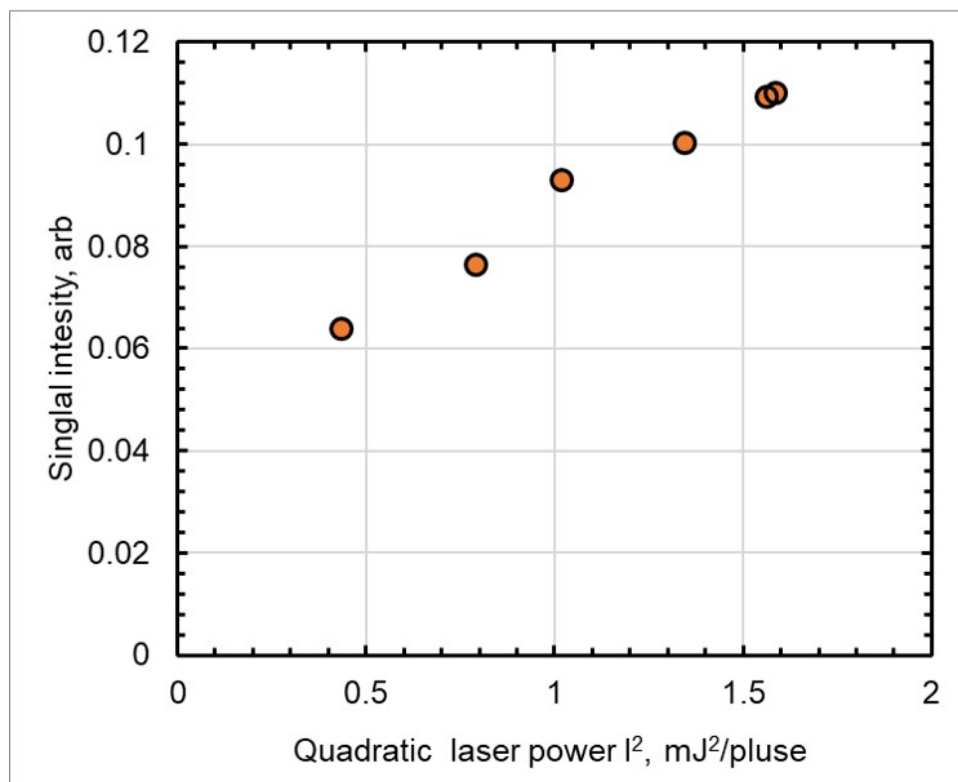


**Fig. 2.27** Intensity of the fluorescence signal with respect to laser power. Experimental condition is cold gas at the flow rate is 2 sccm of DC injection.

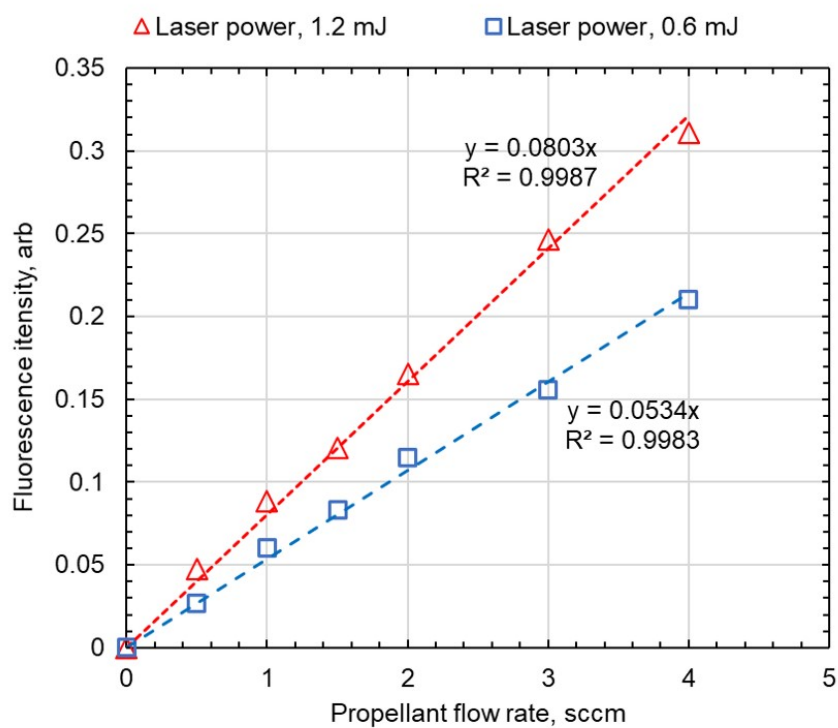


**Fig. 2.28** Intensity of the fluorescence signal with respect to pressure in two kinds of laser power. Red: 1.2 mJ, Blue: 0.6 mJ. Experimental condition is cold gas at the flow rate is 2 sccm of DC injection.

### 2.5.4 Optical window effect

In the measurement, two optical windows were equipped inside the waveguide for laser injection and fluorescence detection. These windows can avoid the leakage of neutral gas, but they are dielectric materials. Hence, these windows may affect the plasma state or microwaves inside waveguide. Thus, the beam currents were compared between with and without optical windows. For instance, the comparison at two kinds of thruster, 'WG injection' and 'DC injection' were shown in Fig. 2.29. The effect of the optical windows in case of WG injection was found to be quite limited especially for flow rates from 1.0 to 2.0 sccm, which is the nominal operational range for this model. In addition, a 1% variation in the beam current was observed. In the case of the DC injection trials, a 0.05 sccm increment in the propellant flow was necessary to achieve the same beam current after installing the windows, even though the windows were completely sealed. This beam current difference was slightly higher than that observed for the WG injection, but still represented only 1–3% of the entire flow rate range. This evaluation confirmed that the installation of the optical windows in the waveguide (as shown in Fig. 2.19) had a minimal effect on the subsequent.

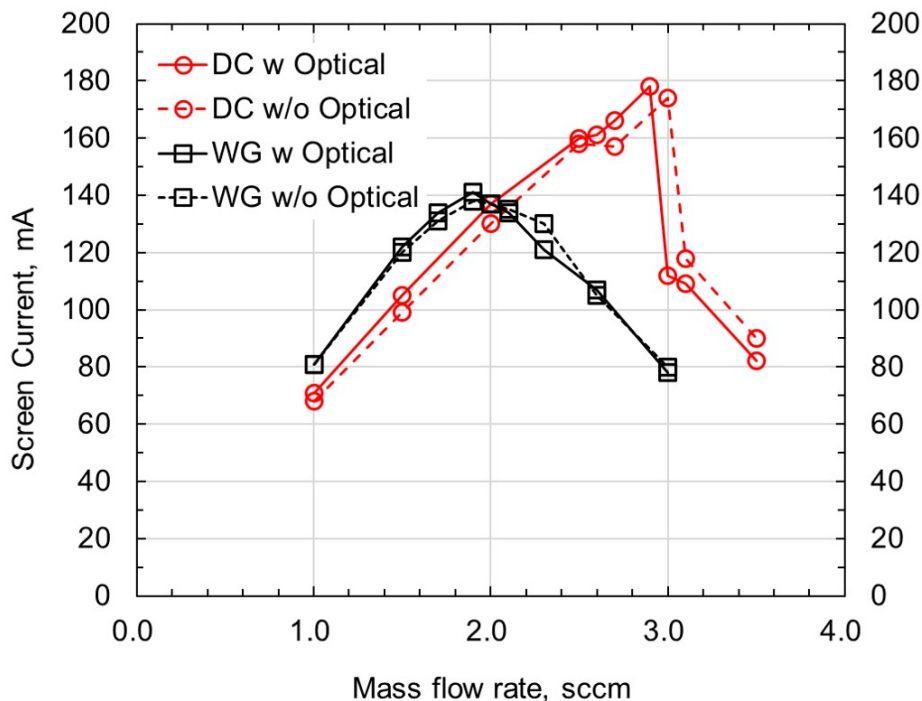


**Fig. 2.29** A comparison of ion beam currents with and without optical windows. Legend: DC = data from the discharge chamber propellant injection inlets, WG = data from the waveguide.

### 2.5.5 Broadening of fluorescence signal

Generally, TALIF signal has the broadening in wavelength domain. Theoretically, broadening of distribution function can be caused by following components.

1. Doppler broadening
2. Pressure broadening
3. Natural broadening
4. Laser width
5. Isotopic shift

Then, Doppler broadening and laser width show Gaussian profile, whereas Pressure broadening and Natural broadening show Lorentzian profile. Thus, if some broadening consists of the measured broadening, the shape is distribution function is convolution of Gaussian profile and Lorentzian profile, i.e., Voigt function [87].

A concern is that if the difference of Doppler broadening between with and without plasma cannot be negligible, the peak of the fluorescence signal can decrease. For instance, Ref [123] reported that the peak signal is decreased by 63% due to increase of neutral temperature from 297 K to 6000 K. To investigate this broadening, TALIF signals were obtained by changing laser wavelength. As well as previous section, there are three kinds of signal: (a) cold gas, (b) without ion extraction, and (c) with ion extraction. Then, the measurement point is  $z = -11.5$  cm and then the experimental condition is flow rate of 2 sccm at DC injection. First, Fig. 2.30 shows the broadening respectively. The vertical shows the fluorescence intensity obtained by integration the fluorescence signal over time domain (Fig. 2.22). The error bar is dispersion of five data sets. Then, in order to compare the relative shapes of the spectra, the intensities were also normalized so that the integrated value becomes 1.0 as shown in Fig.2.31. In addition, to evaluate the broadening quantitatively, the distribution functions are fitted by Voigt function. Generally, Voigt function can be expressed as follows.

$$V(x, \gamma_G, \gamma_L) = \int_{-\infty}^{\infty} G(y, \gamma_G) L(y - x, \gamma_L) dy \quad (2.17)$$

Here,

$$G(y, \gamma_G) = \frac{1}{\gamma_G \sqrt{2\pi}} \exp\left(-\frac{y^2}{2\gamma_G^2}\right) \quad (2.18)$$

$$L(y, \gamma_L) = \frac{1}{\gamma_L \pi (y^2 + \gamma_L^2)}. \quad (2.19)$$

Where,  $\gamma_L$  is dispersion due to Lorentzian broadening, and  $\gamma_G$  is dispersion due to Gaussian broadening. The measured spectra was fitted by Voight function. Because Voight function includes integration form, it is difficult to perform this fitting directly. Instead, the approximated form of Voight function has been proposed within error of 1% [124].

$$V(x, \gamma_G, \gamma_L) \cong \eta G(x, \gamma_G) + (1 - \eta) L(x, \gamma_L). \quad (2.20)$$

Here,

$$\eta = 1.36603 \times \frac{f_L}{f} - 0.47719 \times \left(\frac{f_L}{f}\right)^2 + 0.11116 \times \left(\frac{f_L}{f}\right)^3. \quad (2.21)$$

$$\eta = (f_G^5 + 2.69269 \times f_G^4 f_L + 2.42843 \times f_G^3 f_L^2 + 4.47163 \times f_G^2 f_L^3 + 0.07842 \times f_G f_L^4 + f_L^5)^{\frac{1}{5}}. \quad (2.22)$$

$$f_L = 2\gamma_L, \quad f_G = 2\sqrt{\ln 2} \gamma_G. \quad (2.23)$$

Figure. 2.32 shows the distribution functions fitted by Voight function of Eq.(2.21). Then, each FWHM due to each broadening of Gaussian and Lorentz is summarized in Tab. 2.6. As a results, the FWHM of convolution, Gauss, Lorentz are summarized in . The table shows that FWHM of convolution  $\Delta\lambda_{conv}$ , Gauss  $\Delta\lambda_G$ , Lorentz  $\Delta\lambda_L$  are  $\Delta\lambda_{conv} = 3.3 \sim 3.5$  pm,  $\Delta\lambda_G = 0.69 \sim 0.75$  pm,  $\Delta\lambda_L = 3.2 \sim 3.3$  pm respectively, and these FWHM are not very sensitive to operation mode.

**Table 2.6** Comparison of FWHM obtained by TALIF signal in case of (a) cold gas, (b) w/o ion ext, and (c) w ion ext... These experiment results are fitted by Voight function to evaluate Lorentz and Gaussian broadening.

Case	FWHM (Convolution), nm	FWHM (Gauss), nm	FWHM (Lorentz), nm
(a) Cold Gas	3.5	3.2	0.78
(b) w/o ion ext.	3.3	3.2	0.69
(c) w ion ext.	3.5	3.3	0.73

Generally, Doppler broadening can be estimated by following equation.

$$\Delta\lambda_d = \frac{\lambda_i}{c} \sqrt{8 \ln 2 \frac{kT}{m}}. \quad (2.24)$$

Considering neutral temperature is 400 K typically,  $\Delta\lambda_{D_o} \approx 0.24$  pm. In addition, from the catalog of Dye-laser, the laser broadening is  $\Delta\nu_l = 0.055 \text{ cm}^{-1}$ . Thus, FWHM of laser broadening can be calculated.

$$\Delta\lambda_l = \frac{\Delta\nu_l \lambda_i^2}{c}. \quad (2.25)$$

Substituting  $\Delta\nu_l = 0.055 \text{ cm}^{-1}$  into above equation,  $\Delta\lambda_l \approx 0.27$  pm is obtained. The convolution of Gaussian profile can be calculated by root sum square.

$$\Delta\lambda_{tho,g} = \sqrt{2 \times \Delta\lambda_l^2 + \Delta\lambda_d^2}. \quad (2.26)$$

Here, the factor of 2 is derived from that effective of laser broadening at two-photon excitation [125]. The results indicate that Gauss broadening is computed  $\Delta\lambda_{tho,g} \approx 0.45$  pm. The result indicates that Gauss broadening of theory is about 60 ~ 66% compared to measurement. Thus, it is concluded that the measurement of Gauss broadening is larger than expected value. One cause may be that the laser power broadening. For instance, Matsui and Komurasaki *et al.* [126] reported that the Doppler broadening is wider in case laser power is high at LAS experiment. W.A. Hargus and M.A. Cappelli *et. al* also reported that experimental broadening is wider in case laser power is high [60].

However, the experimental result shows that the fitting lines in these plots indicate a  $-4.5\%$  decrease in the FWHM and a  $-1.2\%$  decrease in the peak intensity for '(b) w/o ion ext.' and a  $4.2\%$  increase in the FWHM and a  $-3.4\%$  decrease in the peak intensity for '(c) w ion ext.', compared with the cold gas mode. Taking into account the 10% measurement uncertainty, assumption neglecting these decreases is reasonable.

Additionally, the bulk velocity of neutral particles, i.e., shift of peak wavelength was not be observed. Generally, Doppler shift of neutral particles is connected with the bulk velocity  $U_n$ .

$$U_n = -c \frac{\Delta\lambda}{\lambda}. \quad (2.27)$$

Considering that the resolution of laser is approximately 0.2 pm, the bulk velocity is smaller than  $|U_n| \leq -c\Delta\lambda/\lambda \approx 268 \text{ m/s}$  at least. On the other hand, the thermal velocity is  $v_n =$

$\sqrt{2k_B T_n / m_n} \approx 224.5$  m/s under neutral temperature  $T_n$  of  $T_n = 400$  K. Because  $|U_n/v_n| \leq 1$  is natural, it is reasonable that the Doppler shift is not observed.

Based on the above discussion, the effect of Doppler Broadening and shift can be negligible considering the measurement accuracy and resolution of laser wavelength. Thus, it is justified that the ground-state neutral densities are evaluated by using the fluorescence intensity at the peak wavelength.

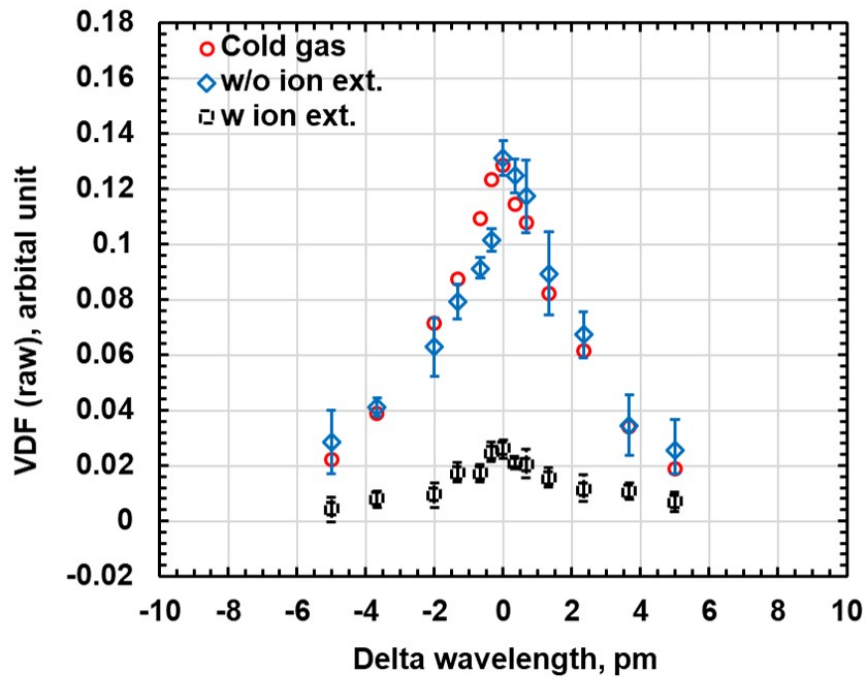


**Fig. 2.30** The fluorescence spectra obtained from cold gas, ionized state and beam extraction measurements. The spectra were recorded at 2.0 sccm from DC injection.

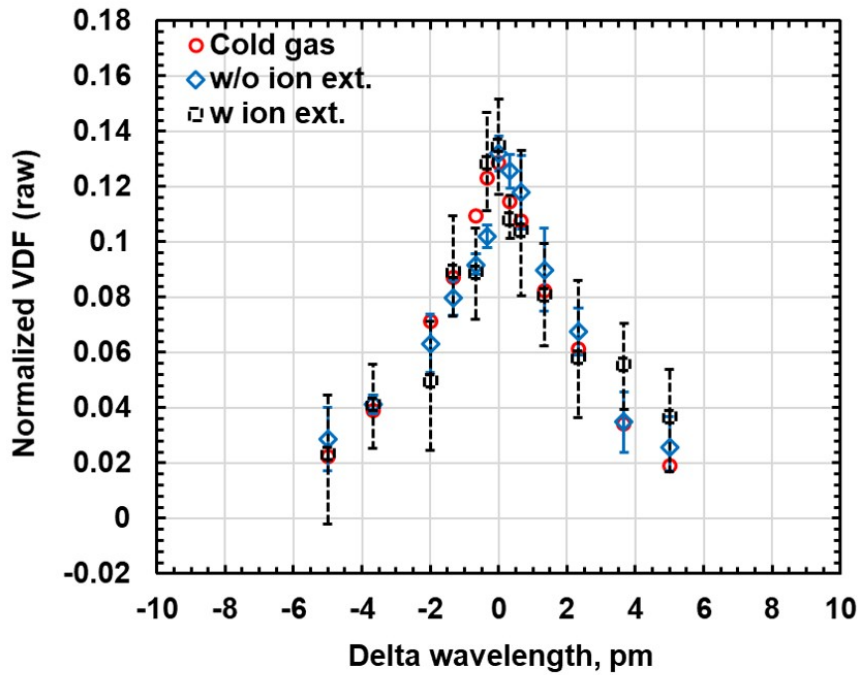


**Fig. 2.31** The fluorescence spectra obtained from cold gas, ionized state and beam extraction measurements. The data was normalized the experimental results (Fig. 2.30). The spectra were recorded at 2.0 sccm from DC injection.

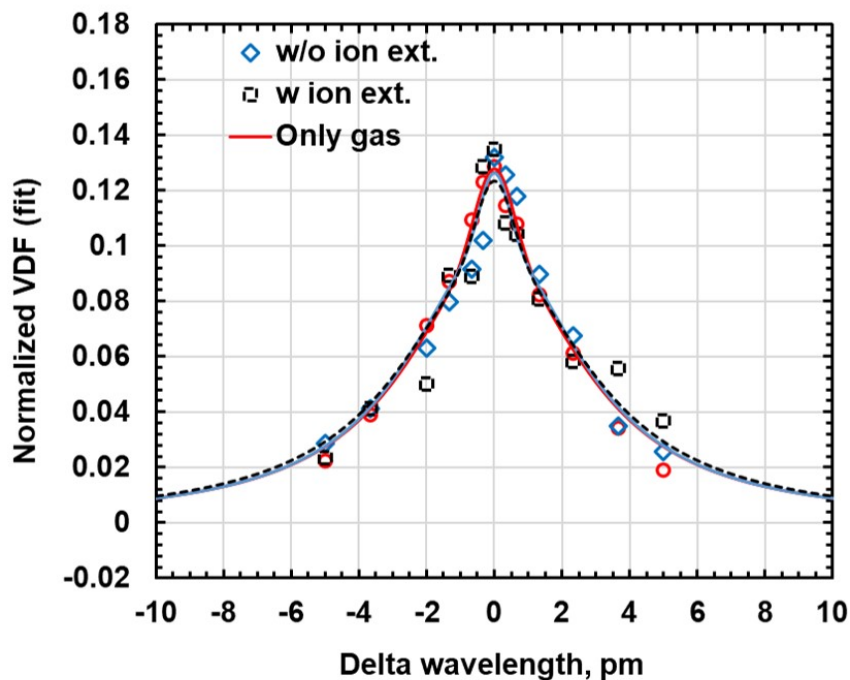


**Fig. 2.32** The fluorescence spectra obtained from cold gas, ionized state and beam extraction measurements. Voigt functions fitted the normalized experimental data (Fig. 2.31). The spectra were recorded at 2.0 sccm from DC injection.

### 2.5.6 Experimental error

In TALIF experiment, it is necessary to move thruster except for one block of waveguide for laser injection and fluorescence detection. Thus, experimental data may include following reproducibility errors.

- (i) Beam current and optimal flow rate
- (ii) Ground-state neutral density and spontaneous emission intensity

Even though the optical window does not exist,  $\mu 10$  thruster has error of beam current of and optimal flow rate. When measuring the axial distribution of ground-state neutral density, the results may include the uncertainty due to thrust performance, for example, ion beam current, optimal flow rate. Therefore, the error of beam current and optimal flow rate is investigated.

First, the ion beam currents with respect to propellant flow rate is shown in Fig. 2.33. Red plots show the results at optimal flow rate. In WG injection, the maximum ion beam current is 138 ~ 139 mA at optimal flow rate of 1.8 sccm. Then, in DC injection, the maximum ion beam current is 168 ~ 175 mA at optimal flow rate. In WG injection, the optimal flow rate is 1.8 sccm in all cases. On the other hand, in DC injection, the optimal flow rate is 2.9 or 3.0 sccm. Since there is an error of 0.1 sccm in the optimum flow rate at the DC injection, the ground-state neutral density and spontaneous emission intensity are shown with result of optimal flow rate (as described later section 2.6).

Second, the experimental error of TALIF measurement was evaluated. The ground-state neutral density includes the uncertainty of calibration (subsection 2.5.2) and the error of plasma condition. Additionally, the experimental results of spontaneous emission intensity include the error of plasma condition. Thus, these are evaluated by repeating these measurements. Specifically, measurement point is -11.5 cm from screen grid, and then thruster is 'DC injection'.

Fig. 2.34 plots the ground-state neutral density and the spontaneous emission intensity with respect to the propellant flow rate. The period of two experimental results are three month. Fig. 2.34-top indicates that results of ground-state neutral densities are good agreement. The detection limit was approximately  $2 \sim 4 \times 10^{18} \text{ m}^{-3}$  due to the fluctuation of plasma emission at 834.68 nm. The error bars changed with respect to the flow rates, the minimum error was  $\pm 2 \times 10^{18} \text{ m}^{-3}$ , whereas the maximum one was  $\pm 4 \times 10^{18} \text{ m}^{-3}$ . Fig. 2.34-bottom indicates that the spontaneous emission intensity has reproducibility with reasonably level.

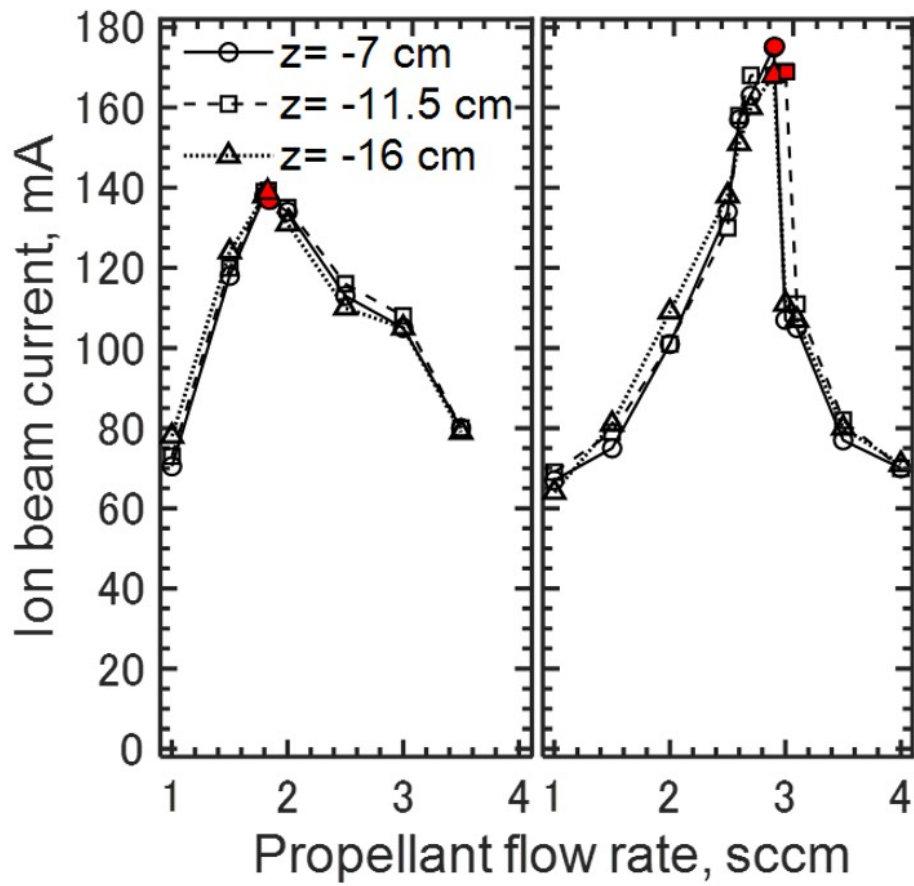


**Fig. 2.33** Ion beam currents with respect to propellant flow rate. Left: WG injection, right: DC injection. Red plot: optimal flow rate.

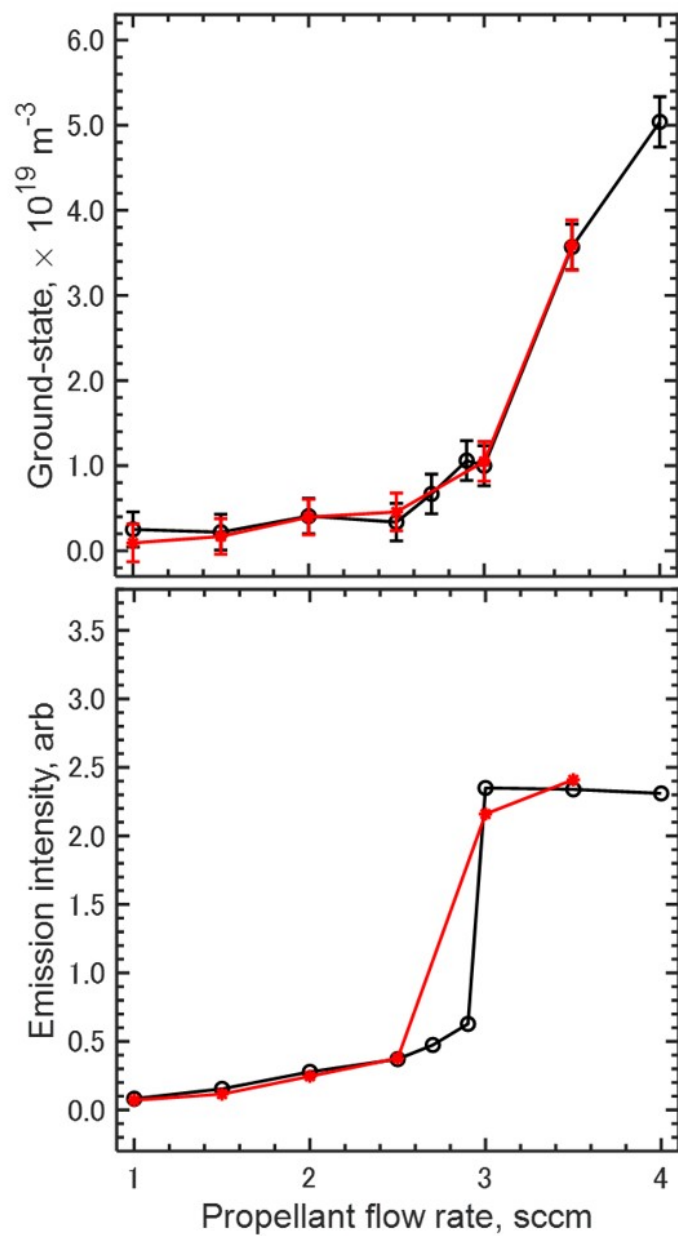


**Fig. 2.34** Reproducibility of TALIF measurement. Top: ground-state neutral density. Bottom: Spontaneous emission intensity. Red: measured by December 2020, Black: measured by September 2020.

## 2.6 Experimental result

Based on the TALIF measurement system as described in section.2.4, ground-state neutral density and the spontaneous emission intensity at 834.68 nm were measured in four kinds of thrusters, (a) WG injection, (b) DC injection, (c) 'w WG ECR', and (d) 'w/o WG ECR'. In this section, the experimental data are discussed following two perspective.

I. Gas injection (Ground-state neutral density distribution)

II. Electron heating inside the waveguide

To investigate I., thruster (a) and (b) were used. On the other hand, to investigate II., thruster (c), (d), and (e) were used.

### 2.6.1 Effect of gas injection

#### 2.6.1.1 Axial distribution of ground-state neutral

First, to clearly show the difference between WG and DC injection, Fig. 2.35 plots the ground-state neutral densities in case of cold gas with respect to the propellant flow rate. Here, the measurement point is  $z=-7.0$  cm from screen grid. The density obtained from WG injection increased at a rate of  $2.58 \times 10^{19} \text{ m}^{-3}$  per 1 sccm, whereas DC injection produced a rate of increase approximately one third lower, at  $1.64 \times 10^{19} \text{ m}^{-3}$  per 1 sccm. Comparing WG injection with DC injection, the ground-state neutral density of WG injection is higher than that of DC injection, which is consistent with DSMC works [116].

Second, the axial distributions of ground-state neutral density are shown in Fig 2.36 and 2.37 respectively. The axial distribution is evaluated by integrating fluorescence signals (Fig. 2.22). The measurement points are  $z=-7.0, -11.5, -16.0$  cm. Note that the optimal flow rate in DC injection is 2.9 or 3.0 sccm depending on the measurement. Since the plasma state changes drastically before and after the optimal flow rate, the neutral density at 2.9 sccm was used for all measurement points. Red plot shows the ground-state neutral density in case of 'w ion ext', and blue plots shows that in case of 'w/o ion ext'. The error of the neutral density is dispersion from five data sets. In the case of DC injection (i) 2.0 sccm, the fluctuation of plasma emission noise becomes the same order of fluorescence signal at 11.5 cm, thus the error bar exceeds negative density.

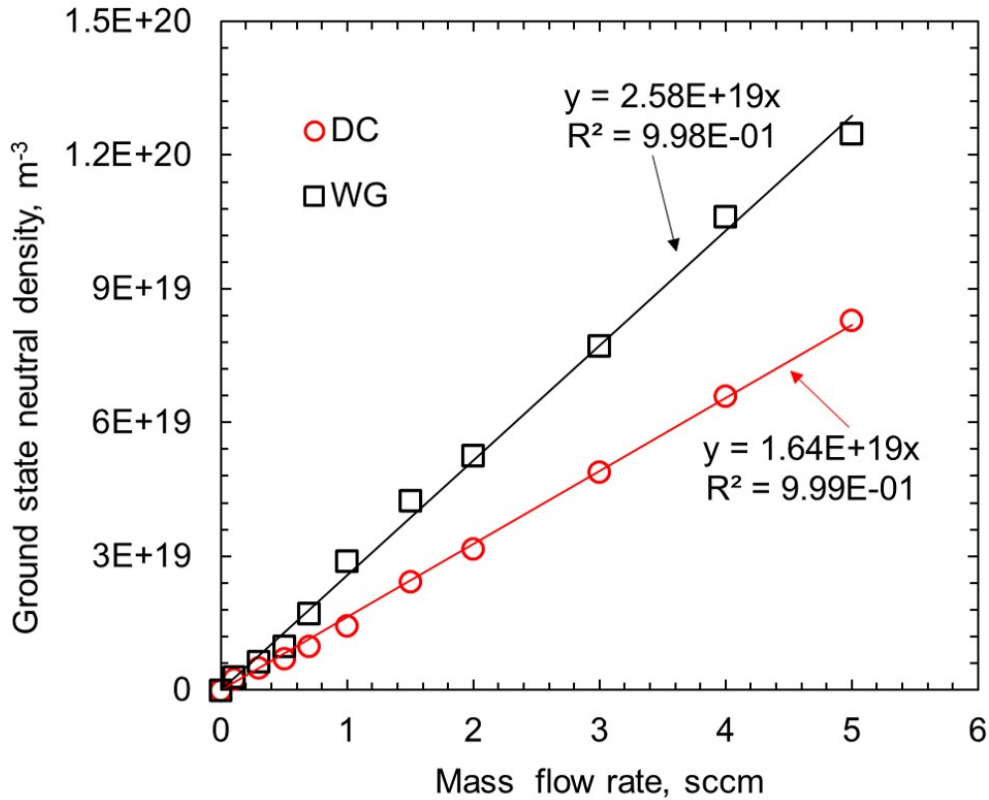


**Fig. 2.35** The ground state neutral densities of the cold gas with respect to propellant flow rate. Legend: WG = data from the waveguide inlet, DC = data from the discharge chamber injection.

Fig. 2.36 and 2.37 suggest that the inhomogeneity of gas injection strongly affects the neutral density distribution. In WG injection, the density gradient is observed in the direction of the discharge chamber in all cases. This is the effect of WG injection, which is consistent with cold gas cases as shown in Fig. 2.35. However, the distribution is locally different without and with ion extraction. In particular, in case (b), at -7 cm, a sharp decrease in the density is observed. Additionally, in DC injection (Fig. 6-right), the distribution becomes flat in the case without ion extraction, which is also consistent with DSMC simulation [12]. However, a density gradient can be seen in cases (b) and (c) with ion extraction. In case (a), no effective density gradient is seen. However, in (b), a density gradient toward the discharge chamber can be seen. However, in (c), a density gradient in the opposite direction can be seen. The difference between with and without ion extraction are discussed in chapter. 3.

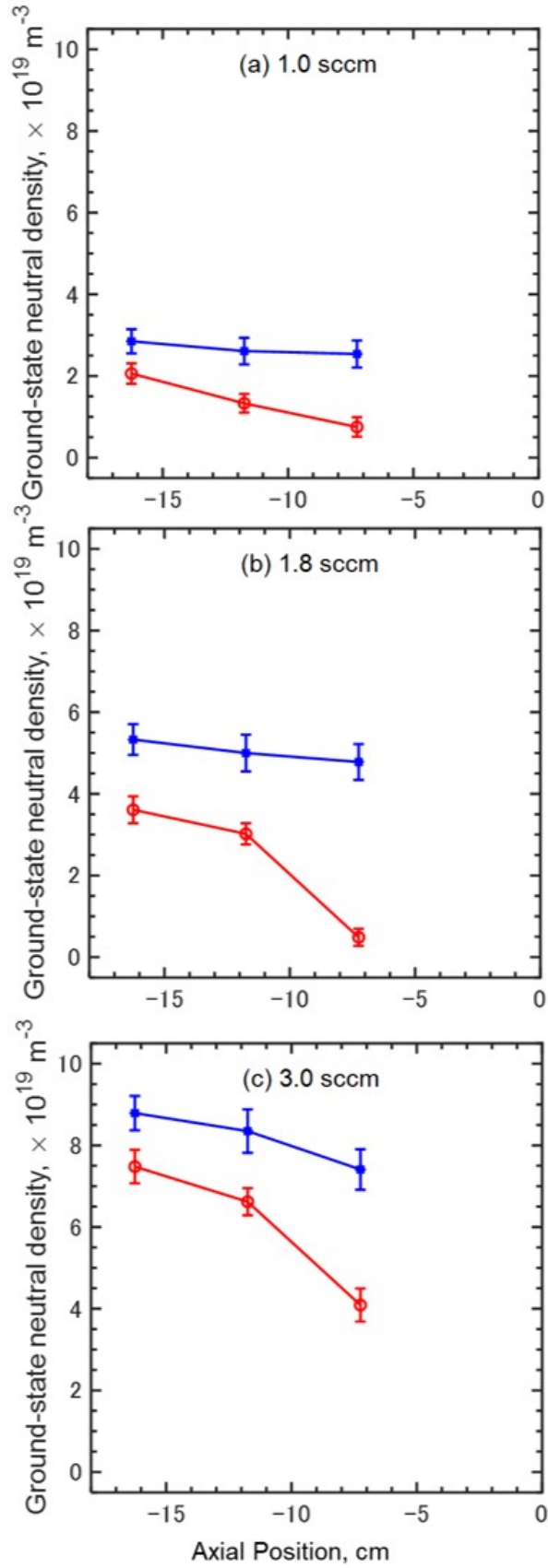


**Fig. 2.36** Axial distribution of ground-state neutral density using TALIF measurement in case of 'WG injection'. Blue line: without ion extraction, red line: with ion extraction. (a) before optimal flow rate (1.0 sccm), (b) optimal flow rate (1.8 sccm), (c) after optimal flow rate (3.0 sccm).

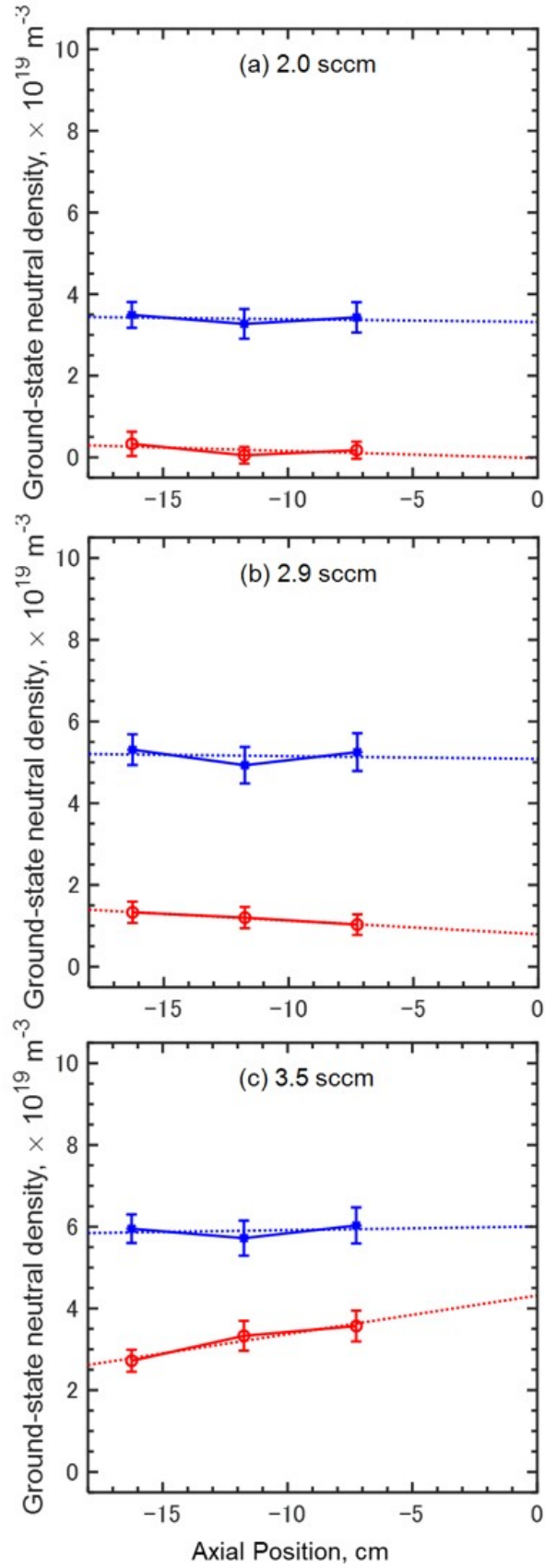


**Fig. 2.37** Axial distribution of ground-state neutral density using TALIF measurement in case of 'DC injection'. Blue line: without ion extraction, red line: with ion extraction. (a) before optimal flow rate (2.0 sccm), (b) optimal flow rate (2.9 sccm), (c) after optimal flow rate (3.5 sccm).

### 2.6.1.2 Comparison of estimated and measured neutral densities

Generally, in gridded ion thrusters, neutral density can be evaluated by 0D continuity equation [22]. Considering the effect of multi-charged ions, 0D neutral density can be expressed as follows.

$$n_n^* = \frac{1}{1 + I_{2+}/I_+ + I_{3+}/I_+} \left( 1 + \frac{1}{2} \frac{I_{2+}}{I_+} \frac{2 - \eta_u}{1 - \eta_u} + \frac{1}{3} \frac{I_{3+}}{I_+} \frac{3 - \eta_u}{1 - \eta_u} \right) \frac{4\dot{m}_{in}}{K_c v_{th} A_{eff}} (1 - \eta_u). \quad (2.28)$$

Here,  $n_n^*$  is the modified neutral density.  $I_+$ ,  $I_{2+}$ ,  $I_{3+}$  are ion beam current due to singly, doubly, and triply charged ions respectively.  $K_c$  is Clausing's function, which is a correction factor by shape of holes. According to  $E \times B$  probe measurements, the current ratios of doubly and triply charged ions are 15-20 % and 5-10 %, respectively [16]. The previous data is not covered the all results on each grid. However, the current ratio is not very sensitive to the propellant flow rate, grid design, and magnetic field [16]. Therefore, we consider the maximum case ( $I_{2+}/I_+ = 20$  %,  $I_{3+}/I_+ = 10$  %) and minimum case ( $I_{2+}/I_+ = 15$  %,  $I_{3+}/I_+ = 5$  %). Then, the result is averaged and attached with maximum and minimum case as the error bar. In circular holes, approximations of  $K_c$  is proposed [127].

$$K_C = \left( 1 + \frac{4L}{3D} + \frac{1}{4D/L + 8/7} \right)^{-1}. \quad (2.29)$$

The conductance  $C_{sum}$  combining the screen grid and the accelerator grid is given by

$$\frac{1}{C_{sum}} = \frac{1}{C_A} + \frac{1}{C_S}. \quad (2.30)$$

From Eq. (??) ~ (2.30), the effective transparency of the grid  $G_{eff}$  be expressed as follows.

$$G_{eff} = \frac{K_{sc} K_{cA} G_s G_A}{K_{sc} G_s + K_{cA} G_A} \quad (2.31)$$

Hence, the effective open area at the grid can be calculated as  $A_{eff} = G_{eff} A_{Ac}$ , where  $A_{Ac}$  is the open area of accelerator grid. The comparison of estimated and measured neutral density was shown in Fig. 2.38.

Though the estimated neutral density is similar curve to TALIF measurement results, the estimation does not match the measured densities quantitatively. The estimation is based on the

continuity equation at the grid. Hence, it is expected that the estimated density exhibits density at the grid. Because the waveguide is far from the grid, the estimated density cannot capture inhomogeneous effects such as gas injection and ionization. For instance, in WG injection, the ground-state neutral density at  $z = -7.0$  cm is smaller than that of estimation in range  $\dot{m} > 1.8$  sccm at  $z = -11.5$  and  $z = -16.0$  cm, however, the ground-state neutral densities are larger than that of estimation. In WG injection, inhomogeneity due to gas injection is large inside the waveguide, thus the estimation cannot capture the neutral density distribution. In addition, in all data of WG injection, sharp decrease of ground-state neutral density was observed at flow rate of  $\dot{m} > 1.8$  sccm. In DC injection, the measured densities are smaller than that of estimation in each location. It is considered that these results caused by the inhomogeneity of ionization. The detailed investigation of inhomogeneous effects such as ionization and gas injection will be discussed in appendix D.

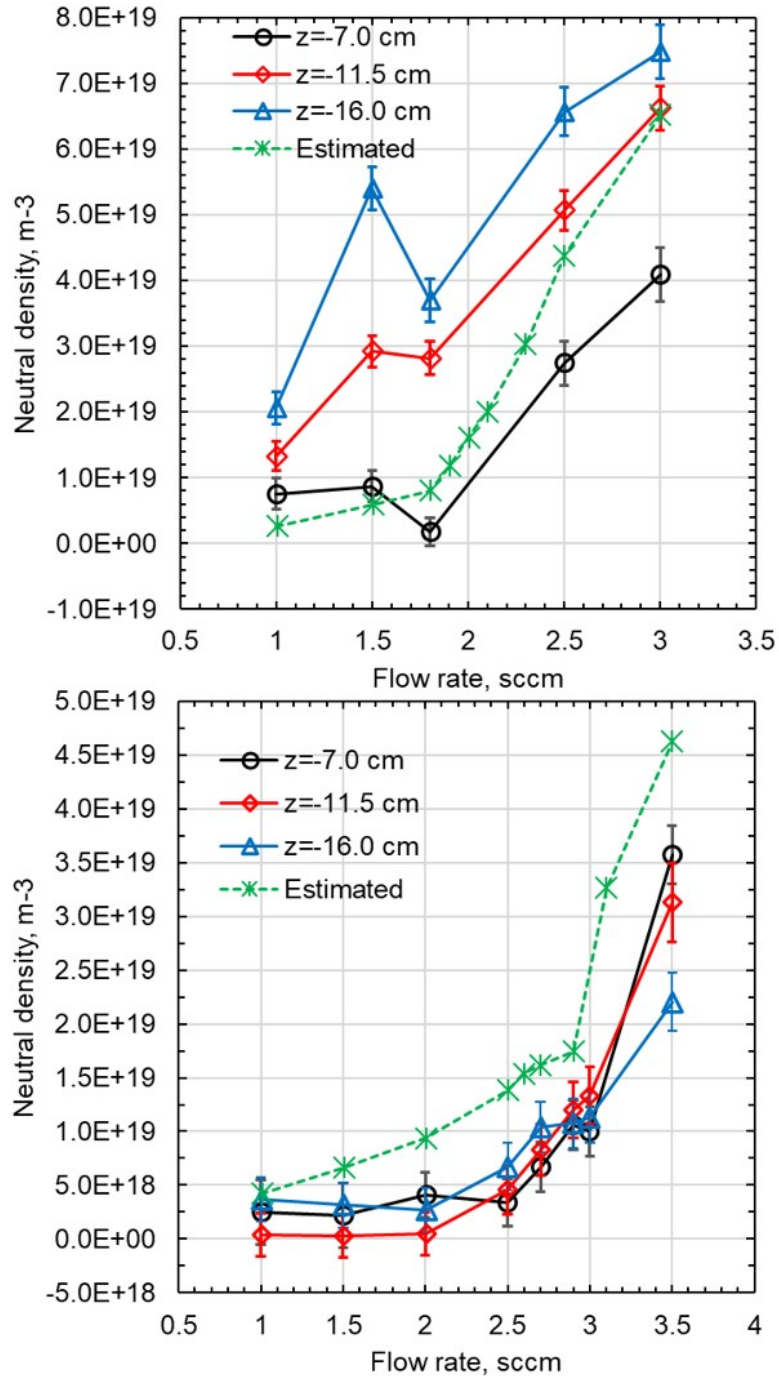


**Fig. 2.38** Comparison of neutral densities between estimation and TALIF measurement. Estimated neutral density was calculated by Eq.(2.28).

### 2.6.1.3 Ground-state neutral density vs Spontaneous emission intensity

Figure. 2.39 shows the spontaneous emission intensity with respect to ground-state neutral density. The red plots show the results at the optimal flow rate. In all cases, the spontaneous emission intensity rapidly increases near optimal flow rate (Red plot). Especially, in WG injection, the ground-state neutral density of 1.8 sccm (optimal flow rate) decreases from 1.5 sccm, but the spontaneous emission intensity increases. In DC injection, the density does not increase or is approximate constant around optimal flow rate, whereas the spontaneous emission intensity increases. Thus, these experimental results indicate that the increase of spontaneous emission intensity cannot be explained from the ground-state neutral density. Additionally, focusing the axial dependence of the spontaneous emission intensity, the maximum value of spontaneous emission decreases only by about 48% from  $z = -7$  cm to  $z = -16$  cm in WG injection, whereas it decreases by about 25% in DC injection. The mechanism on the increase of spontaneous emission intensity and these axial dependence will be discussed in section. 2.7.

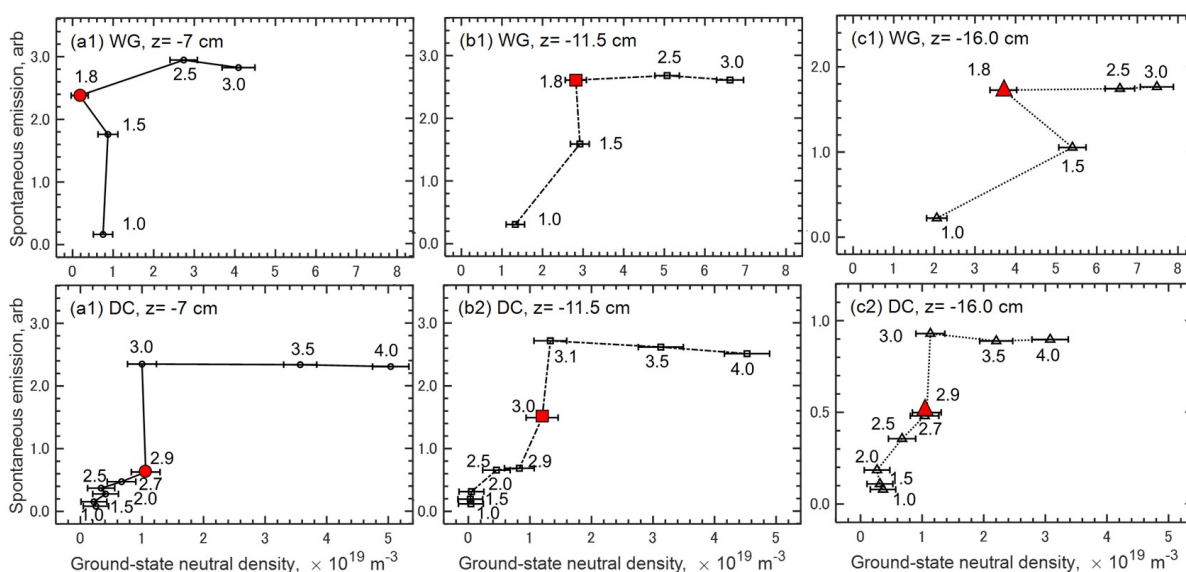


**Fig. 2.39** Spontaneous emission with respect to ground-state neutral density. Top: WG injection, bottom: DC injection. Each value represents a propellant flow rate in units of standard cubic centimetres per minute (sccm). Red plot: optimal flow rate..

## 2.6.2 Electron heating inside the waveguide

### 2.6.2.1 Beam current and photograph view

First, Fig. 2.40 shows the beam current in case of (a) 'w WG ECR', (b) 'w/o WG plasma', and (c) 'w/o WG ECR'. Each configuration is shown in Fig. 2.6. The results show that the maximum beam current of (a), (b), and (c) were 202, 212, and 207 mA respectively, which indicates that the electron heating inside the waveguide is not very sensitive to the maximum ion beam current. However, the plasma hysteresis is deleted in both case (b) and (c), which indicate that plasma state of (b) and (c) is different from that of (a). In case (a), the beam current rapidly decreases after plasma mode-transition, which indicates that the plasma condition is drastically changed between before and after mode-transition. On the other hand, in case (b), the decrease of beam current is reduced, which suggests that the plasma-mode transition is modulated. Additionally, in case (c), the decrease of beam current is more reduced compared to be case (b). Thus, the beam currents after mode-transition suggest that the WG ECR layer is critical parameter for plasma mode-transition. Noted that the case (c) outperformed the nominal case (a) in terms of the maximum thrust and propellant utilization efficiency. However, it cannot use for space mission because the quartz became dirty gradually.

Second, to clearly show the condition of waveguide plasma, the photograph for each case is shown in Fig. 2.41. Beam current of each photograph is shown in Tab. 2.7. Generally, blue and red luminescence shows the spontaneous emission about excited ions and excited neutral particles respectively. Comparing between before and after plasma mode-transition, the red luminescence becomes very strong after plasma mode-transition. Especially, in case (a), the red luminescence is very strong inside the circle of waveguide after plasma mode-transition. On the other hand, the red luminescence becomes small compared to case (a). Considering most of lifetime of excitation is the order of ten ns, the WG plasma and WG ECR layer can suppress the excitation of neutral particles inside the waveguide. However, because the luminescence does not exist inside the circle of waveguide, the excitation inside the waveguide cannot be eliminated completely. Additionally, even if case (c) has the luminescence, the excitation downstream the waveguide exists. Excitation energy is  $8 \sim 11$  eV, whereas the ionization energy is 12.1 eV. Considering that the electrons have a distribution function such as the Maxwellian distribution, the electrons with more than the ionization energy exist. Therefore, when the red luminescence is strong, the plasma is generated inside the waveguide.

However, these information from photograph are not enough because axial resolution are unclear. Thus, in next subsection, excitation and ionization process are investigated by measuring ground-state neutral density and spontaneous emission intensity.

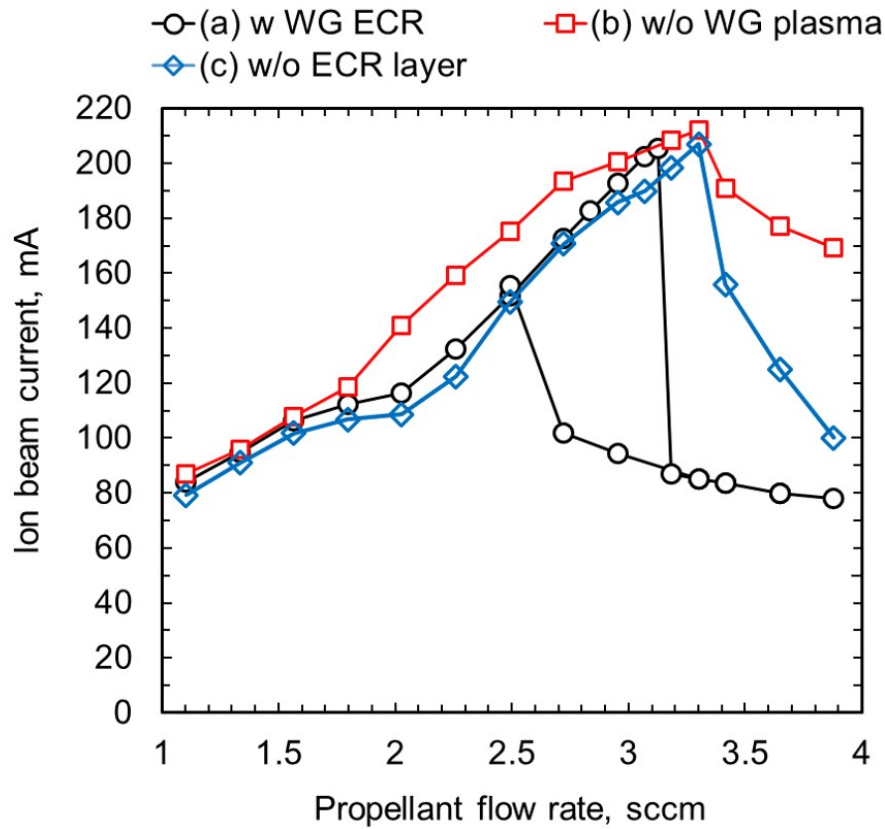


**Fig. 2.40** Ion beam current versus flow rate. In these thrusters, configurations are common and shown in Fig. 2.6

**Table 2.7** Beam current for photograph for four cases. The photograph is shown in Fig. 2.41.

Case	Before optimal flow rate, mA	After optimal flow rate, mA
(a) w WG ECR	205	90
(b) w/o WG plasma	212	156
(c) w/o WG ECR	207	191

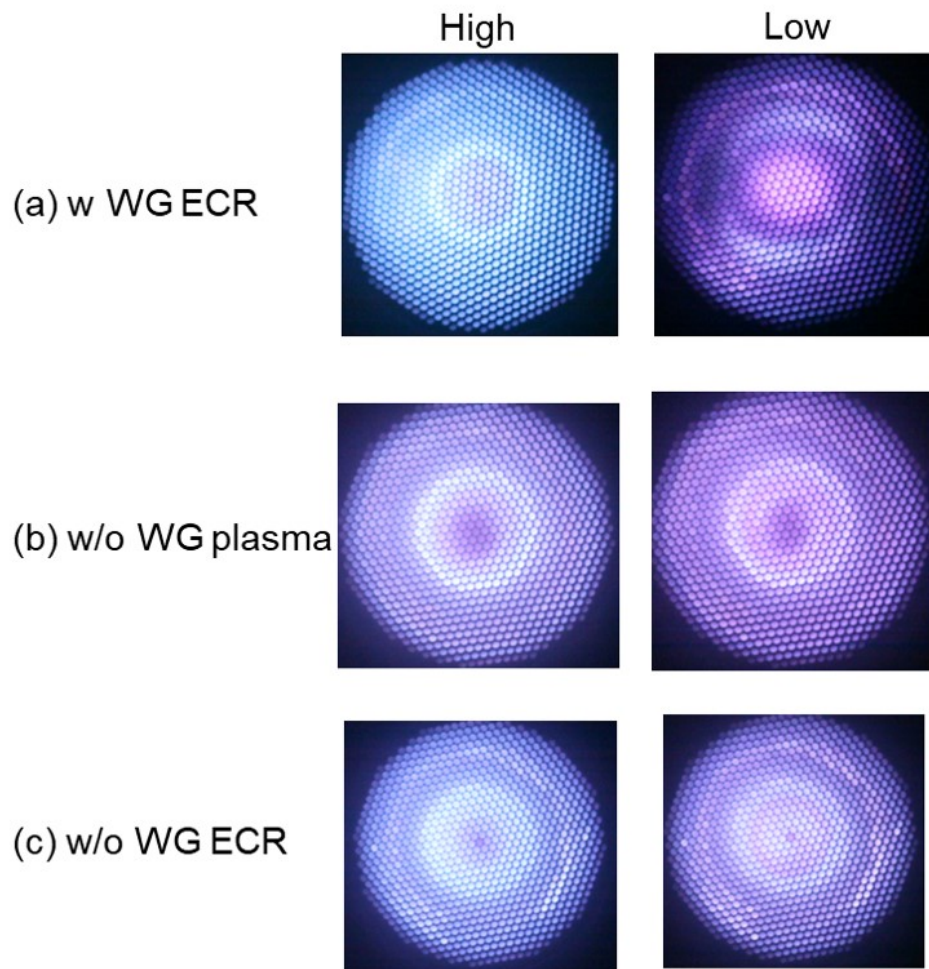


**Fig. 2.41** Photograph before and after plasma mode-transition. The ion beam current is shown in Fig. 2.40. Configurations are summarized in Fig. 2.6. The black dashed circle is the diameter of the waveguide. (a): 'w WG ECR', (b): 'w/o WG plasma', and 'w/o WG ECR'.

### 2.6.2.2 TALIF measurement of WG ECR layer

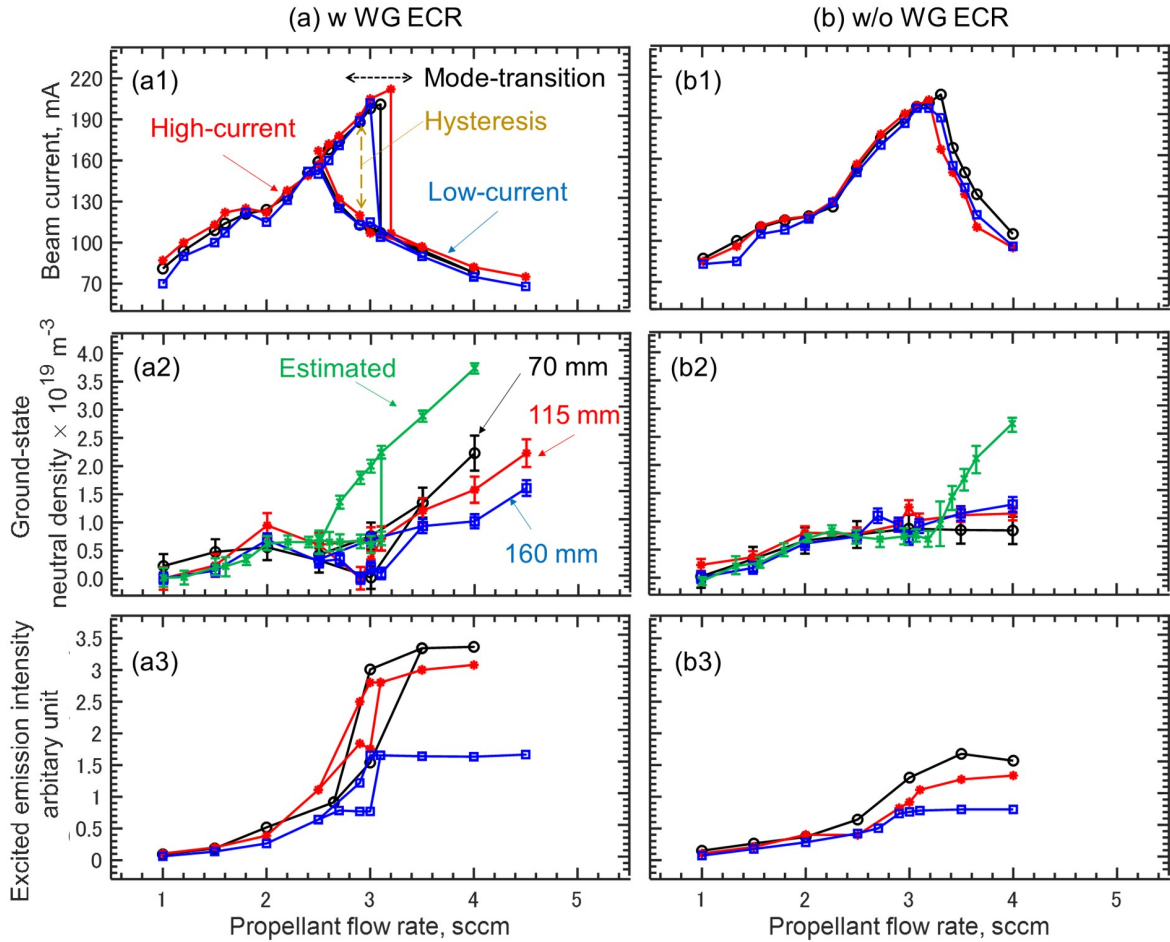
In previous section, the beam current and photograph view are changed after mode-transition by changing electron heating inside the waveguide. In this section, ground-state neutral density and spontaneous emission were measured in each thruster. Because 'w/o WG plasma' does not exist the plasma and neutral particles inside the waveguide, this measurement is applied to two thrusters, 'w WG ECR' and 'w/o WG ECR'.

Fig. 2.42 shows the axial distribution of ground-state neutral density and spontaneous emission intensity at three measurement points;  $z = -7.0, -11.5, 16.0$  cm. Fig. 2.42 (a1) and (b1) show the ion beam current with respect to propellant flow rate. The beam current is obtained at the same time as TALIF measurement. Note that the beam current has a flow rate error of optimal flow rate of 0.1 sccm and a beam current error of 2–10 mA. Fig. 2.42 (a2) and (b2) show the ground-state neutral density with respect to flow rate. The error bar of TALIF is typically  $1.0 \sim 5.0 \times 10^{18} \text{ m}^{-3}$  due to the plasma emission. The fluctuation depends on the condition of thruster operation, and the S/N ratio also depends on the condition of thruster operation. Thus, in some cases, the fluctuation becomes the same order of fluorescence signal, thus some cases have the error bar that exceeds negative density.

Fig. 2.42(a2) shows that the density gradient is observed in the upstream direction of the waveguide. In this thruster, there is no gas injection inside the waveguide; therefore, the distribution of the neutral density indicates that plasma is generated inside or at the exit of the waveguide. On the other hand, unlike Fig. 2.42 (a2), there is no density gradient in Fig. 2.42 (b2), which indicates that the ionization is suppressed by the prevention of ECR heating.

Then, the comparison of estimated and measured neutral densities indicate that the estimation can predict until 2.0 sccm in case of (a) w WG ECR and 2.5 sccm in case of (b) w/o WG ECR. However, in case of (a) at  $\dot{m} > 2.0 \sim 3.1$  sccm, the ground-state neutral density of measurement decreases according to the flow rate. The estimated neutral density also decreases, but the decrease is not consistent quantitatively. To evaluate the excitation process, whether the excited emission intensity is proportional to the ground-state neutral density or not is very important. Hence, TALIF measurement is mandatory for evaluating the excitation process accurately.

Additionally, Fig. 2.43 shows the relationship between the beam current and the ground-state neutral density. Here, the ground-state neutral density and the beam current are obtained



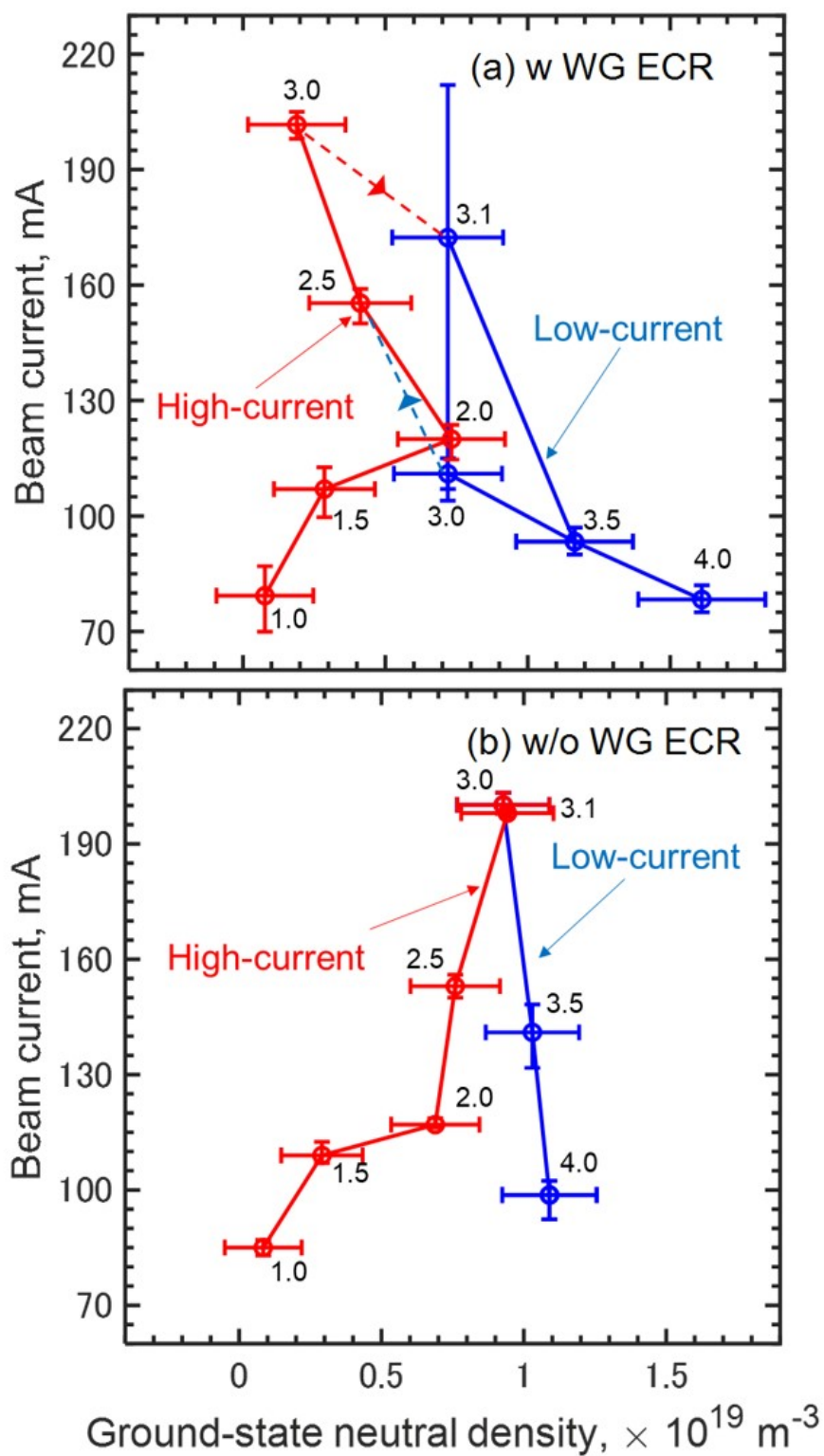
**Fig. 2.42** Beam current, ground-state neutral density, and excited emission intensity with respect to propellant flow rate. In this paper, there are three measurement points at  $z = -7.0, -11.5, -16.0$  cm from the screen grid. Estimated neutral density was calculated by using Eq. (2.28)

by the arithmetic mean of three measurement points. Comparison of (a) with (b) leads to a discussion of the effect of ECR heating inside the waveguide. At a flow rate of 1.0–2.0 sccm, the difference of the beam current and ground-state neutral density is rarely observed, which indicates that the ECR heating inside the waveguide does not affect plasma state. However, with flow rate of 2.5–3.0 sccm, even though beam current does not increase, the ground-state neutral density is very different, which indicates that the ECR heating inside the waveguide is very important in this range. It is considered that because the generated ions inside the waveguide are far from the grid, the ions do not contribute to ion beam current. In case (a), the beam current increases as the density decreases. On the other hand, in case (b), the beam current increases with the ground-state neutral density. Finally, the beam current decreases with a flow rate of 3.1–4.0 sccm, whereas the ground-state neutral density increases for both cases (a) and (b). A number of particles are exhausted as the ions decrease; therefore, the density

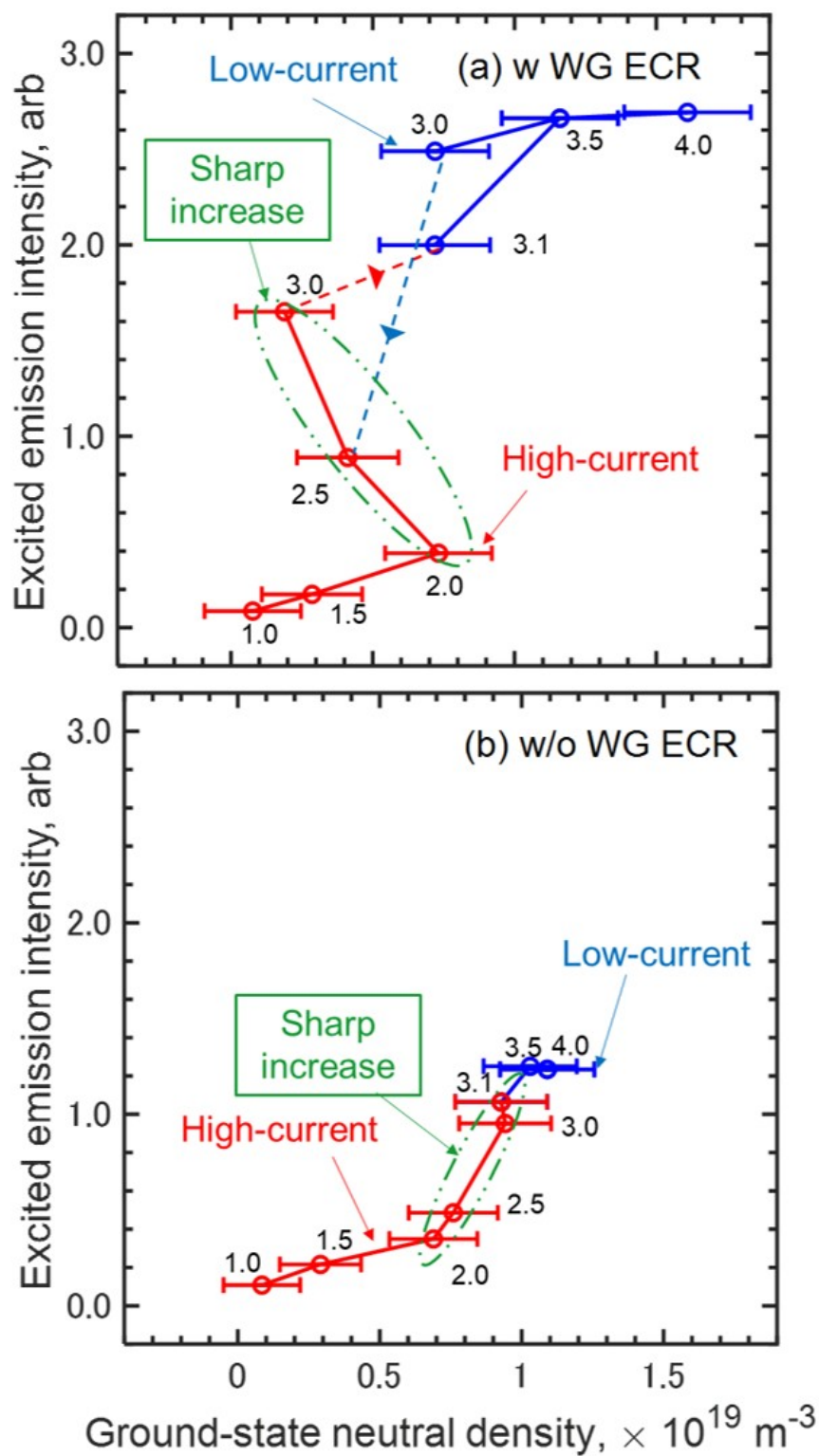
increased. A comparison of (a) with (b) indicates the beam current of (a) is smaller than that of (b). This result indicates that plasma is generated inside the waveguide, which results in insufficient microwaves transmitted to the discharge chamber [12]. In case (b), the plasma generation is reduced by preventing ECR heating inside the waveguide, thus the microwave can be propagated to the discharge chamber compared to case (a).

Figure 2.42 (a3) and (b3) show the spontaneous emission intensity with respect to the propellant flow rate for the two types of thruster. Figure 2.42 (a3) shows that the spontaneous emission intensity increases with the flow rate. The intensity then rapidly increases after the mode-transition. The intensity of the low-current mode is several times larger than that of the high-current mode. The intensity at 11.5 mm is slightly smaller than that at 7.0 cm, and the intensity at 16.0 cm is approximately half as small as that at 11.5 cm. On the other hand, although the intensity is approximately half as small for all flow rates, the tendency of the emission intensity in Fig. 2.42 (b3) is similar to that in Fig. 2.42 (a3), and then the emission is not completely deleted. This result provide a insight that plasma still exists inside the waveguide even if ECR heating inside the waveguide is suppressed.

To clearly show the difference of excitation process as well as Fig. 2.39, Fig. 2.44 shows the relationship between the ground-state neutral density and the spontaneous emission intensity. Here, the ground-state neutral density and the spontaneous emission were obtained by the arithmetic mean of three measurement points. In case (a) at 2.5–3.0 sccm, the spontaneous emission intensity increases, whereas the ground-state neutral density decreases. In case (b) at 2.5–3.1 sccm, although the tendency is relatively small compared to (a), the spontaneous emission intensity sharply increases against the ground-state neutral density. Thus, the increase of spontaneous emission intensity also cannot be explained from the result of ground-state neutral density.



**Fig. 2.43** Beam current with respect to ground-state neutral density. The ground-state neutral density and the beam current are obtained by the arithmetic mean of three measurement points. Each value means the propellant flow rate in sccm unit.



**Fig. 2.44** Spontaneous emission intensity with respect to ground-state neutral density. The ground-state neutral density and the excited emission are obtained by the arithmetic mean of three measurement points. Each value means the propellant flow rate in sccm unit.

## 2.7 Evaluation of excitation and ionization processes

From Fig. 2.39 and Fig. 2.44, the relationship between ground-state neutral density and spontaneous emission intensity suggests that the spontaneous emission rapidly increases according to flow rate near optimal flow rate. In case of 'WG injection' and 'w WG ECR', the intensity increases, whereas the neutral density decreases. In addition, in case of 'DC injection' and 'w/o WG ECR', even though the neutral density increases, the spontaneous emission intensity increases more than the increase in the neutral density of the ground state.

Because the plasma mode-transition is occurred after the increase of spontaneous emission intensity, it is a key phenomena. Thus, in this section, the mechanism of the excitation and ionization process is investigated. The excitation and ionization process are often investigated using an spectrum data and a collisional-radiative model (CRM) [128, 80]. On the other hand, our approach is based on the experimental results of ground-state, spontaneous emission intensity, and excited state densities at metastable state ( $1s_5$ ) and resonance state ( $1s_4$ ). Figure 2.45 shows the proposed investigation of the excitation process. These excited state neutral densities were measured by LAS (Fig. 1.15 and Fig. 1.16).

First, the theoretical formulation of spontaneous emission intensity is established. Generally, spontaneous emission intensity  $I_{h,l}$  from an higher level  $h$  to a lower level  $l$  can be expressed as:

$$I_{h,l} = I_{h,l0}n_h, \quad (2.32)$$

where  $I_{h,l0}$  is a constant value including branch ratio and  $n_h$  is the density at the higher excited state  $h$ . In the case of the observed emission, upper and lower states are  $h = 2p_3$  and  $l = 1s_2$  respectively. Therefore, the observed emission can be expressed as:

$$I_{observed} \approx I_{2p_3,1s_2} = I_0 n_{2p_3}, \quad (2.33)$$

where, the excited neutral density at state  $2p_3$   $n_{2p_3}$  can be calculated by two factors; excitation from a lower level (e.g., ground-state and lower excited state), and transport from other area. Depart from metastable state, the natural lifetime is the order of ten ns at maximum [65]; thus, neglect of the transport is justified and the excited neutral density  $n_{2p_3}$  can be expressed as:

$$n_{2p_3} = \frac{1}{\tau_{2p_3}} \sum_{j=1}^N k_{j,2p_3} n_e n_j, \quad (2.34)$$

where  $n_e$  is the electron density,  $k_{j,2p_3}$  is the rate coefficient from  $j$  to  $2p_3$ , and  $n_j$  is the neutral density at the lower level  $j$  including the ground-state and excited state. Remind that the rate coefficient excited from  $i$  to  $j$  is generally defined as:

$$k_{i,j} = \int_0^\infty \sigma_{i,j}(\varepsilon_e) \sqrt{\frac{2\varepsilon_e}{m_e}} f(\varepsilon_e) d\varepsilon_e, \quad (2.35)$$

where  $\sigma_{i,j}$ ,  $E_e$ ,  $m_e$ ,  $f(E_e)$  are the cross-section excited from  $i$  to  $j$ , the electron energy, electron mass, and electron energy distribution function (EEDF), respectively. The lower state is selected as the ground-state, the metastable state is  $1s_5$ , and the resonance state is  $1s_4$ . In such a condition,  $n_{2p_3}$  is computed as,

$$n_{2p_3} \approx \frac{1}{\tau_{2p_3}} (k_{1s_0,2p_3} n_{1s_0} + k_{1s_5,2p_3} n_{1s_5} + k_{1s_4,2p_3} n_{1s_4}) n_e. \quad (2.36)$$

Finally, using Eqs. (2.35) and (2.36), the observed emission intensity can be expressed as:

$$I_{observed} = (I_{1s_0} + I_{1s_5} + I_{1s_4}) n_e, \quad (2.37)$$

where  $I_g = I_0 k_{1s_0,2p_3} n_{1s_0} / \tau_{2p_3}$ ,  $I_{1s_5} = I_0 k_{1s_5,2p_3} n_{1s_5} / \tau_{2p_3}$ ,  $I_{1s_4} = I_0 k_{1s_4,2p_3} n_{1s_4} / \tau_{2p_3}$ . Equation (2.37) indicates that each spontaneous emission intensity can be calculated by the product of the rate coefficient and the density. Thus, the increase of spontaneous emission intensity can be explained following three factors.

- I. Stepwise (Indirect) excitation
- II. Increase of electron density
- III. Increase of electron temperature

Noted that III. means the increase of rate coefficient  $k_{i,j}$ . In low-temperature region ( $<10$  eV), the rate coefficients rapidly increases according to the electron temperature [38]. Thus, when  $k_{i,j}$  increases, it means that the electron temperature increases.

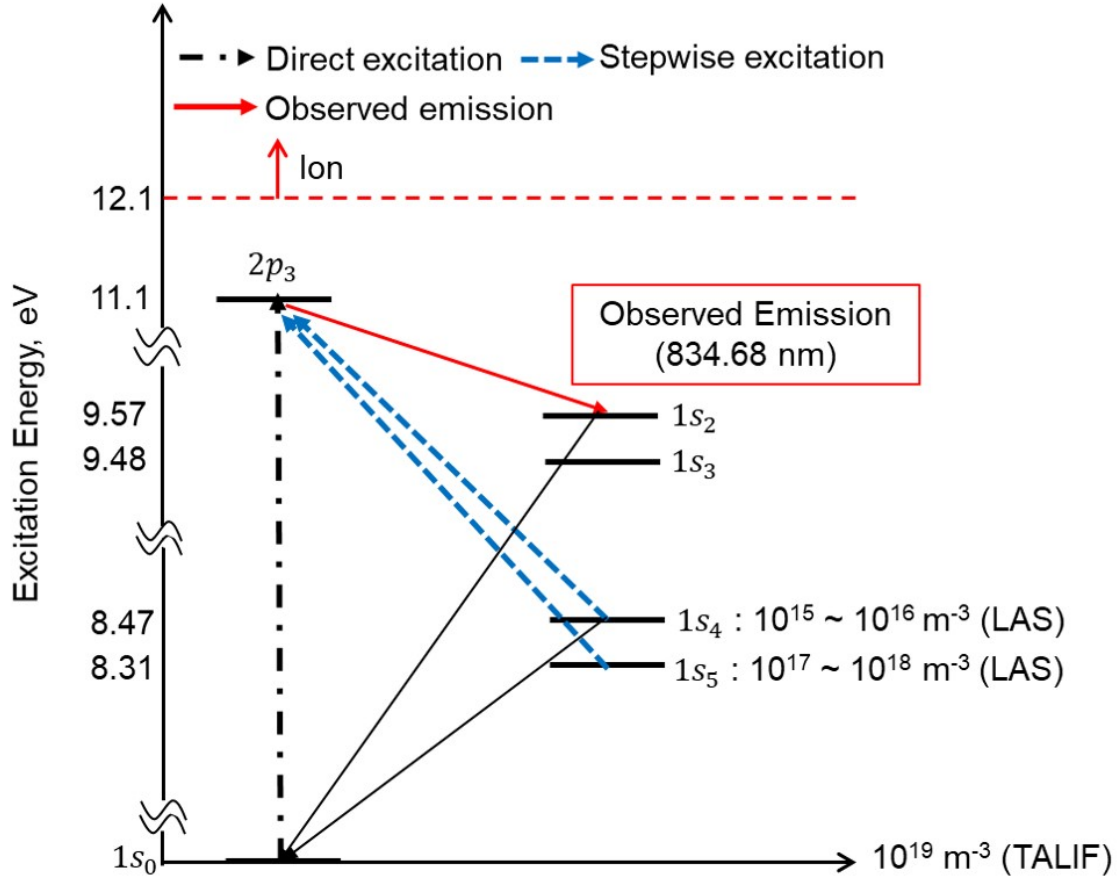


**Fig. 2.45** Excitation process of neutral species. Each density is the result after mode-transition. The excited density is measured by LAS and quoted from reference [10, 11].

### 2.7.1 I. Stepwise excitation

From Eq. (2.37), to evaluate the direct and stepwise excitation quantitatively, the ratio of the density and rate coefficient are necessary. The comparison of direct and stepwise excitation is summarized in Tab. 2.8.

As shown in Fig. 2.45, each density after mode-transition was used. TALIF measurements indicated the ground-state neutral density  $n_{1s_0}(=n_g)$  is the order of  $10^{19} \text{ m}^{-3}$ . On the other hand, the excited neutral density for  $n_{1s_5}$  and  $n_{1s_4}$  are in the order of  $10^{17} \sim 10^{18} \text{ m}^{-3}$  [10] and  $10^{15} \sim 10^{16} \text{ m}^{-3}$  [11] respectively. Therefore, the ratios of the density against the ground-state are  $n_{1s_5}/n_{1s_0} \approx 10^{-2} \sim 10^{-1}$  and  $n_{1s_4}/n_{1s_0} \approx 10^{-4} \sim 10^{-3}$  respectively. Carefully speaking, in the previous LAS measurement, these excited neutral densities are evaluated by assuming equilibrium Boltzmann distribution as,

$$n_{i,eq} = g_i \exp\left(-\frac{E_{excite}}{T_{e,excite}}\right). \quad (2.38)$$

Here,  $T_{e,excite}$  is the excited electron temperature,  $E_{excite}$  is excitation energy, and  $i$  is excited state. Subscription of  $eq$  means equilibrium. Dressler et al. reported the density assuming equilibrium Boltzmann distribution  $n_{i,eq}$  is overestimated compared to that using CR model  $n_{i,CR}$  [129]. However, in the previous LAS measurement,  $T_{e,excite} = 0.4 \sim 0.6$  eV was used based on line pair method [19] and  $T_{e,excite}$  is very smaller than typical electron temperature  $T_e = 3 \sim 5$  eV by probe measurement [26]. Thus, in this study, the discrepancy between  $T_{e,excite}$  and  $T_e$  cancels out the overestimation, i.e.,  $n_{i,eq}(T_{e,excite})$  and  $n_{i,CR}(T_e)$  are in the same order. Eventually, the order estimation of  $n_{1s_5}/n_{1s_0} \approx 10^{-2} \sim 10^{-1}$  and  $n_{1s_4}/n_{1s_0} \approx 10^{-4} \sim 10^{-3}$  are valid.

In addition, the rate coefficient is estimated assuming that the EEDF is an isotropic Maxwellian distribution. The excitation cross-section by simulation of relativistic distorted wave (RDW) approach was then used [13, 14]. Srivastava *et al.* reported that the cross-section can be calculated by considering the fine structure, and some cross-sections validate with experimental results [14]. Figure 2.46 shows the ratio of the rate coefficient between direct and stepwise excitation. For example, from the previous probe measurement, the electron temperature is  $T_e = 3 \sim 5$  eV at 7.0 cm from the screen grid in the case of neutral density  $n_n \approx 6.0 \times 10^{18}$  m<sup>-3</sup> [38]. For example, in the case where the temperature is  $3 \sim 5$  eV, the ratios of  $k_{1s_5,2p_3}/k_{1s_0,2p_3}$  and  $k_{1s_4,2p_3}/k_{1s_0,2p_3}$  are  $20 \sim 25$  and  $120 \sim 300$ , respectively. Considering  $n_{1s_5}/n_{1s_0} \approx 10^{-2} \sim 10^{-1}$  and  $n_{1s_4}/n_{1s_0} \approx 10^{-4} \sim 10^{-3}$ , the ratios of the spontaneous emissions are  $I_{1s_5}/I_{1s_0} \approx 0.2 \sim 2.5$  and  $I_{1s_4}/I_{1s_0} \approx 0.012 \sim 0.3$  respectively. Therefore, the stepwise excitation of  $1s_4 \rightarrow 2p_3$  is one or two orders of magnitude smaller than direct excitation, whereas the stepwise excitation of  $1s_5 \rightarrow 2p_3$  can achieve the same order of the direct excitation.

Based on these order estimations, the relationship between the ground-state neutral density and the spontaneous emission was investigated, as shown in figure 11. Here, the ground-state neutral density and the spontaneous emission were obtained by the arithmetic mean of three measurement points. In case (a) for w WG ECR at  $2.5 \sim 3.0$  sccm, the spontaneous emission intensity increases, whereas the ground-state neutral density decreases. In case (b) for w/o WG ECR at  $2.5 \sim 3.1$  sccm, although the tendency is relatively small compared to (a), the sponta-

neous emission intensity sharply increases against the ground-state neutral density. Based on the ratios of  $I_{1s_5}/I_{1s_0}$  and  $I_{1s_4}/I_{1s_0}$ , the observed the spontaneous emission intensity  $I_{observed}$  can be approximated as:

$$I_{observed} \approx I_0(k_{1s_0,2p_3}n_{1s_0} + k_{1s_5,2p_3}n_{1s_5})n_e \quad (2.39)$$

Of course, because the metastable has the distribution as shown in Fig. 1.15, the location of stepwise excitation is limited. Though the natural lifetime of the metastable is the order of ten second, the actual lifetime can be drastically reduced due to the collision with other particle and wall diffusion. For instance, considering the lifetime of quenching collision with ground-state neutral density  $\tau_{1s_0,1s_5}$  can be calculated as:  $\tau_{1s_0} = 1/k_{1s_0,1s_5}n_{1s_0} \approx 11 \sim 17$  s. Here, we use the  $k_{1s_0,1s_5} = 75 \sim 113 \times 131 P_a^{-1}s^{-1}$  [130] and  $n_{1s_0} \approx 10^{19} \text{ m}^{-3}$ . Then, assuming that thermal velocity  $v_{th,1s_5} = \sqrt{2k_B T_{1s_5}/m_i} \approx 160$  m/s under temperature of metastable particles is 400 K, the mean free path  $L_{1s_0,1s_5} \approx v_{th,1s_5} \times \tau_{1s_0,1s_5} \approx 1.8 \sim 2.7$  m is very larger than the length waveguide. Thus, the quenching effect does not limit the transport process of metastable particles. Second, the mean free path of metastable with collisions of electrons  $L_{1s_5,e}$  are evaluated. There are many kinds transition from metastable particles, but the author considers that the total cross-section is  $10^{19} \text{ m}^2$  at maximum. Then, assuming thermal electron velocity  $10^6$  m/s, the rate coefficient  $k_{1s_5,e} = 10^{19} \times 10^6 \approx 10^{-13} \text{ m}^3/\text{s}$ . Thus, considering the electron density is  $n_e \approx 10^{16} - 10^{17} \text{ m}^{-3}$  based on full-kinetic simulations [18], the mean free path becomes  $L_{1s_5,e} = k_{1s_5,e}v_{th} \approx 16 \sim 160$  mm and  $L_{1s_5,e}$  is smaller than the length of waveguide. Thus, the collision with electrons limits the transport process and then the metastable density is expected to be decreased as the bottom the waveguide, which is consistent with axial distribution of metastable particles [10] and the spontaneous emission (Fig. 2.42 (a3) and (b3)). A more detail about the source and transport processes of metastable neutral particles will be simulated in chapter 3.

## 2.7.2 II. Increase of electron density

Generally, there are two causes to increase the electron density; ionization and transport from other areas. However, in the thruster, because electron are strongly magnetized ( $\Omega \approx 10^3 \sim 10^4$ ), they cannot be transported easily from the magnetic confined region to the waveguide. Hence, the ionization (plasma generation) seems to be dominant for the increase of electron

**Table 2.8** Evaluation of stepwise excitation against direct excitation. These rate coefficients are calculated using Eq. (2.35) assuming that the electron velocity distribution function is an isotropic Maxwellian distribution with an electron temperature of 3–5 eV [26]. The density is quoted from the result after the mode-transition.

Ratio against from direct excitation (ground-state)	$1s_5$ (Metastable)	$1s_4$ (Resonance)
Density	$10^{-2} \sim 10^{-1}$	$10^{-4} \sim 10^{-3}$
Rate coefficient	20 ~ 25	120 ~ 300
Spontaneous emission intensity	0.2 ~ 2.5	0.012 ~ 0.3

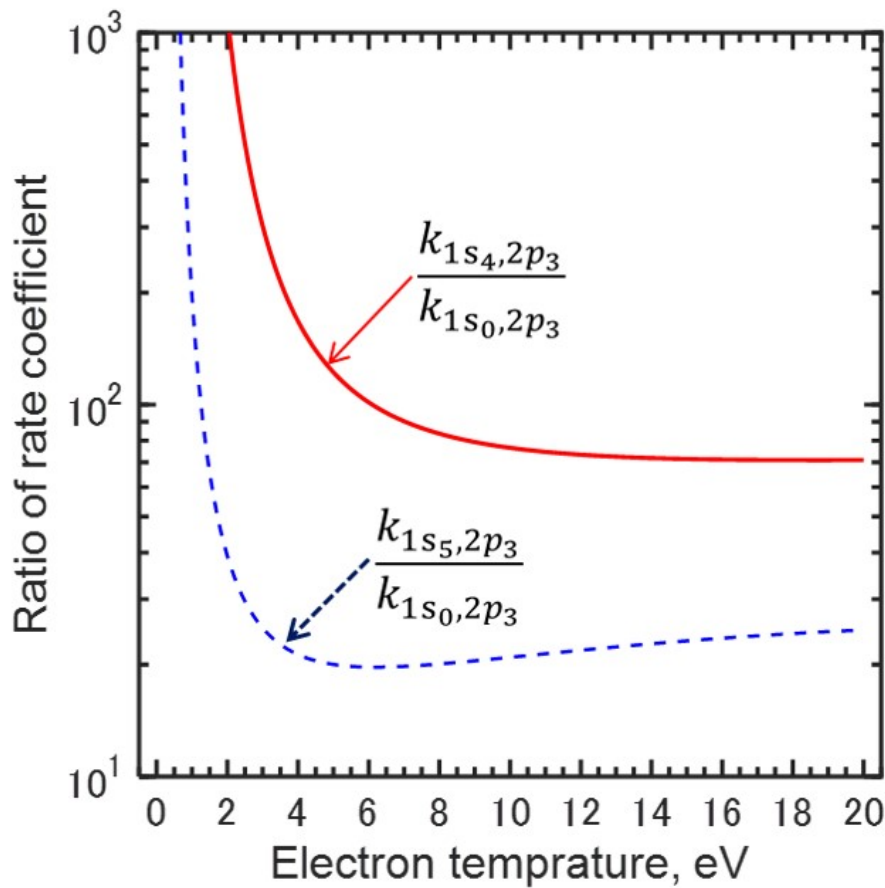


**Fig. 2.46** Ratio of rate coefficient between direct and stepwise excitation. The cross-section uses by RDW approach [13, 14].

density.

Generally, there are two types of ionization that differ from direct ionization; Penning ionization and stepwise (Indirect) ionization by electron-impact ionization. However, in the thruster, Penning ionization can be neglected due to low pressure (section 1.3.2). Based on the analysis of stepwise excitation (Tab. 2.8), the stepwise ionization from metastable state  $1s_5$  are evaluated. The minimum energy of ionization is 12.1 eV, whereas the excitation energy

of upper level  $2p_3$  is approximately 11.1 eV, which indicates that the difference of energy and the ionization and the excitation is only 1 eV [65]. Considering the electrons have a distribution function such as a Maxwellian distribution, the stepwise (Indirect) ionization can be also occurred as along with the stepwise excitation. In fact, the comparison of stepwise excitation and stepwise ionization is shown in Fig. 2.47. Here, Fig. 2.47 shows the ratio against direct excitation and ionization respectively. The cross-section of the stepwise ionization from the metastable state  $1s_5$  is quoted from Ton-That and Flannery work [15]. Figure 2.47 indicates that at the electron temperature 3 ~ 5 eV [26], the ratio is 10 ~ 30, thus the stepwise ionization cannot be neglected. Once the ionization begins to occur, the electron density increases, which can explain the sharp increase of spontaneous emission intensity. This is the mechanism of plasma generation inside the waveguide and may cause the mode-transition.

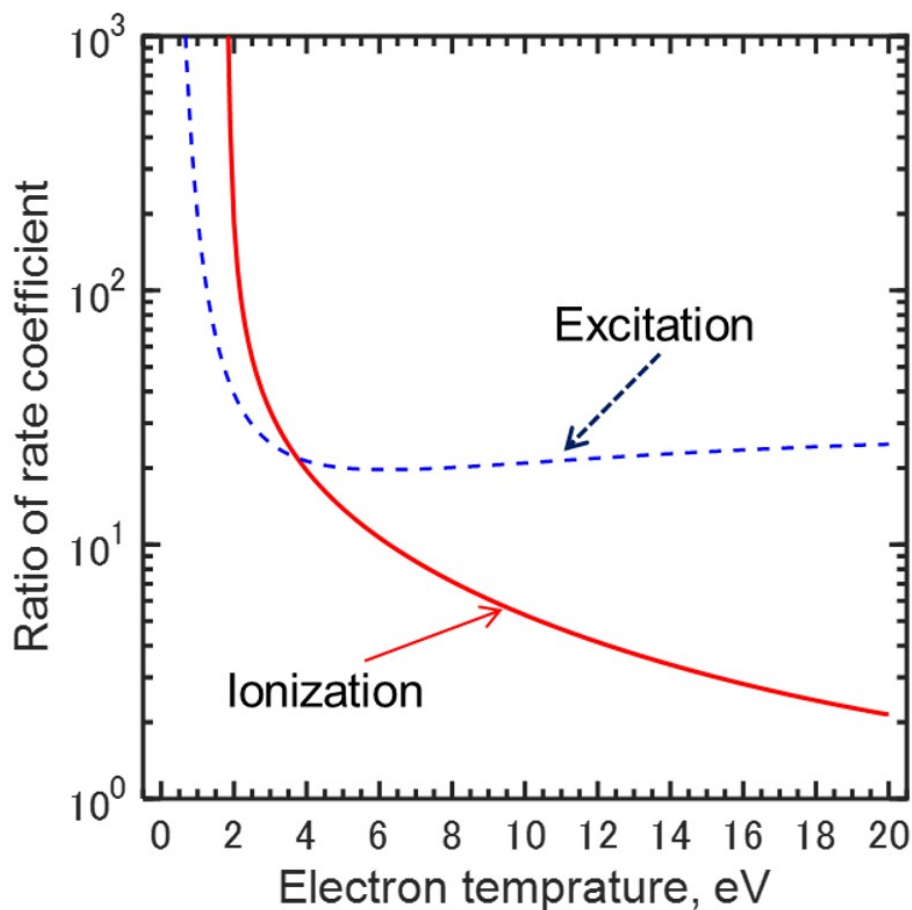


**Fig. 2.47** Ratio of the rate coefficient between direct and stepwise for excitation and ionization. The cross-section of ionization from metastable state  $1s_5$  is quoted from Ton-That and Flannery work [15].

### 2.7.3 III. Increase of electron temperature

The increase of electron temperature can increase the rate coefficient of the direct excitation and stepwise excitation. In case of 'WG w ECR', it is possible that the increase of electron temperature can partially explain the increase of the spontaneous emission. However, in case of 'WG w/o ECR', the cause increasing electron temperature cannot be explained by ECR heating because the ECR layer is eliminated. Therefore, when increasing electron temperature, another electron heating different from ECR is considered to occur.

As one electron heating different from ECR heating, collisional heating with neutral species is considered. The perspective is based on two evidences of experiment. First, from this current study, it was revealed that the ground-state neutral density significantly increases after the optimal flow rate. Before optimal flow rate at 1 ~ 2 sccm, the neutral density is  $n_n \approx 1.0 \times 10^{18} \text{ m}^{-3}$  at 1.0 sccm before the optimal flow rate and the neutral density is approximately  $n_n \approx 1.0 \times 10^{19} \text{ m}^{-3}$  at 3.1 sccm (Fig. 2.42). Second, from the previous EO probe measurement [11], the electric field of microwaves inside the waveguide is 5 ~ 10 times larger than that in the discharge chamber after mode-transition. Generally, ECR and collisional heating per volume  $p_{ECR}$ ,  $p_{coll}$  are given by[56],

$$p_{ECR} = n_{e,ECR} \times \frac{e^2}{m} \times E_{\perp,ECR}^2 \times \frac{\pi}{v_{\parallel} \left| \frac{\partial B}{\partial s} \right|_{ECR}} \times \nu_{ECR}, \quad (2.40)$$

$$p_{coll} = n_{e,coll} \times \frac{e^2}{m} \times E_{\perp,coll}^2 \times \frac{1}{\nu_{coll}^2 + (\omega_m - \omega_{ce})^2} \times \nu_{coll}. \quad (2.41)$$

Here,  $n_e$  is electron density, the  $E_{\perp}$  is the electromagnetic field of microwaves perpendicular to the magnetic field,  $v_{\parallel}$  is the electron thermal velocity perpendicular to the magnetic field,  $\left| \frac{\partial B}{\partial s} \right|_{ECR}$  is the gradient of the magnetic field parallel to the magnetic field line,  $\omega_m$  and  $\omega_{ce}$  are the frequencies of microwaves and electron cyclotron motion, respectively, and  $\nu$  is the frequency of electron heating. The ECR and coll subscripts indicate the region of ECR and collision with neutral particles. In magnetic confined region, electrons are continuously heated by ECR, thus the ECR heating is occurred. Thus,  $E_{\perp,ECR}$  is used by experimental data around ECR layer ( $r = 15 \text{ cm}$ ,  $z = -5 \text{ cm}$ ) in the magnetic confined region. Then, from the experimental results in the magnetic confined region and  $E_{\perp,coll}$  is used inside the waveguide because the electromagnetic field is the largest and the intensities differ by about twice at maximum

from ( $r = 0$  cm,  $z = -10$  cm) to ( $r = 0$  cm,  $z = -5$  cm). Thus,  $E_{\perp, coll}$  is quoted maximum and minimum value in range of  $z = -10 \sim -5$  cm. Noted that inside the waveguide, the magnetic field line is parallel to central axis, thus, electric field perpendicular to magnetic field  $E_{\perp, waveguide} = E_{r, waveguide}$ , here  $E_r$  is the electric field of microwaves in the radial direction. On the other hand, in the magnetic confined area, assuming that the propagation direction is axial direction in the magnetic confined region, i.e.,  $E_{\perp, discharge} \approx E_{r, discharge} \sin 45$  deg. At 1 sccm (before optimal flow rate),  $E_{r, discharge} \approx 6 \times 10^3$  V/m and  $E_{r, waveguide} \approx 3 \times 10^3 \sim 4 \times 10^3$  V/m are used. At 3 sccm (after optimal flow rate),  $E_{r, discharge} \approx 2 \times 10^3$  V/m and  $E_{r, waveguide} \approx 8 \times 10^3 \sim 15 \times 10^3$  V/m. Based on these data, the ratio of electric field of microwaves can be estimated as:  $E_{\perp, ECR}/E_{\perp, coll} \approx 1.1 \sim 1.4$  at 1 sccm (before optimal flow rate),  $E_{\perp, ECR}/E_{\perp, coll} \approx 0.09 \sim 0.18$  at 3 sccm (after optimal flow rate) respectively. Based on the experimental data of microwaves, Eqs. (2.40) and (2.41) are used to yield the ratios of ECR and collisional heating, given by:

$$\alpha_{E,C} = \frac{p_{ECR}}{p_{coll}} = \left( \frac{E_{\perp, ECR}}{E_{\perp, coll}} \right)^2 \times \frac{(\omega_m - \omega_{ce})^2}{v_{\parallel} \left| \frac{\partial B}{\partial s} \right|_{ECR}} \times \frac{\nu_{ECR}}{\nu_{coll}} \quad (2.42)$$

Here, for simplicity,  $n_{e, coll} = n_{e, ECR}$  is assumed. Figure 2.48 shows the distribution of magnetic field strength  $|\vec{B}|$  and gradient of magnetic field in the direction of magnetic field line  $|\partial|\vec{B}|/\partial s|$  respectively. Here, the magnetic field is calculated by Finite Element Method Magnetics software (FEAM) [131]. In magnetic confined region, electrons are continuously heated by ECR and trapped by mirror magnetic field, i.e., bounce motion. Neglecting the change of magnetic moment, the electrons move  $2L_{cusp}$  and across the ECR layer four times until they come back to their same position. Thus, the frequency of ECR heating can be approximated by  $\nu_{ECR} = 4 \times v_{\parallel}/2L_{cusp} = 2v_{\parallel}/L_{cusp}$  [132]. Then, the frequency of collision with neutral particles  $\nu_{coll}$  can be approximated by  $\nu_{coll} = \sigma v_e n_n = \sigma \sqrt{3} v_{\parallel} n_n$ . Thus, by using these expressions of  $\nu_{ECR}$  and  $\nu_{coll}$ , the ratio  $\alpha_{E,C}$  can be written as,

$$\alpha_{E,C} = \frac{p_{ECR}}{p_{coll}} = \left( \frac{E_{\perp, ECR}}{E_{\perp, coll}} \right)^2 \times \frac{(\omega_m - \omega_{ce})^2}{v_{\parallel} \left| \frac{\partial B}{\partial s} \right|_{ECR}} \times \frac{4}{\sqrt{3} \sigma n_n L_{ECR}}. \quad (2.43)$$

In addition, the author assumes typical parameters;  $v_{\parallel} \approx 10^6$  m/s,  $\sigma \approx 1 \times 10^{-19}$  m<sup>-3</sup>. Then, from Fig. 2.48, the gradient of magnetic field at the ECR layer is  $|\partial|\vec{B}|/\partial s|_{ECR} \approx 10$  T/m ( $r = 150$  mm,  $z = -50$  mm), the length of bounce motion is  $L_{cusp} \approx 10$  cm, and the magnetic

field strength related to collisional heating  $\omega_{ce}/2\pi \approx 1.5$  GHz ( $r = 0$  mm,  $z = -100$  mm). Finally, setting experimental condition  $\omega_m/2\pi = 4.25$  GHz, the ratio can be calculated as,

$$\alpha_{E,C} \approx \left( \frac{E_{\perp, ECR}}{E_{\perp, coll}} \right)^2 \times \frac{2 \times 10^2}{n_n \times 1 \times 10^{-19}}. \quad (2.44)$$

Before the mode-transition, the neutral density is  $n_n \approx 1.0 \times 10^{18} \text{ m}^{-3}$  at 1.0 sccm before the optimal flow rate (Fig. 2.42) and  $E_{\perp, ECR}/E_{\perp, coll} \approx 1.1 \sim 1.4$ , so that the ratio is,

$$\alpha_{E,C} \approx 2.4 \times 10^3 \sim 3.9 \times 10^3. \quad (2.45)$$

Equation (2.45) indicates that collisional heating can be neglected. However, under the mode-transition, the neutral density is approximately  $n_n \approx 1.0 \times 10^{19} \text{ m}^{-3}$  at 3.1 sccm (Fig. 2.42) and  $E_{\perp, ECR}/E_{\perp, coll} \approx 0.09 \sim 0.18$ , so that the ratio is

$$\alpha_{E,C} \approx 1.6 \sim 6.5. \quad (2.46)$$

Equation (2.46) indicates that the collisional heating  $p_{coll} = p_{ECR}/\alpha_{E,C} \approx 0.15p_{ECR} \sim 0.63 p_{ECR}$ , which indicates that the collisional heating accounts for 15 ~ 63% of the ECR heating. Therefore, the collisional heating may become important after the plasma mode-transition. Note that these ratios do not include the effect of volume and electron density.

It is difficult to conclude whether the collisional heating is dominant or not at optimal flow rate. However, even though collisional heating is dominant, it is difficult to generate the high-energy electrons that can generate the direct ionization and excitation. This is because ECR heating locally heats some electrons [18, 50], whereas collisional heating heats all electrons. For instance, each electrons are heated during the lost at the wall,

$$E_{coll} = \frac{p_{coll}}{n_e} \times \tau_e. \quad (2.47)$$

Here,  $\tau_e$  is the free path of electrons.  $\tau_e$  is estimated as follows [22].

$$E_{coll} = \frac{L_e}{v_{th}}. \quad (2.48)$$

Then, considering the  $L_e \approx 1$  m,  $\tau_e \approx L/v_{th} \approx 10^{-6}$  s. Thus, in the condition after mode-transition, each electron is heated by  $E_{coll} \approx 0.06 \sim 0.2$  eV. Similarly, ECR heating makes electrons heat by  $E_{ECR} = \alpha_{E,C} \times E_{coll}$ . However, because  $E_{ECR}$  is averaged value, some

electrons gaining much more than average energy  $E_{ECR}$ . For instance, electron can be heated by approximately several eV during one bounce [18, 50].

From the above estimation, the collisional electron heating energy are very small compared to the direct ionization energy 12.1 eV and excitation energy 8.3 eV. On the other hand, the stepwise ionization and excitation from metastable state  $1s_5$  is required by only  $3 \sim 4$  eV. Therefore, it is concluded that the collisional heating can contribute to the stepwise ionization and excitation from metastable state  $1s_5$ .

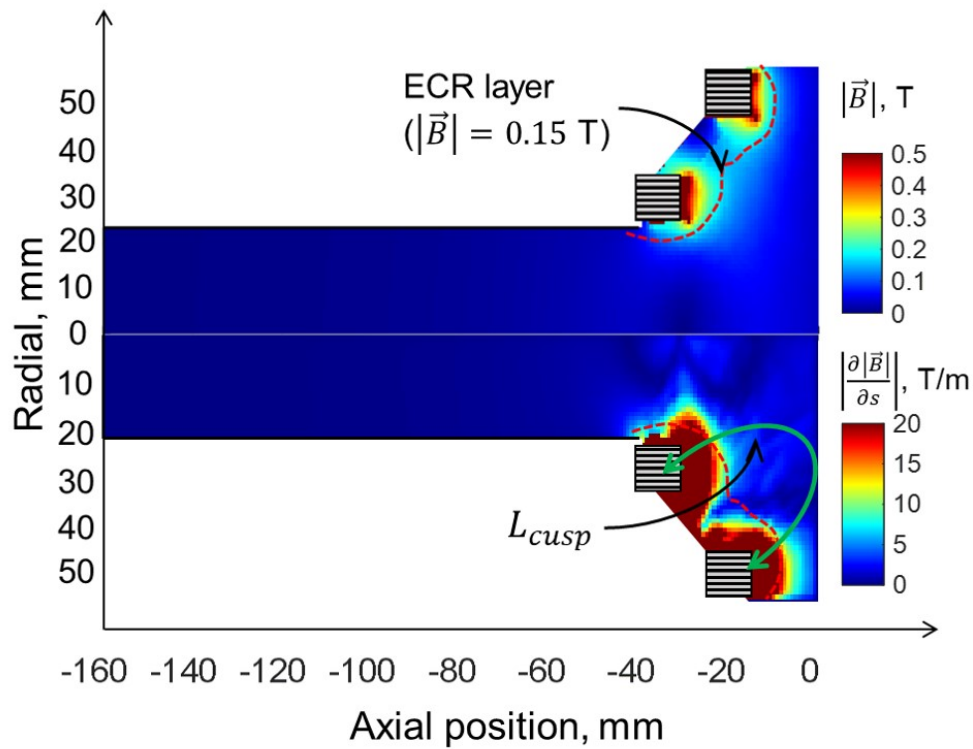


**Fig. 2.48** Magnetic field strength  $|\vec{B}|$  and gradient of magnetic field in the direction of magnetic field line  $|\partial|\vec{B}|/\partial s|$ .  $|\vec{B}|$  and  $|\partial|\vec{B}|/\partial s|$  are related to evaluation of collisionless and collisional heating in Eq. (2.40) and (2.41).

## 2.8 Possible mechanism of plasma mode-transition

Based on the analysis of spontaneous emission intensity, it was found that the main cause of plasma generation inside the waveguide is the stepwise ionization from metastable  $1s_5$  as shown in Fig. 2.49. Of course, from the experiment of 'WG w ECR' and 'WG w/o ECR', by suppressing the electron heating inside the waveguide, the plasma generation is also reduced. However, even if these case, plasma mode-transition are observed and the sharp increase of spontaneous emission are not deleted perfectly. Hence, the main cause of plasma generation inside the waveguide is the stepwise ionization from metastable  $1s_5$ . After plasma generation inside the waveguide, microwave cannot be transmitted to the discharge chamber by cutoff phenomena by EO probe measurement. Therefore, the process of '*plasma generation by stepwise ionization*'  $\rightarrow$  '*cutoff of microwaves*' is the plasma mode-transition. In next chapter, these experimental results are analyzed in more detail by numerical simulation.

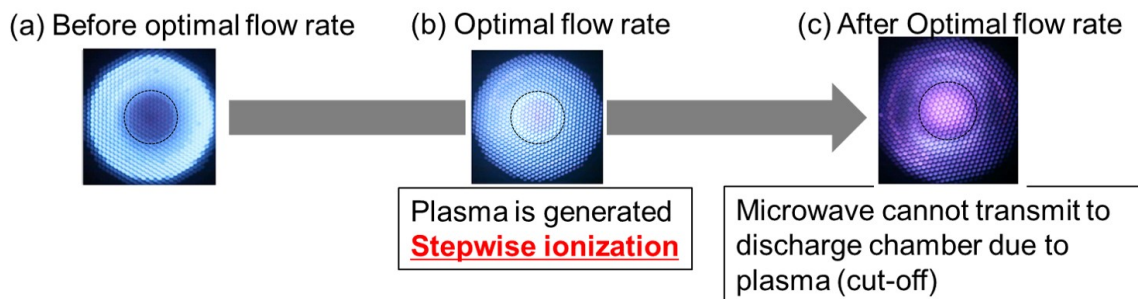


Fig. 2.49 Hypothesis of plasma mode-transition based on experimental results.

## 2.9 Short conclusion and achievement

In this chapter, to investigate the plasma mode-transition in ECR gridded ion thruster  $\mu 10$ , the ground-state neutral density and the spontaneous emission by electron impact excitation inside the thruster were directly measured under TALIF experimental setup. First, to measure the ground-state neutral density inside the thruster, TALIF measurement technique was developed.

Based on the measurement, physical mechanism of the plasma mode-transition is investigated by following two perspective; I. the effect of gas injection (ground-state neutral density distribution), II. the effect of electron heating inside the waveguide. Then, five kinds of thruster, 'WG injection', 'DC injection', 'w WG ECR', 'w/o WG plasma', and 'w/o WG ECR' were

tested. Additionally, measurement of ground-state neutral density and the spontaneous emission intensity was applied to four kinds of thruster, 'WG injection', 'DC injection', 'w WG ECR', and 'w/o WG ECR'. As a result, the following conclusions and achievements were obtained.

- TALIF measurement system.

1. Ground-state neutral density measurement was successfully employed to monitor the interior of a microwave ion thruster by three techniques: two optical windows for laser injection and fluorescence detection, averaging 3,000 signals, and the selection of optimized wavelength from the trade off between fluorescence intensity and noise due to spontaneous emission.
2. Evaluation method of excitation and ionization processes was proposed by measuring ground-state neutral density and spontaneous emission intensity. These parameters can be measured at the same time in TALIF set-up by using a characteristic that two-photon excitation process is the same as the electron-impact excitation process. The relationship between the ground-state neutral density and the spontaneous emission intensity can estimate whether the stepwise ionization and excitation are occurred or not.
3. The optical windows of the thruster, which were newly introduced to allow for the present analyses, had a negligible effect on thruster performance. During the DC injection case, the windows caused a change in the maximum ion beam current of less than 5 mA and modified the propellant flow rate by only 0.1 sccm. In the case of WG injection, the effects of the windows on the ion beam current and flow rate were even lower.
4. The detection limit of ground-state neutral density was from  $2 \times 10^{18} \text{ m}^{-3}$  to  $5 \times 10^{18} \text{ m}^{-3}$  depending on the flow rates. Following ionization in the thruster, the highest signal intensities decreased by approximately  $5 \pm 10\%$  relative to those for the non-ionized state. This decreases three factors; ionization, excitation, and thermal accommodation effects. Though three factors cannot be distinguished, the ground-state neutral particles accounts for all of neutral particles by 85% at least.
5. By extracting ions from the grid, the density is rapidly decreased. This decrease is reasonably agreement with the estimation of OD equation:  $n_n = n_{n0}(1 - \eta_u)$  in DC injection,

whereas is not good agreement in WG injection, which suggests that the non-0D effects includes in WG injection.

6. The sensitivity of fluorescence intensity against the laser power was investigated. This result implies that the fluorescence intensity increases according to the laser power, but it does not proportional to square of laser power, which indicate that the excitation state is the middle of the weak-excitation and saturation. Then, the fluorescence intensity linearly increases according to pressure, which indicates that the quenching effect is negligible due to low pressure. Photon-ionization due to high laser power can be also negligible.
7. Broadening of TALIF signal in wavelength domain is evaluated in all cases: 'Cold gas', 'w/o ion ext.', and 'w/o ion ext.' These broadening are fitted by Voigt function to evaluate the FWHM of Gauss and Lorentz respectively. As a results, computed Gaussian broadening considering the Doppler effect and laser width is 63% of the FWHM obtained by experiment, which indicates that other broadening effects, e.,g, laser power is considered. However, these spectra are in agreement for the fluorescence signal at central wavelength with 4.5%, which indicates that the assumption neglecting the difference of broadening is reasonable considering the measurement accuracy is approximately 10% due to the plasma emission. Additionally, these signal are also agreement for the peak wavelength, which indicates that the Doppler shift is not observed under resolution of laser wavelength 0.2 pm. From the results of the broadening and Doppler shift, it is enough to measure the fluorescence signal at the only peak wavelength for evaluating the density.
8. Estimated neutral density by using 0D flux conservation (Eq.(2.28)) compares with the TALIF measurement. Though the estimated neutral density is similar curve to TALIF measurement results, the estimation does not perfect match the measured densities. For instance, the estimation does not capture inhomogeneous effect such as gas injection, and the inhomogeneous effect is important for explaining the difference of WG and DC injection. In addition, in case of 'w WG ECR' at 2.5 ~ 3.0 sccm, the estimated neutral densities are not consistent with TALIF measurement quantitatively. To evaluate the excitation process, whether the excited emission intensity is proportional to the ground-state neutral density or not is very important. Hence, TALIF measurement is necessary for evaluating the excitation process accurately.

- Investigation of plasma mode-transition.

1. Comparing 'WG injection' with 'DC injection', the ground-state neutral density of 'WG injection' is higher than that of 'DC injection' in cold gas state, which is consistent with DSMC works. Then, this trend is maintained in case of without and with ion extraction. In WG injection, the axial distribution indicates that the density becomes higher as bottom of waveguide.
2. In both cases of WG and DC injection, the spontaneous emission intensity rapidly increases according to propellant flow rate near optimal flow rate. In case of 'WG injection', the ground-state neutral density decreases, whereas the spontaneous emission intensity increases. In addition, in case of 'DC injection', though the neutral density also increases, the spontaneous emission intensity increases more than that in the neutral density of the ground state. Both results indicate that the spontaneous emission intensity can not be explained from the direct excitation from ground-state.
3. To investigate the electron heating inside waveguide against the plasma mode-transition, the beam current between 'w WG ECR', 'w/o WG plasma', and 'w/o WG ECR' were evaluated. The experimental results revealed that the maximum beam current is almost same, but the beam current is different after plasma mode-transition. In case 'w WG ECR', the beam current rapidly decreases after plasma mode-transition. On the other hand, in case 'w/o WG plasma', the decrease of beam current is mitigated, which suggests that the plasma-mode transition is modulated. Additionally, in case 'w/o WG ECR', the decrease of beam current is more reduced compared to be case (b). Thus, these results suggest that the WG ECR layer is critical parameter for plasma mode-transition, and then the existence of plasma inside waveguide is also important for plasma mode-transition. Then, this perspective is agreement with photograph between before and after mode-transition.
4. To investigate the electron heating inside waveguide in more detail, the ground-state neutral density and the spontaneous emission intensity were measured in two kinds of thrusters: 'w WG ECR', and 'w/o WG ECR'. The measurements revealed that the spontaneous emission intensity rapidly increases near optimal flow rate as well as 'WG injection' and 'DC injection'. The tendency for this increase was relatively small with the

partial prevention of ECR heating; however, the mode-transition was not deleted.

5. The sharp increase of the spontaneous emission can be caused by three factors: the stepwise excitation from lower excited states, the increase of electron density, and the increase of electron temperature. First, estimation of the stepwise excitation by using rate coefficient and excited and ground-state neutral densities indicated that the stepwise excitation from the metastable can be comparable to the direct excitation. Second, stepwise ionization from the metastable state can also be non-negligible because the minimum ionization energy differs from the observed upper-level energy by only 1 eV. Once occurring the stepwise ionization, the electron density increases, which is the physical mechanism of plasma generation inside the waveguide. Finally, the increase of electron temperature partially can be explained the sharp increase. However, in case w/o WG ECR, the cause increasing electron temperature cannot be explained by ECR heating. Therefore, if increasing electron temperature, another electron heating different from ECR is considered to occur such as collisional heating. Collisional heating was evaluated based on the measurement results. Before the plasma mode-transition, collisional heating is negligibly small compared to ECR heating. However, after the plasma mode-transition, collisional heating cannot be neglected by the transition of the neutral density and electric field of microwaves. Note that increase of each electron energy due to collisional heating is small compared to be direct ionization and excitation energy, but it can contribute to the stepwise ionization and excitation.
6. Based on the analysis of spontaneous emission intensity, it was found that the main cause of plasma generation inside the waveguide is the stepwise ionization from metastable  $1s_5$ . Though suppressing the electron heating inside the waveguide, the plasma generation is also reduced. However, even if these case, plasma mode-transition are observed, thus the main cause of plasma generation inside the waveguide is the stepwise ionization from metastable  $1s_5$ . After plasma generation inside the waveguide, microwave cannot be transmitted to the discharge chamber by cutoff phenomena by EO probe measurement [12]. Therefore, the process of '*plasma generation by stepwise ionization*'  $\rightarrow$  '*cutoff of microwaves*' is the plasma mode-transition.

## Chapter 3

# Numerical estimation of ionization and excitation rate distributions

### 3.1 Objective

In chapter 2, from the experimental investigation of excitation process measuring the ground-state neutral density and spontaneous emission intensity, it is suggested that the plasma mode-transition is the process: 'plasma generation by stepwise ionization  $\rightarrow$  cutoff of microwaves'. However, there are still two unclear parts by only the results.

- I. Distribution of stepwise ionization from metastable neutral particles.
- II. Ratio of stepwise and direct ionization

Transition of the stepwise ionization distribution depending on the flow rate is important to understand the plasma generation inside the waveguide. And then, the ratio of stepwise and direct ionization is essential parameter to show the importance of stepwise ionization. To elucidate above two perspectives, the ionization distribution and excitation distribution at metastable state are essential parameters. However, the directly measurement of the reaction rate distribution is very difficult (described in section 1.3.2). Instead, in this study, ionization and excitation rate distributions are estimated by numerical simulation approach based on experimental data. Specifically, following three simulations were performed.

- I. Ground-state neutral particles
- II. Metastable neutral particles
- III. Electric field of microwaves

Then, these simulation results compare with the experimental results. Each objective will be introduced respectively.

### 3.1.1 Ground-state neutral particles

TALIF measurements show the ground-state neutral density distribution is very different between gas injection (WG and DC injection). Then, in case of the ion extraction, the ground-state neutral density is drastically reduced. Hence, the ground-state neutral density is simulated assuming some ionization distributions. And then, from the comparisons of ground-state neutral density between simulation and TALIF experiment, the ionization distributions are specified.

### 3.1.2 Metastable neutral particles

As discussed in 2.7, the lifetime of metastable state is drastically reduced by collision with other particles and wall diffusion, which indicates that the transport area of metastable is limited. In other words, the movement of the particles cannot be neglected. Hence, in this study, as well as the simulation of ground-state neutral particles, the particle simulation of metastable state was performed assuming some excitation distributions. And then, from the comparisons of metastable neutral density between simulation and LAS experiment, the excitation distributions are specified.

### 3.1.3 Electric field of microwaves

The electric field of microwave strongly depends on the plasma density. Actually, the experimental data measured by EO probe [12] shows that the microwave cannot be propagated, i.e., cut-off, after plasma mode-transition. In other words, the plasma density can be estimated by the comparison of the electric field between simulation and experiment. Additionally, when simulating the plasma density, the author uses plasma diffusion equation [56] to understand the contribution of ionization term including the direct and stepwise ionization based on the ground-state and metastable state neutral densities. This simulation can reveal whether stepwise ionization is essential phenomenon for plasma generation inside the waveguide or not.

## 3.2 Ground-state neutral particles

### 3.2.1 Modeling ground-state neutral particles including ionization and recombination

A schematic of neutral flow with and without ion extraction is shown in Fig. 3.1. The neutral density distribution was determined by gas injection  $\dot{m}_{in}$ , ionization  $\dot{m}_{ioni}$ , and ion recombination  $\dot{m}_{recom}$ . Here,  $\dot{m}$  is mass flow rate per unit volume. Subscripts of *in*, *ioni*, *recom* mean gas injection, ionization, and ion recombination at the wall respectively. Then, we define normalized function  $f(\vec{x})$  as follows.

$$f(\vec{x}) = \frac{\dot{m}}{\dot{M}}, \quad (3.1)$$

Here,  $\dot{M} = \iiint \dot{m} dV$  is total mass flow rate.  $f(\vec{x})$  exhibits inhomogeneous effects (e.g., gas injection, ionization, and ion recombination), and  $\iiint f dV = 1$  is satisfied. Then, the ion extracted efficiency  $\eta_{ex}$  and propellant utilization efficiency  $\eta_u$  are defined as follows.

$$\eta_{ex} = \frac{I_b}{I_p}, \quad (3.2)$$

$$\eta_u = \frac{m_n I_b}{e \dot{M}_{in}}. \quad (3.3)$$

Here,  $I_p$  is the total ionization rate current,  $m_n$  is the mass of ion, and  $I_b$  is the measured ion beam current by experiment. By using these definitions,  $\dot{M}_{ioni}$  and  $\dot{M}_{recom}$  can be expressed.

$$\dot{M}_{ioni} = \frac{1}{e} \frac{I'_b}{\eta_{ex}} = \frac{\alpha_m \eta_u}{\eta_{ex}} \dot{M}_{in}, \quad \dot{M}_{recom} = \frac{\alpha_m (1 - \eta_{ex}) \eta_u}{\eta_{ex}} \dot{M}_{in}. \quad (3.4)$$

Here,  $I'_b = \alpha_m I_b$  is the modified ion beam current by considering the effect of doubly and triply charged ions, where  $\alpha_m$  is the correction factor [24]. For instance, in the thruster,  $\eta_u$  and  $\eta_{ex}$  are typically  $\eta_u \approx 0.8$ ,  $\eta_{ex} \approx 0.5$  [17]. Therefore,  $\dot{M}_{recom}$  and  $\dot{M}_{ioni}$  are calculated as  $\dot{M}_{recom} \approx 0.8 \dot{M}_{in}$ ,  $\dot{M}_{ioni} \approx 1.6 \dot{M}_{in}$ , which indicates that both the wall loss current and ionization rate are not negligible compared to  $\dot{M}_{in}$ .

In the absence of ion extraction, the ion beam current is not extracted from the grid. Some ions are lost in the accelerator grid and the rest are exhausted from the accelerator grid. Thus, the ratio of ion recombination at the grid accelerator grid  $\eta_i$  is defined as follows.

$$\dot{M}_{recom,g}^* = \eta_i \frac{m_n I'_b}{e} = \alpha_m \eta_i \eta_u \dot{M}_{in}. \quad (3.5)$$

Here,  $\dot{M}_{recom,g}^*$  is the additional flow rate by the ion recombination at the accelerator grid.

In this situation, Eq. (3.5) can be approximated  $\dot{M}_{re,g}^* \approx \alpha_m \eta_u \dot{M}_{in}$ .

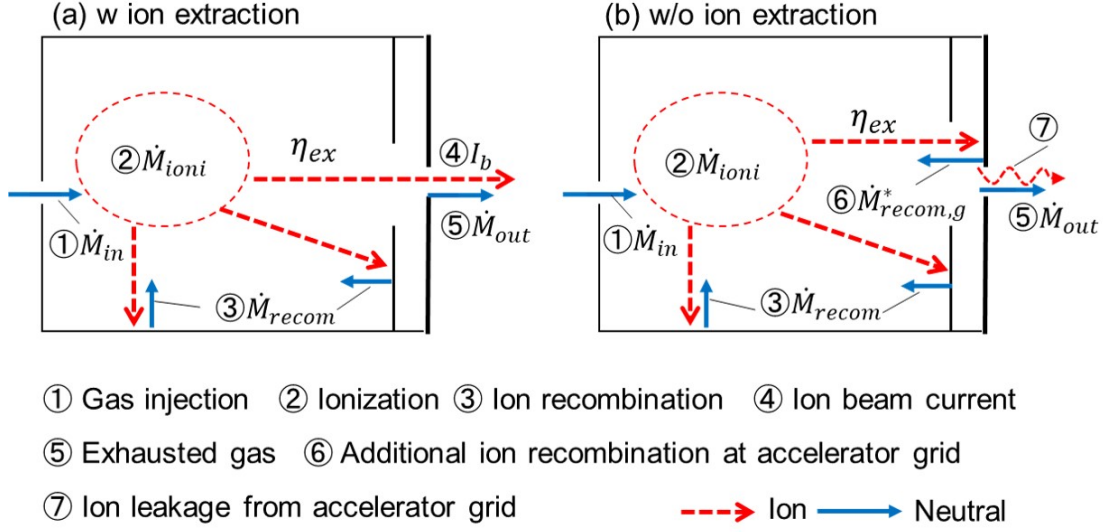


**Fig. 3.1** Schematics of neutral flow with and without ion extraction. Without ion extraction, additional ion recombination is generated at the accelerator grid.

### 3.2.1.1 Ion recombination

According to equation (3.4), to evaluate the ion recombination distribution  $\dot{M}_{recom} f_{re}(\vec{x}_{re})$ , experimental parameters  $\alpha_m$ ,  $I_b$ ,  $\eta_u$ ,  $\eta_{ex}$  are necessary.  $\alpha_m$  can be computed as follows [22].

$$\alpha_m = \frac{1 + \frac{I_{2+}/I_+}{2} + \frac{I_{3+}/I_+}{3}}{1 + I_{2+}/I_+ + I_{3+}/I_+}. \quad (3.6)$$

From previous  $E \times B$  measurements, it was reported that the current ratios of doubly and triply charged ions are 15–20 % and 5–10 %, respectively [16]. By considering the maximum case ( $I_{2+}/I_+ = 20\%$ ,  $I_{3+}/I_+ = 10\%$ ) and minimum case ( $I_{2+}/I_+ = 15\%$ ,  $I_{3+}/I_+ = 5\%$ ),  $\alpha_m$  is 0.87, 0.91 respectively. This means that the current ratio is not very sensitive to the propellant flow rate or gas injection. Thus, in this paper,  $\alpha_m$  is fixed at half value  $(0.87 + 0.91)/2 = 0.89$  for simplicity. The ion beam current  $I_b$  and  $\eta_u$  can be obtained by thruster operation in the current study. In addition, probe measurement data were used for  $\eta_{ex}$  and  $f_{recom}(\vec{x}_{recom})$  [17]. The distribution of the ion wall loss current was obtained by measuring the ion saturation current at each wall by using planar probe with guard-ring. Generally, in probe measurement, the disturbance may be generated. However, this measurement is confirmed that this probe does not disturb the ion beam current [17].

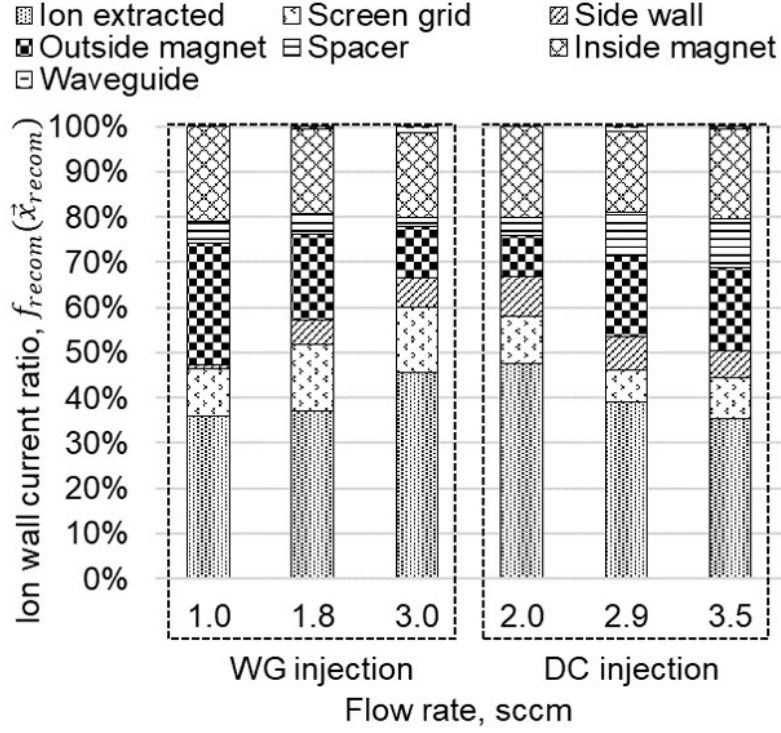


**Fig. 3.2** Ion current ratio measured by planar probe [16, 17]. These results are utilized as ion recombination distribution  $f_{recom}(\vec{x}_{recom})$  in various flow rate condition in WG and DC injection. These data are utilized data as the distribution function of ion recombination. Each location is illustrated in [18].

### 3.2.1.2 Ionization

Though total ionization rate can be evaluated  $\dot{M}_{ioni}$  as well as  $\dot{M}_{recom}$ , the ionization distribution  $f_{ioni}(\vec{x}_{ioni})$  is an unknown parameter. Thus, the ionization distribution model is proposed based on characteristics of microwave discharge ion thruster. The microwave discharge ion thruster, the ionization rate is concentrated by the magnetic confined region because the electrons are continually heated and confined, which has been observed in several plasma simulations [50]. In addition, from previous optical measurements in the  $\mu 10$  thruster, it was revealed that the plasma appears to be generated inside the waveguide as the propellant flow rate increases [9, 11]. Thus, we suggest a model of  $\dot{m}_{ioni}(\vec{x}_{ioni})$  by using two driven parameters  $R$  and  $L_w$ . As illustrated in Fig. 3.3 the ratio of the ionization rates in the two regions  $R$  is written as follows.

$$I_p = RI_{p,waveguide} + (1 - R)I_{p,discharge} \quad (3.7)$$

Here,  $I_{p, discharge}$  and  $I_{p, waveguide}$  are ionization current inside the magnetic confined region, and waveguide. In addition, the location of ionization inside the waveguide is also an

unknown parameter. Therefore, we set the parameter  $L_w$  as another driven parameter. Here,  $L_w$  means the distance of the ionization area from the screen grid as shown in Fig. 3.3. Finally, it is necessary to determine the ionization process in each area. Generally, the local mass flow rate of ionization  $\dot{m}_{ioni}$  can be written:  $\dot{m}_{ioni} = m_n \langle \sigma v \rangle n_e n_n$ , where  $\langle \sigma v \rangle$  is the rate coefficient of ionization,  $n_e$  is the electron density. In this simulation, the electron parameter  $\langle \sigma v \rangle n_e$  is constant in each region for simplicity. Based on above assumptions, the ionization model  $f(\vec{x}_{ioni})$  can be expressed as follows.

$$f(\vec{x}_{ioni}) = \left\{ \begin{array}{l} \frac{(1-R)n_n}{\iint\int_{\Omega_1} n_n dV} (\Omega_1 | rA_{\theta,min} \leq rA_{\theta} \leq rA_{\theta,max}) \\ \frac{Rn_n}{\iint\int_{\Omega_2} n_n dV} (\Omega_2 | rA_{\theta} \leq rA_{\theta,min}, -L_w \leq z \leq 0) \\ 0 \text{ (other areas)} \end{array} \right\}. \quad (3.8)$$

Here,  $A_{\theta}$  is vector potential of magnetic field in the azimuthal component. The vector potential is calculated by Finite Element Method Magnetics (FEMM) [131].

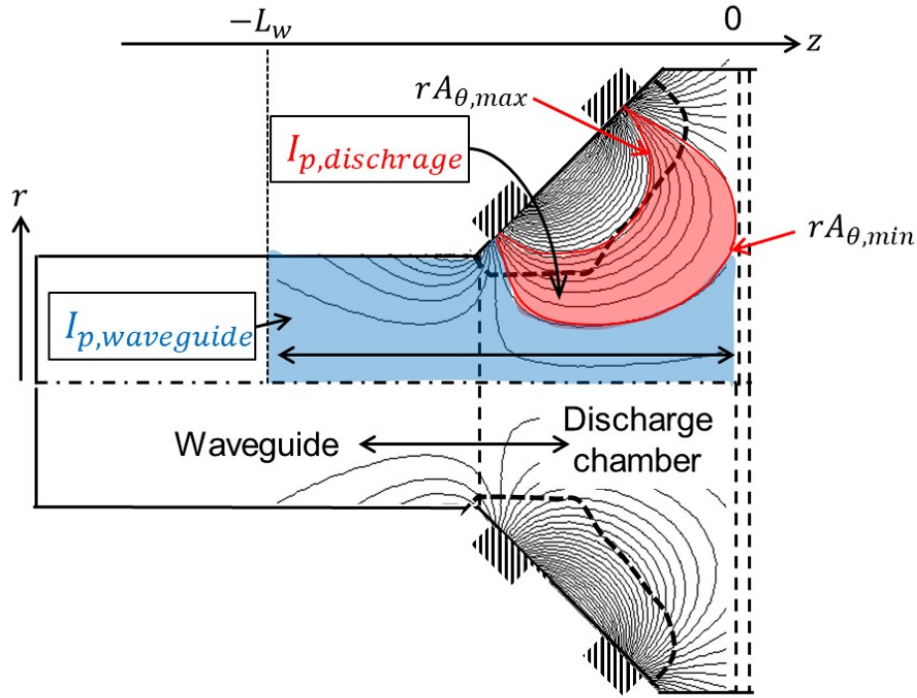


**Fig. 3.3** Model of ionization rate by using two driven parameters:  $R$  and  $L_w$ .  $R$  is the ratio of the ionization rates in the waveguide and the discharge chamber.  $L_w$  is the distance of the ionization area from the screen grid.

### 3.2.1.3 Grid modeling

The transparency of the grid determines the absolute value of the ground-state neutral density. However, it is difficult to reproduce the holes of accelerator grid because there are several hundred holes. Because the grid is far from the injection point, neutral mean velocity can be neglected. In such a situation, the transparency of grid can be evaluated by  $G_{eff}$  as shown in Eq.(2.31).

### 3.2.2 Gas injection

Generally, the propellant is injected through a mass flow controller. Then, the upstream pressure of the mass flow controller is the order of 1 – 100 Pa. On the other hand, the pressure of the discharge chamber is the order of 0.01 – 0.1 Pa. Hence, the neutral flow varied from the continuum flow to the free molecular flow, and it is difficult to determine the pressure at the injected point. In the present model, we use the following assumption. The number of injecting neutral particles during  $dt$  can be calculated by  $\dot{m}_{in}\Delta t$  simply. In this calculation, the flux returning from the discharge chamber to the injected point is assumed to be 0. In addition, the distribution function of neutral particles is assumed to be a Maxwellian distribution with neutral mean velocity  $u_n$

$$f(v) = \left( \frac{m_n}{2\pi kT_n} \right)^{\frac{3}{2}} \exp \left\{ -m_n \frac{(v_x - U_n)^2 + v_y^2 + v_z^2}{2kT_n} \right\} \quad (3.9)$$

The surface area at the injection point is the smallest of all areas, which indicates the neutral flow is thought to be choked here. Thus, the neutral mean is 1, i.e.,  $U_n \approx \sqrt{k_B T_n / m_n}$ . Of course, this velocity is an approximate assumption. However, since the difference of the performance derived from the surface area at the injection point has not been observed in the experiment, the assumption is considered to be sufficient.

### 3.2.3 Boundary condition

When neutral particles reach the wall, they are fully diffused according to the wall temperature  $T_{wall}$ .  $T_{wall}$  is assumed to be  $T_{wall} = 400$  K. Additionally, the neutral velocity by the ion recombination is considered. In this simulation,  $\alpha_{th} = 1.0$  was employed. Remind that if  $\alpha_{th} < 1$ , neutral particles by the ratio of  $1 - \alpha_{th}$  has the energy before collision, thus the velocity is very higher than thermal velocity. Because this particles rapidly the exhaust from

the grid, the density can be decreased. However, as well as  $\eta_i$ , comparison of the TALIF results between cold gas and w/o ion ext. (Fig. 2.22) revealed that  $\alpha_{th} \approx 1.0$  is valid. Hence, it is concluded that the velocity of neutral particles generated by ion recombination are assumed to be Maxwellian with the wall temperature  $T_{wall}$ .

### 3.2.4 Simulation flow

Fig. 3.4 shows flow chart of the simulation. First, injected neutral particles are generated according to distribution function expressed in Eq. (3.9). Each velocity is determined by random number, and then the only case of  $v_s > 0$  is chosen, where  $s$  is the direction of gas injection. The neutral particles are moved by  $\vec{x}^{n+1} = \vec{x}^n + \vec{v}\Delta t$ . If reaching the wall, the neutral particles are reflected according to the boundary condition (section 3.2.3) and the time step is  $6.0 \times 10^{-7}$  s. Noted that if neutral particles reach the grid, the neutral particles are exhausted by the probability of  $G_{eff}$  and reflected by that of  $1 - G_{eff}$  as shown in Eq.(2.31). Then,  $\dot{M}_{recom}$  and  $\dot{M}_{ioni}$  are calculated by Eq. (3.4).  $f_{recom}(\vec{x}_{recom})$  was used by ion wall current data (3.2), and  $f_{ioni}(\vec{x}_{ioni})$  was used by the proposed ionization model (Fig. 3.3). The neutral particles are moved according to boundary condition. Typically, the simulation is converged within 30,000-60,000 time steps. After converging, the density distribution was obtained from the position of neutral particles. Specifically, the particle positions are output only in the radial direction  $r = \sqrt{x^2 + y^2}$  and axial direction  $z$ , and the two dimensional density distribution is obtained by performing interpolation. In addition, to reduce the statistical noise owing to particle simulation, the simulation was additionally iterated 25,000 time steps and then the density is averaged in time domain. The number of superparticles is set 300,000. Usually, in case without collision between neutral particles, the number of superparticles is not a critical problem except for the statistical error. However, in case the neutral species is deleted by ionization, the simulation may be suspended due to the lack of neutral particles in ionization area. Therefore, a sufficient number of superparticles is required.

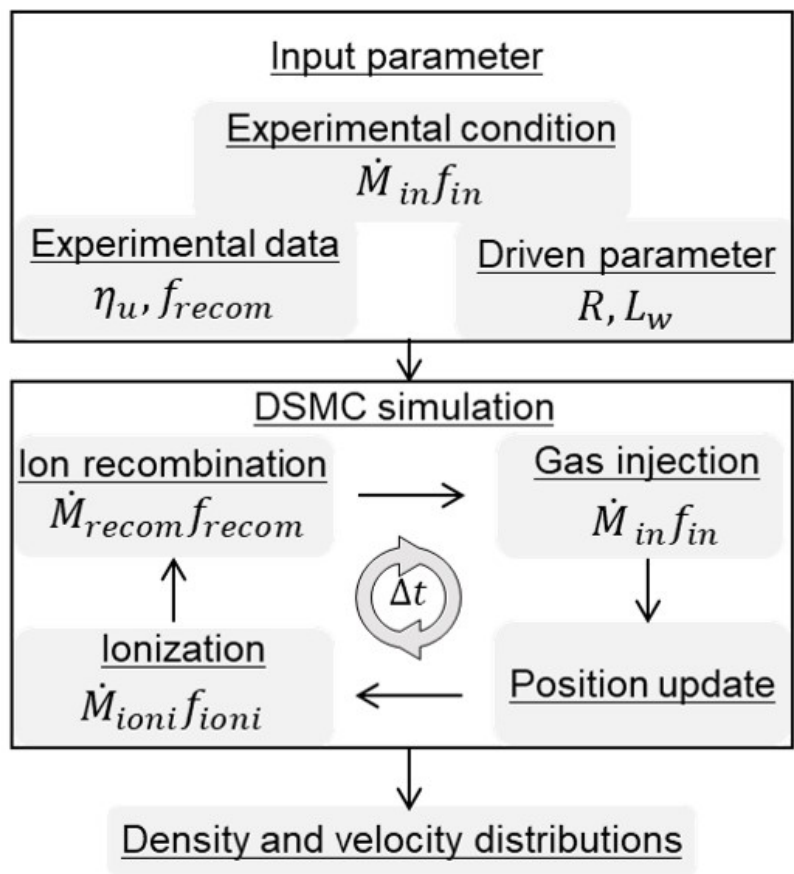


Fig. 3.4 Simulation flow of DSMC model.

### 3.2.5 Simulation results

#### 3.2.5.1 Neutral density distribution in case with and without ion extraction

First, to understand the effect of ion extraction, Fig. 3.5 shows the simulation results with and without ion extraction. Here, to clarify the effect of ion extraction, the distribution of ion recombination was the same with and without ion extraction. For this simulation, the optimal flow rate was used as the simulation condition (Fig. 3.4). The driven parameter on the ionization rate was employed in two cases (i)  $R = 0.0$  and (ii)  $R = 0.5$ , and was  $L_w=18$  cm based on a comparison with the experimental results (described later). Top-figure shows the results of WG injection, and bottom-figure shows the results of DC injection. Table. 3.1 summarizes the maximum, minimum, and average neutral density.

The comparison of WG and DC injection shows that this DSMC simulation can capture the effect of gas injection against the neutral density distribution. In the absence of ion extraction (Fig. 3.5 (a)), the neutral density distribution is not sensitive to the distribution of the ionization rate. As listed in Tab. 3.1, differences of only a few percent were observed between (i) and (ii) for the maximum, minimum, and average neutral density in both WG and DC injection. The neutral density of the DSMC simulation was found to be about 5-10 % higher than the TALIF measurement in all cases. This difference may include effects due to the approximation of  $\eta_i \approx 1$  and  $\alpha_{th} \approx 1$ , but these effects are outside the scope of the present study.

On the other hand, in the presence of ion extraction (Fig. 3.5 (b)), the density distribution is sensitive to the distribution of the ionization rate. In WG injection, the average neutral density is decreased by  $(2.2-1.7)/2.2 \approx 23$  % from (i) to (ii). In DC injection, the average neutral density is also decreased by  $(1.4-1.1)/1.4 \approx 21$  % from (i) to (ii). Additionally, the inhomogeneity of the neutral density distribution increases as listed in Tab. 3.1. For instance, in WG injection (i), the neutral density only varies from  $4.0 \times 10^{19} \text{ m}^{-3}$  to  $9.8 \times 10^{19} \text{ m}^{-3}$  without ion extraction, but varies from  $0.2 \times 10^{19} \text{ m}^{-3}$  to  $9.0 \times 10^{19} \text{ m}^{-3}$  with ion extraction.

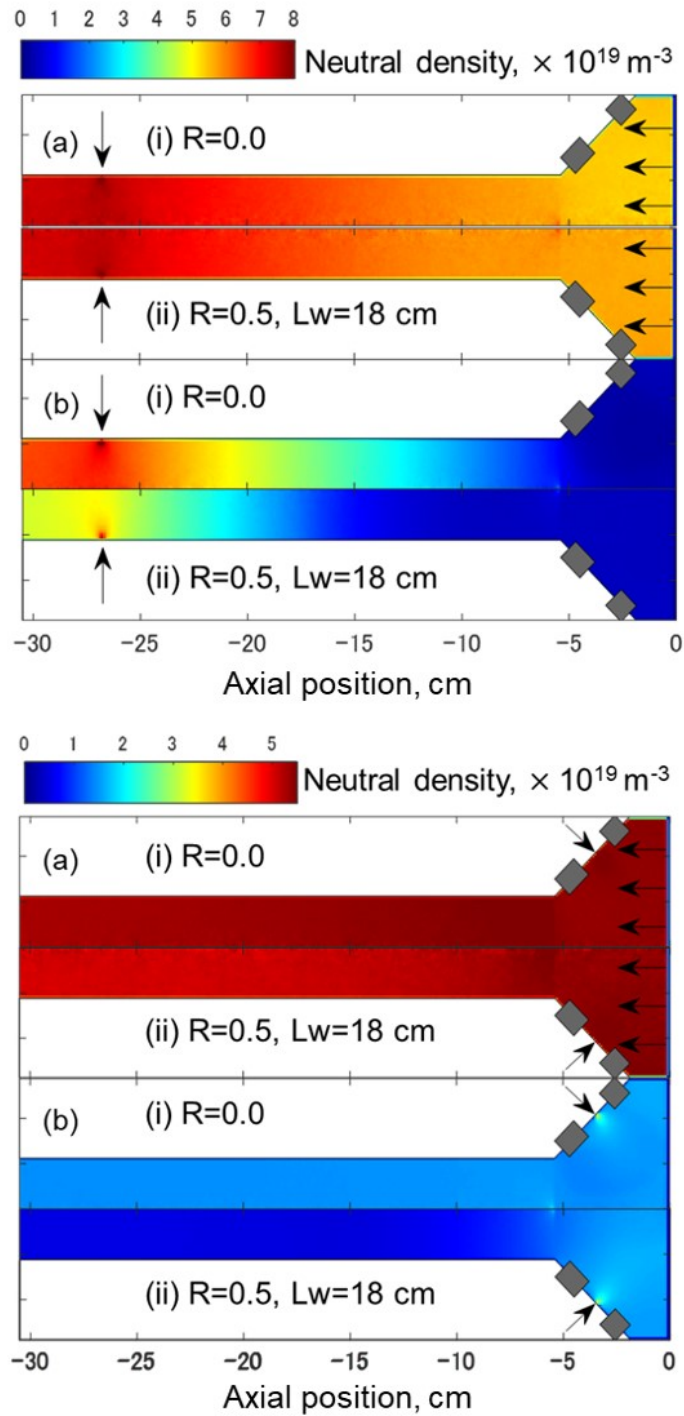


**Fig. 3.5** Comparison of neutral density distributions (a) without ion extraction, (b) with ion extraction. Left: WG injection, right: DC injection. Arrow shows the gas injection.  $R$  and  $L_w$  are defined in Eq. (3.7) and Fig. 3.3. In both WG and DC injections, the simulation condition is (ii) optimal flow rate .

**Table 3.1** Comparison of the maximum, minimum, average neutral densities for WG and DC injection. Results of this table are obtained from Fig. 3.5.

Condition		Neutral density, $\times 10^{19} \text{ m}^{-3}$		
WG, (a) w/o ion ext.	(i)	9.8	4.0	6.0
WG, (a) w/o ion ext.	(ii)	9.6	3.9	6.0
WG, (b) w ion ext.	(ii)	9.0	0.22	2.2
WG, (b) w ion ext.	(ii)	8.9	0.38	1.7
DC, (a) w/o ion ext.	(i)	6.3	5.2	5.4
DC, (a) w/o ion ext.	(ii)	6.1	4.9	5.3
DC, (b) w ion ext.	(ii)	3.3	0.72	1.4
DC, (b) w ion ext.	(ii)	3.3	0.40	1.1

### 3.2.5.2 Axial velocity distribution in case with and without ion extraction

To provide insight about the role of ion extraction, the axial velocity distribution is shown in Fig. 3.6. Noted that information about velocity is important for understanding the neutral dynamics, but it cannot be detected by TALIF measurement due to resolution of laser wavelength. The axial velocity is calculated by averaging individual axial velocities:

$$U_{n,z} = \frac{1}{N} \sum_{k=1}^N v_{n,z,k}. \quad (3.10)$$

Here,  $N$  is the number of superparticles, and  $v_{n,z,k}$  is the individual axial velocity. In WG injection, the positive velocity is generated, which is the effect of WG injection. However, in the presence of ion extraction, the velocity is 10 times larger. Here, the steady-state 1D axial momentum equation is considered [52].

$$m_n n U_{n,z} \frac{\partial U_{n,z}}{\partial z} = -\frac{\partial P_n}{\partial z} - m_n n_n U_{n,z} \nu_{wall}. \quad (3.11)$$

where,  $P_n$  is the pressure of neutral particles and  $\nu_{wall}$  is collision frequency at the wall inside the waveguide. On the the right-hand side, the first term is the force of pressure gradient, and the second term is the drag due to thermalization at the wall. In the presence of ion extraction, the neutral density in the discharge chamber is reduced about 5 ~ 10 times (Fig. 3.6) because the ion recombination at the grid is reduced. Near the gas injection, the maximum density is almost the same, between with and without ion extraction (Tab. 3.1). Thus, Ion extraction makes  $-\partial P_n/\partial z$  larger, and then the axial neutral velocity also becomes larger from the force of pressure (density) gradient  $-\partial P_n/\partial z$  as evident in Eq (3.11).

In case of DC injection, the ionization is occurred inside the waveguide (case (ii)), the negative velocity is observed at  $z=-15 \sim -5$  cm (Fig. 3.6). In the absence of ion extraction, the ion recombination at the grid is about  $1/(1 - \alpha_m \eta_u) \approx 3.5$  times larger. Thus, even if ionization is occurred inside the waveguide, these neutral particles generated in the ion recombination are thermalized sufficiently because large ion recombination flow. However, in the case with ion extraction, the neutral particles are not thermalized sufficiently until ionization is occurred. Thus, this incoming flow, i.e., the negative velocity is maintained. In case (ii),  $L_w = 18$  cm is set; thus, this negative velocity is not observed due to no ionization at  $z < -L_w$ . This incoming flow is ionized from the exit of the waveguide successively, which creates a density gradient

inside the waveguide. Of course, this ionization distribution is just an assumption. However, because a similar density gradient can be observed in TALIF of DC injection case (iii) 3.5 sccm (Fig. 2.37 (b)), similar ionization distribution can be occurred. In case (ii) of WG injection, this incoming flow combines with the flow generated by the gas injection.

Based on above comparison of density and velocity distribution, it was found that in the case with ion extraction, the ion recombination at the grid is reduced, and this decrease makes the neutral density distribution more sensitive to the ionization distribution and increases the inhomogeneity of the density distribution.

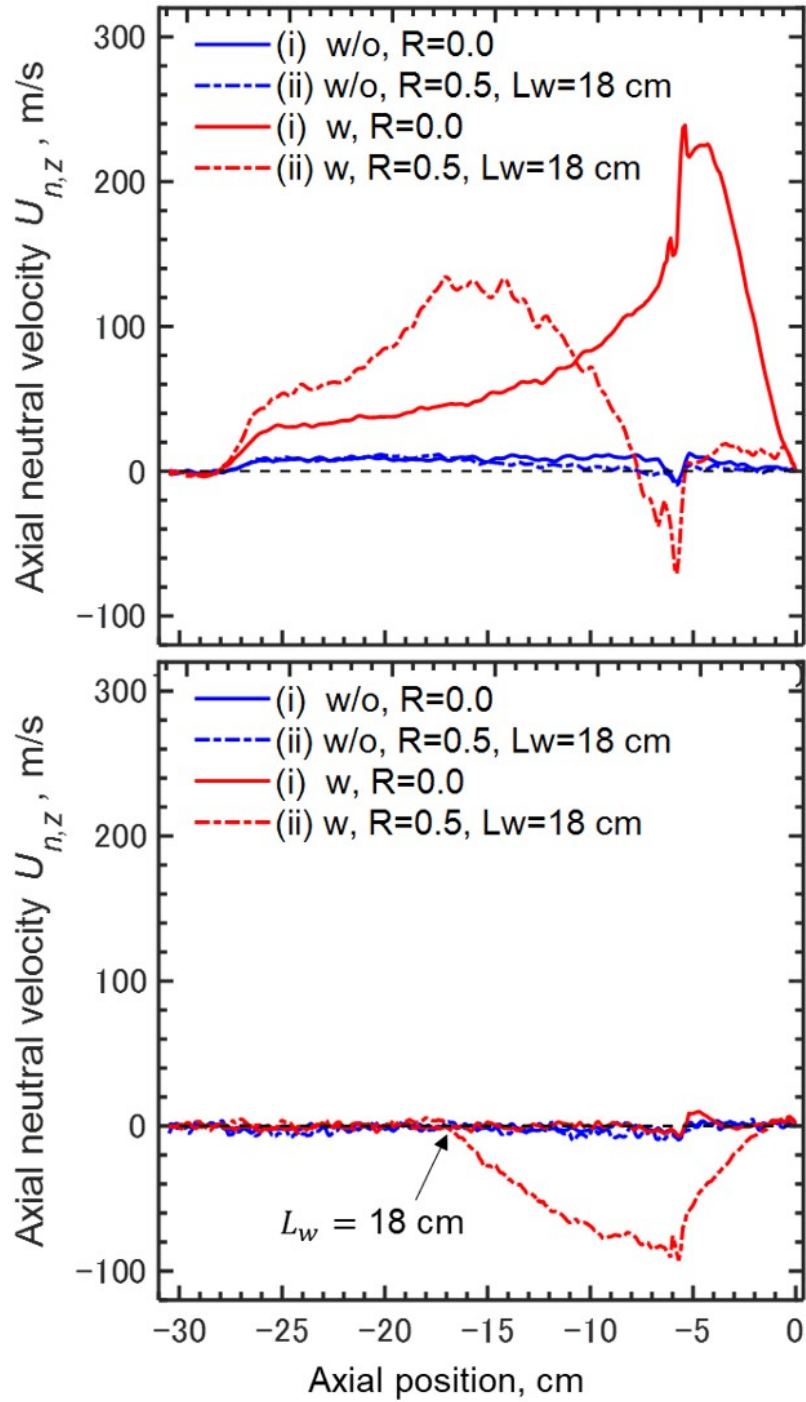


**Fig. 3.6** Comparison of time-averaged axial velocity along central axis. Top: WG injection, bottom: DC injection. Blue line: without ion extraction, red line: with ion extraction. The velocity is calculated by Eq. (3.10).  $R$  and  $L_w$  are defined in Eq. (3.7) and Fig. 3.3.

### 3.2.5.3 Estimation of ionization rate distribution

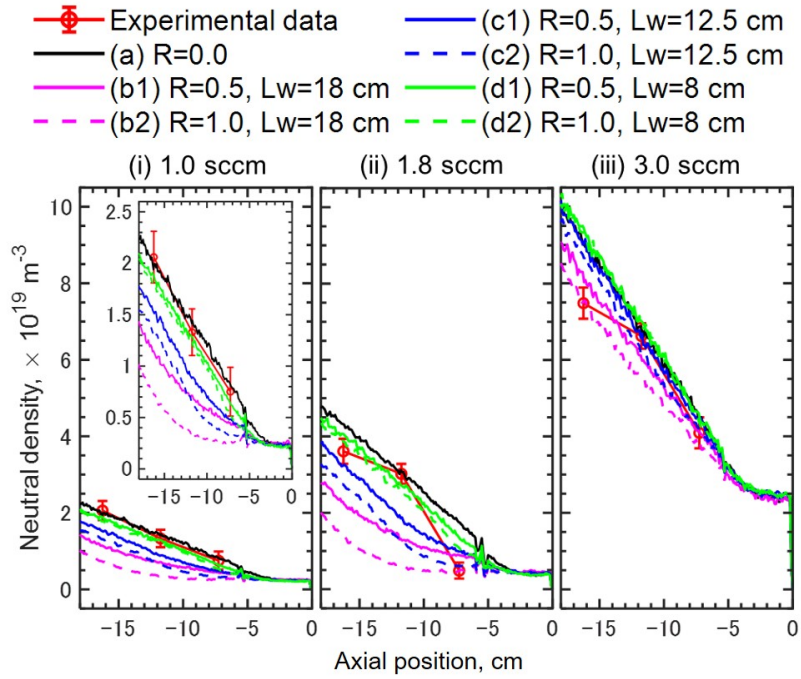
From section 3.2.5, it is found that the distribution of neutral density is sensitive to the distribution of ionization rate in the presence of ion extraction. By using this high-sensitivity and comparing simulation results with TALIF measurement, ionization rate distribution is estimated. As described in section 3.2.1, two parameters,  $R$  and  $L_w$  are varied. Here,  $R$  is changed by 0.5,  $L_w$  is opted to three cases: 18, 12.5, 8 cm. Noted that 18 cm is determined by the measurement of optical emission [9]. Since most of the emission has a life time of only about  $10^{-9} \sim 10^{-6}$  s, the absence of emission suggests that no electrons exist there.

Fig. 3.7 and 3.8 show the sensitivity of the ionization rates against the neutral density in WG and DC injection. The experimental results are quoted from Fig.2.36 and Fig.2.37. In case (i) of WG injection, (a), (d1), and (d2) are in good agreement with TALIF measurement quantitatively. However, in case (c) and (d), relatively small ionization ( $R = 0.0 \sim 0.5$ ) can be consistent with the experiment. Therefore, in this case, it is presumed that the ionization inside the waveguide is small, or even if it is generated inside the waveguide, the location is near the exit of the waveguide. In case (ii) 1.8 sccm, since the experimental results cannot be explained at  $R = 0.0$ . Especially, a large decrease in density was observed at  $z = -7$  cm, which indicates that a large ionization occurred around here. The region of waveguide is  $z < -5$  cm, and thus it is possible that the ionization is occurred near the exit of waveguide. In case (iii) 3.0 sccm, the ionization rate is not very sensitive to the distribution of neutral density. In this case, the propellant utilization efficiency is about 0.4, which indicate that the amount of ionization is relatively small.

In DC injection, in case (i) 2.0 and (ii) 2.9 sccm, the TALIF measurement does not agree with the case (a)  $R=0.0$ , which indicates that the ionization occurred inside the waveguide. However, the quantitative evaluation of ionization rate inside the waveguide is difficult due to large uncertainty of experimental data. However, in (iii) 3.5 sccm, the density gradient of experiment was observed, which is qualitatively consistent with the simulation results in case ionization occurs inside the waveguide ( $R > 0$ ). Hence, though the comparison does not match quantitatively, one hypothesis is that the ionization occurs inside the waveguide. In this case, the propellant utilization efficiency is relatively small, but the ionization inside the waveguide has the high sensitivity because there is no gas injection inside the waveguide.

The estimating approach of ionization rate found that some cases can expect the ionization

rate distribution, but the rest case cannot be specified by two reason: experimental uncertainly and low sensitivity of ionization rate distribution. Based on above comparisons, one hypothesis on the transition of ionization rage distribution is proposed as shown in Fig. 3.9. In low flow rate, the ionization is concentrated in magnetic confined region. Then, as the flow rate increases, the ionization is started to be occurred inside the waveguide. However, this approach does not reveal the kind of ionization, i.e., direct and stepwise ionization and the axial dependence of ionization cannot be captured. In addition, this estimation is not enough to determine the ionization distribution, and thus estimating excited neutral density is also necessary to investigate whether the estimation of ionization distribution is consistent with that of excitation distribution or not.



**Fig. 3.7** Comparison of neutral density distribution between TALIF spectroscopy and DSMC simulation in the presence of ion extraction at WG injection. The explanation of  $R$  and  $L_w$  are written in section 3.2.1.

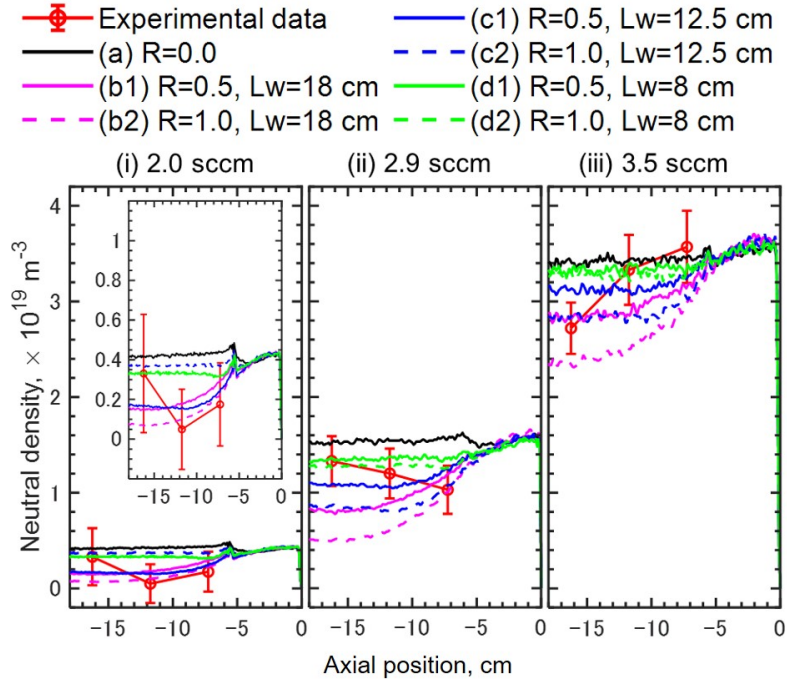


**Fig. 3.8** Comparison of neutral density distribution between TALIF spectroscopy and DSMC simulation in the presence of ion extraction at WG injection. The explanation of  $R$  and  $L_w$  are written in section 3.2.1.

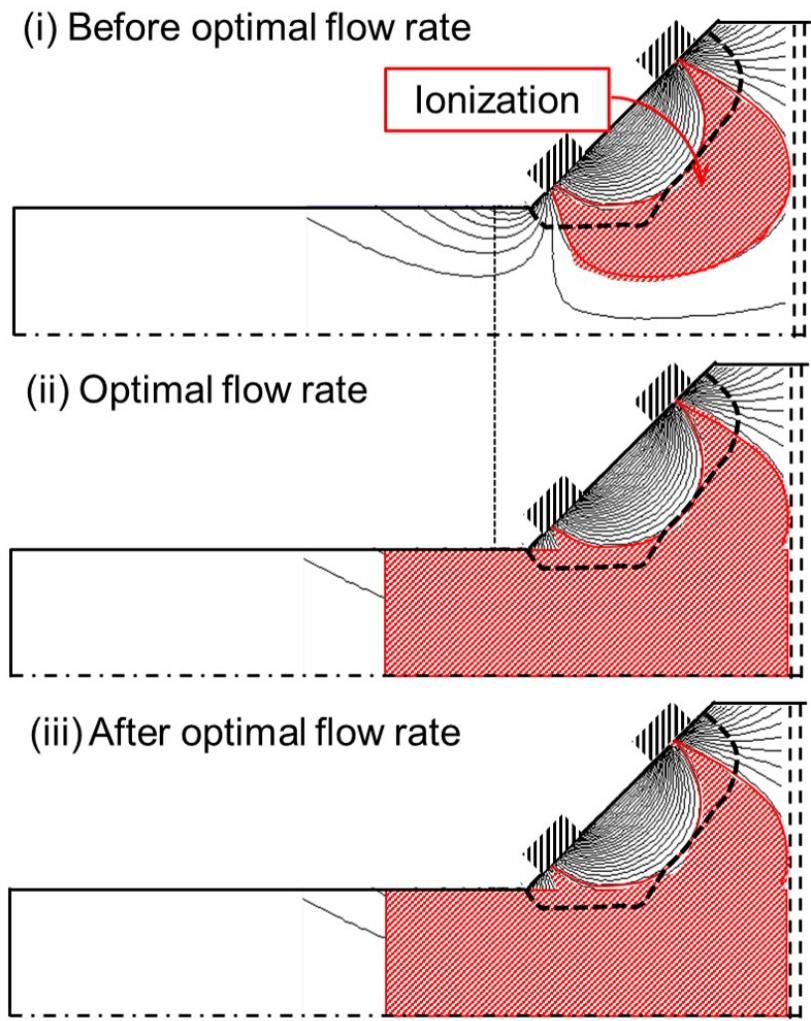


**Fig. 3.9** Spatial structure of ionization from estimation of ground-state neutral particles.

### 3.3 Metastable neutral particles

#### 3.3.1 Modeling of metastable neutral particles

To evaluate the transport process of the metastable neutral particles, it is necessary to consider the lifetime of de-excitation due to collision of electrons and the wall diffusion. Continuity equation of metastable neutral particles can be expressed as follows.

$$\frac{\partial n_{1s_5}}{\partial t} + \vec{\nabla} \cdot \vec{U}_{1s_5} = k_{ex} - \nu_{de} n_{1s_5} \quad (3.12)$$

Considering thruster length  $L_t \approx 10$  cm and thermal velocity of metastable neutral particles  $v_{th} \approx 10^2$  m/s,  $\nu_{wall} \approx L_t/v_{th} \approx 10^3$  Hz is estimated. Then, there are two possible types of collisions: collisions with ground-state neutral particles  $\nu_{1s_0}$  and collisions with electrons  $\nu_e$ , that is,  $\nu_{coll} = \nu_e + \nu_{1s_0}$ . However, estimating  $\nu_g$  under  $n_g \approx 10^{18} - 10^{19}$  m<sup>-3</sup>,  $\nu_{1s_0} \approx 10^{-1} - 10^0$  Hz is obtained [130], which indicates that  $\nu_{1s_0}$  can be negligible compared to  $\nu_{wall}$ . In addition, collision frequency of electrons  $\nu_e$  can be expressed as  $\nu_e = \sigma_{1s_5} n_e v_e$ , where  $\sigma_{total}$  is total cross-section of de-excitation,  $v_e$  is electron particle velocity,  $n_e$  is electron density. Total cross-section can be expressed as follows [80, 129].

$$\sigma_{1s_5} \approx \sum_i \sigma_{1,i} + \sum_k \sigma_{2,k}. \quad (3.13)$$

The sum over  $i$  occurs for transition from upper state ( $2p_i, 3d_i, 2s_i, 3p_i$ ) to  $1s_4$  that are optically coupled to the ground state, and intra-transition from  $1s_5$  and  $1s_i$  ( $i = 1, 2, 3, 4$ ). The sum over  $k$  occurs stepwise ionization including singly-charged and multiply-charged. From the probe measurement and full-kinetic simulation, electron temperature in the discharge chamber and waveguide is varied from  $T_e = 1 - 20$  eV. From the simulated cross-section by relativistic distorted wave (RDW) approach [13, 14],  $\sigma_{1,k} \approx 10^{-20} - 10^{-19}$  m<sup>2</sup> in range of  $T_e = 1 \sim 20$  eV. Then, from experimental data, the stepwise ionization is  $\sigma_{2,k} \approx 10^{-20} - 10^{-19}$  m<sup>2</sup> in range of  $T_e = 1 - 20$  eV [15]. Thus, in this paper, considering 36 fine structures in xenon neutral atoms,  $\sigma_{1s_5} \approx 10^{-19} - 10^{-18}$  m<sup>2</sup> is valid in range of  $T_e = 1 - 20$  eV, and this estimation is consistent with Karabadzha work [80]. Finally, other reactions are discussed. First, there is a possibility that the de-excited particles will reproduce, but this reproduction is not dominant [129]. Penning ionization can also be neglected due to low pressure as described in section 1.3.2 [63]. Hence, other reactions do not affect the order estimation of  $\sigma_{1s_5} \approx 10^{-19} - 10^{-18}$

m<sup>2</sup>.

From the full-kinetic simulation [18], inside the discharge chamber, electron density is  $n_e \approx 10^{16} - 10^{17} \text{ m}^{-3}$ . Thus, estimating electron velocity  $v_e \approx 10^6 \text{ m/s}$ ,  $\nu_e \approx 10^3 - 10^5 \text{ Hz}$  is obtained. However, inside the waveguide, the electron density can be less than that in the discharge chamber, especially near the bottom of the waveguide. If electron density  $n_e \leq 10^{16} \text{ m}^{-3}$ ,  $\nu_e$  can be smaller than  $\nu_{wall}$ , which indicates that wall diffusion can be dominant. Emphasized that this conclusion is different from the condition of Hall effect thrusters inside the channel. As pointed out Karabadzhak *et al* [80], under typical condition of Hall effect thrusters;  $n_e \approx 10^{18} - 10^{19} \text{ m}^{-3}$ ,  $\nu_e \approx 10^5 - 10^7 \text{ Hz}$  is obtained, which indicates  $\nu_e \gg \nu_{wall}$  establishes. Based on above estimation of de-excitation due to collision with electrons and wall diffusion, it is necessary to consider both de-excitation of collision and wall diffusion. For instance, some paper reports that the wall diffusion model [56, 133].

$$\nu_{wall} = \left( \frac{2.405^2 D_r}{r^2} \right)^{-1} + \left( \frac{\nu_0}{r} \right)^{-1}. \quad (3.14)$$

However, in the thruster, it is difficult to model the diffusion between the waveguide and discharge chamber. Thus, in this study, the wall diffusion is directly evaluated by particle simulation.

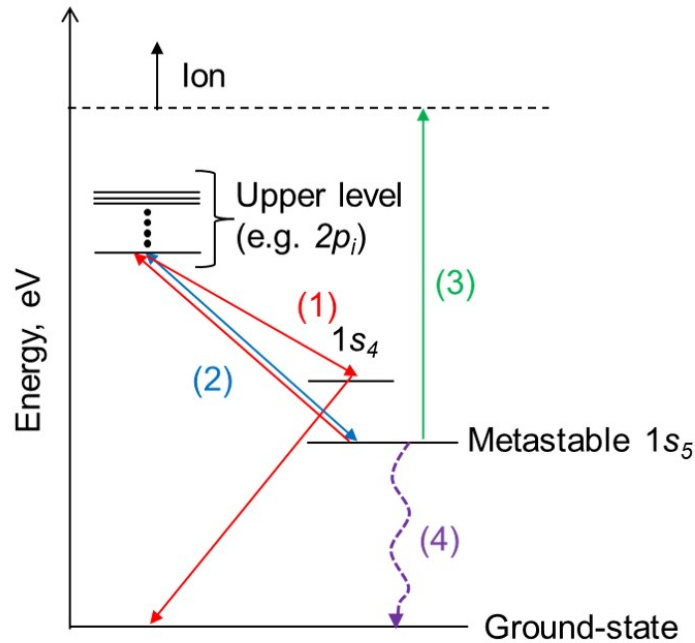


**Fig. 3.10** De-excitation process of metastable neutral particles. (1): Excitation to higher excited state and transition to resonance state ( $1s_4$ ), (2): excitation to higher excited state and reproduces metastable state ( $1s_5$ ), (3): stepwise ionization including singly, multiply charged ions, (4) wall diffusion inside thruster.

Last, source term of  $K_{ex}$  is modeled. According to the ionization model Fig. 3.3, generated distribution of metastable neutral particles was proposed using driven parameter  $\eta_w$ ,  $L_w$  as well as ionization model (Fig. 3.3). First,  $\eta_w$  is defined as linear interpolation of the excitation production rate at waveguide and magnetic confined region  $K_{ex,wave}$ ,  $K_{ex,mag}$  as well as ionization model (Fig. 3.3).

$$K_{ex,total} = \eta_w K_{ex,wave} + (1 - \eta_w) K_{ex,mag}. \quad (3.15)$$

Here,  $K_{ex,total}$  is the total excitation production rate. Then, the generation length  $L_w$  as another parameter is employed as illustrated in Fig. 3.11.

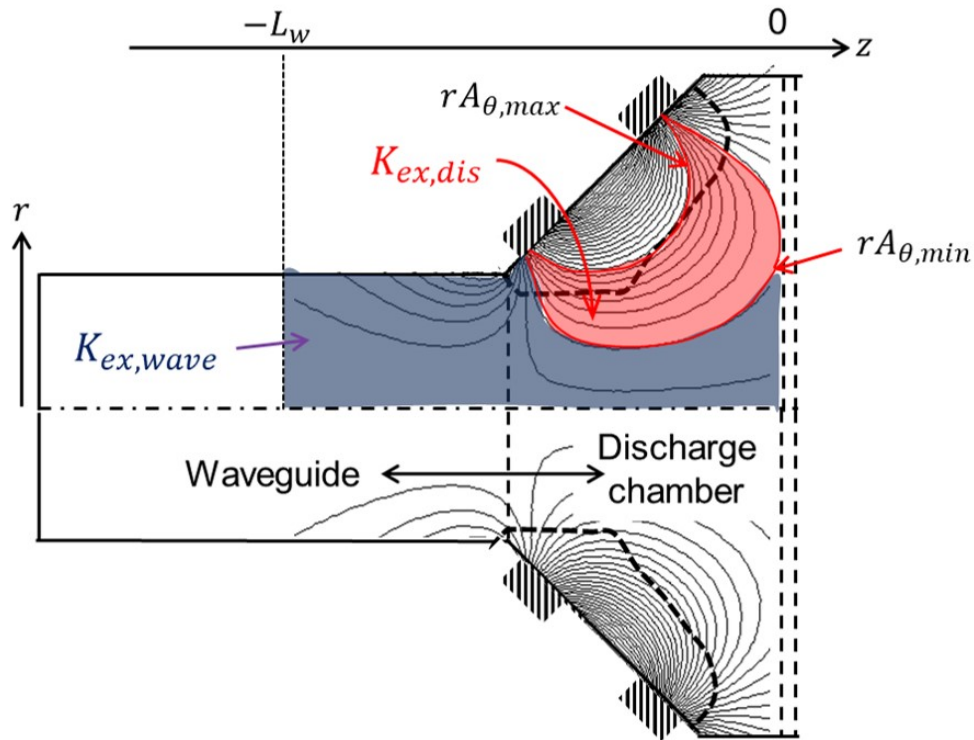


**Fig. 3.11** Model of metastable generation by using two driven parameters:  $\eta_w$  and  $L_w$ .  $\eta_w$  is the ratio of the ionization rates in the waveguide and the discharge chamber.  $L_w$  is the distance of the ionization area from the screen grid.

### 3.3.1.1 Numerical aspect

The wall diffusion is directly calculated by particle simulation. Specifically, the de-excitation due to wall diffusion is simulated by deleting particles when the particles reach the wall. Then, to simulate the collision with electrons, Monte Carlo approach was used. Probability of the collision  $P_{de}$  during simulation time step  $\Delta t$  can be expressed as follows.

$$P_{de} = 1 - \exp(-\nu_e \Delta t). \quad (3.16)$$

In this paper, to evaluate the probability within numerical error of 1 %,  $\nu_e \Delta t = 1/50$  was selected [107]. Then, the number of the de-excitation  $N_{de}$  can be evaluated:  $N_{de} = P_{de} N_{simulated}$ , where  $N_{simulated}$  is the number of simulation particles. Then, the simulated particles are randomly deleted during  $\Delta t$ . In this simulation, the metastable neutral particles are generated randomly in each magnetic confined region and the waveguide. To specify the magnetic field line, vector potential of magnetic field in the azimuthal component is calculated by FEMM [131]. Then, in this work, because the normalized distribution compares with experimental results, modeling of absolute value does not consider.

### 3.3.2 Numerical result

#### 3.3.2.1 Effect of de-excitation due to collision

As explained in section 3.3.1, de-excitation  $\nu_{de}$  can be varied:  $\nu_{wall} \approx 10^3 \text{ Hz} \leq \nu_{de} \leq \nu_{wall} + \nu_{coll} \approx 10^5 \text{ Hz}$ . Thus, to evaluate the sensitivity of  $\nu_{de}$  against the metastable neutral density distribution, four cases; (a)  $\nu_{coll} = 0 \text{ Hz}$ , (b)  $\nu_{coll} = 10^3 \text{ Hz}$ , (c)  $\nu_{coll} = 10^4 \text{ Hz}$ , (d)  $\nu_{coll} = 10^5 \text{ Hz}$  were simulated. As example, Fig. 3.12 and 3.13 show the normalized two-dimensional metastable neutral density distribution in two cases; (i)  $\eta_w = 0\%$  (ii)  $\eta_w = 100\%$ ,  $L_w = 10 \text{ cm}$ . The simulation results indicate that in both cases of (i) and (ii),  $\nu_{coll}$  is very sensitive to the density distribution in case  $\nu_{coll} \geq 10^4 \text{ Hz}$  because  $\nu_{wall}$  is the order of  $10^3 \text{ Hz}$ .

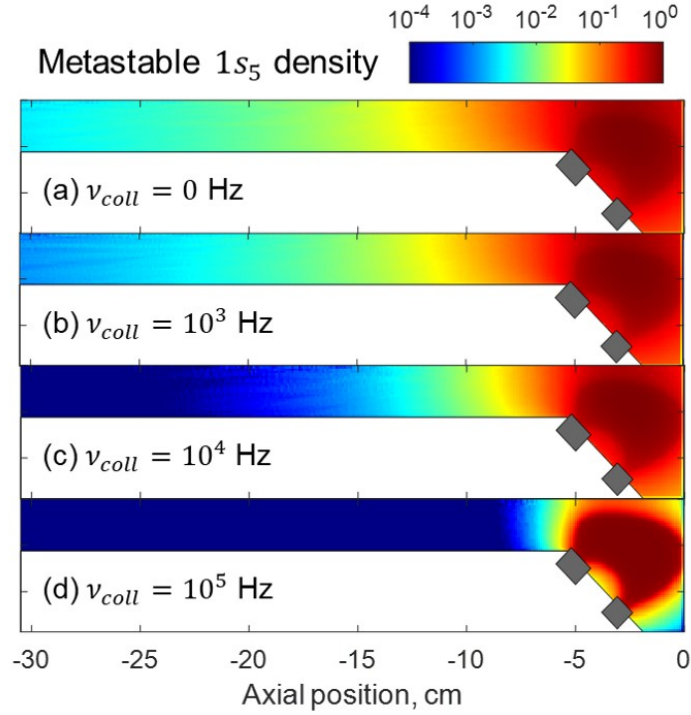


**Fig. 3.12** Sensitivity of de-excitation time against metastable neutral density distribution. (a)  $\nu_{coll} = 0$  Hz, (b)  $\nu_{coll} = 10^3$  Hz, (c)  $\nu_{coll} = 10^4$  Hz, (d)  $\nu_{coll} = 10^5$  Hz. The source term of metastable neutral particles shows two cases.  $\eta_w = 0\%$

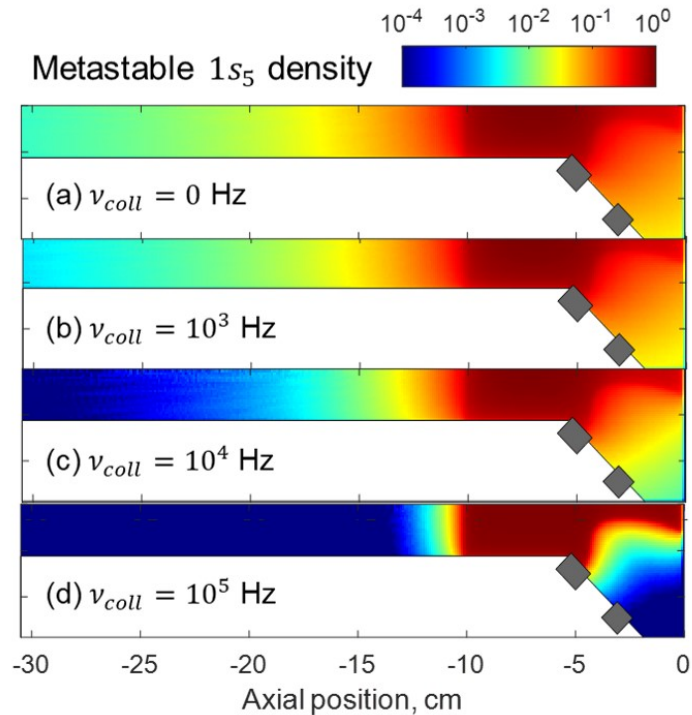


**Fig. 3.13** Sensitivity of de-excitation time against metastable neutral density distribution. (a)  $\nu_{coll} = 0$  Hz, (b)  $\nu_{coll} = 10^3$  Hz, (c)  $\nu_{coll} = 10^4$  Hz, (d)  $\nu_{coll} = 10^5$  Hz. The source term of metastable neutral particles shows two cases.  $\eta_w = 100\%$ ,  $L_w = 10$  cm

### 3.3.2.2 Estimation of excitation rate distribution in metastable state

The simulation results of metastable neutral density  $1s_5$  compares with the experimental results in central axis obtained by LAS [10, 11]. In numerical simulations, it is difficult to accurately match the absolute value of excitation rate with the experiment. Thus, in this study, each absolute value of metastable neutral density is matched with the experimental result.

This numerical simulation model has three kinds of input parameters: de-excitation due to collision  $\nu_{coll}$ , generated length  $L_w$ , and the ratio  $\eta_w$  (Fig. 3.11). Based on try and error of numerical simulation, it was found that  $L_w$  is an important parameter to determine the gradient curve of metastable neutral density distribution. Five cases on  $L_w$ :  $L_w = 6, 7, 8, 9, 10$  cm were simulated. Then, as evident in Fig. 3.12 and 3.13, because  $\nu_{coll}$  are sensitive to density distribution, four cases on de-excitation;  $\nu_{coll} = 0, 10^3, 10^4, 10^5$  Hz were simulated at each  $L_w$ . Last, five cases;  $\eta_w L_w = 0, 0.25, 0.5, 0.75, 1.0$ , were simulated at each  $L_w$  and  $\nu_{coll}$ . In total,  $4 \times 5 \times 5 = 100$  cases were simulated to reproduce the experiment data. And then, the excitation rate distribution is specified so that the discrepancy between experiment and simulation is minimized.

Fig. 3.14 shows the axial  $1s_5$  distribution of simulation and experimental results. Each simulation result include the minimum and maximum value due to variation of  $\nu_{coll} = 0 \sim 10^5$  Hz. One of the most notable result is that for at (a1) WG 1 sccm and (a2) DC 2 sccm, the result for  $\eta_w = 0\%$  is in the best agreement with the experiment. This indicates that metastable  $1s_5$  is generated in only the magnetic confined region. In case of (b1) and (c1), the results for  $\eta_w = 75\%$  ( $L_w = 10$  cm), are in the best agreement with the experiment. This indicates that 75% of metastable neutrals are generated in the waveguide. At  $z = -10 \sim 15$  cm, the density gradient is shown, which indicates the metastable neutral particles diffuse from the production area of  $z > -10$  cm. Since the maximum value of the simulation agrees with the experiment, it is suspected that the electron density is very low in this region. Finally, in (b2),  $\eta_w = 25\%$  ( $L_w = 7$ cm) cm is the best agreement, and in case of (b3),  $\eta_w = 25\%$  ( $L_w = 10$  cm) cm is the best agreement. Compared to the WG injection, the production fraction inside the waveguide is reduced. Comparing (b2) with (b3),  $L_w$  is larger, which suggests that the production position of metastable neutral particles take place more in the bottom of the waveguide as the flow rate increases.

Of course, the except for the case of  $\eta_w = 0\%$ , the quantitative evaluation of  $\eta_w$  and  $L_w$ , but

the transition of metastable neutral particle depending on flow rate can be captured qualitatively. Based on above estimation, the schematic of the generation and transport on the metastable neutral particles is shown in Fig. 3.15.

At the low flow rate, the excitation rate distribution in the metastable state is concentrated in magnetic confined region, and then the generated metastable neutral particles transport to the exit of the waveguide and inside the waveguide. As the flow rate increases, the location of the generation are transited from the magnetic confined region to the waveguide, and then more particles are transported to inside the waveguide. After the optimal flow rate, the metastable neutral density and moves at the bottom of waveguide and the absolute value increases, which suggests that the plasma density also increases inside the waveguide.

Generally, the process of generating  $1s_5$  is two causes. First, the ground-state neutral particles are excited to higher excited state that than, and then transit to  $1s_5$ . Second, directly excited from the ground-state to  $1s_5$ . Thus, to generate the metastable neutral particles, electron energy is required approximately  $8.3 \sim 11$  eV as shown in Tab. 1.1. Thus, given that electron has VDF, the excitation distribution of metastable and ionization must be close, which is consistent with result of the ionization the excitation distributions. Additionally, the particle simulation firstly revealed that the transition of the excitation distribution corresponds to the diffusion of metastable neutral particles, which suggests that the stepwise ionization can spread by the diffusion of metastable state neutral particles. The ratio of stepwise ionization against the direct one will be evaluated by numerical simulation of electromagnetic field of microwaves.

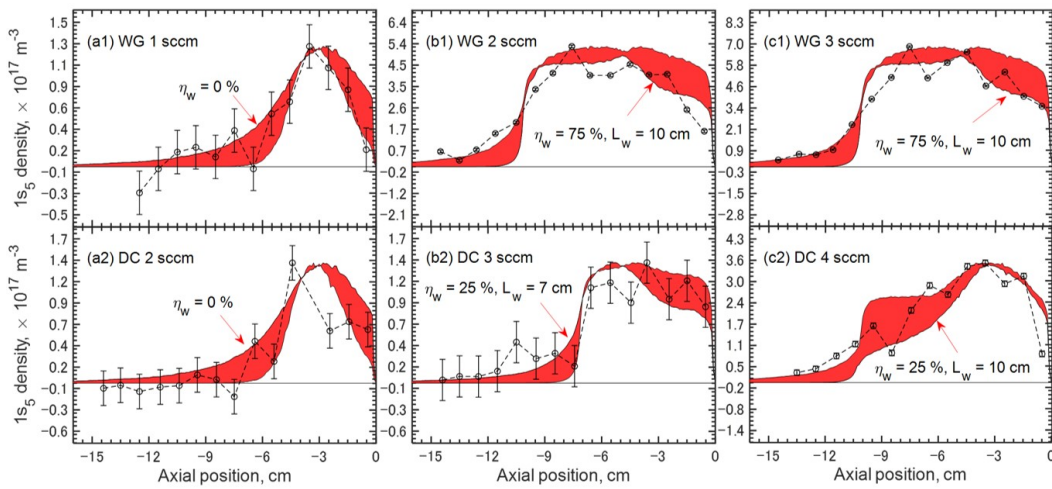


**Fig. 3.14** Comparison of metastable neutral density distributions. Black line: LAS experiment results quoted from ref. [19], red and blue line: simulation results considering the plasma mode-transition. Simulation results include the minimum and maximum value due to variation of  $\nu_{coll} = 0 \sim 10^5$  Hz.

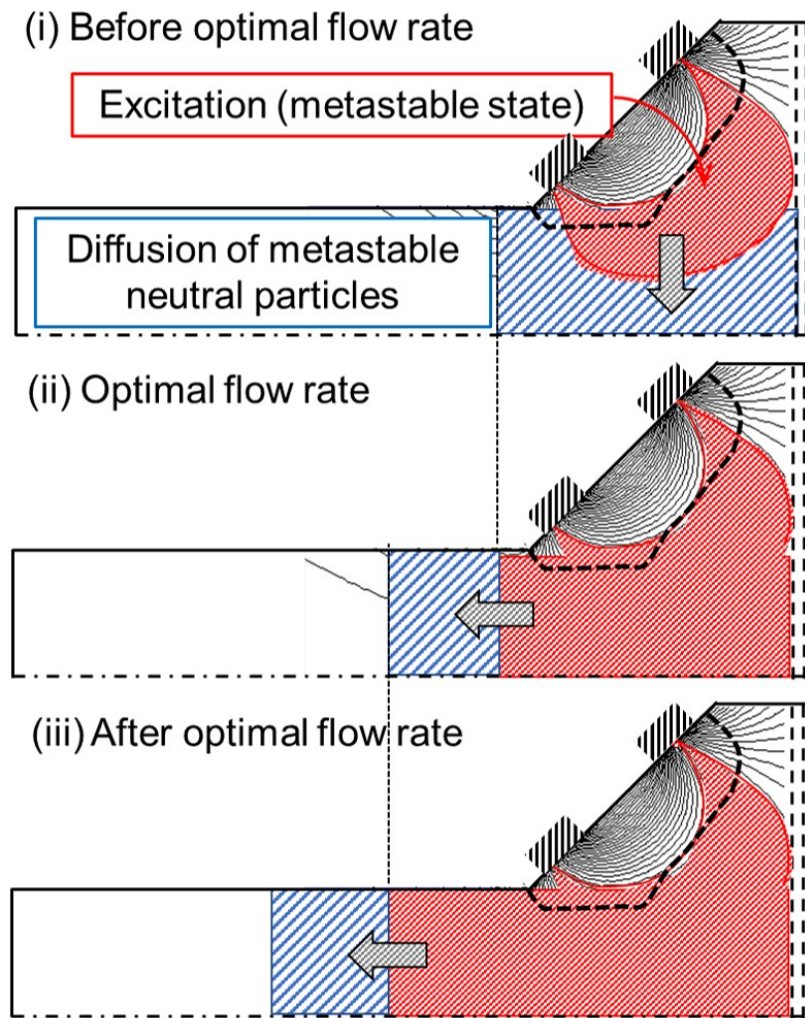


Fig. 3.15 Spatial structure of generation and diffusion on metastable neutral particles  $1s_5$ .

### 3.4 Effect of stepwise ionization from metastable neutral particles

#### 3.4.1 Modeling of plasma diffusion equation and microwave propagation

By specifying electromagnetic field is harmonic field with microwave frequency, i.e.,  $\widetilde{E}_y(z) \approx E_y(z) e^{i\omega_m t}$  [134], following equation can be obtained.

$$\left( \nabla_t^2 + \frac{\partial^2}{\partial z^2} + \varepsilon_0 \mu_0 \omega_m^2 \right) \widetilde{E}_y(z) = i\omega_m \mu_0 \widetilde{J}_y(z). \quad (3.17)$$

Here,  $\omega_m$  is frequency of microwaves.  $\nabla_t^2$  is the transverse part of the Laplacian. The equation indicates that distribution of  $E_y$  is decided by one Helmholtz equation (3.17). Here, for simplicity, quasi-1D simulation model was employed. That is, to simulate the propagation of microwaves in 1D axis model, it is necessary to evaluate the transverse component, i.e.,  $\nabla_t^2$ . Here, the author uses the idea of paraxial approximation [135]. In this approximation, the electric field is expressed as follows.

$$\widetilde{E}_y(z) = \widetilde{E}_{y0}(z) e^{-ik_z z}. \quad (3.18)$$

Here,  $k_z$  is the wavenumber. This formulation means the electric field is expressed by using the amplitude and wavenumber  $k_z$ . In paraxial approximation, the second derivative in  $z$  direction can be expressed as follows.

$$\frac{\partial^2 \widetilde{E}_y}{\partial z^2} = \left( -k_z^2 \widetilde{E}_{y0} - 2ik_z \frac{\partial \widetilde{E}_{y0}}{\partial z} + \frac{\partial^2 \widetilde{E}_{y0}}{\partial z^2} \right) e^{-ik_z z} \approx -k_z^2 \widetilde{E}_{y0} e^{-ik_z z} = -k_z^2 \widetilde{E}_y. \quad (3.19)$$

In other words, the approximation is assumed following two relationships.

$$\left| \frac{\partial \widetilde{E}_{y0}}{\partial z} \right| \ll |k_z \widetilde{E}_{y0}|. \quad (3.20)$$

$$\left| \frac{\partial^2 \widetilde{E}_{y0}}{\partial z^2} \right| \ll |k_z^2 \widetilde{E}_{y0}|. \quad (3.21)$$

In paraaxial approximation, the assumption of Eq. (3.21) is often employed. In this condition, Eq. (3.17) can be written in cylindrical coordinate.

$$\left( \frac{\partial^2}{\partial r^2} + \frac{1}{r} \frac{\partial}{\partial r} + \frac{1}{r^2} \frac{\partial^2}{\partial \theta^2} + k_c^2 \right) \widetilde{E}_{y0}(z) = 0. \quad (3.22)$$

Here,  $k_c^2 = k_z^2 - k_m^2$  and  $k_m^2 = \mu_0 \varepsilon_0 \omega_m^2$ . The mode of microwaves can be divided into three modes: Transverse Electromagnetic Wave (TEM), Transverse Electric Wave (TE), Transverse Magnetic Wave (TM) modes. From the 3D FDTD simulations [12], it was revealed that the propagation mode is  $TE_{11}$  mode, which is natural because the eigenvalue of  $TE_{11}$  mode is the smallest in cylindrical waveguide. This result is natural because the eigenvalue of  $TE_{11}$  mode is the smallest in cylindrical waveguide. In the TE mode, it is determined by the eigenvalue problem on  $H_{z0}(z)$ .

$$\left( \frac{\partial^2}{\partial r^2} + \frac{1}{r} \frac{\partial}{\partial r} + \frac{1}{r^2} \frac{\partial^2}{\partial \theta^2} + k_c^2 \right) \tilde{H}_{z0}(z) = 0, \quad \frac{\partial \tilde{H}_{z0}(z)}{\partial r} = 0 \text{ at } r = R \quad (3.23)$$

Of course, the above operation can be established other fields, i.e., magnetic field in  $z$  direction. It is generally known that the analytical solution of Eq.(3.23) is Bessel function and then it is satisfied with following condition.

$$k_c^2 = \left( \frac{\xi_{m,n}}{R} \right)^2 \quad (3.24)$$

where  $\xi_{m,n}$  is the  $n$ -th positive root of  $\partial J_m(\xi)/\partial r = 0$ , where  $J_m$  is  $m$ -th the Bessel function. In case  $m = 1$  and  $n = 1$ ,  $\xi_{1,1}$  is  $\xi_{1,1} \approx 1.8411$ . By using this approximation, the transverse part of Laplacian can be expressed as follows. In this situation, Eq. (3.17) can be simplified as follows.

$$\nabla_t^2 = -k_c^2 = - \left( \frac{\xi_{1,1}}{R} \right)^2. \quad (3.25)$$

By using this approximation, Eq. (3.17) can be simplified as follows.

$$\left\{ - \left( \frac{\xi_{1,1}}{R} \right)^2 + \frac{\partial^2}{\partial z^2} + \varepsilon_0 \mu_0 \omega_m^2 \right\} \tilde{E}_y(z) = 0. \quad (3.26)$$

The similar idea was also proposed in reference [136]. Without plasma case  $J_y = 0$ , the electromagnetic field of microwaves in central axis is shown in Fig. 3.16. The simulation result indicates that the electric field calculated by quasi-1D approximation are good agreement with the results of 3D FDTD simulation and EO probe measurement with inside the waveguide [12]. On the other hand, the 10% discrepancy of electromagnetic field exists inside the discharge chamber. This discrepancy is derived from the approximation described in Eqs. (3.20) and (3.21).

In addition, for simplicity, the plasma current is estimated by cold-electron approximation, i.e.,  $\tilde{J}_y(z) \approx \sigma_p \tilde{E}_y e^{i\omega_m t}$ , where  $\sigma_p$  is plasma conductivity [56]. This plasma conductivity  $\kappa_p$  is complex variable given by,

$$\kappa_p = \frac{e^2 n_p}{m [\nu_m^2 + (\omega_m - \omega_{ce})^2]} [\nu_m - i(\omega_m - \omega_{ce})]. \quad (3.27)$$

By using Eq.(3.27) and (3.25), one Helmholtz equation can be obtained.

$$\left\{ -\left(\frac{\rho_{1,1}}{R}\right)^2 + \frac{\partial^2}{\partial z^2} + \varepsilon_0 \mu_0 \omega_m^2 - i\omega_m \mu_0 \kappa_p \right\} \tilde{E}_y(z) = 0. \quad (3.28)$$

For instance, considering the cut-off case in infinite space domain ( $\partial^2/\partial z^2 \rightarrow 0$ ), the cut-off density  $n_{p,cut}$  can be obtained by Eq.(3.28).

$$n_{p,cut} = \frac{m_e \varepsilon_0 (\omega_m^2 - \omega_w^2) \{\nu_m^2 + (\omega_m - \omega_{ce})^2\}}{e^2 \omega_m (\omega_m - \omega_{ce})}. \quad (3.29)$$

Here,  $\omega_w = 1/(\varepsilon \mu_0) \times (\rho_{1,1}/R)^2$  is cut-off frequency due to waveguide. Further assuming that collision frequency can be negligible compared to microwave frequency ( $\nu_m \ll \omega_m$ ) and the non-magnetized case ( $\omega_{ce} \approx 0$ ), the cut-off density can be simplified as follows.

$$n_{p,cut} \approx \frac{m_e \varepsilon_0 (\omega_m^2 - \omega_w^2)}{e^2}. \quad (3.30)$$

Substituting the radius of the waveguide  $R = 22.5$  cm into Eq. (3.30), the cut-off density can be calculated by

$$n_{p,cut} \approx 0.15 n_{p,cut}^*. \quad (3.31)$$

Here,  $n_{p,cut}^*$  is cut-off density in the case without waveguide,  $n_{p,cut}^* \approx 2.2 \times 10^{17} m^{-3}$  at the microwave frequency of 4.25 GHz. Thus, the results indicate that cut off density is 15% of  $n_{p,cut}^*$ . However, in this thruster, the radius length gradually becomes large at the discharge chamber. Thus, to simulate the microwave attenuation due to the plasma, it is necessary to simulate at least quasi-1D simulation model.

Additionally, to consider the effect of plasma, 1D plasma diffusion equation was utilized.

$$-\frac{\partial}{\partial x} \left( D_p \frac{\partial n_p}{\partial x} \right) = s_{ioni} = \nu_{iz,g} n_{1s_0} + \nu_{iz,1s_5} n_{1s_5}. \quad (3.32)$$

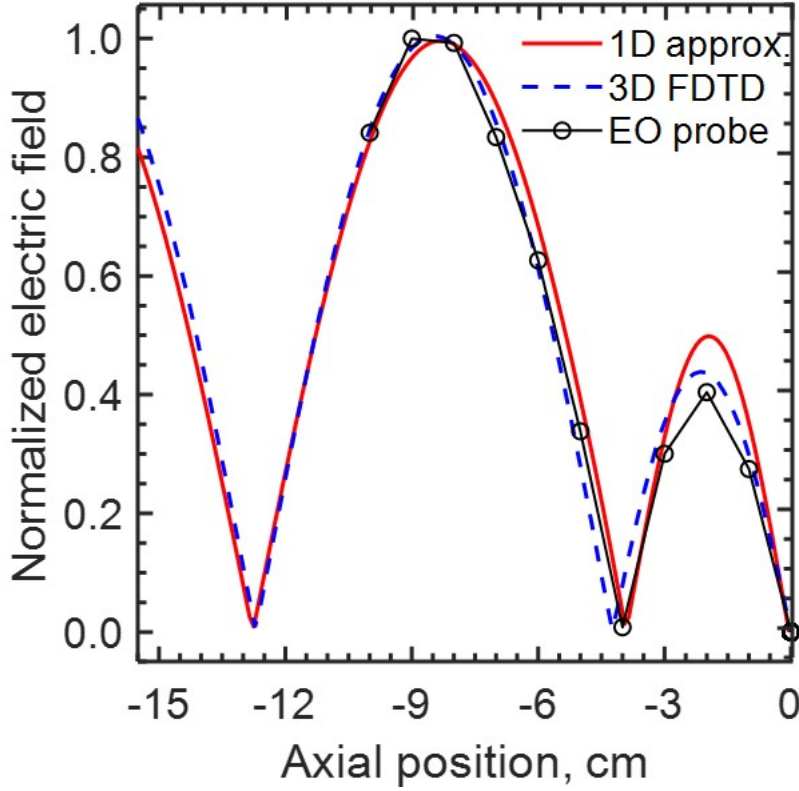


**Fig. 3.16** Electric field of microwaves parallel component  $E_y$  in central line. Results of 3D FDTD simulation and EO probe are quoted by [12].

Where,  $s_{ioni}$  is source term,  $\nu_{iz,1s_0}$  and  $\nu_{iz,1s_5}$  are the collision frequencies from ground-state and metastable neutral particles. Here,  $D_p$  is diffusion coefficient and was evaluated by non-magnetized case [41] because the magnetic field is parallel to the axial direction in the central axis. Eq. (3.32) means that the ionization source term, i.e.,  $s_{ioni} = \nu_{iz,1s_0}n_{1s_0} + \nu_{iz,1s_5}n_{1s_5}$  decides the plasma density distribution. In this thesis, to investigate the plasma density, sensitivity of stepwise ionization against the plasma density, the ratio of ground-state neutral density and metastable neutral density, i.e.,  $n_{1s_5}/n_{1s_0}$  were varied based on experimental results, and then the electric field of microwaves in the presence of plasma was calculated by Eq. (3.28).

Carefully speaking that, this equation is based on quasi-neutrality and the 1D dimensional simulation and kinetic effects is neglected [51]. Collision frequency of  $\nu_{iz,1s_0}$  and  $\nu_{iz,1s_5}$  include the electron density, thus the diffusion equation (3.32) is not consistent perfectly and it is necessary to solve the energy-conservation for determining the plasma density consistently. However, in this section, it is enough because the purpose calculating the plasma density is to

capture the sensitivity of stepwise ionization.

### 3.4.2 Numerical aspect

To solve Eqs. (3.28) and (3.32) numerically, Tridiagonal matrix algorithm (TDMA) was used. Then, Perfect Electrical conductivity (PEC) condition, i.e.,  $\widetilde{E}_y = 0$  employs to solve the electromagnetic field of microwaves as the boundary of condition at the grid and the bottom of waveguide. In addition,  $-D\partial n_p/\partial x = \Gamma_B$  was employed at the grid. Here,  $\Gamma_B$  is Bohm flux:  $\Gamma_B = n_p v_b \exp(-1/2)\eta_{sc}$ , where  $v_b$  is Bohm velocity and  $\eta_{sc}$  is effective transparency of screen grid [118]. At the bottom of waveguide, artificial boundary condition employs that  $n_p = 0$  from a certain length inside the waveguide at certain area. The artificial boundary condition is derived from radial transport of electrons, i.e., wall loss inside the waveguide. Of course, in central axis, the magnetic field is parallel to central axis, but the magnetic field penetrates the wall inside the waveguide as shown in thruster configuration. Because the plasma are strongly restricted along the magnetic field, the plasma is lost the wall. It is difficult to express the lost consistently, thus this length is empirically determined by the agreement of experimental results of microwaves.

### 3.4.3 Simulation result

#### 3.4.3.1 Correction between plasma density and electric field of microwaves

First, Fig. 3.17 shows that the correlation between plasma density and electric field of microwaves. Here, the density profile is assumed to be step function as follows.

$$n_p = n_{p,cut}^* (-L_w < z < 0), \quad n_p = 0 (z < -L_w). \quad (3.33)$$

The experimental results are quoted under experimental condition: 2 sccm at WG injection, which corresponds around optimal flow rate. The simulation results exhibit that the peak amplitude of microwaves are strongly depends on  $L_w$ , i.e., where the plasma locates inside the waveguide. From this parametric study, it was revealed that the position of the peak amplitude of  $L_w = 7$  cm is the good agreement in that of experimental data; however, the decay curves cannot be reproduced. Given that the higher plasma density is, the less microwave can propagated, the plasma density of numerical simulation is overestimated. Thus, four cases;  $n_p/n_{p,cut}^* = 0.5, 0.6, 0.7, 0.8$  were simulated under  $L_w = 7$  cm.

Fig. 3.18 shows the correction between the plasma density and microwave propagation under  $L_w = 7$  cm. The simulation results indicate that the case of  $n_p/n_{p,cut}^* = 0.6$  is good agreement in experimental data, which indicates that the electron density can exceed  $n_p = 0.6n_{p,cut}^* \approx 1.2 \times 10^{17} \text{ m}^{-3}$ . Inside the waveguide, the plasma density is more limited compared to the discharge chamber, as shown in Eq. (3.31). For instance, in case of  $n_p/n_{p,cut}^* = 0.5$ , the amplitude of  $E_y$  is attenuated inside the waveguide, but  $E_y$  is relatively high in the discharge chamber. Considering that the experimental is not such a profile, the plasma density profile is expected to be largest in the discharge chamber and gradually decreases inside the waveguide.

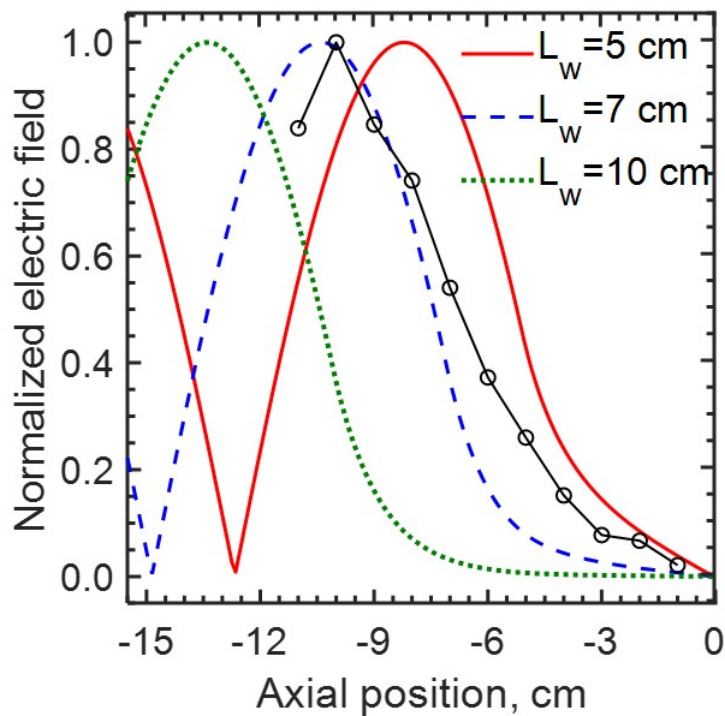


**Fig. 3.17** Correlation between the location of plasma inside the waveguide and microwave propagation. Three case on  $L_w$ ;  $L_w = 5, 7, 10$  cm are simulated. The experimental results are quoted by EO probe measurement.

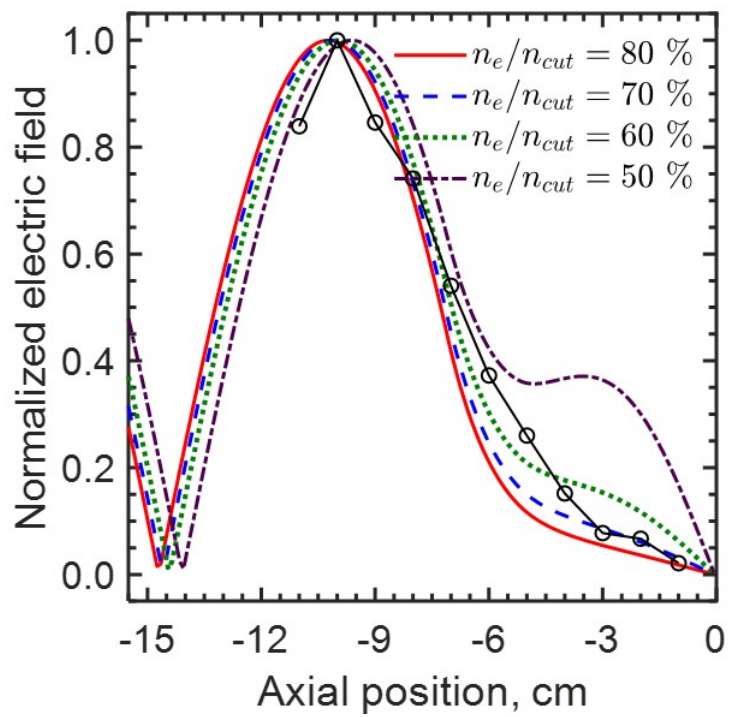


**Fig. 3.18** Correlation between the plasma density and microwave propagation under  $L_w = 7$  cm. The experimental results are quoted by EO probe measurement [12].

### 3.4.3.2 Contribution of stepwise ionization

In the previous section, the relationship between the plasma density and electric field microwaves has three properties.

- I. Location of plasma inside the waveguide determines the location of peak amplitude of microwaves
- II. Plasma density determines the waveguide decay curve of microwaves
- III. The plasma density profile is the largest in the discharge chamber and gradually decreases inside the waveguide.

To express the properties of I. and III., empirical boundary condition at the side of waveguide, i.e.,  $n_p = 0$  at  $z < -9$  cm, was employed as explained in subsection 3.4.1. And then, to express the properties of II., the plasma density is assumed to be  $n_p = 10^{17} \text{ m}^{-3}$  based on the result of Fig. 3.18. Last, the ground-state neutral density is assumed to be  $n_{1s_0} = 10^{19} \text{ m}^{-3}$  based on the TALIF measurement.

Based on the above simulation setup, plasma diffusion equation is solved as varying the ratio of ground-state neutral density and metastable neutral particles, i.e.,  $n_{1s_5}/n_{1s_0}$ . From the experimental results of TALIF and LAS, the ground-state neutral density is varied from the 1 ~ 10 %. Then, assuming that electron temperature is 3 eV, the ratio of stepwise ionization and direct ionization is  $\nu_{iz,1s_5}/\nu_{iz,1s_0} = 20$ .

Figure 3.19 shows the plasma density and electric field of microwaves by varying the ratio of metastable neutral density  $n_{1s_5}/n_{1s_0}$ . Here, four cases;  $n_{1s_5}/n_{1s_0} = 0, 1, 5, 10$  % were simulated. In case of  $n_{1s_5}/n_{1s_0} > 5\%$ , the microwave cannot be transported into discharge chamber, i.e, cut-off phenomena is occurred. Of course, even if the stepwise ionization is not occurred, this phenomena is occurred considering the large ground-state neutral density. For instance, if three times ground-state neutral density,  $n_{1s_0}^* = 2 \times 10^{19} \text{ m}^{-3}$ , the source term is the same value, the plasma density and electric field of microwave can be obtained. However, it is emphasized that before mode-transition, such case is not occurred in experiment. From Fig. 2.39 and 2.44, it was found that the ground-state neutral density is approximately constant or decreases around optimal flow rate. In contrast, from Fig. 3.14, metastable neutral density increases according to flow rate. Thus, near the optimal flow rate,  $n_{1s_5}/n_{1s_0}$  also increases. In

such a condition, the stepwise ionization is essential phenomenon for the plasma density and electric field of microwaves.

After the flow rate exceeds the optimal flow rate, the peak of electric field of the microwaves moves to the bottom of waveguide as shown in Fig. 1.17. From the simulation results of the electric field under various plasma density distribution on  $L_w$  (Fig. 3.17), the plasma density distribution transition to the bottom of the waveguide.

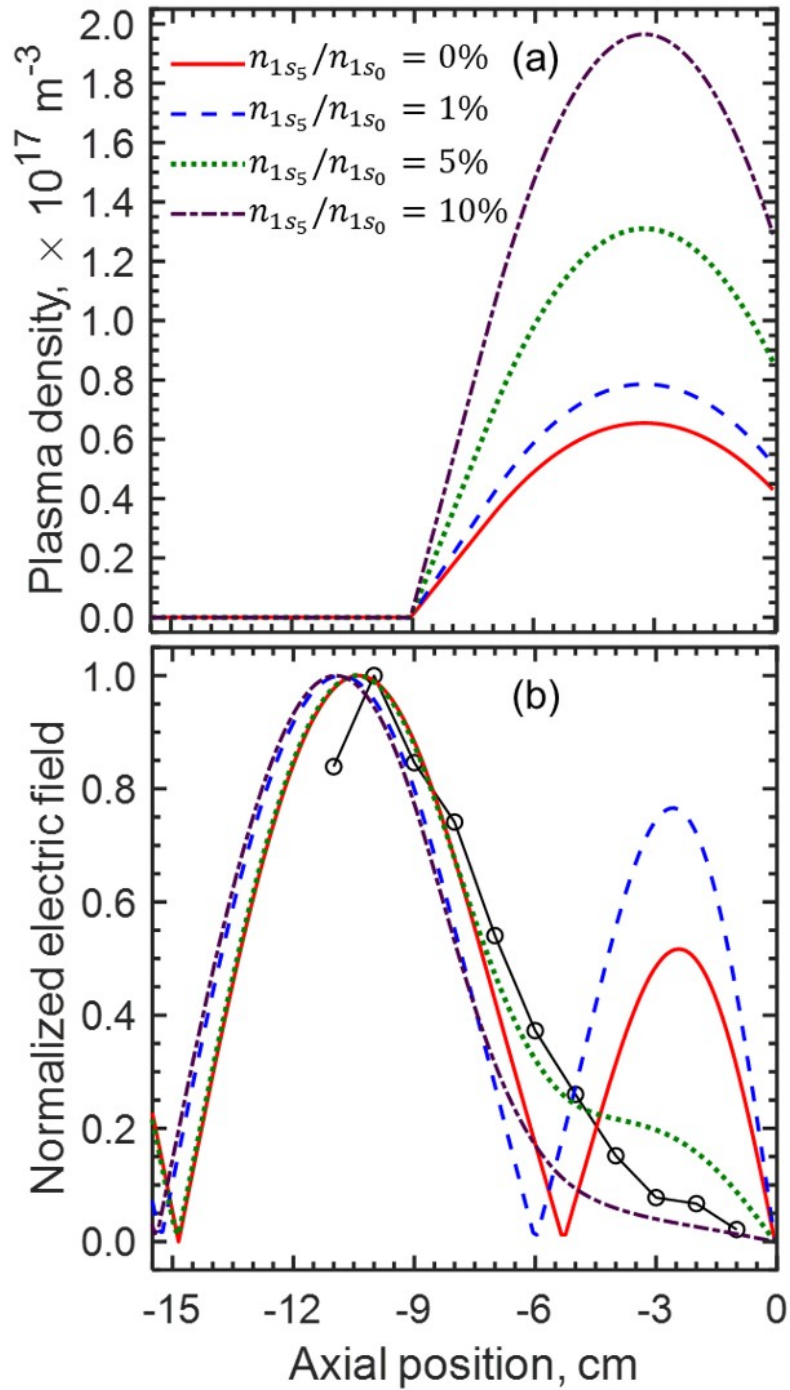


**Fig. 3.19** Correction between stepwise ionization from metastable neutral particles, plasma density, and electric field of microwave density and electromagnetic field of microwaves.

### 3.5 Spatial structure of plasma mode-transition

Based on experimental data and numerical investigation of plasma mode-transition (section 3.2, 3.3, and 3.4), Fig. 3.20 shows spatial structure of plasma mode-transition. Specifically, there are three steps depending on the flow rate.

- (i) At low flow rates (e.g., WG: 1sccm, DC: 2 sccm), direct ionization and excitation is occurred in the magnetic confined region. Then, the generated metastable neutral particles transport to the exit of the waveguide and inside the waveguide.
- (ii) From the transported metastable neutral particles, indirect excitation and ionization is occurred the exit of the waveguide and inside the waveguide, and the particles are more transported to inside the waveguide.
- (iii) When the plasma density inside the waveguide is high enough to prevent the propagation of microwaves, the plasma mode-transition occurs.

Each step is justified following experimental and numerical evidence.

- (i) : Estimation of excitation rate distribution at metastable state (Fig. 3.14 (a)) and ionization rate distribution (Fig. 3.7 (a)).
- (ii) : Estimation of excitation rate distribution at metastable state (Fig. 3.14 (b)) and ionization rate distribution (Fig. 3.7 (b)), and the correlation between ground-state neutral density and spontaneous emission intensity (Fig. 2.39 and 2.44).
- (iii) : Electric field of microwaves (Fig. 3.19).

Above above step (i) ~ (iii) are consistent with the result of photograph (Fig. 2.49) qualitatively. Based on the step of (i) ~ (iii), the difference between WG and DC injection are discussed. The ground-state neutral density of WG injection is larger than that of DC injection at the same propellant flow rate. Thus, WG injection enhances the step of (ii) and (iii), which causes plasma mode-transition at lower flow rates compared to DC injection. Then, focusing the axial dependence of the spontaneous emission intensity, the maximum value of spontaneous emission decreases only by about 48% from  $z = -7$  cm to  $z = -16$  cm in WG injection, whereas it decreases by about 25% in DC injection. This difference indicate that the

density becomes higher towards the bottom of the waveguide in WG injection and reach the large ratio of excitation rate  $\eta_w$  as shown in Fig. 3.14.

Therefore, the step of (i) ~ (iii) can explain the difference between WG and DC injection in view of ground-state neutral density, spontaneous emission intensity, and metastable neutral density.

It should be noted that after the step (iii), the beam current decreases according to the flow rate as shown in Fig. 2.43. The cause can be explained by following four steps.

- (a) When the microwaves cannot be transmitted to the discharge chamber, the beam current decreases because the plasma density inside the discharge chamber decreases.
- (b) The ground-state neutral density increases as shown in Eq. (2.15) and the result of TALIF measurement (Fig. 2.39 and 2.44).
- (c) The excitation rate distribution in metastable state inside the waveguide increase and the distribution transition to the bottom of the waveguide as shown in Fig. (3.14).
- (d) In this situation, In this situation, the plasma density also increases inside the waveguide and the more microwaves cannot be transmitted as shown in Fig. 1.17 and then the beam current decreases again.

Therefore, the above cycles can explain the mechanism why the beam current decreases according to the flow rate. Actually, decrease of beam current was mitigated in case thruster of 'w/o WG plasma' and 'w/o WG ECR layer' as shown in Fig. 2.40. That is, the decrease or absence of the plasma inside the waveguide moderate the decrease of the beam current after optimal flow rate, which is consistent the reason why the beam current decreases according to the flow rate. After occurring the step (iii) on the plasma mode-transition, the beam current cannot be enhanced even if the flow rate increases. Because it is difficult to suppress the step (i), the suppression of the step (ii) and (iii) is important for improving the thrust performance. For instance, to suppress step (iii), the author proposed an idea; the diameter of waveguide is expanded described in appendix A.

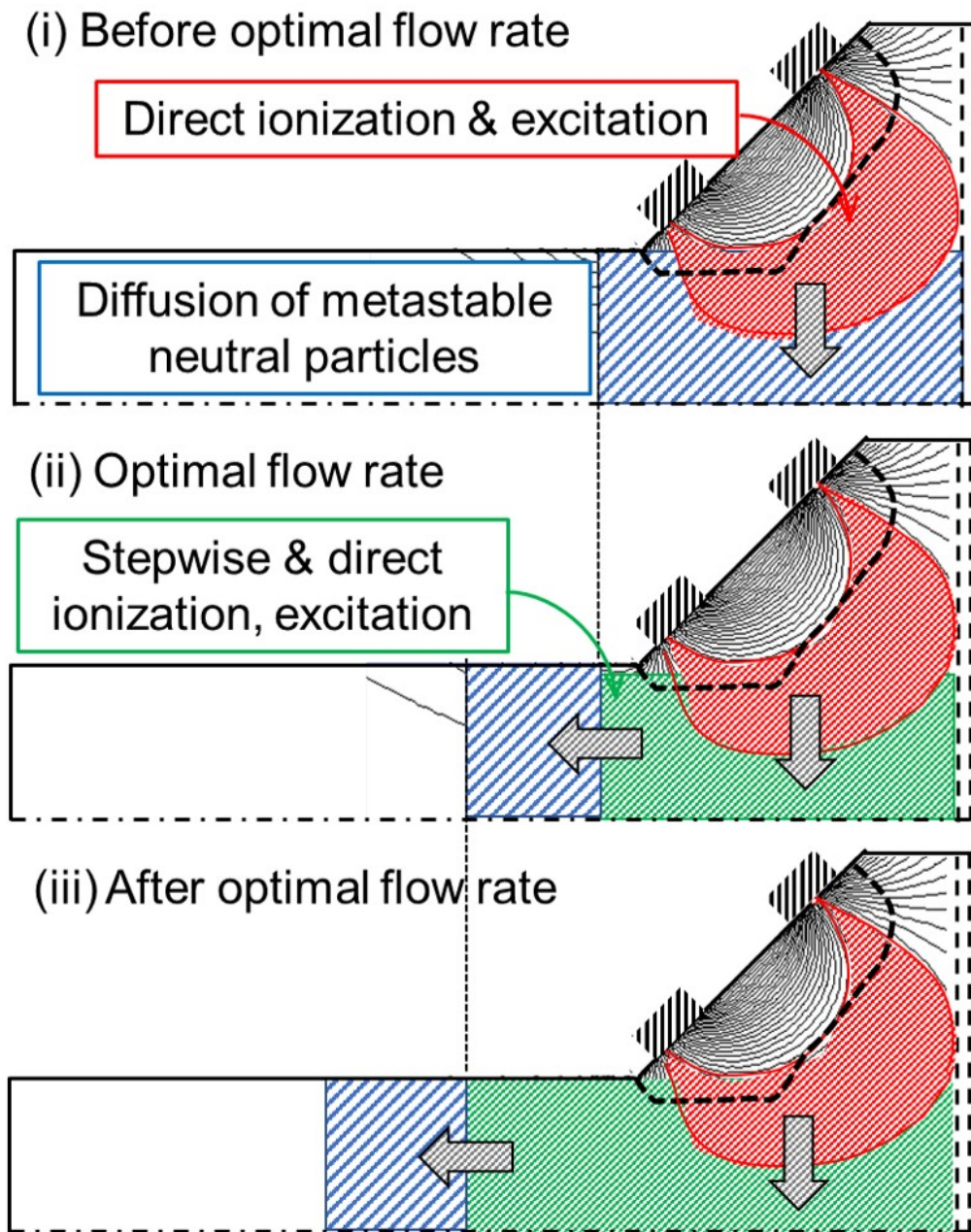


**Fig. 3.20** Spatial structure of plasma mode-transition. (i) At low flow rates, direct ionization and excitation is occurred in the magnetic confined region, and then the generated metastable neutral particles transport to the exit of the waveguide and inside the waveguide. (ii) From the transported metastable neutral particles, indirect excitation and ionization is occurred the exit of the waveguide and inside the waveguide, and the particles are more transported to inside the waveguide. When the plasma density inside the waveguide is high enough to prevent the propagation of microwaves, the plasma mode-transition occurs.

### 3.6 Short conclusion

In this chapter, to investigate the stepwise ionization distribution, three kinds of numerical simulation, ground-state neutral particles, metastable neutral particles, and electric field of microwaves, were performed. These numerical simulation provided better insight about the spatial resolution of stepwise ionization distribution. Additionally, correlation between each parameter, e.g., ground-state, metastable state, and electric field of microwave was revealed. Specifically, each simulation is summarized as below.

#### 1. Ground-state neutral particles

DSMC simulation considering the ionization and ion recombination was performed. Here, the effect of ionization and ion recombination can be comparable to the inject of flow rate. And then, the ionization rate was estimated by varying the location of ionization and gas injection.

- (a) The numerical simulation can reproduce the effect of gas injection with the good agreement in TALIF experimental results. The ionization rate distribution is not sensitive to the neutral density distribution in absence of ion extraction. In contrast, it is very sensitive to that in the presence ion extraction. The main cause is the decrease of the ion recombination at the grid. In the absence of ion extraction, the density that is recombined at the accelerator grid returns to the discharge chamber, and then the inhomogeneity of the density distribution is reduced.
- (b) By using the high-sensitivity of ionization rate against the neutral density in the presence of ion extraction, the ionization rate distribution was specified. In the case of large  $\eta_u$ , the inhomogeneity of ionization has a larger effect on the density distribution. Additionally, even if  $\eta_u$  is relatively small, this inhomogeneous effect increases if the ionization is occurred far from the location of gas injection.
- (c) Comparing simulation results of density distribution driven by ionization with experimental results of TALIF, it was found that some cases can expect the ionization rate distribution, but the rest case cannot be specified by two reason: experimental uncertainty and low sensitivity of ionization rate distribution. As a results, from the comparison between TALIF and DSMC, one hypothesis on ionization distribution was proposed. In low flow rate, ionization is concentrated on the magnetic confined re-

gion at low flow rate, but the location transits to the waveguide as flow rate increases. By performing the metastable particle simulation, the hypothesis is consistent with the excitation rate distribution.

## 2. Metastable state neutral particles

To estimate the excitation rate distribution at metastable state  $1s_5$  and transport process, the particle simulation including the de-excitation of collision and wall diffusion was performed. As a result, the simulated metastable neutral density distribution can reproduce the experimental results.

- (a) Comparing the simulation results with experimental ones, the excitation distribution at metastable state was estimated. The most notable result is that the excitation rate distribution is concentrated in magnetic confined region at low flow rate (e.g., WG :1 sccm, DC: 2sscm), and then the generated metastable neutral particles transport to the exit of the waveguide and inside the waveguide. As flow rate increases, the location of the generation are transited from the magnetic confined region to the waveguide, and then the particles are more transported to inside the waveguide.
- (b) Transition of the excitation rate distribution at metastable state is good agreement with the that of ionization rate distribution. This fact is natural considering that the excitation has strongly correlates with the ionization and then this fact enhance the reliability of this estimation approach. Then, the numerical simulation provided the evidence that the transition of metastable neutral particles corresponds to the diffusion of metastable neutral particles, which suggests that the stepwise ionization can include the ionization.

## 3. Electric field of microwaves

To investigate how the stepwise ionization enhance the plasma density, electric field of microwaves are numerically obtained by using quasi-1D simulation model.

- (a) Under the step function of the plasma density, correlation between plasma density and electric field of microwaves was investigated. As a result, it was found that Location of plasma inside the waveguide determines the location of peak amplitude of microwaves. Then, plasma density determines the waveguide decay curve of mi-

crowaves. To reproduce the experimental results, the plasma density profile is the largest in the discharge chamber and gradually decreases inside the waveguide.

- (b) Based on the simulation result under the step function of plasma density, plasma diffusion equation as varying the ratio of ground-state neutral density and metastable neutral particles, i.e.,  $n_{1s_5}/n_{1s_0}$ . As a result, in case of  $n_{1s_5}/n_{1s_0} > 5\%$ , the microwave cannot be transported into discharge chamber, i.e, cut-off phenomena is occurred. Experimental results of ground-state neutral and metastable neutral density suggests that ground-state density is approximately constant or decreases around optimal flow rate, but  $n_{1s_5}/n_{1s_0}$  also increases as flow rate increases. In such a condition, the stepwise ionization is essential phenomena for explaining about the plasma generation inside the waveguide.

Three kinds of numerical approaches reveled the spatial structure of stepwise ionization at each phase of flow rate. First, at low flow rate (e.g., WG: 1sccm, DC: 2 sccm), direct ionization and excitation is occurred in the magnetic confined region. Then, the generated metastable neutral particles transport to the exit of the waveguide and inside the waveguide. Second, from the transported metastable neutral particles, stepwise excitation and ionization is occurred the exit of the waveguide and inside the waveguide, and the particles are more transported to inside the waveguide. Last, when the plasma density inside the waveguide is high enough to prevent the propagation of microwaves, the plasma mode-transition occurs. These steps are consistent with the result of photograph qualitatively and can explain the can explain the difference of WG and DC injection on ground-state neutral density, spontaneous emission, and metastable neutral density. Because it is difficult to avoid the decrease of beam current after optimal flow rate, the suppression of stepwise ionization and cut off phenomenon under high plasma density (and higher flow rate) is clue of thrust improvement.

## Chapter 4

### Conclusion

The plasma mode-transition in microwave discharge ion thrusters, which determines the maximum thrust, was investigated. Specifically, one of the most important questions, *why plasma is generated outside for the mirror magnetic field* which induces the plasma mode-transition, was investigated using the following two approaches.

**Chapter 2:** Experimental evaluation of excitation and ionization processes measuring ground-state neutral density and spontaneous emission intensity at the same time.

**Chapter 3:** Particle simulation and simulation of the electric field of microwaves to estimate the ionization and excitation rate distributions and correlation between each measurement parameters, e.g., the ground-state and metastable-state neutral densities [10, 19] and the electric field of microwaves [11, 12].

#### Chapter 2

First, to measure the ground-state neutral density inside the thruster, three techniques were employed; two optical windows were installed and used for laser injection and fluorescence detection while thruster performance was maintained; 3,000 signals were averaged. And then, the optimized wavelength from the trade-off between fluorescence intensity and noise due to spontaneous emission was selected. By using three efforts, the author succeed in measuring the ground-state neutral density inside the thruster with nominal thruster operation for the first time.

Second, the measurement was applied to two kinds of thrusters, 'WG injection', 'DC injection' to investigate the effect of gas injection on the plasma mode-transition. Comparing 'WG

injection' with 'DC injection', the ground-state neutral density of 'WG injection' was higher than that of 'DC injection' in the cold gas state, which is consistent with DSMC works [116]. Then, this trend was maintained in case of without and with ion extraction. In WG injection, the axial distribution indicates that the density becomes higher as bottom of waveguide. In both WG and DC injection, the spontaneous emission intensity rapidly increased according to the flow rate around the optimal flow rate. In the case of 'WG injection', the ground-state neutral density decreased. In addition, in case of 'DC injection', though the neutral density also increases, the spontaneous emission intensity increased more than the increase in the neutral density of the ground state. Additionally, to understand the aspect of electron heating inside waveguide against the plasma mode-transition, the measurement was applied to two kinds of thrusters; 'w WG ECR', and 'w/o WG ECR'. The measurements indicates that the spontaneous emission intensity is rapidly increased near optimal flow rate for both 'WG injection' and 'DC injection'. This increase was relatively small with the partial prevention of ECR heating; however, the mode-transition was not eliminated. Additionally, the beam current of 'w WG ECR', 'w/o WG plasma', and 'w/o WG ECR' were evaluated. The experimental results revealed that the maximum beam current was almost the same, but the beam current was different after the plasma mode-transition. In the case 'w/o WG plasma', the decrease in beam current was reduced, which suggests that the plasma-mode transition was modulated. This result suggests that the ECR layer inside the waveguide is critical parameter for plasma mode-transition, and then the existence of plasma inside waveguide is also important for plasma mode-transition.

The observed sharp increase in the spontaneous emission can be caused by three factors; the stepwise excitation from lower excited states, an increase in the electron density, and an increase in the electron temperature. Estimation of the stepwise excitation by using rate coefficients and excited and ground-state neutral densities indicated that the stepwise excitation from the metastable state can be dominant compared to the direct excitation. Second, the stepwise ionization from the metastable state can also be non-negligible. Once the stepwise ionization occurs, the electron density increases, which is the physical mechanism for plasma generation inside the waveguide. Last, the increase of electron temperature can partially explain the sharp increase. However, in the case w/o WG ECR, the increase in electron temperature cannot be explained by ECR heating. Therefore, if the electron temperature increases, another cause of electron heating different from ECR is considered to occur such as collisional

heating. Collisional heating was evaluated based on the measurement results. As a result, though collisional heating can be important after the plasma mode-transition, the heating to each electron is very small compared to direct ionization energy. Thus, it can be concluded that the main cause of plasma generation inside the waveguide is the stepwise ionization from metastable  $1s_5$ . After plasma generation inside the waveguide, microwaves cannot be transmitted to the discharge chamber due to cutoff phenomenon [12]. Therefore, the process of '*plasma generation by stepwise ionization*'  $\rightarrow$  '*cutoff of microwaves*' is the plasma mode-transition.

### Chapter 3

First, to estimate the ionization and excitation rate distribution based on experimental data, two particle kinetic simulations of neutral particles in ground and metastable states were performed. For the estimation of the ionization rate distribution, the ground-state neutral density distribution obtained by TALIF was utilized. Though some cases cannot be estimated due to experimental uncertainty and the low sensitivity of the ionization rate, one hypothesis on transition of the ionization rate depending on flow rate can be proposed; at a low flow rate, ionization is concentrated in the magnetic confined region, but the location transitions to the waveguide as the flow rate increases. Additionally, to estimate the excitation rate distribution, metastable-state neutral density distribution obtained by LAS was utilized. The transition of the excitation rate distribution in the metastable state is in good agreement with the that of ionization rate distribution. This fact is to be expected considering that the excitation strongly correlates with the ionization which enhances the reliability of this estimation approach.

Second, to explain the contribution of stepwise ionization to the plasma density, a quasi-1D simulation of the plasma and the electric field was performed. Based on the simulation results under a step function plasma density, the plasma diffusion equation as varying the ratio of ground-state neutral density and metastable neutral particles, i.e.,  $n_{1s_5}/n_{1s_0}$ . As a result, in the case of  $n_{1s_5}/n_{1s_0} > 5\%$ , the microwave cannot be transported into the discharge chamber, i.e, cut-off phenomenon occurs. Experimental results for the ground-state neutral and metastable neutral densities suggest that the ground-state density is approximately constant or decreases around optimal flow rate, but  $n_{1s_5}/n_{1s_0}$  also increases as the flow rate increases. In such a condition, stepwise ionization is a key phenomenon to explain the plasma generation inside the

waveguide.

Three kinds of numerical approaches provided insight into the spatial structure of plasma mode-transition, and these numerical simulation provided better insight into the mode-transition, especially the spatial resolution and correlation between parameters. At low flow rate (e.g., WG: 1sccm, DC: 2 sccm), direct ionization and excitation occur in the magnetic confined region. Then, the metastable neutral particles generated are transported to the exit of the waveguide and inside the waveguide. As the flow rate increases, the stepwise ionization from the metastable state occurs at the exit of the waveguide and inside the waveguide, and more metastable neutral particles are transported to inside the waveguide. When the plasma density inside the waveguide is high enough to prevent the propagation of microwaves, the plasma mode-transition occurs. These steps are qualitatively consistent with the photographic results and can explain the differences of WG and DC injection in terms of ground-state neutral density, spontaneous emission, and metastable neutral density. Because it is difficult to avoid the decrease of beam current after optimal flow rate, the suppression of stepwise ionization and cut off phenomenon under high plasma density (and higher flow rate) is clue of thrust improvement.

# Appendices

# Appendix A

## Thruster Performance in various grid and magnetic field configuration

### A.1 Outline

The thrusters in various designs on grid configuration and magnetic geometry were tested. And then, the author will discuss about the experimental results based on the physical mechanism of plasma mode-transition.

### A.2 Grid parameter

#### A.2.1 Grid design

In this study, there are two kinds of screen and accelerator grids. The geometrical parameters are summarized in Tab. A.1. Here, 0D-equation of neutral density can be used assuming singly charged ions for simplicity [122].

$$n_n = \frac{4\dot{m}_{in}}{K_c v_{th} A_{Ac}} (1 - \eta_u). \quad (\text{A.1})$$

Because the diameter of accelerator grid is very smaller than that of screen grid, it mainly decides neutral confinement. Thus, the opening surface area  $A_{Ac}$  can be changed by changing the diameter of the accelerator grid. Additionally, considering the beam current  $I_b$  can be written as  $I_b = \eta_{ex} I_p$ , where  $I_p$  is the ion production current, Eq. (A.1) can be rewritten as follows.

$$n_n = \frac{4\dot{m}_{in}}{K_c v_{th} A_{Ac}} (1 - \eta_{ex} I_p). \quad (\text{A.2})$$

Equation (A.2) indicates that the neutral density can be varied by changing the ion extrac-

tion efficiency  $\eta_{ex}$ . From the Child-Langmuir law (Eq.(1.4)), the ion extraction efficiency is determined partly by the thickness of the screen grid. The ion extraction efficiency is better for a thinner screen grid [9]; thus, two kinds of thickness on screen grid were tested.

**Table A.1** configuration of screen and accelerator grids.

Name	Thickness, mm	Diameter	Number of apertures	Open area, %
Sc-1	0.5	3.05	855	68.2
Sc-2	0.8	3.05	855	68.2
Ac-1	1.0	1.2	855	10.6
Ac-2	0.8	3.05	218( $\phi$ 1.2, D > 45 mm), 637( $\phi$ 1.4, D < 45 mm)	13.4

### A.2.2 Experimental results

Figure. A.1 shows the beam current versus the propellant flow rate. A comparison of the results revealed two characteristics. First, comparisons of ‘Sc-1 and Ac-1’ with ‘Sc-2 and Ac-1’ and ‘Sc-1 and Ac-2’ with ‘Sc-2 and Ac-2’ indicate that the difference in the maximum beam current is about 30 mA in both accelerator grids. ‘Sc-2’ was used in the Hayabusa2 mission. ‘Sc-1’ is necessary to achieve a 200-mA class ion beam current. Second, comparisons of ‘Sc-1 and Ac-1’ with ‘Sc-1 and Ac-2’ and ‘Sc-2 and Ac-1’ with ‘Sc-2 and Ac-2’ indicate that though propellant utilization efficiency of Ac-1 is larger than that of Ac-2, the maximum beam current does not very change.

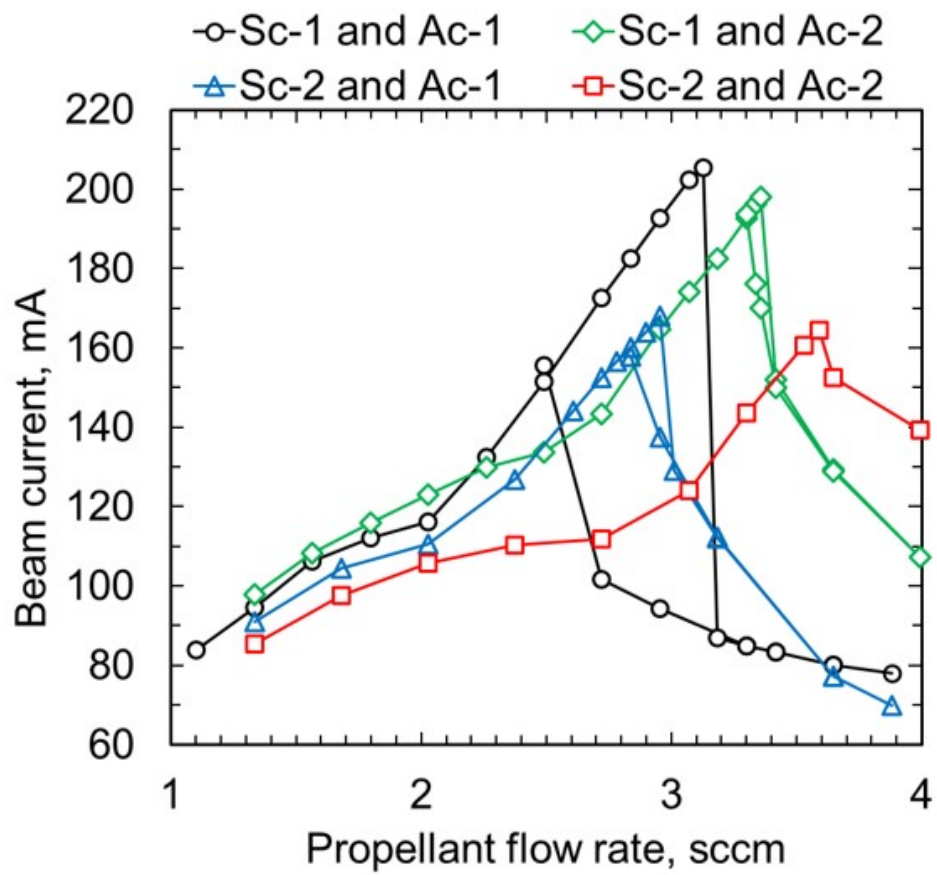


**Fig. A.1** Ion beam current with respect to propellant flow rate. For each experimental result, the maximum error was  $\pm 0.1$  sccm for propellant flow and  $\pm 5$  mA for ion beam current.

### A.2.3 Discussion of grid parameter

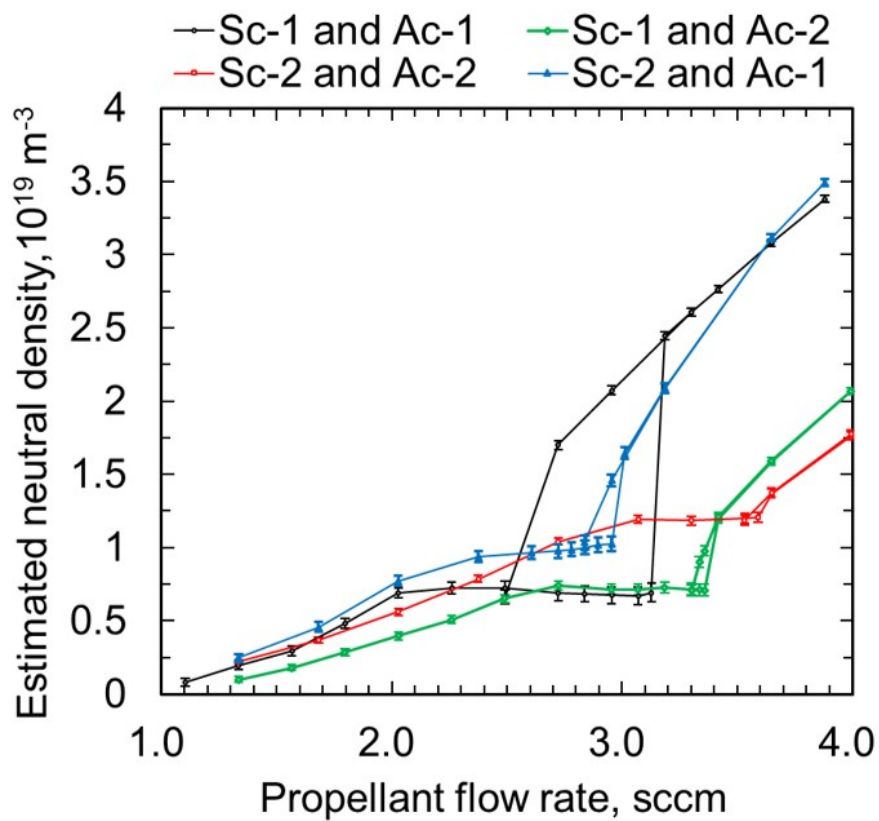
Because the neutral density is important parameter for plasma mode-transition, the difference of beam current between each grid configuration is discussed based on the neutral density. Each neutral density is estimated from the grid parameter and beam current (propellant utilization efficiency) based on Eq. (A.1). It should be noted that Eq. (A.1) has two assumptions. First, Eq. (A.1) is assumed that the plasma and gas distribution are uniform. These assumptions are not valid in case of WG injection as shown in Fig. 2.22 and is not appropriate when comparing different discharge. Therefore, the author uses this equation in case of the relatively evaluation on the grid configuration. Second, the effect of doubly and triply charged ions is neglected in Eq. (A.1). Thus, the density was modified by using Eq.(2.28).

Figure A.2 shows the relationship between the estimated neutral density and propellant flow rate. For example, in case (a) 'Sc-1 and Ac-1', the neutral density increases in 1-2 sccm, does not change much in 2-3 sccm, and a rapid increase is observed in 3-4 sccm. This tendency is consistent with other grid configurations qualitatively and TALIF results (e.g., Fig. 2.34). The thicker the screen grid, the higher the ion extraction efficiency. Thus, if the ion extracted efficiency is low, the neutral density becomes high, which suggests that the plasma mode-transition is occurred relatively low flow rate. Additionally, the beam current also decreases due to low ion extracted efficiency. Thus, ion extracted efficiency is very sensitive parameter to maximum ion beam current because it also leads the decrease of optimal flow rate.

Second, as shown in Fig. A.2, the neutral densities between 'AC-1' and 'AC-2' are approximately same within 10% at optimal flow rate. Thus, following equation can be established.

$$n_n = \frac{4\dot{m}_{in,1}}{K_c v_{th} A_{Ac1}} (1 - \eta_{u1}) \approx \frac{4\dot{m}_{in,2}}{K_c v_{th} A_{Ac2}} (1 - \eta_{u2}). \quad (\text{A.3})$$

Here, for simplicity, Eq. (A.1) was used. Thus, difference of diameter, i.e., conductance, cancel outs the difference of optimal flow rate and propellant utilization efficiency. For instance, even if the open area is small, the maximum beam current does not change because the optimal flow rate also becomes low.



**Fig. A.2** Estimated neutral density versus propellant flow rate. The grid configurations are summarized in Tab. A.1. The neutral density is estimated using Eq. (2.28). The error bars show the uncertainty due to the current ratio of the doubly and triply charged ions.

## A.3 Magnetic field geometry and height of discharge chamber

In this section, the author focuses on the thrust performance with respect to the magnetic field geometry and the height of the discharge chamber.

### A.3.1 Hypothesis

Here, the author focuses on the volume of magnetic confined region  $V_{confined}$  from following two perspectives.

1. To enhance the beam current, it is necessary to decrease the excitation rate that generates metastable state particles and to enhance ionization (ion density). Generally, the rate coefficient of excitation is larger than that of ionization in low electron temperature. For instance, in case of xenon, the rate coefficient of excitation is larger than that of ionization less than 10 eV [22]. The region where electron temperature less than 10 eV exists except for mirror magnetic confined region in the probe measurement [26] and full-kinetic simulation [18]. Therefore, to decrease the excitation rate, while to enhance the ionization rate, it is better to heat electrons locally than to heat the whole electrons. ECR can heat electrons locally, high-energy electrons (non-Maxwellian electrons) may become large. Noted that the ECR heating should be occurred under mirror magnetic field. This is because if ECR heating is occurred except for the mirror magnetic field, electron energy loss to the wall can be increased.
2. When two magnets are used to generate a mirror magnetic field, a region that is not a mirror field is also formed. If plasma is generated in this region or transported from the magnetic confined region, the plasma can enhance the plasma generation inside the waveguide. Therefore, the mirror magnetic field should be formed as large as possible and then volume except for the mirror magnetic should be small.

Based on above hypothesis, to enhance the thrust performance,  $V_{confined}$  must be large. The authors evaluate the maximum beam current in different magnetic geometry based on  $V_{confined}$ . Here, in addition to convectional thrusters ('Hayabusa 2 model', Enhanced model', and 'Enhanced model 2'), five new thrusters were experimented. First, based on simplicity of magnet in 'Enhanced model 2', the magnet is changed by two kinds; Samarium cobalt magnet (Sm) and Neodymium magnet (Nd). In nominal case, Sm was used by both inner and outer

magnets . Noted that the volume of magnetic field cannot be defined in case the ECR layer splits. For instance, when the distance between two magnets is large, the ECR layer is splits as shown in Fig. A.5. In this case outside magnet is tilted by 30 degrees. Additionally, the previous work revealed that thruster performance is very related to the height of the discharge chamber [16] and  $V_{confined}$  is also function the height of discharge chamber. Thus, the optimal height is specified in each thruster by 5 mm.

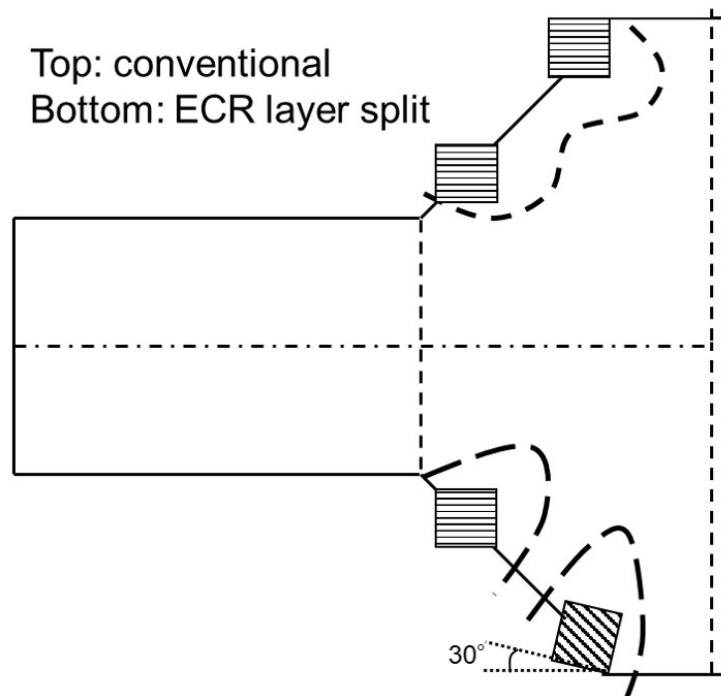


**Fig. A.3** Case of ECR layer splitting.

### A.3.2 Experimental results

Figure. A.4 shows the screen current on each magnet of thruster. The results indicates that the thrust screen current depends on the kind of the magnet, which indicates that the screen currents depends on the strength of magnetic field. Then, each thruster has the optimal height of thruster, and these are different. Additionally, Figure A.5 shows the screen current in case of ECR layer spiting. Even if the discharge height is varied, the screen current cannot achieve 200 mA.

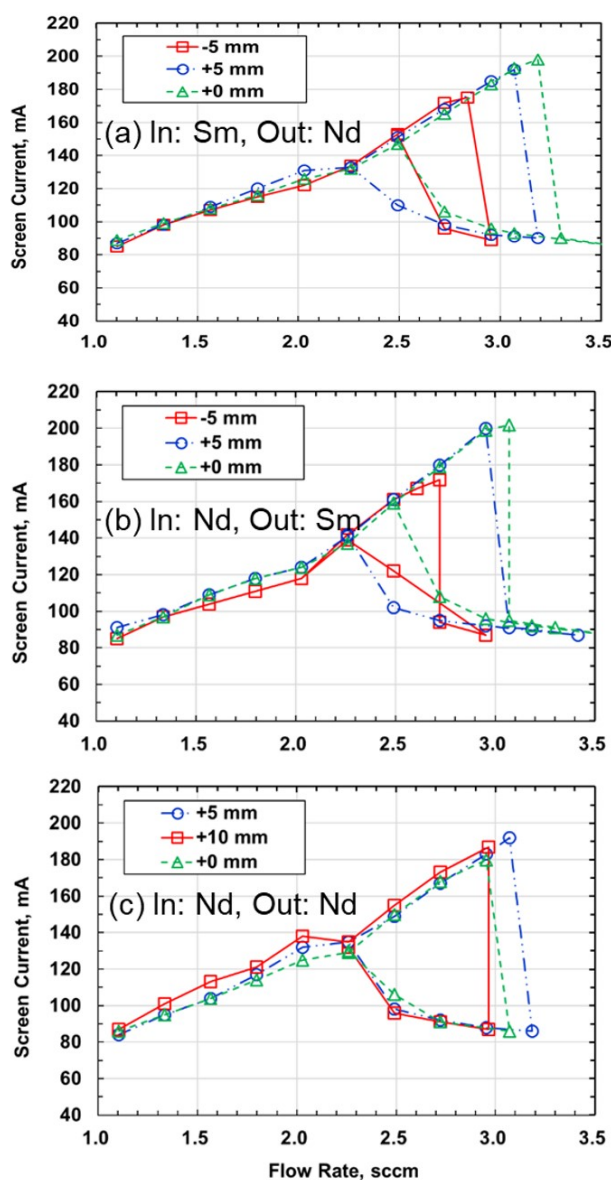


Fig. A.4 Screen current in the combination of Samarium cobalt magnet (Sm) and Neodymium magnet (Nd).

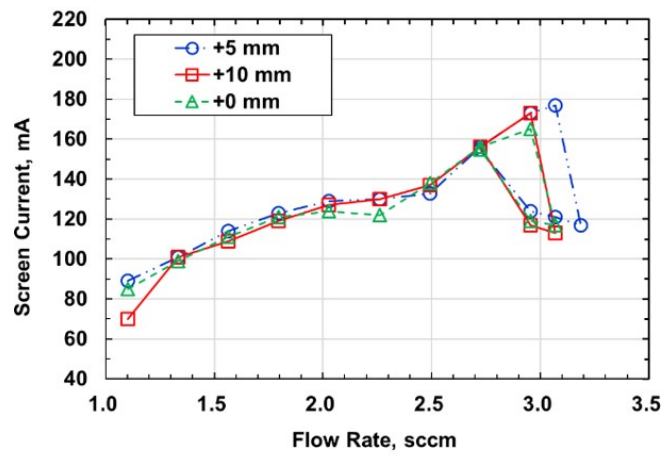


Fig. A.5 Screen current in case of ECR layer splitting.

### A.3.3 Discussion of magnetic field geometry and height of discharge chamber

The maximum beam current in each height of discharge chamber is summarized in Fig. A.6. Here, the results of ‘Hayabusa2’ and ‘Enhanced model 1’ are quoted from references [16, 117] respectively.

As described in subsection A.3.1, key parameter is considered to be  $V_{confined}$ . Noted that  $V_{confined}$  cannot be defined in case of the ECR layer splitting. However, as shown in Fig. A.5, the case is not undesirable. Thus,  $V_{confined}$  is calculated under ECR layer connecting. In this thesis,  $V_{confined}$  is calculated by Monte Carlo Sampling method.

- (I) Calculate the magnetic field shape by FEMM [131], output of the vector potential field  $rA_\theta(r, z)$  in grid mesh  $(i, j)$ .
- (II) A sampling particle is randomly generated within a region of reference volume  $V_{ref}$  that can calculate the volume analytically. Then, from particle position  $(r_p, z_p)$ , detect the number of grid mesh where is the nearest  $(i, j)$ . Then,  $rA_\theta(r_p, z_p)$  is calculated by interpolation from four data  $rA_\theta(i, j)$ ,  $rA_\theta(i + 1, j + 1)$ ,  $rA_\theta(i, j + 1)$ , and  $rA_\theta(i + 1, j)$  such as particle-in-cell simulation.
- (III) Because the magnetic field line shows  $rA_\theta = \text{const}$ , when  $rA_{\theta, \min} \leq rA_\theta(r_p, z_p) \leq rA_{\theta, \max}$ , the particles are counted  $N_{confined} = N_{confined} + 1$ .
- (IV) Procedure of (I) and (II) is repeated by  $N_{sum}$  times. Then,  $V_{confined}$  is calculated from  $V_{confined} \approx N_{confined} / N_{sum} \times V_{ref}$ . Of course, the number of  $N_{sum}$  should be determined by particle convergence, i.e.,  $V_{confined}$  is not sensitive to  $N_{sum}$ .

Figure A.7 shows the relationship between the ion beam current and the height of discharge chamber. Here,  $V_{confined}$  is normalized by the volume of thruster  $V_{thruster}$ . As shown in Fig. A.7,  $V_{confined}$  increases corresponding to the height of discharge chamber in all cases. First, different type thrusters; ‘Hayabusa 2 model’, ‘Enhanced model 1’, and ‘Enhanced model 2’, are compared. It can be seen that  $V_{confined}$  of ‘Enhanced model 1’ is larger than that of ‘Hayabusa 2 model’, thus the thruster performance improvement of ‘Enhanced model 1’ can be explained by  $V_{confined}$ . In addition, the difference between ‘Enhanced model 1’ and ‘Hayabusa 2 model’ becomes larger in large  $H$ . Considering optimal  $H$  is + 5 mm in ‘Enhanced model 1’ and -5 mm in ‘Hayabusa 2 model’, the tendency of thruster is good agreement with that of  $V_{confined}$ .

‘Enhanced model 2’ is slightly inferior to ‘Enhanced model 1’ in term of  $V_{confined}$ . The thrust of ‘Enhanced model 1’ is slightly larger than that of ‘Enhanced model 2’ by  $2 \sim 5$  mA ( $1 \sim 2$  %). However, considering the experimental error has about 5 mA, these beam current should be almost the same, thus the difference of thrust performance cannot be explained by  $V_{confined}$ . Comparing between ‘Enhanced model 2’ in different magnet cases, the case of the largest thrust is ‘In: Sm, out: Sm’, the smallest case is ‘In: Nd, out: Nd’, which indicates that the difference can be explained by  $V_{confined}$  reasonably.

Thus, it can be concluded that  $V_{confined}$  is effective for the estimation of the thrust performance and very useful for the thruster design. Of course, this estimation remains some issues. First, this estimation does not determine the optimal height of discharge chamber. One hypothesis is that the trade-off between  $V_{confined}$  and ion extracted efficiency. As shown in Fig. A.7,  $V_{confined}$  increases according to the height. In contrast, the ion extracted efficiency should be decreased according to the height because the surface area of the grid decreases by that of side wall; however, this problem can be solved practically. First, the magnetic field is designed so that  $V_{confined}$  is maximized in any heights (e.g., Enhanced model 1), and then the height is optimized by experimental parametric study. Second, the distribution of  $V_{confined}$  is not considered. Full-kinetic simulation indicates that the more locally inside the magnetic confined area [18], which is also observed in 1 cm class microwave discharge ion thrusters [50]. In addition, the mechanism of electron wall loss in the mirror magnetic field is more complicated [53], and the effect related to mirror ratio is not considered. Last, ECR heating is strongly related to the gradient of magnetic field and the electric field of microwaves perpendicular to magnetic field [56]. For instance, H. Koizumi proposed design method of the antenna considering gradient of magnetic field and the electric field of microwaves perpendicular to magnetic field in 1 cm class microwave discharge ion thruster [137]. This method approximates that distribution of electric field of microwaves are constant between with and without plasma. This approximation is based on two assumptions; (1) ”the thruster diameter must be sufficiently smaller than the microwave wavelength. (2) ”the microwave electric field due to the plasma is negligible. This is effective for small 1cm-class microwave ion thrusters by 3D-full-kinetic simulation [50]. However, the assumption of (1) is not valid in case of the  $\mu 10$  thruster. In addition, near the optimal flow rate, electric field of microwaves significantly change, thus the validity of (2) is more difficult [12].

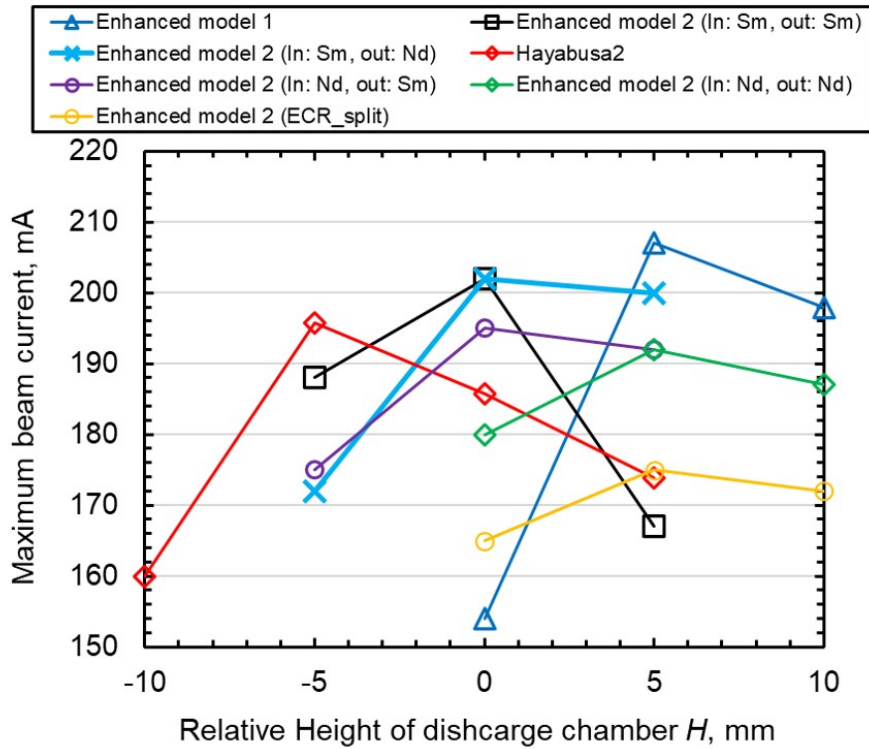


**Fig. A.6** The relationship between the height of discharge chamber and volume ratio of magnetic confined region. Here, the relative height of discharge chamber  $H = 0$  means the height of the Hayabusa 2 model. In: inner magnet, out: outer magnet.

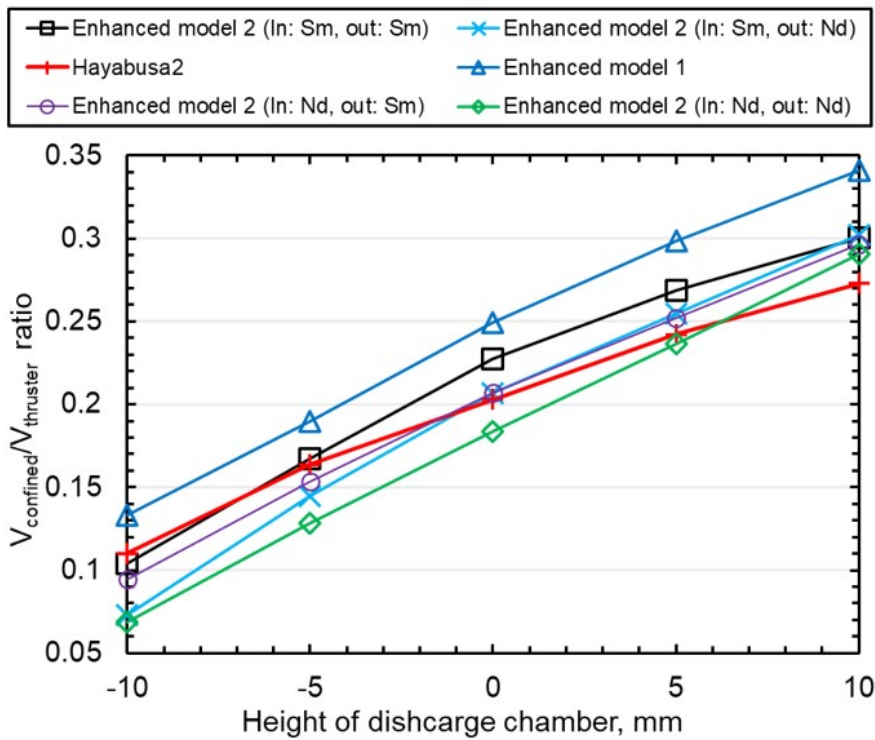


**Fig. A.7** The relationship between the height of discharge chamber and volume ratio of magnetic confined region. Here, the relative height of discharge chamber  $H = 0$  means the height of the Hayabusa 2 model. In: inner magnet, out: outer magnet.

#### A.4 Other possible improvements

Based on the physical mechanism of the plasma mode-transition, one solution of the thrust improvement is to enhance the cut-off density inside the waveguide. Reminded that the cut-off density in case infinite domain ( $\partial^2/\partial z^2 \rightarrow 0$ ) can be expressed as follows.

$$n_{p,cut} = \frac{m_e \varepsilon_0 (\omega_m^2 - \omega_w^2) \{ \nu_m^2 + (\omega_m - \omega_{ce})^2 \}}{e^2 \omega_m (\omega_m - \omega_{ce})}. \quad (\text{A.4})$$

Here,  $\omega_w = 1/(\varepsilon \mu_0) \times (\rho_{1,1}/R_w)^2$  is cut-off frequency due to waveguide. In collisionless case ( $\nu_m \approx 0$ ), the cut-off density can be simplified as follows.

$$n_{p,cut} \approx \frac{m_e \varepsilon_0 (\omega_m^2 - \omega_w^2)}{e^2} \left( 1 - \frac{\omega_{ce}}{\omega_m} \right). \quad (\text{A.5})$$

Thus, one solution to enhance the cut-off density is that magnetic field inside the waveguide is weak. Another solution is that the radius of the waveguide is expanded. Further assuming non-magnetized case, the cut-off density can be simplified as follows.

$$n_{p,cut} \approx \frac{m_e \varepsilon_0 (\omega_m^2 - \omega_w^2)}{e^2}. \quad (\text{A.6})$$

Current design is the radius of  $R_w = 22.5$  cm, and the cut-off density inside the waveguide is

$$n_{p,cut} \approx 0.15 n_{p,cut}^* \approx 3.4 \times 10^{16} \text{m}^{-3}. \quad (\text{A.7})$$

Here,  $n_{p,cut}^* = m_e \varepsilon_0 \omega_m^2 / e^2$ . For instance, the radius of inner magnet is 25 cm in 'Enhanced model 2', thus the radius of waveguide can be expanded to  $R_w = 25$  cm. In this situation, the cut-off density can be calculated,

$$n_{p,cut} \approx 0.32 n_{p,cut}^* \approx 7.0 \times 10^{16} \text{m}^{-3}. \quad (\text{A.8})$$

Thus, the cut-off density becomes two times, thus this expansion can be very effective for thrust improvement. Finally, to increase the microwave frequency. Actually, this trial was performed in  $\mu 20$  and it succeeded in increasing the thrust performance. For instance, if microwave frequency can be changed 5.8 GHz, the cut-off density can be calculated in case of  $R_w = 22.5$  cm;

$$n_{p,cut} \approx 2.25 \times 10^{17} \text{m}^{-3}. \quad (\text{A.9})$$

This cut-off density is approximately 7 times larger than that of 4.25 GHz. Thus, if the power supply with a frequency higher than 4.25 GHz can be available in space, the use of higher microwave frequency can be very effective.

#### A.4.1 Short conclusion

In this appendix, thruster performance in many kinds of thruster is discussed based on the physical mechanism of plasma mode-transition. As a results, following results and insights are obtained.

1. Parametric study of grid configuration was preformed. First, the thickness of the screen grid is very important for the maximum thrust performance; this result can be explained by the neutral density. The thicker the screen grid, the higher the ion extraction efficiency and optimal flow rate. The diameter of the accelerator grid affects the propellant utilization efficiency, while does not very sensitive to the maximum ion beam current; this result can be also explained by the neutral density. Difference of diameter, i.e., conductance, cancel outs the difference of optimal flow rate and propellant utilization efficiency.
2. Parametric study of magnetic field and height of discharge chamber was preformed. As a result, both magnetic field geometry and strength affects the maximum thrust performance. Then, optimal height of discharge chamber also depends on the magnetic field geometry and strength. The case of ECR layer splitting is not desirable. The volume of the magnetic confined region can explain the difference of the thrust performance partly and it is very useful for thruster design. However, it remains the some unclear parts; non-uniformity of plasma parameter and optimal height of discharge chamber.
3. Other possible thrust improvement was discussed. One solution is to enhance the cut-off density inside the waveguide. To enhance the cut-off density under the same microwave frequency, the expand of the radius of the waveguide can be effective. Additionally, if the power supply with higher microwave frequency can be available, use of higher microwave frequency can be effective for the thrust performance improvement.

## Appendix B

# Plasma hysteresis caused by high-voltage breakdown

### B.1 Objective

In gridded ion thrusters, high-voltage breakdowns between screen and accelerator grids are often observed. For example, in DAWN mission, the breakdown was observed 65 times during 16,000 h [138]. In Hayabusa and Hayabusa2 missions, the breakdowns were observed 1,000 ~ 2,000 times during 12,000 h and 500 ~ 2,500 times during 6,000 h respectively [7].

High voltage breakdowns can be cause of damage against the power supply and the grid. To avoid the potential damage, some ion thrusters perform the specific operation; for example, in DC discharge ion thrusters, a recovery method was employed when high-voltage breakdown occurs, which is called recycle [138, 76]. During recycling, the discharge current is first decreased and then gradually increased to the nominal level. The purpose of this sequence is to avoid an excessive ion beam current to the accelerator grid (i.e., one that would exceed the power supply capability) and to reduce ion sputtering on the accelerator grid. In contrast, in Hayabusa and Hayabusa2 missions, the breakdowns were not a critical problem [7] for the power supply and the grid. Therefore, when a high-voltage breakdown occurs, the thrust can be recovered by simply reapplying the high-voltage. However, the thrust enhanced type ('Enhanced model 1' and 'Enhanced model 2') exhibit the plasma hysteresis caused by high-voltage breakdowns. Specifically, these thrusters have two modes of the ion beam current (thrust), namely high- and low-current modes at the same flow rate. In nominal operation, the ion beam operates in high-current mode. Once a high-voltage breakdown occurs, the ion beam current transitions to and remains in low-current mode (described in detail later Fig. B.1). Even if the high voltage between the screen and accelerator grids is reapplied, the ion beam current

remains low-current mode. Low-current mode is unsuitable for space operation because of its low specific impulse and thrust. Thus, it is necessary to recover from the low-current model to the high-current mode.

The plasma hysteresis means the irreversible plasma-mode transition on input parameters such as propellant flow rate and microwave power. Thus, in this appendix, based on the physical mechanism of plasma mode-transition described in main content, the characteristic of plasma hysteresis is described.

## B.2 Plasma hysteresis of the microwave discharge ion thruster

Fig. B.1 shows the ion beam current versus propellant flow rate with and without hysteresis in the microwave discharge ion thruster. This figure is typical beam current under space operation; the ion beam current is adjusted by changing the flow rate while maintaining the input microwave power at 34 W. In Fig. B.1, the arrows show the directions along which the flow rate can be changed. Fig. B.1 (a) shows the case without hysteresis. The flow rate can be changed in any direction. Even if a high-voltage breakdown occurs, the ion beam current is maintained. Fig. B.1(b) shows the case with hysteresis. Referring to Fig. B.1(b), the state of the ion beam current can be divided into three regions, namely high-current mode without hysteresis (region A), high-current mode with hysteresis (region B), and low-current mode with hysteresis (region C). In region B, the current transitions to region C and cannot return to region B after a high-voltage breakdown occurs. To transition from region C to region B (high-current mode), it is necessary to reduce the flow rate to the boundary between regions A and B.

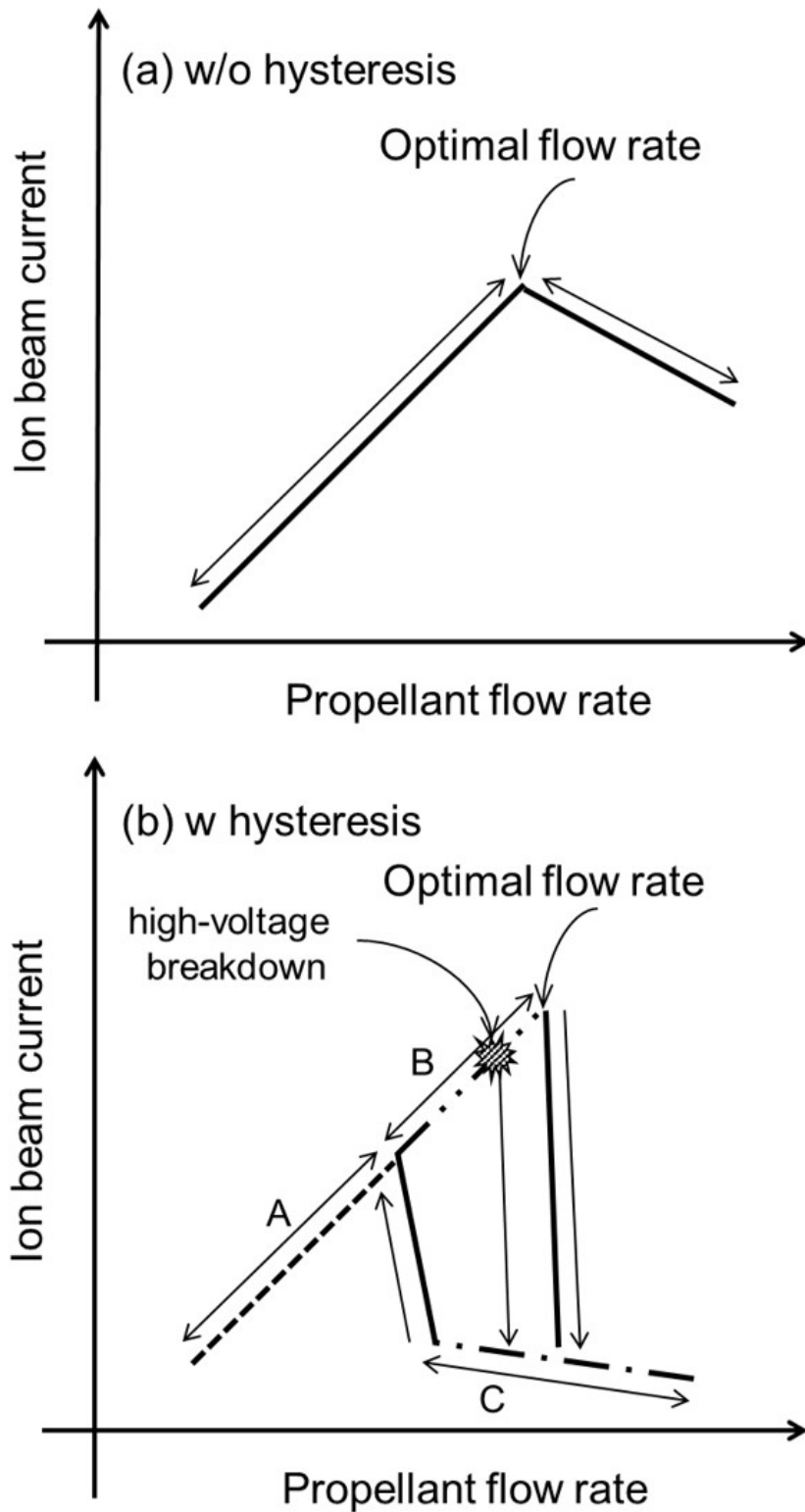


**Fig. B.1** Schematic diagrams of ion beam current versus propellant flow rate (a) without and (b) with hysteresis. The arrows show the directions along which the propellant flow rate can be changed

## B.3 Proposed recovery method

### B.3.1 Concept

Fig. B.2 shows a flow chart of the recovery method from the low-current mode to high-current mode. When a high-voltage breakdown occurs in region B (see Fig. B.1), the beam current transitions to and remains in low-current mode. To recover high-current mode, the author proposes a recovery method by temporarily stopping the propellant flow. If a high-voltage breakdown occurs, the propellant flow should be suspended by closing a valve in the mass flow controller. Then, the valve should be open and the high voltage reapplied. In our experiments, the time that the valve remains closed was experimentally determined to be several seconds. Because this operation only closes the valve and opens it after a few seconds, it is easy to automate for ground test. After the optimal flow rate is exceeded, the beam current transitions to low-current mode.

### B.3.2 Demonstration

The recovery method by temporarily stopping the propellant flow was demonstrated. As a results, it was founded that the recovery operation was successful even though the gas stop time is varied from 2 to 30 s. The appropriate stop time range is not very sensitive to the length of the propellant pipe from the mass flow controller to the thruster. If the stop time is too short, the neutral density will not be small enough for a transition from low- to high-current mode. If it is too long, the plasma will disappear after the high voltage is reapplied because the propellant will be too low. Based on above results, this method is effective for the thruster and it can automate this operation for ground test.

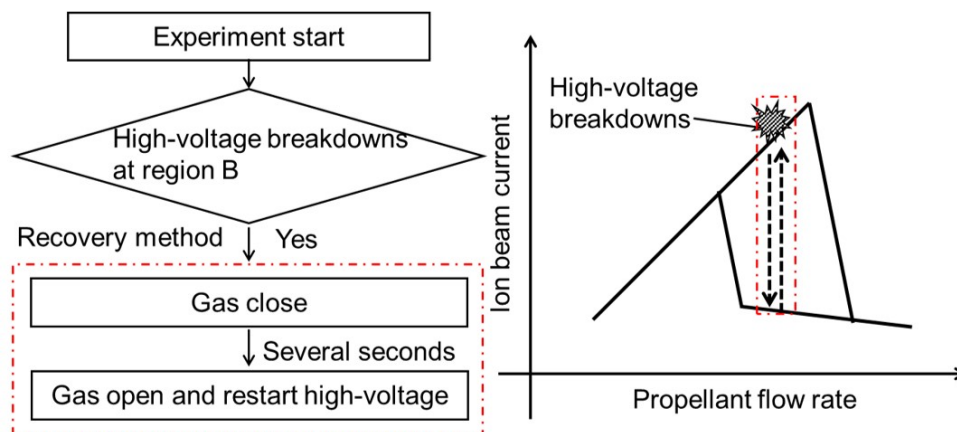


**Fig. B.2** Flow chart of recovery method.

## B.4 Characteristics of plasma hysteresis

### B.4.1 Grid parameter

Figure. A.1 shows the plasma hysteresis strongly depends on the screen and accelerator grid configurations. Table B.1 shows the difference of the neutral density between high- and low-current modes  $\Delta n_n$  in each grid configuration. Both neutral densities in high- and low-current modes are calculated from the ion beam current at the reference propellant flow rate. In the case  $\Delta n_n$  is large, the hysteresis-region is also large. The results indicate that the increase of neutral density by grid expands the hysteresis-region.

As described in chapter 2 and 3, the neutral density is very important for the plasma mode-transition. In the case of gridded ion thrusters, because the neutral density is passively determined by the beam current as shown in Eq. (2.28), the mode transition can lead to hysteresis. Specifically, in case the difference of the neutral density is large, the difference of plasma state is also large, result in expanding the hysteresis-region.

Usually, an accelerator grid is designed based on a trade-off between propellant utilization efficiency and accelerator loss current. For predicting accelerator loss current, ion optics have been simulated considering the plasma parameters (e.g., current density and electron temperature) of the discharge chamber [22]. In addition, a quasi-coupled simulation of the discharge chamber and grid optics has recently been developed for a 1-cm class microwave ion thruster [139]. However, these simulations do not include the effects of the discharge chamber and grid parameters on the neutral density. Thus, it can be concluded that the hysteresis cannot be captured by present numerical simulations and that experimental evaluation is necessary.

**Table B.1** Relationship between the hysteresis region and the neutral density. Grid parameters are summarized in Tab. A.1. The densities were estimated using Eq. (2.28).  $n_{n,h}$  and  $n_{n,l}$  show the neutral densities in case of high-current and low-current mode respectively. The densities are calculated from the ion beam current at the reference propellant flow rate.  $\Delta n_n = n_{n,l} - n_{n,h}$  shows the difference of the neutral density between high- and low-current modes.

Case	Reference, sccm	Hysteresis, sccm	$n_{n,h}, 10^{19} \text{ m}^{-3}$	$n_{n,l}, 10^{19} \text{ m}^{-3}$	$\Delta n_n, 10^{19} \text{ m}^{-3}$
Sc-1 and Ac-1	3.1	2.5-3.1	$0.69 \pm 0.06$	$2.44 \pm 0.03$	$1.75 \pm 0.09$
Sc-1 and Ac-2	3.3	3.2-3.3	$0.71 \pm 0.04$	$1.19 \pm 0.03$	$0.48 \pm 0.07$
Sc-2 and Ac-1	3.0	2.8-3.0	$1.02 \pm 0.05$	$1.64 \pm 0.04$	$0.62 \pm 0.04$
Sc-2 and Ac-2	-	-	-	-	-

## B.4.2 Plasma conditions inside waveguide

Figure 2.40 shows that the plasma hysteresis was eliminated in case of 'w/o WG ECR' and 'w/o WG plasma'. As described in subsection B.4.1, the plasma mode-transition can lead to the plasma hysteresis because the neutral density is passively determined from the beam current. Thus, the suppression of the plasma mode-transition, i.e., to decrease the difference of the beam current between before and after the optimal flow rate, which result in reducing the hysteresis-region. Thus, the case of 'w/o WG ECR' and 'w/o WG plasma' can eliminate the plasma hysteresis.

### B.4.2.1 Difference between regions A, B, and C

Photograph of region A, B, and C corresponds to the that at low flow rate, optimal flow rate, and after optima flow rate reptically in Fig. 2.49. According to the red luminescence inside the waveguide, the plasma is rarely generated at region A. In region B, the red luminescence starts to be generated, which indicates plasma starts to be generated. In region C, the red luminescence is concentrated. Therefore, in region C, microwaves are not sufficiently transmitted to the discharge chamber due to the plasma inside the waveguide. Therefore, the reason why hysteresis does not exist in region A is that the plasma in the waveguide decreases as the flow rate decreases.

## B.4.3 Short conclusion

The enhanced ion thruster exhibits plasma hysteresis caused by a high-voltage breakdown. Once a high-voltage breakdown occurs, the ion beam transitions to and remains in low-current mode, which significantly decreases the thrust efficiency. Therefore, for next space mission DESTINY<sup>+</sup>, it is necessary to establish a recovery method from the low-current to high-current mode. In this appendix, the author proposes temporarily stops method. Then, the physical mechanism of the plasma hysteresis was discussed based on that of the plasma mode-transition.

1. Temporarily stopping the propellant flow is an effective method for recovery from low- to high-current mode for this thruster. This method is successful even though the stop time is varied from 2 to 30 s; this time range is not very sensitive to the length of the propellant pipe.
2. The hysteresis strongly depends on the grid parameters. If the propellant utilization ef-

efficiency is high, the difference in neutral density between high- and low-current modes results in mode transition (hysteresis). This tendency of mode transition is consistent with other ECR sources. However, for gridded ion thrusters, mode transition can become large and leads to hysteresis because the neutral density is passively determined by the ion beam current. The sensitivity of grid configuration against the hysteresis cannot be captured by present numerical simulations and experimental evaluation is necessary. Thus, the suppression of the plasma mode-transition can eliminate the hysteresis. Actually, in case of 'w/o WG ECR' and 'w/o WG plasma', it was not observed.

3. Low-current mode is sustained because the plasma inside the waveguide is maintained, which indicates that the microwaves are not transmitted sufficiently to the discharge chamber. In addition, the plasma generation inside the waveguide becomes small at a low propellant flow rate, resulting in the lack of observed low-current mode.

# Appendix C

## Development of full kinetic particles in cell simulation

### C.1 Outline

As described in chapter 2, to understand the plasma mode-transition, the experimental approach measuring ground-state neutral density and spontaneous emission intensity were measured. Additionally, in chapter 3, to further understand the mode-transition, numerical approach were performed. These approaches succeed in revealing the physical mechanism of plasma mode-transition. However, the numerical approach do not solve the overall process; gas injection, plasma generation, and ion transport to grid. Because the thrusters have many kinds of design parameters, e.g., magnetic field, and grid optics, the numerical approach that can simulate the overall process is strongly desired to find the optimized design. Thus, in this appendix, to accomplish this objective in the future, in this appendix, the numerical simulation model has been developed.

Generally, method of plasma simulation can be divided into two approach physically; fluid and kinetic model. Although the fluid model can be calculated faster than the particle model [102], the velocity distribution function (VDF) need to be assumed. In addition, in magnetized case, to capture the phenomena related to magnetic field (e.g., mirror magnetic confinement) [140], fluid model suffers from closure problem (modeling heat flux) [141, 142] and increase the number of governing equation (e.g., ten-moment approach [143]). In contrast, kinetic approach requires larger simulation cost than fluid model, whereas this algorithm is simple, and can capture VDF consistently. Kinetic approach can be divided into two method numerically; grid-based approach, and particle approach. Grid-based approach is to solve the Boltzmann equation directly by discretizing both spatial and velocity domains [38]. In contrast, the par-

particle approach is to solve the trajectory of individual particles. In real system, because the number of particles are tremendously large, the macroscopic particles (superparticles) that represents many real particles are used, and then grid-based Maxwell equations are solved by coupling with particle charge and current at grid (stencil), which is call particle-in-cell (PIC). Though PIC approach has potential issue of the statistical noise due to superpartices [38], this simulation cost is smaller than that of Grid-based approach.

Because electron is lighter than ion, the simulation time step and grid size are restricted by electrons. Thus, to mitigate the restriction, ions are tread as kinetic model, whereas electrons are treated as fluid model, which is called hybrid-PIC [47, 118]. In contrast, the kinetic model that electrons and ions are treated as kinetic model is generally called full-PIC. In ECR plasma sources, to treat electrons as kinetic model is desired following three reasons. Firstly, electrons are heated by ECR and this is kinetic heating. Secondly, some paper reports non-Maxwellian electrons are observed [50, 73]. In this appendix, following two kinds of full-kinetic simulations are developed.

#### I. Explicit electrostatic (ES) full-PIC simulation

#### II. Semi-implicit electromagnetic (EM) full-PIC simulation

Apart from the clarification between fluid and kinetic models, plasma simulation model are generally divided into electrostatic and electromagnetic models. In electrostatic PIC algorithm, electric field is assumed to be electrostatic. The simulation of ES full-PIC simulation is easier than that of EM-PIC simulation in view of simulation cost and numerical stability. Thus, firstly, explicit electrostatic (ES) full-PIC simulation is applied to the thruster and the microwaves is treated as external electric field. The ES-full-PIC simulation can provide the fundamental characteristic of ECR plasma source from small scale phenomena (e.g., ECR heating and electron confined) and large scale (e.g., ion transport to grid).

On the other hand, as described in chapter 2 and 3, because plasma mode-transition is occurred by the cut-off phenomenon, electromagnetic treatment is inevitable effect for reproducing the mode-transition. However, EM full-PIC simulation is still challenging in view of numerical stability and simulation cost. To mitigate numerical restriction of grid size and time step and to enhance numerical stability, implicit-PIC (fully-implicit and semi-implicit) has been developed mainly in filed of computer physics [144, 145, 21, 146, 147]. For explicit PIC sim-

ulation, the algorithm is very simple and thus can be applied to many applications, but the grid size is strictly limited to the Debye length [148] and the time step is limited to the Courant-Friedrichs-Lewy (CFL) condition [148]. If these conditions are not satisfied, the simulation will diverge because the plasma becomes numerically heated (e.g., finite grid instability) [149, 150]. In simulations of a plasma source, to obtain the steady state, the simulation continues until the ionization rate equals the wall loss rate. In this case, if non-negligible numerical heating occurs, the electrons are numerically heated. Then, the excessive electron energy induces the plasma density and the Debye length condition is violated. In such a condition, the numerical heating is further enhanced. Therefore, once numerical heating occurs, the simulation slowly diverges. Implicit treatment can meet the conservation law, e.g., energy-conservation, numerical stability is enhanced.

Though there are many kinds of implicit simulation models, the author focuses on a recently developed algorithm, namely the energy-conserving semi-implicit method (ECSIM) suggested by Lapenta [145]. This numerical model has a simple algorithm, low simulation cost, and a linear solution, making it suitable for many types of plasma simulation. The original algorithm does not satisfy Gauss's law. To satisfy Gauss's law, Chen proposed a Gauss's law satisfying ECSIM (GL-ECSIM) [151] and Pagès proposed charge-conserving ECSIM (Ch-ECSIM) [152]. In addition, ECSIM can be applied in cylindrical coordinates [153]. In the field of electric propulsion, a plasma source is used as an ion source and the cathode is a gridded ion thruster, a Hall effect thruster, or a hollow cathode. In simulations, to obtain the steady state,  $10^6$  to  $10^9$  time steps are required [50, 38], and thus a highly efficient numerical solver with long-term accuracy is required. In addition, the boundary conditions and geometry of a plasma source are relatively complicated, and thus a highly robust simulation model is necessary. Therefore, semi-implicit PIC simulation model is suitable for electron propulsion due to the high robustness and the low simulation cost. For example, Cho applied a semi-implicit electrostatic PIC simulation to a Hall thruster and obtained novel results [154, 155]. However, semi-implicit electromagnetic PIC simulation has not been established yet. Here, we establish a semi-implicit electromagnetic PIC simulation by using ECSIM.

In this appendix, to extend ECSIM to many practical problems, one approximation method that reduce simulation cost is proposed. In electric propulsion, the plasma is low-temperature plasma, and thus the thermal velocity ( $v_{th}$ ) is much smaller than the speed of light ( $c$ ); typ-

ically,  $v_{th}/c \cong 0.001 - 0.01$ . Even if  $c\Delta t > 1$  is used in an implicit PIC simulation, the accuracy at high frequency decreases if a very large simulation time step is used. In addition, in a conventional sub-cycle method, particles are updated every several time steps of the field solver, which may be dangerous because several papers reported that this increases numerical instability [156, 157]. Additionally, when a sub-cycle method is used, ECSIM algorithm does not meet because the current density is implicitly determined to satisfy energy conservation. To overcome this problem, we propose a sub-cycle method that maintains ECSIM and is suitable for highly efficient parallel computing. Secondly, the highly accurate update of velocity for gyro motion proposed by Zenitani [158] is implemented in the ECSIM algorithm. In EP devices, plasma is strongly magnetized and thus the accuracy of gyro motion is very important.

Additionally, implicit PIC algorithm is more complicated than explicit one. To establish high reliable code, benchmark problem is necessary. Thus, this paper demonstrated code-verification by using Weibel instability. However, in practical problems such as EP devices, to select benchmark problem is generally very difficult. the authors tries to use code-verification by using conservation-law (e.g., charge, momentum, and energy). This verification is very useful for practical problem because any problems can meet conservation-law within good simulation condition (e.g., grid size and time step). Finally, recently, the PIC simulations try to reproduces time-resolved phenomena, e.g, instability. To reproduce the time-resolved phenomena, simulation condition of time-step and grid-size are very important. Thus, in this thesis, to estimate the effect of numerical schemes, and sensitivity to the time step and grid size, are evaluated using numerical dispersion relation.

## C.2 Super Computer facility

In this thesis, the following two supercomputers were used for the calculation in this research.

1. Kyoto University Super Computer System.
2. JAXA JSS2.

## C.3 Explicit ES-full-PIC simulation

### C.3.1 Numerical model

#### C.3.1.1 Particle mover

Generally, the motion of charged particle is given by

$$m \frac{d\vec{v}}{dt} = e(\vec{E} + \vec{v} \times \vec{B}_s). \quad (\text{C.1})$$

where,  $m$  is the mass of charged particles,  $e$  is elementary charge,  $\vec{v}$  is individual velocity,  $\vec{E}$  is electric field, and  $\vec{B}$  is magnetic field. In case of electrons, electric field is assumed:  $\vec{E} = \vec{E}_{ex} + \vec{E}_s$ , where  $\vec{E}_{ex}$  is external field due to microwave and  $\vec{E}_s$  is the electrostatic field generated by charged density.  $\vec{E}_{ex}$  oscillates by frequency of  $\omega_m$ . The detailed treatment will be written in this section. In contrast, in case of ions, electric field is assumed:  $\vec{E} = \vec{E}_s$  because the ion plasma frequency is much larger than the microwave frequency. Then, magnetic field is assumed to be static field generated by permanent magnets because this amplitude is much larger than that of varying magnetic field generated by microwaves. Ions are removed when they collide with the wall, while electrons are reflected with the possibility of the open area fraction of the screen grid for a potential between the screen grid and the acceleration grid of 1500 V. Thus, in this study, electrons that reach grid are reflected with the probability of  $\eta_{trans} \approx 0.7$ .

To advance individual velocity and position, Boris and leap-frog method were used [148].

### C.3.1.2 Collision model

In this simulation, we consider three kinds of collisions with neutral particles,

1. Elastic:  $\text{Xe} + e^- \rightarrow \text{Xe} + e^-$
2. Excitation:  $\text{Xe} + e^- \rightarrow \text{Xe}^* + e^-$
3. Ionization:  $\text{Xe} + e^- \rightarrow \text{Xe}^+ + 2e^-$

The excitation energy loss and ionization loss are assumed to be  $E_{ex} = 8.3$  eV and  $E_i = 12.1$  eV repulsively. In this study, the neutral number density is assumed to be  $1 \times 10^{19} \text{m}^{-3}$  and is uniform in the discharge chamber. These collisions are calculated by the MCC method using the cross section [22]. To reduce the simulation time, the null collision method was employed [107].

### C.3.2 Electrostatic field

The electrostatic field  $\vec{E}_s$  is calculated by solving the cylindrical Poisson equation:

$$\left( \frac{\partial^2}{\partial r^2} + \frac{1}{r} \frac{\partial}{\partial r} + \frac{\partial^2}{\partial z^2} \right) \phi = -\frac{\rho(r, z)}{\epsilon_0} \quad (\text{C.2})$$

$$\vec{E}_s = -\vec{\nabla}\phi \quad (\text{C.3})$$

Here  $\phi$  is the electrostatic potential,  $\rho(r, z)$  is the charge density as function of  $r$  and  $z$ ,  $\epsilon_0$  is the vacuum permittivity. The charge density is calculated from the interpolation of individual ions and electrons charge. In this simulation the change of the plasma potential in the azimuthal direction to reduce the simulation time. Therefore, the charge density is distributed in a cylindrical stencil, i.e.,  $(r, z)$ . It should be noted that reference [159, 160] show that the three-dimensional numerical analysis of the 1-cm class microwave discharge ion thruster and neutralizer has time oscillation of the electrostatic field in the azimuthal direction. Therefore, the simulation can be valid only for the time averaged values of plasma parameters. Eq. (C.2) is solved by the Successive Over-Relaxation (SOR) method. The potential of the wall is  $\phi = 0$  V and the central axis applies the Neumann condition ( $\partial\phi/\partial r=0$ ). The mesh size is 0.2 mm, which satisfies the simulation condition [148].

### C.3.2.1 Electromagnetic field of microwaves

Generally, Faraday's law and Ampere's circuital law are given by

$$\vec{\nabla} \times \vec{B}_m = -\mu_0\epsilon_r\epsilon_0 \frac{\partial \vec{E}_m}{\partial t} + \vec{J} \quad (\text{C.4})$$

$$\vec{\nabla} \times \vec{E}_m = \frac{\partial \vec{B}_m}{\partial t} \quad (\text{C.5})$$

Here  $\vec{J}_p$  is the plasma current and  $\vec{B}_m$  is the magnetic field of the microwaves. By taking the inner product with  $\vec{E}_m$  in Eq. (C.4) and with  $\vec{B}_m$  in Eq. (C.5), the following equation is obtained in the form of the integral.

$$\int \vec{\nabla} \cdot \vec{S} dV = \frac{\partial}{\partial t} \int_V \left( \frac{1}{2}\epsilon_0 |\vec{E}_m|^2 + \frac{1}{2}\mu_0 |\vec{B}_m|^2 \right) + \int_V \vec{J} \cdot \vec{E}_m dV \quad (\text{C.6})$$

Here,  $V$  is the volume of the discharge chamber and waveguide, and  $S = \vec{E} \times \vec{B} / \mu_0$  is Poynting vector. In Eq. (C.6), the first term physically means the energy transition of electromagnetic field of microwaves, and the second term means the absorbed microwave power of plasma  $P_{abs}$ . Comparing without and with plasma, it is considered that  $\vec{E}_m$  is changed corresponding to plasma current  $\vec{J}_p$  at the same input microwave power. In past experiment, it was confirmed that  $\vec{E}_m$  is changed corresponding to the plasma state in 20-cm class microwave discharge ion

thruster [161]. In our codes, the initial condition of electromagnetic field of microwaves  $\vec{E}_m^0$  without plasma by Finite-difference time-domain (FDTD) method. After FDTD simulation,  $P_{abs}$  is calculated by PIC-MCC simulation. Because  $P_{abs}$  is equal to the time change of the energy in the charged particles,  $P_{abs}$  is given by

$$P_{abs} = \frac{\partial}{\partial t} \left( \sum_{k=1}^{N_i} \frac{1}{2} m_i v_{i,k}^2 + \sum_{k=1}^{N_e} \frac{1}{2} m_e v_{e,k}^2 \right) \quad (\text{C.7})$$

Here  $W$  is the weight of a super particle. Although the ions are not affected by the microwaves directly, they acquire power through the electrostatic field  $\vec{E}_s$ . Then,  $\vec{E}_m$  is adjusted so that  $P_{abs}$  matches the set absorbed power  $P_{set}$  which is an initial parameter. However,  $\vec{E}_m$  cannot be determined in advance since  $P_{abs}$  is calculated after  $\vec{E}_m$  is applied. Therefore,  $\vec{E}_m$  is determined by the feedback control. The amplitude of electromagnetic field  $E_{ex}$  is updated by

$$E_{ex}^{new} = E_{ex}^{old} \left\{ 1 + K_p \frac{(P_{set} - P_{abs})}{P_{set}} \right\} \quad (\text{C.8})$$

Here  $E_{ex}^{new}$  is the electromagnetic field of the new time step,  $E_{ex}^{old}$  is the electromagnetic field of the old time-step, and  $k$  is a constant term. In this study, input microwave power  $P_{set}$  to 12 W and  $k$  set to 0.1. The model indicates that the transition of the intensity of  $E_m$  by the plasma is considered, but the transition of phase of  $\vec{E}_m$  by the plasma is neglected to reduce the simulation time and to avoid numerical instability. However, under this treatment, the cut-off of microwave cannot be captured.

### C.3.3 Numerical procedure

A flow chart of the simulation is shown in Fig. C.1. Before simulating the PIC-MCC, the static magnetic field  $\vec{B}_s$  and the initial of the electromagnetic field  $\vec{E}_m^0$  are simulated by FEMM [131] and  $\vec{E}_m^0$  is simulated by the 3D-FDTD simulation [12].

In the PIC-MCC simulation, the limit of the time step is different for each calculation. Therefore, a sub-cycle time method was employed to reduce the calculation time. The time step of electron trajectory  $\Delta t_e$  is 1/40 of microwave cycle ( $\Delta t_e \approx 5.88 \times 10^{-12}$  s). Then, the time step of ion trajectory  $\Delta t_i$ , the time step of the collision  $\Delta t_c$ , and the time step of update the electromagnetic field  $\Delta t_m$  is the one microwave cycle ( $\Delta t_i = \Delta t_c = \Delta t_m \approx 2.35 \times 10^{-10}$ ) s. The iteration of PIC-MCC is continued until the change of the time-averaged values of the plasma density and electron temperature are less than 10 %. Typically, the simulation time is

two month.

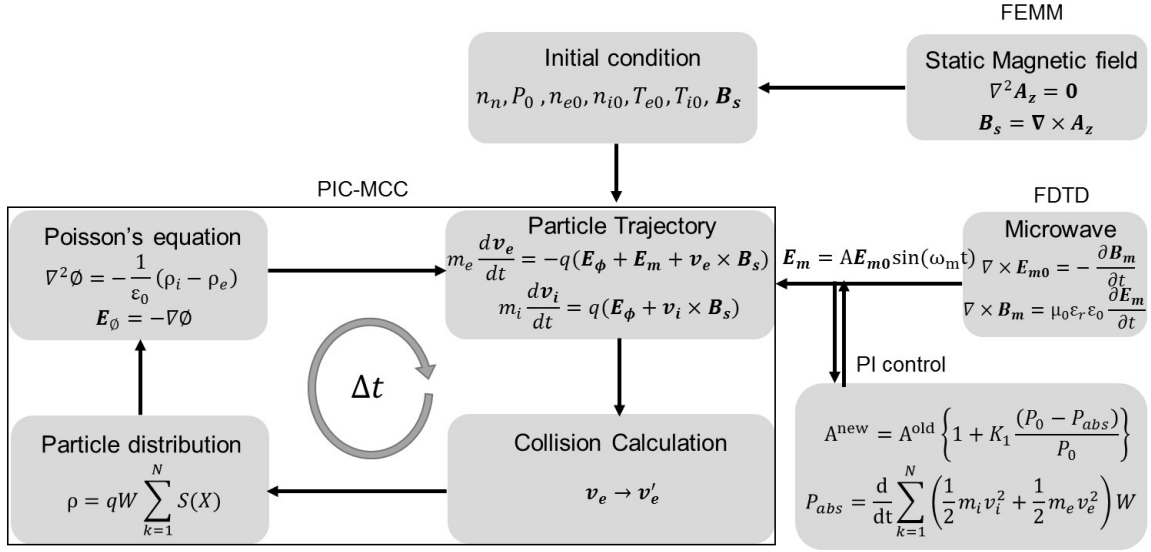


Fig. C.1 Schematics of microwave ion thruster  $\mu 10$  in physical view

### C.3.4 Macroscopic quantities

After the steady state, the macroscopic parameter, e.g, electron density and temperature are averaged during 5,000 microwave cycles. Figure C.2 shows the distribution of plasma parameter: electron temperature, electron density, ionization rate, and plasma potential. As illustrated in Fig. C.2, electron temperature  $T_e$  is around 5–15 eV and the highest along the ECR layer. High electron temperature is spread due to electron bounce motion. In contrast, the electron temperature outside the confined region is 3 – 5 eV, which is lower than that in the confined region. This is because the electron are not heated by ECR outside the magnetic confined region. In the electrostatic probe measurements, the highest electron temperature of 12 eV is measured near the ECR layer, and the electron temperature in the other regions is about 1 – 5 eV, which indicates that the electron temperature distribution of numerical simulation is good agreement in that of probe measurement [26]. The plasma density in magnetic confined region is approximately  $1.5 \times 10^{17} \text{ m}^{-3}$  at Maximum and then it is one order larger than that in other regions. The electrostatic probe measurements of the plasma density at the magnet indicate that the plasma density is  $3.3 \times 10^{16} \text{ m}^{-3}$  in the confined region, again about ten times larger than other regions. Based on the above results, it is found that the plasma density and electron temperature are qualitatively consistent with the electrostatic probe measurements.

Figure C.2 (c) shows the distribution of ionization rate  $g_{iz}$ . The result indicates that  $g_{iz}$  is

concentrated in the confined region and is at most  $1.57 \times 10^{22} \text{ m}^{-1}\text{s}^{-1}$ . In contrast, in the other region,  $g_{iz}$  is very small. Due to high electron density and temperature, ionization is also concentrated in magnetic confined region. From the probe measurement, it is found that the distribution of ion saturation current is mainly high in the confined region and consistent with the results of the ionization rate. It should be noted that the ionization distribution does not include the stepwise ionization from metastable state; thus the plasma density outside the magnetic confined region is underestimated. The ionization rate  $g_{iz}$  by using the experimental result of beam current  $I_b$  and extracted efficiency  $\eta_{ex}$ .  $I_b$  is  $40 \sim 60$  mA at the microwave power of 12 W, 26 and  $\eta_{ex} \approx 0.511$ . Because ionization current  $G_{iz}$  which is the volume integration of  $g_{iz}$  can be estimated;  $G_{iz} = I_b/\eta_{ex} \approx 80 \sim 120$  mA [34]. On the other hand, by volume integration of simulation result  $g_{iz}$ ,  $G_{iz}$  is computed 72.9 mA. Therefore, the ionization current of the simulation is lower than that of experiment by 10–50 mA. This difference is generated by the input parameter of neutral density, do not consider the stepwise ionization, and electromagnetic effect.

Figure C.2 (d) shows the distribution of plasma potential. The plasma potential is 10–20 eV in the confined region, with the highest value of 30 eV in the waveguide, which quantitatively agrees with electrostatic probe measurements [162]. The plasma potential is about 30 eV near the spacer, which is the cause of the difference of the mobility perpendicular to magnetic field between electrons and ions. If the plasma potential is non-uniform parallel to magnetic field line, the non-uniformity is deleted by moving electrons. On the other hand, in the direction perpendicular to magnetic field, electrons cannot be cross-field, thus the plasma potential becomes high [41]. Noted that this simulation does not consider the electrostatic field in azimuthal direction. The azimuthal electric fluctuation induces cross-field transport, thus the plasma potential may become small compared to this simulation.

### C.3.5 Electron-scale phenomena

To investigate the electron trajectory, the author performed test particles simulation obtained by PIC simulation results. There are three components in the electromagnetic field to consider, the static magnetic field  $\vec{B}_s$ , the electric field of the microwaves  $\vec{E}_m$ , and the electrostatic field  $\vec{E}_s$ . Thus, three cases; (a)  $\vec{B}_s$ , (b)  $\vec{E}_m + \vec{B}_s$ , and (c)  $\vec{E}_m + \vec{E}_s + \vec{B}_s$  were simulated. Noted that the collision with neutral particles are neglected. To compare the effect of the electromagnetic field, the initial velocities and positions of the electrons are the same for all three cases.

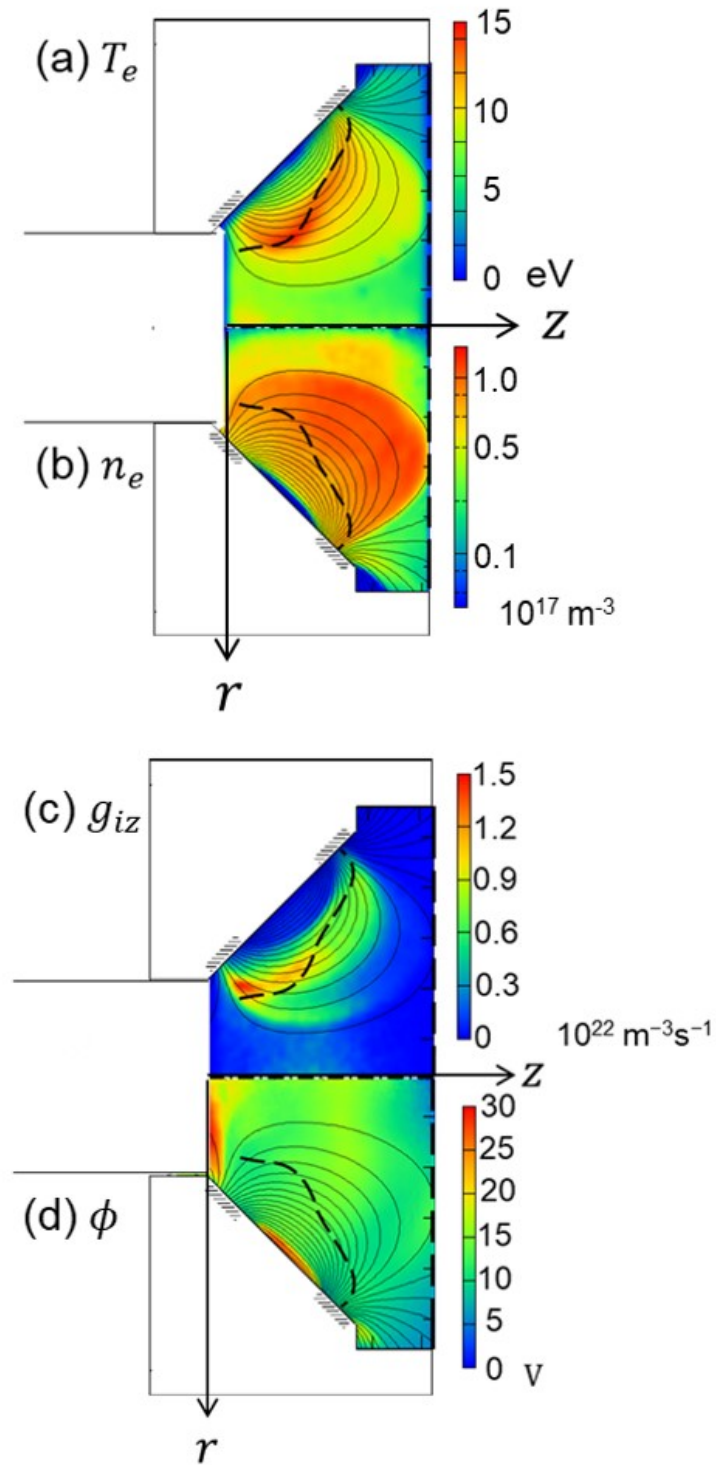


**Fig. C.2** Macroscopic quantities of the numerical simulation. (a) Electron temperature, (b) electron density, (c) ionization rate, and (d) plasma potential in the  $r$ - $z$  plane.

Figure C.3 shows the electron energy history in three cases. In case (a), of course the electron energy is conserved because of no electric field and then the electron is permanently confined by mirror magnetic field. In contrast, case (b) indicates that the electron energy is

changed by crossing the ECR layer, and the electrons are eventually lost at the inside magnet. By crossing the ECR layer, the electron velocities perpendicular to the magnetic field line are changed. As a result, when the electrons lose energy by crossing the ECR layer, the mirror ratio decreases, and the electrons may collide with the wall. Because ECR heating is an averaged heating, it is possible that electrons lose their energy by crossing the ECR layer. Last, case (c) shows the the electrons are reflected by the plasma sheath and the energy is changed by crossing the ECR layer. Because the plasma sheath has an energy of about 15 eV, electrons with energy less than 15 eV are confined by the plasma sheath. Therefore, low energy electrons are confined by the plasma sheath and mirror magnetic field. In contrast, high energy electrons are confined by only the mirror magnetic field. Thus, the loss mechanism of electrons at the wall in case (c) is that high-energy electron change direction of velocity by collision (or anomalous collision) and then the electrons the enter the loss-cone, which is described in reference [53].

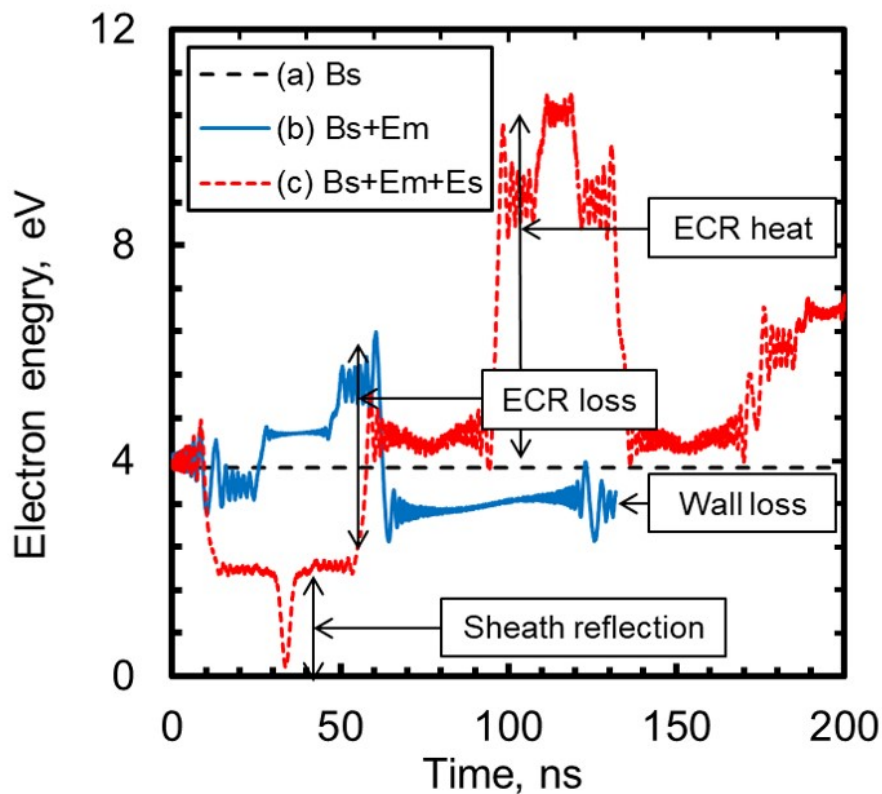


**Fig. C.3** Single electron motion using the plasma parameters from the simulation results to study the effects of electromagnetic fields. The figure shows the time function of the electron energy in three cases; (a)  $\vec{B}_s$ , (b)  $\vec{E}_m + \vec{B}_s$ , and (c)  $\vec{E}_m + \vec{E}_s + \vec{B}_s$

The trajectories of electrons indicate that the electron energy distribution function (EEDF) is not a Maxwellian distribution because the confinement of the electrons depends on the electron

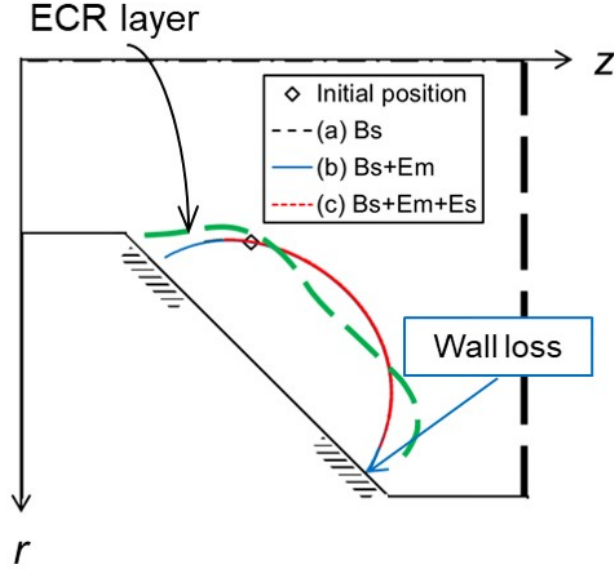


**Fig. C.4** Single electron motion using the plasma parameters from the simulation results to study the effects of electromagnetic fields. The figure shows each trajectory in three cases; (a)  $\vec{B}_s$ , (b)  $\vec{E}_m + \vec{B}_s$ , and (c)  $\vec{E}_m + \vec{E}_s + \vec{B}_s$ .

energy. Figure C.5 shows time-averaged normalized EEDF. Generally, EEDF can be expressed as follows.

$$F(\varepsilon) = 4\pi \left( \frac{m_e}{2\pi k T_e} \right)^{3/2} n_e \sqrt{2\varepsilon} \exp \left( -\frac{\varepsilon}{k T_e} \right) \quad (\text{C.9})$$

Thus, by plotting the  $F(\varepsilon)$ , the EEDF is a linear function on a log scale. However, the EEDF is a combination of two linear functions. Therefore, the EEDF is the combination of two Maxwell distributions. By fitting the EEDF in Fig. C.5, a hot electron temperature  $T_{eh}$  of 15.1 eV, a cold electron temperature  $T_{ec}$  of 3.61 eV, and a ratio of hot and cold electrons is  $N_{eh}/N_{ec} = 3.4\%$  are computed. The combination of two temperature distributions has been experimentally confirmed for other ECR plasma sources [73], and this distribution is considered to be one of the important features of ECR plasmas. Based on the result of electron trajectories, if electron energy is at least lower than the sheath potential, the electrons are confined by the sheath. On the other hand, if the energy of the electron exceeds the sheath potential, the electron is confined only by the mirror magnetic field. Therefore, the cause of two Maxwellian distributions is thought to be that the confinement method is divided into two methods depending on whether electron energy exceeds the sheath potential.

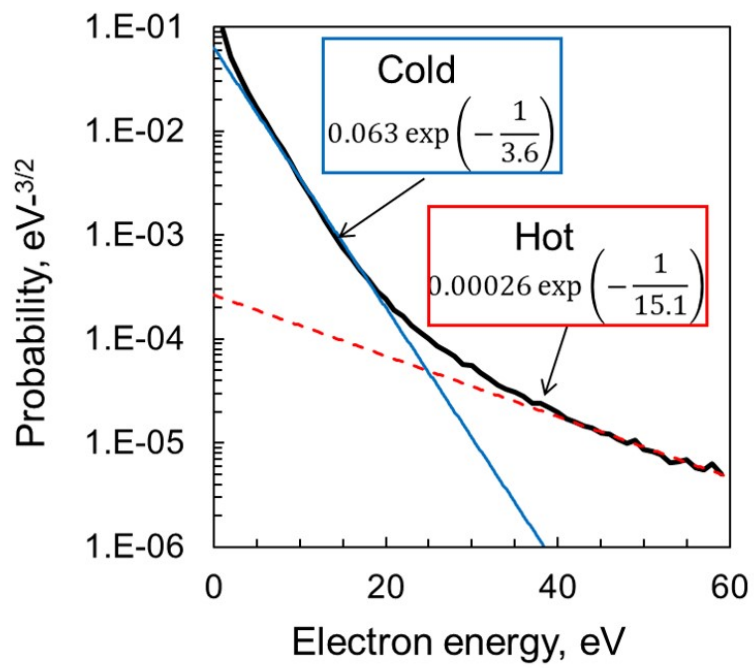


**Fig. C.5** Time averaged electron energy distribution function of the discharge chamber.

### C.3.6 Ion-scale phenomena

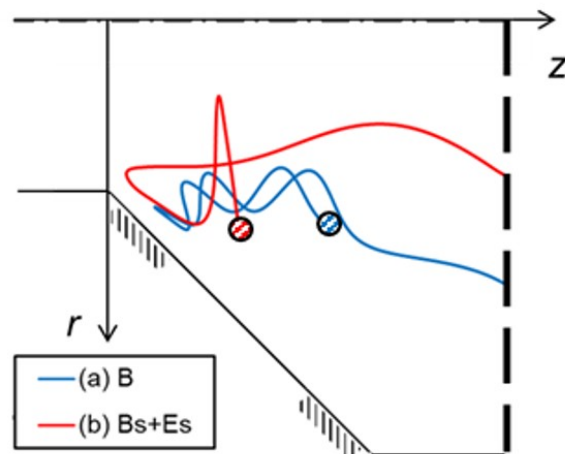
As well as electron test particle simulation, test ion simulation is also performed. In case of ions, there are two components to the electromagnetic field, the static field  $\vec{B}_s$  and  $\vec{E}_s$ . Thus, two simulation cases; (a)  $\vec{B}_s$ , (b)  $\vec{E}_s + \vec{B}_s$  were simulated.

Figure C.6 shows the trajectory of ions. From Fig. C.6(a) and (b), it can be seen that ions are reflected by the magnetic field and reach the grid, demonstrating that ions are affected by the magnetic field even if  $E_s$  is considered. Additionally, macroscopic azimuthal ion velocity of two cases are shown in Fig. C.7. Here, initial position is the distribution of ionization (Fig. C.2). The results indicate that the azimuthal ion drift exists due to gradB, curvature drift, and  $E \times B$  drift, which indicates that the ions are weakly magnetized. The azimuthal ion velocity is main cause of the roll torque derived from one thruster and is agreement in LIF measurement [163].

Secondly, the current percentage at each wall is shown in Fig. C.8. Here, “Electron (simulation)” and “Ion (simulation)” show the numerical results of the current percentage of ions and electrons. “Ion (Experiment)” is the experimental results of ion current percentage in the WG injection (Hayabusa) and DC injection (Hayabusa2) measured using the electrostatic probe under optimal flow rate. The “surface area” represents the percentage of the surface area. The results indicate that the current percentage is different between ions and electrons, which shows the difference of mobility between electrons and ions. Focusing on the ion extracted efficiency, 61 % of ions are transported to the grid from the ionization area. Experimental data shows the efficiency of 56 %, which indicates that the numerical results are good agreement in experimental result [16]. The surfaces where the current percentage of ions is larger than that of electrons are the grid, the spacer, and the sidewall. On these surfaces, there is a component of the magnetic field parallel to the surface. The current percentage of electrons is larger than that of ions in the magnets, which maintains the quasi-neutrality of the plasma. Therefore, the mobility with respect to the magnetic field produces difference of current percentage between ion and electron.

Comparing the ion current and the surface area percentage, it is found that the ion current percentage in the grid is larger than the surface area percentage. This is the proof that the ions are efficiently transported to the grid by the magnetic field. The effect of the magnetic field can be divided into the effects of the mirror magnetic field and the diffusion perpendicular to

the magnetic field line. In the inside magnet, the effect of the mirror magnetic field is clear because ions are reflected at the upper magnet, as shown in Fig.C.6. The result of experiment is also qualitatively consistent with these results. Based on the above, to improve the ion transport efficiency, the Larmor radius of ions  $r_{L,i}$  should be less than the radius of the thruster  $L$ . The criterion is considered to be effective for a magnetic field which achieves both plasma generation and transport, such as the microwave discharge ion thruster. In the thruster,  $r_{L,i}$  is of the order of  $0.1 \sim 1$  cm and  $L$  is 5 cm. Hence,  $r_{L,i}/L \approx 0.02 \sim 0.2$ , satisfies the criterion. On the other hand, very small thrusters are difficult to meet the criterion, and their ion losses are expected to increase. In a 1 cm class microwave discharge ion thruster, it is stated that the loss is reduced by making the magnetic field strong at the sidewall [50].



**Fig. C.6** Single ion motion using the plasma parameters from the simulation results to study the effects of electromagnetic fields. The figure shows each trajectory in two cases; (a)  $\vec{B}_s$ , (b)  $\vec{E}_s + \vec{B}_s$ .

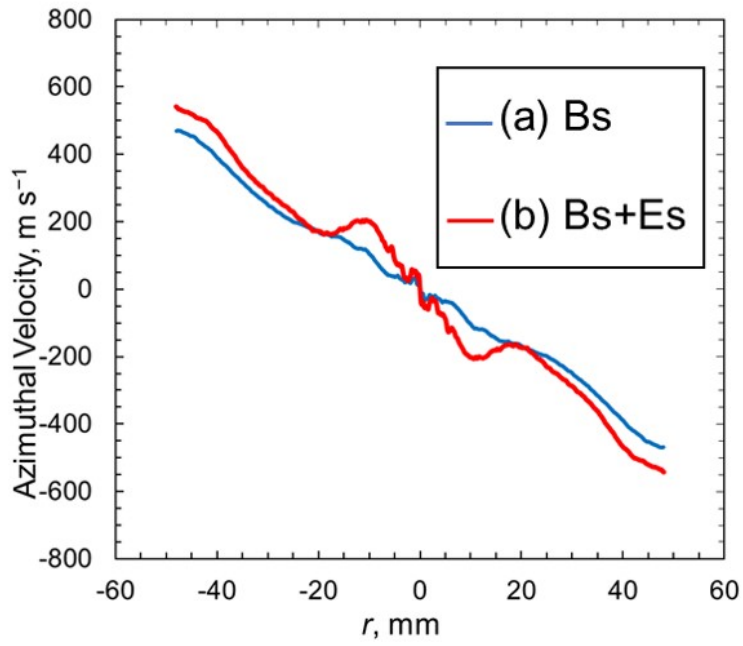


**Fig. C.7** Macroscopic azimuthal ion velocity distribution in two cases; (a)  $\vec{B}_s$ , (b)  $\vec{E}_s + \vec{B}_s$ .

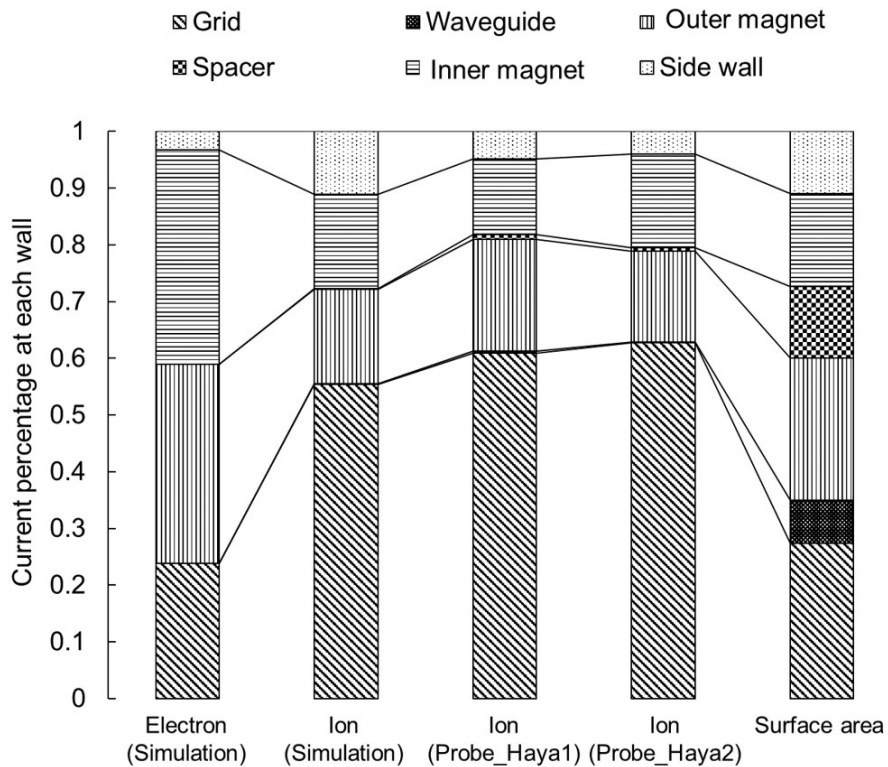


**Fig. C.8** Current percentage distribution of ions and electrons and surface area percentage. Electron (simulation) and ion (simulation) show the numerical results of the current ratio of ion and electron. Ion (experiment) is the results of measurement using the electrostatic probe in the Hayabusa mode and quoted from Ref. 11. The surface area represents the area at each wall.

## C.4 Implicit EM full-PIC simulation

### C.4.1 Review of ECSIM

Firstly, ECSIM [145] and GL-ECSIM [21] are reviewed in terms of particle and velocity updates and the field solver.

#### C.4.1.1 Position and velocity update

The updates of position and velocity are given by the following equation.

$$\vec{x}_p^{n+\frac{1}{2}} = \vec{x}_p^{n-\frac{1}{2}} + \Delta t \vec{v}_p^n \quad (\text{C.10})$$

$$\frac{\vec{v}_p^{n+1} - \vec{v}_p^n}{\Delta t} = \frac{q}{m} \left( \vec{E}_p^{n+\theta} + \bar{v}_p \times \vec{B}_p^n \right), \quad (\text{C.11})$$

where  $q$  is the elementary charge,  $m$  is the mass of charged particles,  $v_p$  is the velocity of an individual particle,  $x_p$  is the position of an individual particle,  $\vec{E}_p^{n+\theta}$  is the electric field at  $n + \theta$ , and  $\vec{B}_p^n$  is the magnetic field. Here, the electric field is defined as a linear interpolation.

$$\vec{E}_p^{n+\theta} = (1 - \theta) \vec{E}_p^n + \theta \vec{E}_p^{n+1}. \quad (\text{C.12})$$

Usually,  $\theta$  is set to 0.5 in conventional ECSIM. The electric field and magnetic field are interpolated using particle position  $\vec{x}_p^{n+\frac{1}{2}}$ .  $\bar{v}_p$  is the average  $(\vec{v}_p^{n+1} + \vec{v}_p^n) / 2$  of the velocities at  $n + 1$  and  $n$ . Note that if the electric field is explicit, the scheme is similar to the Boris solver [148]. The Boris mover is a physics-based scheme because the Lorentz force does not disturb the particle energy even if the time step is large [158]. As shown in the Boris solver, Eq. (C.11) can be solved for  $\bar{v}_p$  as follows.

$$\bar{v}_p = \vec{v}_{exp} + \vec{v}_{imp} = \bar{\alpha}_p^n \vec{v}_p^n + \bar{\alpha}_p^n \beta_p \vec{E}_p^{n+\theta}. \quad (\text{C.13})$$

Here,  $\beta_p = q\Delta t / 2m$  and  $\bar{\alpha}_p^n$  is a matrix of the magnetic field, expressed as follows.

$$\bar{\alpha}_p^n = \begin{bmatrix} \alpha_{xx} & \alpha_{xy} & \alpha_{xz} \\ \alpha_{xy} & \alpha_{yy} & \alpha_{yz} \\ \alpha_{zx} & \alpha_{zy} & \alpha_{zz} \end{bmatrix} = \frac{1}{1 + (\beta_p |\vec{B}_p^n|)^2} \left( I + \beta_p I \times \vec{B}_p^n + \beta_p^2 \vec{B}_p^n \vec{B}_p^n \right). \quad (\text{C.14})$$

The matrix can be explicitly calculated because the magnetic field is defined at  $n$ . Equations

(C.13) and (C.14) indicate that the averaged velocity  $\bar{v}_p$  consists of the explicit component  $\vec{v}_{exp} = \bar{\alpha}_p^n \vec{v}_p^n$  and the implicit component  $\vec{v}_{imp} = \bar{\alpha}_p^n \beta_p \vec{E}_p^{n+\theta}$ . Therefore, using Eq. (C.13), the update of particle velocity can couple with field solver through  $\vec{E}_p^{n+\theta}$ . After the electric field is calculated,  $\bar{v}_p$  can be obtained. The velocity at  $n + 1$  can then be calculated as,

$$\vec{v}_p^{n+1} = 2\bar{v} - \vec{v}_p^n. \quad (\text{C.15})$$

#### C.4.2 Electromagnetic field update

In the ECSIM scheme, Maxwell's equations are expressed as follows.

$$\vec{\nabla} \cdot \vec{E}_g^{n+1} = \frac{\rho^{n+1}}{\epsilon_0}, \quad (\text{C.16})$$

$$\vec{\nabla} \cdot \vec{B}_g^{n+1} = 0, \quad (\text{C.17})$$

$$\vec{\nabla} \times \vec{E}_g^{n+\theta} + \frac{\vec{B}_g^{n+1} - \vec{B}_g^n}{\Delta t} = 0, \quad (\text{C.18})$$

$$-\frac{1}{\mu_0 \epsilon_0} \nabla \times \vec{B}_g^{n+\theta} + \frac{\vec{E}_g^{n+1} - \vec{E}_g^n}{\Delta t} = -\frac{1}{\epsilon_0} \vec{J}^{n+\frac{1}{2}}. \quad (\text{C.19})$$

In the ECSIM scheme, to obtain the electromagnetic field, equations (C.18) and (C.19) are used. The treatment of equations (C.16) and (C.17) is described later. By removing  $\vec{B}_g^{n+1}$  from Eqs (C.19) and (C.18), an elliptic equation on  $\vec{E}_g^{n+1}$  is obtained as follows.

$$\begin{aligned} & \left[ \vec{E}_g^{n+1} - \frac{(\theta \Delta t)^2}{\mu_0 \epsilon_0} \left\{ \nabla \left( \nabla \cdot \vec{E}_g^{n+1} \right) - \nabla^2 \vec{E}_g^{n+1} \right\} \right] = \\ & \left[ \vec{E}_g^n + \frac{\theta(1-\theta)\Delta t^2}{\mu_0 \epsilon_0} \left\{ \nabla \left( \nabla \cdot \vec{E}_g^n \right) - \nabla^2 \vec{E}_g^n \right\} \right] \\ & + \frac{\Delta t}{\mu_0 \epsilon_0} \nabla \times \vec{B}_g^n - \frac{\Delta t}{\epsilon_0} \vec{J}^{n+\frac{1}{2}} \left( \vec{E}_g^{n+\theta} \right) \end{aligned} \quad (\text{C.20})$$

This physics-based precondition has advantages in terms of both numerical and physical considerations [5,41,42].

## C.5 Satisfying Gauss-law

To satisfy Gauss's law of magnetism (Eq. (C.17)), the Yee scheme is often used [164]. Then, to satisfy Gauss's law in the explicit scheme, a charge conservation scheme and divergence cleaning are often used. Usually, in a charge conservation method, the current density is obtained by interpolation to satisfy current conservation [165, 166, 167, 168]. Then, divergence cleaning is used to modify the electric field so that Gauss's law is satisfied [169]. However, it is impossible to apply these methods to ECSIM because the current density includes an implicit component on the electric field and the electric field is determined to satisfy energy conservation. Chen, and Pagès proposed algorithms to satisfy Gauss's law respectively [21, 152]. Chen proposed several methods that modify particle position to satisfy Gauss's law directly. Pagès proposed an explicit charge conservation scheme that is applied after the field solver. In this study, the particle position is modified, as proposed by Chen, in GL-ECSIM; this is called the approximate global correction [21]. In this paper, the coefficient for the maximum allowed relative displacement is  $c_0 = 0.1$  [21]. In the field of EP devices, cylindrical coordinates are often used [18, 134, 154] because the geometry of a thruster is cylindrical. ECSIM can use cylindrical coordinates [153]. However, it is difficult to apply a charge conservation scheme in cylindrical coordinates because of a singularity at  $r = 0$  [170]. The author confirmed that GL-ECSIM can use in cylindrical coordinate.

### C.5.1 Proposed improvement for LTPs

Here, to reduce the simulation cost, a sub-cycle method is proposed. Additionally, for magnetized plasma source, high-accurate Boris solver is implemented in ECSIM.

#### C.5.1.1 Sub-cycle method that maintains ECSIM

In LTPs, the electron thermal velocity  $v_{th}$  is two or three orders of magnitude lower than the speed of light ( $v_{th}/c \cong 0.001 - 0.01$ ). Therefore, the CFL condition for electrons and light is very different. Therefore, we proposed a sub-cycle method that is suitable for the simulation of plasma sources. In a PIC simulation, the stage with the highest computational cost is that where particle information is collected and converted into information in grid cells, such as current density. It is difficult to make this stage efficient because random access is involved [171, 172, 173]. In this paper, this operation called particle interpolation is reduced to decrease

the simulation cost. The proposed sub-cycle method is based on three assumptions. First, because  $v_{th} \ll c$ , the position update of a particle can be neglected during a sub-cycle. This assumption can be expressed as

$$\vec{x}_p^{n+\frac{1}{2}+\frac{k}{L}} \cong \vec{x}_p^{n+\frac{1}{2}} \quad (\text{C.21})$$

where  $L$  is the number of cycles and  $k(1 < k < L)$  indicates the particle position. Second, the variable magnetic field has a constant effect on the particle trajectory during a sub-cycle. Therefore, the matrix  $\bar{\alpha}_p^{n+k/L}$  can be approximated as follows:

$$\bar{\alpha}_p^{n+\frac{k}{L}} \left( \vec{x}_p^{n+\frac{1}{2}+\frac{k}{L}} \right) \cong \bar{\alpha}_p^n \left( \vec{x}_p^{n+\frac{1}{2}} \right) \quad (\text{C.22})$$

For example, for an ECR plasma source, the approximation is valid because the static magnetic field is much larger than the magnetic field of microwaves. In this case, the matrix is fixed at the initial condition  $\bar{\alpha}_p^n \cong \bar{\alpha}_p^0$ . Even if there is numerical error of the magnetic field, the energy conservation is maintained because the Lorentz force does not affect the particle energy [148]. Third, the weight function is the nearest grid point (NGP) [148]. The proposed algorithm is summarized in Fig. C.9. If  $k = 0$  (the particle has just moved), the current density is calculated by interpolating the particles, which is the same as done in conventional ECSIM. However, during a sub-cycle ( $k \geq 1$ ), the electromagnetic field and the current density are updated using only the information defined by the grid points. Then, the velocity of a particle is updated by the electric field  $\vec{E}_g^{n+k/L}$ . However, it is not necessary to communicate from the particle to the field because particle interpolation is not used during a sub-cycle. In a typical PIC simulation, the field solver and the update of particles cannot be calculated separately. In contrast, during a sub-cycle, our method can separate the field solver and the update of particle velocity. Because it is not necessary to wait for the update of particle velocity, the calculation time can be substantially reduced by using parallel computing. The sub-cycle method is based on the fact that the explicit current density that contributes to  $n + (k + 1/2)/L$  is the same between the interpolation of each particle velocity and the macroscopic current density. The proof of this is given.

For simplicity, the velocity is assumed to have two dimensions ( $x$  and  $y$ ). This proof can be extended to three dimensions of position and velocity. The explicit velocity that contributes to

$n + (k + 1/2)/L$  can be written as follows:

$$v_{x,exp}^{n+\frac{k+\frac{1}{2}}{L}} = \alpha_{xx}^{n+\frac{k}{L}} \left( \vec{x}_p^{n+\frac{1}{2}+\frac{k}{L}} \right) v_x^{n+\frac{k}{L}} + \alpha_{xy}^{n+\frac{k}{L}} \left( \vec{x}_p^{n+\frac{1}{2}+\frac{k}{L}} \right) v_y^{n+\frac{k}{L}}. \quad (C.23)$$

Using equations (C.21) and (C.25) yields

$$v_{x,exp}^{n+\frac{k+\frac{1}{2}}{L}} \cong \alpha_{xx}^n \left( \vec{x}_p^{n+\frac{1}{2}} \right) v_x^{n+\frac{k}{L}} + \alpha_{xy}^n \left( \vec{x}_p^{n+\frac{1}{2}} \right) v_y^{n+\frac{k}{L}}. \quad (C.24)$$

Then, the explicit current density that contributes to  $n + (k + 1/2)/L$  at  $\vec{X}_i$  can be written as follows:

$$\begin{aligned} J_{x,exp}^{n+\frac{k+\frac{1}{2}}{L}} \left( \vec{X}_i \right) &= q \sum_{m=1}^{N_i} W \left( \vec{X}_i - \vec{x}_{p,m}^{n+\frac{1}{2}} \right) v_{x,exp,m}^{n+\frac{k+\frac{1}{2}}{L}} \\ &\cong q \sum_{m=1}^{N_i} W \left( \vec{X}_i - \vec{x}_{p,m}^{n+\frac{1}{2}} \right) \left\{ \alpha_{xx}^n \left( \vec{x}_{p,m}^{n+\frac{1}{2}} \right) v_{x,m}^{n+\frac{k}{L}} + \alpha_{xy}^n \left( \vec{x}_{p,m}^{n+\frac{1}{2}} \right) v_{y,m}^{n+\frac{k}{L}} \right\} \end{aligned} \quad (C.25)$$

where  $N_i$  is the number of particles at  $\vec{X}_i$  and  $\vec{x}_{p,m}^{n+\frac{1}{2}}$  is the particle velocity at node  $\vec{X}_i$ . If the weight function is NGP, the weight function is

$$W \left( \vec{X}_i - \vec{x}_{p,1}^{n+\frac{1}{2}} \right) = W \left( \vec{X}_i - \vec{x}_{p,2}^{n+\frac{1}{2}} \right) = \dots = W \left( \vec{X}_i - \vec{x}_{p,N_i}^{n+\frac{1}{2}} \right) = W_0 \quad (C.26)$$

Therefore, the matrix is the same at node  $\vec{X}_i$ .

$$\bar{\alpha}_p^n \left( \vec{x}_{p,1}^{n+\frac{1}{2}} \right) = \bar{\alpha}_p^n \left( \vec{x}_{p,2}^{n+\frac{1}{2}} \right) = \dots = \bar{\alpha}_p^n \left( \vec{x}_{p,N_i}^{n+\frac{1}{2}} \right) = \bar{\alpha}_p^n \left( \vec{X}_i \right) \quad (C.27)$$

If the weight function is not NGP (e.g., cloud-in-cell), equation (C.32) does not hold. Using equations (C.32) and (C.25), the explicit current density  $n + (k + 1/2)/L$  can be written as follows:

$$\begin{aligned} J_{x,exp}^{n+\frac{k+\frac{1}{2}}{L}} \left( \vec{X}_i \right) &\cong q \sum_{m=1}^{N_i} W_0 \left\{ \alpha_{xx}^n \left( \vec{X}_i \right) v_{x,m}^{n+\frac{k}{L}} + \alpha_{xy}^n \left( \vec{X}_i \right) v_{y,m}^{n+\frac{k}{L}} \right\} \\ &= q W_0 \alpha_{xx}^n \left( \vec{X}_i \right) \sum_{m=1}^{N_i} v_{x,m}^{n+\frac{k}{L}} + q W_0 \alpha_{xy}^n \left( \vec{X}_i \right) \sum_{m=1}^{N_i} v_{y,m}^{n+\frac{k}{L}} \end{aligned} \quad (C.28)$$

By interpolating particles to cells, the current density can be written as follows:

$$J_{x,exp}^{n+\frac{k+\frac{1}{2}}{L}}(\vec{X}_i) = \alpha_{xx}^n(\vec{X}_i) J_x^{n+\frac{k}{L}}(\vec{X}_i) + \alpha_{xy}^n(\vec{X}_i) J_y^{n+\frac{k}{L}}(\vec{X}_i) \quad (C.29)$$

This equation indicates that the current density consists of only macroscopic information such as  $J_{x,m}^{n+k/L}$ . Note that if  $k=0$  (the particle has just moved), the explicit current density must be calculated by interpolating particles to cells as follows:

$$J_{x,exp}^{n+\frac{1}{2}}(\vec{X}_i) = q\alpha_{xx}^n(\vec{X}_i) \sum_{m=1}^{N_i} v_{x,m}^n \left( \vec{x}_p^{n+\frac{1}{2}} \right) + q\alpha_{xy}^n(\vec{X}_i) \sum_{m=1}^{N_i} v_{y,m}^n \left( \vec{x}_p^{n+\frac{1}{2}} \right) \quad (C.30)$$

Then, similar to the explicit current density, the implicit current density can be expressed as follows:

$$J_{x,imp}^{n+\frac{k+\frac{1}{2}}{L}}(\vec{X}_i) = \beta_p \left\{ \alpha_{xx}^n(\vec{X}_i) E_x^{n+\frac{k}{L}}(\vec{X}_i) + \alpha_{xy}^n(\vec{X}_i) E_y^{n+\frac{k}{L}}(\vec{X}_i) \right\} \quad (C.31)$$

This equation indicates that the implicit current density can be updated using only information at the grid points. Therefore, the validity of the sub-cycle method is proven mathematically.

We prove the validity numerically later

$$J_{x,imp}^{n+\frac{k+\frac{1}{2}}{L}}(\vec{X}_i) = \beta_p \left\{ \alpha_{xx}^n(\vec{X}_i) E_x^{n+\frac{k}{L}}(\vec{X}_i) + \alpha_{xy}^n(\vec{X}_i) E_y^{n+\frac{k}{L}}(\vec{X}_i) \right\} \quad (C.32)$$

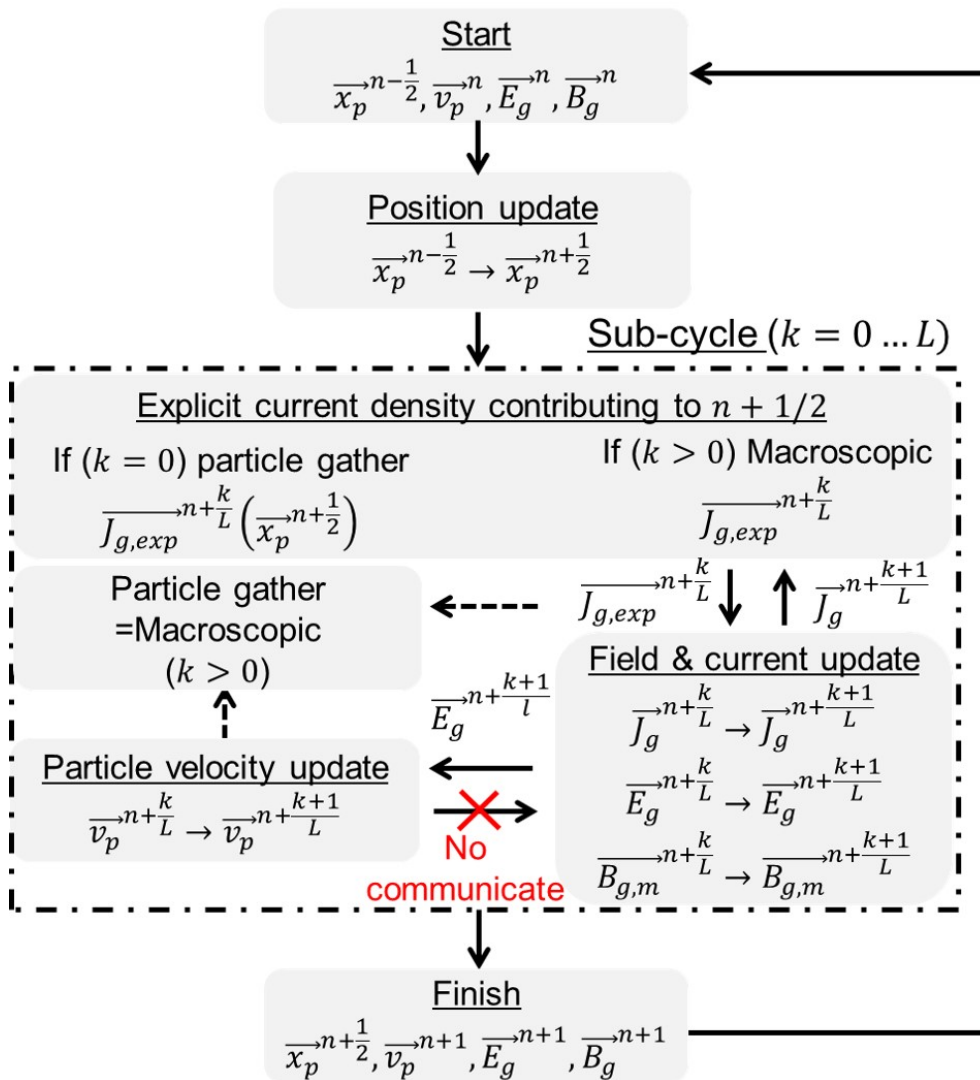


**Fig. C.9** Sub-cycle method that maintains ECSIM. During a sub-cycle, particle interpolation for the current density is not necessary.

### C.5.1.2 High-accurate Boris solver

The update of velocity is the same as the Boris solver if the electric field is explicit. In the Boris algorithm, a numerical error in cyclotron frequency is generated if the time step is large [148, 158]. Although an implicit PIC simulation can select a large time step, a critical problem occurs if the numerical error is non-negligible. In some plasma sources, the plasma is strongly magnetized to suppress wall loss, and thus the accuracy of gyro motion is very important. In ECR plasma sources, the maximum electron cyclotron frequency is larger than the plasma frequency. Therefore, the accuracy of particle orbits depends on the magnetic field. In addition, it is very important for the accuracy of electron cyclotron frequency in the ECR heating process (described later). In this paper, the high-accuracy Boris solver proposed by Zenitani [158] is implemented in ECSIM. If the time step is relatively large, the cyclotron frequency lower than the actual cyclotron frequency. The cyclotron frequency can be expressed as follows [148],

$$\left(\frac{\omega_{ce}^{comp}\Delta t}{2}\right) = \tan^{-1}\left(\frac{\omega_{ce}\Delta t}{2}\right). \quad (\text{C.33})$$

Then, if  $\omega_c\Delta t \gg 1$ ,  $\omega_{ce}^{comp}\Delta t \cong \pi$ , which indicates that particles move back and forth (odd-even) [174]. To avoid numerical error, the rotation angle is precisely defined. To correct for phase error, the phase angle is modified as follows:

$$\frac{\omega_{ce}^{comp}\Delta t}{2} \rightarrow \tan\left(\frac{\omega_{ce}^{comp}\Delta t}{2}\right) = \tan(\beta_p|\vec{B}_p^n|). \quad (\text{C.34})$$

With this modification, the cyclotron frequency becomes exact. The scheme is effective even if  $\omega_{ce}\Delta t > 2$ . However, if  $\omega_{ce}\Delta t = \pi$ ,  $\tan(\beta_p|\vec{B}_p^n|) \rightarrow \infty$ . Thus, to avoid this numerical divergence, the sine and cosine functions were utilized suggested by Zenitani [158]. Substituting Eq. (C.34) into Eq. (C.14) yields the following definition of  $\alpha_p^n$ :

$$\begin{aligned} \bar{\alpha}_{p,exact}^n &= \cos^2(\beta_p|\vec{B}_p^n|)I \\ &+ \sin(\beta_p|\vec{B}_p^n|)\cos(\beta_p|\vec{B}_p^n|)\left(I \times \frac{\vec{B}_p^n}{|\vec{B}_p^n|}\right) + \sin^2(\beta_p|\vec{B}_p^n|)\frac{\vec{B}_p^n \cdot \vec{B}_p^n}{|\vec{B}_p^n|^2} \end{aligned} \quad (\text{C.35})$$

This scheme is nonlinear on the magnetic field; however, this non-linearity does not collapse ECSIM because ECSIM is explicit on the magnetic field. In this paper, this scheme is called

the exact-gyro GL-ECSIM (EG-GL-ECSIM).

### C.5.2 Benchmark problem

To confirm the validity of the code and several proposed schemes, we simulated 1D3V Weibel instability [20]. Note that the proposed sub-cycle method cannot be used for Weibel instability because the limitation of the magnetic field cannot be satisfied. The initial magnetic field is  $B_z = B_{z0} \cos(kx)$ . The calculation domain is  $L/de = 2\pi$  and the number of particles per cell is 100. The bulk velocity is  $v_0 = 0.8c$ , where  $c$  is the speed of light. The electron thermal velocity is  $v_{th} = 0.01c$ . Ions are in the background and stationary. In this simulation, we used a time step of  $c\Delta t = 2$  and a grid size of  $2.5\lambda_D$ . The linear growth rate is theoretically given by [41]

$$\gamma = \frac{\omega_{pe}v_0}{c}. \quad (\text{C.36})$$

Numerical growth rates are shown in Fig. C.10. Note that the energy conservation is perfectly matched if  $\theta = 0.5$ . However, we found that the diffusive error is large, as mentioned in several reports [5]. For practical problems, because high robustness is very important, we selected  $\theta=0.51$ , as suggested by Chen and Tanaka *et al.* [175, 176]. The results indicate that all numerical schemes are in good agreement with the theoretical prediction. At  $\omega_{pe}\Delta t = 100$ , the ECSIM scheme at  $\theta = 0.51$  damped by 0.08 %. Therefore, for practical problems,  $\theta$  must be carefully selected and the accuracy of energy conservation must be carefully checked. The exact-gyro scheme does not impact Weibel instability because the magnetic field is relatively small.

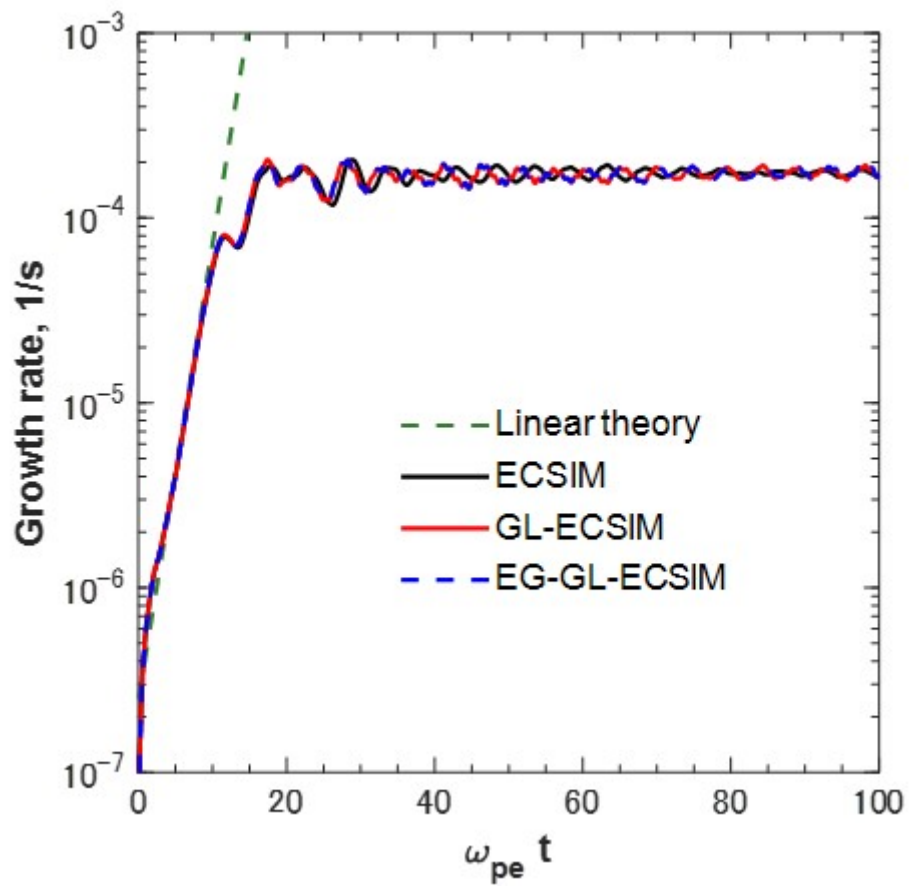


**Fig. C.10** Time development of growth rate in Weibel instability [20]. GL refers to Gauss's law satisfying ECSIM proposed by Chen [21]. EG refers to the exact-gyro scheme proposed in subsection C.5.1.

### C.5.3 Macroscopic conservation

For practical problems, it is difficult to obtain a theoretical relation such as the Weibel instability. In addition, the boundary conditions in the plasma source are complicated. Therefore, we need to validate the code and determine the effect of the scheme in practical problems. Here, a check of the macroscopic conservation for code validation and the effect of the numerical scheme are utilized. Because a PIC simulation is based on the Boltzmann equation, the macroscopic (fluid) conservation should be satisfied except for numerical error. In this thesis, computational conservation-law is derived in case of ECSCIM.

#### C.5.3.1 Charge conservation (Continuity equation)

By taking the inner product of  $\vec{\nabla}$  in Eq. (C.19), the following equation can be obtained:

$$\vec{\nabla} \cdot \left( \frac{\vec{E}_g^{n+1} - \vec{E}_g^n}{\Delta t} \right) = -\frac{1}{\varepsilon_0} \left( \vec{\nabla} \cdot \vec{J}^{n+\frac{1}{2}} \right). \quad (\text{C.37})$$

If Gauss's law is satisfied at  $n + 1$  and  $n$ , the equation can be rewritten as follows:

$$\frac{\rho^{n+1} - \rho^n}{\Delta t} = -\vec{\nabla} \cdot \vec{J}^{n+\frac{1}{2}} + N_{gauss}. \quad (\text{C.38})$$

where  $N_{gauss}$  is the numerical error of Gauss's law. Here,  $N_{gauss}$  is defined as follows:

$$\frac{\rho^{n+1} - \rho^n}{\Delta t} = -\vec{\nabla} \cdot \vec{J}^{n+\frac{1}{2}} + N_{gauss}. \quad (\text{C.39})$$

$$N_{gauss} = -\varepsilon_0 \frac{\kappa^{n+1} - \kappa^n}{\Delta t}. \quad (\text{C.40})$$

$\kappa^n$  is defined as follows:

$$\kappa^n = \vec{\nabla} \cdot \vec{E}_g^n - \frac{\rho^n}{\varepsilon_0}. \quad (\text{C.41})$$

Therefore, by satisfying Gauss's law, the numerical error can be eliminated.

### C.5.4 Momentum conservation

From the update of velocity (Eq. (C.11)), the following equation can be obtained:

$$\vec{F}^{n+\frac{1}{2}} = m \sum_{p=1}^N \frac{v_p^{n+1} - v_p^n}{\Delta t} = \frac{m}{e} \frac{\vec{J}_g^{n+1} - \vec{J}_g^n}{\Delta t} = \rho_g^{n+\frac{1}{2}} E_g^{n+\theta} + J_g^{n+\frac{1}{2}} \times B_g^n. \quad (\text{C.42})$$

Here, the charge density at  $n + 1/2$  is defined by the interpolation formula at  $n + 1$  and  $n$  as follows:

$$\rho^{n+\frac{1}{2}} = \gamma \rho^{n+1} + (1 - \gamma) \rho^n. \quad (\text{C.43})$$

Then, using Eqs (C.41) and (C.43), the charge density at  $n + 1/2$  can be written as,

$$\begin{aligned} \rho^{n+\frac{1}{2}} &= \varepsilon_0 \gamma \left\{ \left( \vec{\nabla} \cdot \vec{E}_g^{n+1} \right) + \kappa^{n+1} \right\} + \varepsilon_0 (1 - \gamma) \left\{ \left( \vec{\nabla} \cdot \vec{E}_g^n \right) + \kappa^n \right\} \\ &= \varepsilon_0 \vec{\nabla} \cdot \vec{E}_g^{n+\frac{1}{2}} + \varepsilon_0 \kappa^{n+\frac{1}{2}} + \varepsilon_0 \left( \gamma - \frac{1}{2} \right) \left\{ \left( \vec{\nabla} \cdot \vec{E}_g^{n+1} \right) - \left( \vec{\nabla} \cdot \vec{E}_g^n \right) \right\}. \end{aligned} \quad (\text{C.44})$$

Here,  $\kappa^{n+\frac{1}{2}}$  is defined as follows:

$$\kappa^{n+\frac{1}{2}} = \gamma \kappa^{n+1} + (1 - \gamma) \kappa^n. \quad (\text{C.45})$$

Then, by considering  $\vec{E}_g^{n+1/2} = \vec{E}_g^{n+\theta} - (\theta - 0.5) (\vec{E}_g^{n+1} - \vec{E}_g^n)$ , Eq. (C.44) can be rewritten as follows:

$$\begin{aligned} \rho^{n+\frac{1}{2}} \vec{E}_g^{n+\theta} &= \varepsilon_0 \left( \vec{\nabla} \cdot \vec{E}_g^{n+\theta} \right) \vec{E}_g^{n+\theta} + \varepsilon_0 \kappa^{n+\frac{1}{2}} \vec{E}_g^{n+\theta} \\ &+ \varepsilon_0 \left( \gamma - \frac{1}{2} \right) \left( \vec{\nabla} \cdot \vec{E}_g^{n+1} - \vec{\nabla} \cdot \vec{E}_g^n \right) \vec{E}_g^{n+\theta} \\ &- \varepsilon_0 \left( \theta - \frac{1}{2} \right) \left( \vec{\nabla} \cdot \vec{E}_g^{n+1} - \vec{\nabla} \cdot \vec{E}_g^n \right) \vec{E}_g^{n+\theta}. \end{aligned} \quad (\text{C.46})$$

Using Maxwell's equations (C.18) and (C.19), the Lorentz force can be written as

$$\begin{aligned} \vec{J}_g^{n+\frac{1}{2}} \times \vec{B}_g^n &= -\varepsilon_0 \frac{\partial}{\partial t} \left( \vec{E}_g \times \vec{B}_g \right)^{n+\frac{1}{2}} + \frac{1}{\mu_0} \left( \nabla \times \vec{B}_g^{n+\theta} \right) \times \vec{B}_g^{n+\theta} \\ &+ \varepsilon_0 \left( \nabla \times \vec{E}_g^{n+\theta} \right) \times \vec{E}_g^{n+\theta} - \theta \vec{J}_g^{n+\frac{1}{2}} \times \left( \vec{B}_g^{n+1} - \vec{B}_g^n \right). \end{aligned} \quad (\text{C.47})$$

Then, using Gauss's law of magnetism Eqs. (C.17), (C.46), and (C.47), the following momentum conservation can be obtained:

$$m \sum_{p=1}^N \frac{\vec{v}_p^{n+1} - \vec{v}_p^n}{\Delta t} + \varepsilon_0 \frac{\partial}{\partial t} \left( \vec{E}_g \times \vec{B}_g \right)^{n+\frac{1}{2}} = \vec{\nabla} \cdot \vec{T}_F^{n+\theta} + N_{gauss} + N_{position} + N_{theta} + N_{Lorentz}. \quad (\text{C.48})$$

where  $\bar{T}_F^{n+\theta}$  is the Maxwell stress tensor. These numerical errors are summarized as follows:

$$\begin{aligned}
N_{gauss} &= \varepsilon_0 k^{n+\frac{1}{2}} \vec{E}_g^{n+\theta}, \\
N_{position} &= \varepsilon_0 \left( \gamma - \frac{1}{2} \right) \left( \vec{\nabla} \cdot \vec{E}_g^{n+1} - \vec{\nabla} \cdot \vec{E}_g^n \right) \vec{E}_g^{n+\theta}, \\
N_{theta} &= -\varepsilon_0 \left( \theta - \frac{1}{2} \right) \left( \vec{\nabla} \cdot \vec{E}_g^{n+1} - \vec{\nabla} \cdot \vec{E}_g^n \right) \vec{E}_g^{n+\theta}, \\
N_{Lorentz} &= -\theta J^{n+\frac{1}{2}} \times \left( \vec{B}_g^{n+1} - \vec{B}_g^n \right).
\end{aligned} \tag{C.49}$$

$N_{gauss}$  can be eliminated by satisfying Gauss's law.  $N_{position}$  is not generally 0 because the position is not guaranteed at the middle time  $\gamma = 1/2$  because the position is updated using a leap-frog scheme.  $N_\theta$  is generated by de-centering  $\theta$ , which can be removed in conventional ECSIM.  $N_{Lorentz}$  is generated due to the Lorentz force being defined at time  $n$ .

#### C.5.4.1 Energy conservation

The energy change at each lattice point is divided into the energy of the electromagnetic field and that of each particle. It can be written as follows:

$$\Delta P_{field} = \frac{1}{\mu_0} \bar{B}_g \cdot \frac{(\vec{B}_g^{n+1} - \vec{B}_g^n)}{\Delta t} + \varepsilon_0 \bar{E}_g \cdot \frac{(\vec{E}_g^{n+1} - \vec{E}_g^n)}{\Delta t}. \tag{C.50}$$

Using Maxwell's Eqs (C.18) and (C.19) yields

$$\begin{aligned}
\Delta P_{field} &= -\frac{1}{\mu_0} \nabla \cdot \left( \vec{E}_g^{n+\theta} \times \vec{B}_g^{n+\theta} \right) - \bar{J}_g \cdot \vec{E}_g^{n+\theta} \\
&\quad - (\theta - 0.5) \left\{ \frac{1}{\mu_0} \frac{(\vec{B}_g^{n+1} - \vec{B}_g^n)^2}{\Delta t} + \varepsilon_0 \frac{(\vec{E}_g^{n+1} - \vec{E}_g^n)^2}{\Delta t} \right\}.
\end{aligned} \tag{C.51}$$

In addition, the change in particle energy is given by

$$\Delta P_{particle} = m \sum_{p=1}^N \bar{v}_p \frac{v_p^{n+1} - v_p^n}{\Delta t}. \tag{C.52}$$

Using the inner product of  $\vec{\nabla}$  in Eq. (C.11), the change in particle energy can be written as follows:

$$\frac{1}{2} m \frac{(v_p^{n+1})^2 - (v_p^n)^2}{\Delta t} = q \bar{v}_p \cdot \vec{E}_p^{n+\theta}. \tag{C.53}$$

Using these equations, the following energy conservation can be obtained:

$$m \sum_{p=1}^N \bar{v}_p \frac{\vec{v}_p^{n+1} - \vec{v}_p^n}{\Delta t} + \frac{1}{\mu_0} \bar{B}_g \cdot \frac{(\vec{B}_g^{n+1} - \vec{B}_g^n)}{\Delta t} + \varepsilon_0 \bar{E}_g \cdot \frac{(\vec{E}_g^{n+1} - \vec{E}_g^n)}{\Delta t} = \frac{1}{\mu_0} \nabla \cdot (\vec{E}_g^{n+\theta} \times \vec{B}_g^{n+\theta}) + N_{energy}. \quad (C.54)$$

where  $N_{energy}$  is the numerical error of energy, and is defined as

$$N_{energy} = -(\theta - 0.5) \left\{ \frac{1}{\mu_0} \frac{(\vec{B}_g^{n+1} - \vec{B}_g^n)^2}{\Delta t} + \varepsilon_0 \frac{(\vec{E}_g^{n+1} - \vec{E}_g^n)^2}{\Delta t} \right\}. \quad (C.55)$$

The equation indicates that when  $\theta = 0.5$ , the energy conservation law is completely satisfied.

If  $\theta > 0.5$ , the energy damps. If  $\theta < 0.5$ , the energy increases.

### C.5.5 Application of conservation-law to benchmark problem

Based on above derivation, charge, momentum, and energy is generally given by

$$\frac{\partial \vec{Q}}{\partial t} = \frac{\partial \vec{F}}{\partial x} + N_{error}. \quad (C.56)$$

where matrix  $\vec{Q}$  is the time variable, matrix  $\vec{F}$  is the flux vector, and  $N_{error}$  is the numerical error. In the 1D3V case, the matrices  $\vec{Q}$  and  $\vec{F}$  are given as follows:

$$\vec{Q} = \begin{bmatrix} \rho_g \\ \frac{m}{e} J_{g,x} + \varepsilon_0 E_{g,y} B_{g,z} \\ \frac{1}{2} \rho_g u_g^2 + \frac{1}{2\mu_0} B_{g,z}^2 + \frac{\varepsilon_0}{2} (E_{g,x}^2 + E_{g,y}^2) \end{bmatrix} \quad (C.57)$$

$$\vec{F} = \begin{bmatrix} -J_{g,x} \\ T_{g,xx} \\ -\frac{1}{\mu_0} E_{g,y} B_{g,z} \end{bmatrix} \quad (C.58)$$

where  $T_{g,xx}$  is the  $xx$  component of the Maxwell stress tensor [177]. As an example, the macroscopic conservation for the Weibel instability is shown in Fig. C.11.  $\partial \vec{Q} / \partial t$  and  $\nabla \cdot \vec{F}$  are the time variable and flux defined in Eq. (C.58). Here, the result of the EG-GL-ECSIM scheme was used. Noted that similar results were obtained with other schemes. GL-ECSIM provides high accuracy for charge conservation and energy conservation, but momentum conservation is not guaranteed. However, as shown in Fig. C.11, all conservation laws are well satisfied.

Accuracy depends on the grid size, time step, and the application. For practical problems, numerical error can affect these conservation. Therefore, the check should always be performed even if the code does not change. This validation contributes to the comparison of several numerical models. Generally, is very difficult to develop code for an implicit PIC simulation. Therefore, this validation is also very useful for code development.

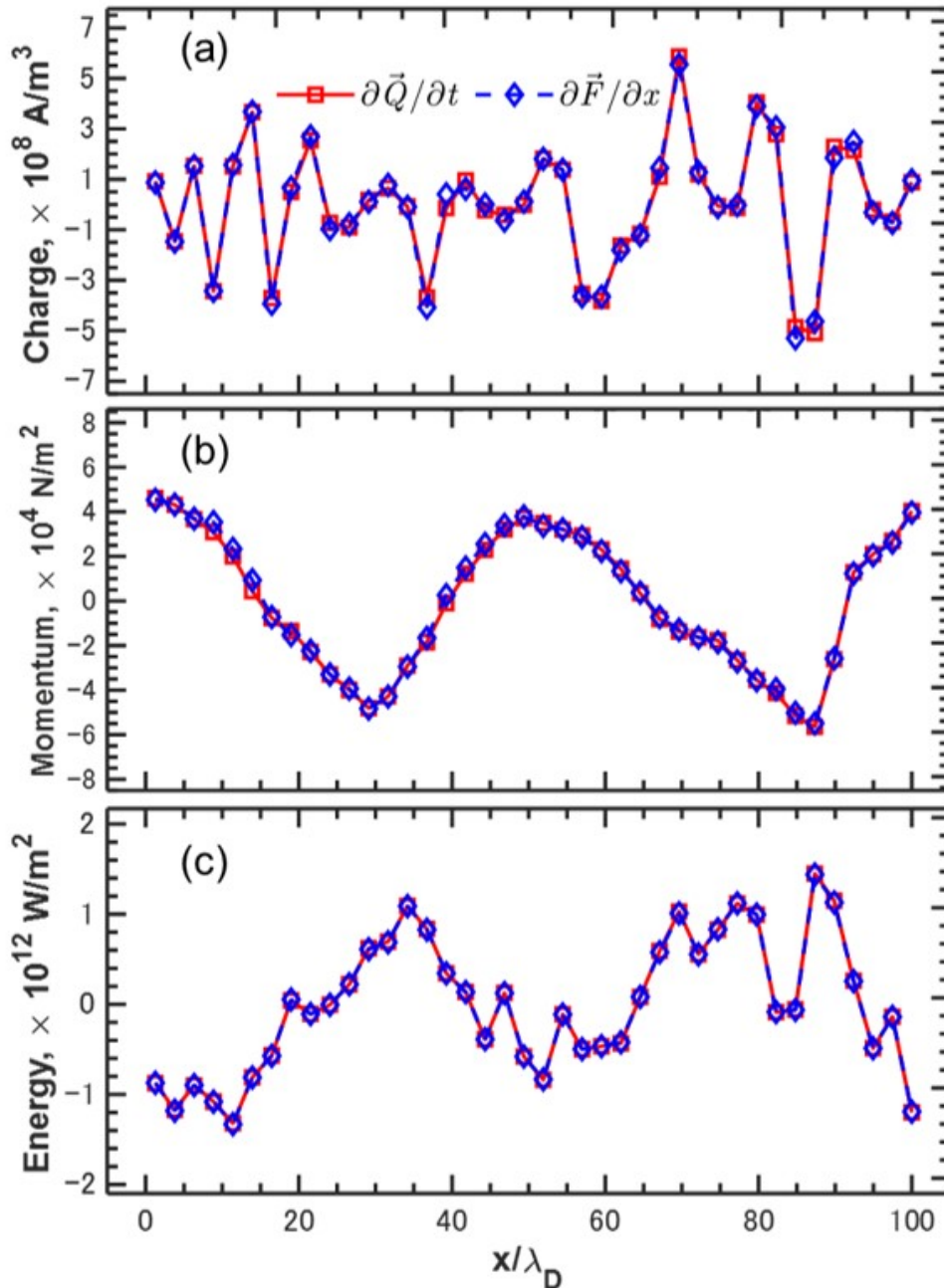


**Fig. C.11** Discrete difference of macroscopic conservation obtained at  $\omega_{pe}\Delta t = 100$ . (a) Charge, (b) momentum, and (c) energy.  $\partial\vec{Q}/\partial t$  and  $\partial\vec{F}/\partial x$  are the time variable and flux defined in Eq. (C.56).

## C.5.6 Application to ECR plasma source

### C.5.6.1 Single particle test

Firstly, very simple test simulation was preformed. Here, initial velocity is  $v_{x0} = 10^6$  m/s and  $v_y = 0$  m/s. Then, the magnetic field is only  $z$  direction and the amplitude is  $B_z = 0.5$  T. In this case, theoretical solution is given by

$$v_x = v_{x0} \cos \omega_c t \quad (\text{C.59})$$

Then, time step condition is  $\Delta t = T_m/20, T_m/40$ , where  $T_m = 2\pi/\omega_m$  is the microwave cycle. Figure C.12 shows the comparison of electron cyclotron motion between conventional and high-accurate Boris solver. Top and bottom figure are conventional is high-accurate results respectively. In conventional scheme, the cyclotron frequency is damped as the time step increases, which is consistent with Eq. (C.33). In contrast, in case of high-accurate Boris solver, even if the time step increases, the phase error is not observed.

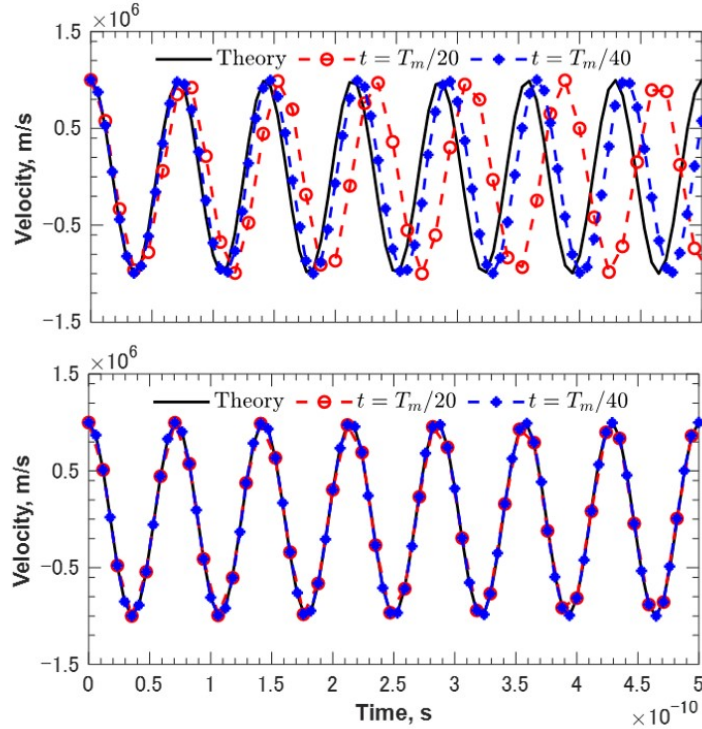


**Fig. C.12** Comparison of electron cyclotron motion between conventional and high-accurate Boris solver. Top: conventional, and bottom: high-accurate.

### C.5.6.2 ECR heating

Secondly, high-accurate Boris solver demonstrates the ECR heating process. Here, the magnetic field was set to  $B_{ECR} = m_e \omega_m / e$ . Here, typical parameters for a microwave discharge ion thruster,  $\omega_m / 2\pi = 4.25$  GHz and  $E_x = 5 \times 10^3$  V/m were used. The dimensions were  $\vec{B} = (0, 0, B_{ECR})$ ,  $\vec{E} = (E_x, 0, 0)$ , and  $\vec{v} = (v_x, v_y, 0)$ . The initial electron velocity was 0. The simulation results are shown in FIG. 4. Four kinds of time steps, namely  $dt = T_m/200$ ,  $T_m/40$ ,  $T_m/20$ , and  $T_m/10$  were simulated. The results indicate that the heating process strongly depends on the time step in the conventional scheme. If the time step is larger than  $T_m/20$ , the electrons are not heated precisely. In the exact scheme, the heating process does not depend much on the time step. For  $T_m/20$ , there is a clear difference in the heating process between the conventional and exact schemes. In practice, an explicit PIC simulation is limited to  $T_m/40$  to obtain the steady state, as reported in our previous study [18]. Takao et al. selected a time step of  $T_m/40$  for an explicit PIC simulation [50]. For  $T_m/40$ , the heating process only slightly damps, which indicates that the scheme is not very effective for an explicit PIC simulation for the ECR heating process. This scheme is very effective in an implicit PIC simulation for a large time step.

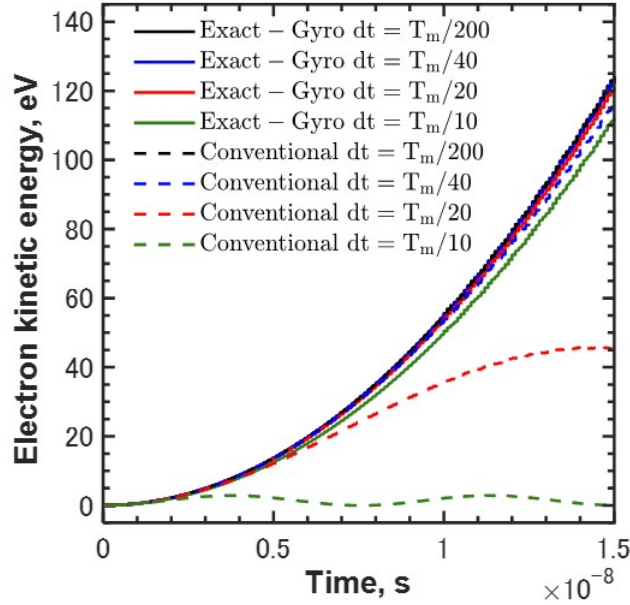


**Fig. C.13** Comparison of conventional and exact-gyro (EG) Boris push in ECR heating process. Here,  $T_m$  is one cycle of microwaves.

### C.5.6.3 Numerical dispersion relation

Although implicit PIC simulations can select a large time step, the accuracy at high frequency decreases if the simulation time step is very large. Thus, to determine the time step based on the trade-off between simulation cost and accuracy, the numerical dispersion relation is useful. It is emphasized that the ECSIM scheme consists of only linear solvers [145], and thus the numerical dispersion relation can be obtained using the Fourier transform. Note that the numerical dispersion relation is also obtained from the simulation results. However, it is very important to estimate the time step before performing the simulation. Thus, in this paper, the Fourier transform is directly applied to the discrete equation. The numerical dispersion relation is calculated using the discrete Fourier transform as  $P_i^n = \tilde{P}e^{-i(k\Delta x - \omega n\Delta t)}$ . It is noted that in the ECSIM scheme, linear interpolation is used for  $n + \theta$ . Therefore, the Fourier transform is  $P_i^{n+\theta} = \tilde{P}e^{-ik\Delta x} \{ \theta e^{i\omega(n+1)\Delta t} + (1 - \theta) e^{i\omega n\Delta t} \}$ , not  $P_i^{n+\theta} = \tilde{P}e^{-i(k\Delta x - \omega(n+\theta)\Delta t)}$ . In this paper, the numerical dispersion relation is simulated for extraordinary waves [41] because this is very important for an ECR plasma source. Therefore, following dimensions:  $\vec{E} = (E_x, E_y, 0)$ ,  $\vec{B} = (0, 0, B_z + B_0)$ ,  $\vec{v} = (v_x, v_y, 0)$ , and  $\vec{x} = (x, 0, 0)$  are set. Based on these numerical setups, following equation  $\bar{A}\vec{P} = 0$  can be obtained. Here,  $\vec{P} = [\tilde{E}_x, \tilde{E}_y, \tilde{B}_z, \tilde{v}_x, \tilde{v}_y]^T$  and  $\bar{A}$  are as follows for the ECSIM scheme:

$$\bar{A} = \begin{bmatrix} S_{\omega^*} & 0 & 0 & \frac{qn}{\epsilon_0} \Delta t & 0 \\ 0 & S_{\omega^*} & -\frac{S_{k'} c^2 \Delta t \lambda_\theta}{\Delta x} & 0 & \frac{qn}{\epsilon_0} \Delta t \\ 0 & -\frac{S_{k'} \Delta t \lambda_\theta}{\Delta x} & S_{\omega^*} & 0 & 0 \\ -2\beta_p \lambda_\theta & -2\beta_p \omega_{ce}^* \lambda_\theta & 0 & S_{\omega^*} + \omega_{ce}^{*2} C_{\omega^*} & -2\omega_{ce}^* e^{-i\omega^*} \\ 2\beta_p \omega_{ce}^* \lambda_\theta & -2\beta_p \lambda_\theta & 0 & 2\omega_{ce}^* e^{-i\omega^*} & S_{\omega^*} + \omega_{ce}^{*2} C_{\omega^*} \end{bmatrix}. \quad (\text{C.60})$$

where  $S_{\omega^*} = 2 \sin \omega^*$ ,  $C_{\omega^*} = 2 \cos \omega^*$ ,  $\lambda_\theta = \theta e^{\omega^*} + (1 - \theta) e^{-\omega^*}$ ,  $S_{k'} = 2 \sin k^*$ ,  $k^* = k\Delta x/2$ ,  $\omega^* = (\omega\Delta t/2)$ , and  $\omega_{ce}^* = (\omega_{ce}\Delta t/2)$ . By solving  $\det A = 0$ , we obtain the numerical dispersion relation. Unfortunately, it is very difficult to solve analytically, and thus we numerically solved it using MATLAB. The author confirmed that the simplified case of  $E_y \cong 0$ ,  $B_z \cong 0$ , and  $v_y \cong 0$  is consistent with the work of Lapenta [145]. The theoretical dispersion relation is given as follows [41].

$$\frac{(kc)^2}{\omega^2} = 1 - \frac{\omega_{pe}^2}{\omega^2} \frac{\omega^2 - \omega_{pe}^2}{\omega^2 - \omega_{he}^2} \quad (\text{C.61})$$

where  $\omega_{he}$  is the upper hybrid resonance of electrons, defined as follows [41]:

$$\omega_{he} = \sqrt{\omega_{ce}^2 + \omega_{pe}^2} \quad (\text{C.62})$$

A comparison of the theoretical and numerical dispersion relations is shown in Fig. C.14. In this case,  $\omega_m = \omega_{ce}$  and  $\omega_{pe} = 0.5\omega_{ce}$  are assumed. Here,  $\omega_m$  is the frequency of the electromagnetic field.  $\omega_{Re}$  and  $\omega_{Le}$  are defined as follows [31].

$$\omega_{Re} = \frac{1}{2} \left\{ \omega_{ce} + \sqrt{\omega_{ce}^2 + 4\omega_{pe}^2} \right\}, \quad \omega_{Le} = \frac{1}{2} \left\{ -\omega_{ce} + \sqrt{\omega_{ce}^2 + 4\omega_{pe}^2} \right\} \quad (\text{C.63})$$

Figure C.14 shows the comparison of dispersion relation and numerical and theory in three cases; top ( $T_m/40$ ), center ( $T_m/20$ ), and bottom ( $T_m/10$ ). The results indicate that the numerical dispersion relation is in good agreement with the theory for  $T_m/40$ . For  $T_m/20$ , there is a small error, but the match is reasonable. For  $T_m/10$ , the numerical error is relatively large, which indicates that the numerical simulation can generate a difference larger than  $T_m/10$ . In the EG scheme, it is possible to suppress errors in the high-frequency region ( $\omega^* > \omega_{Re}^*$ ) especially ECR, which indicates that this scheme is also superior to the conventional scheme in terms of the numerical dispersion relation. Therefore, based on these numerical dispersion relations, it is predicted that time step that less than  $T_m/20$  can reproduce the plasma phenomenon.

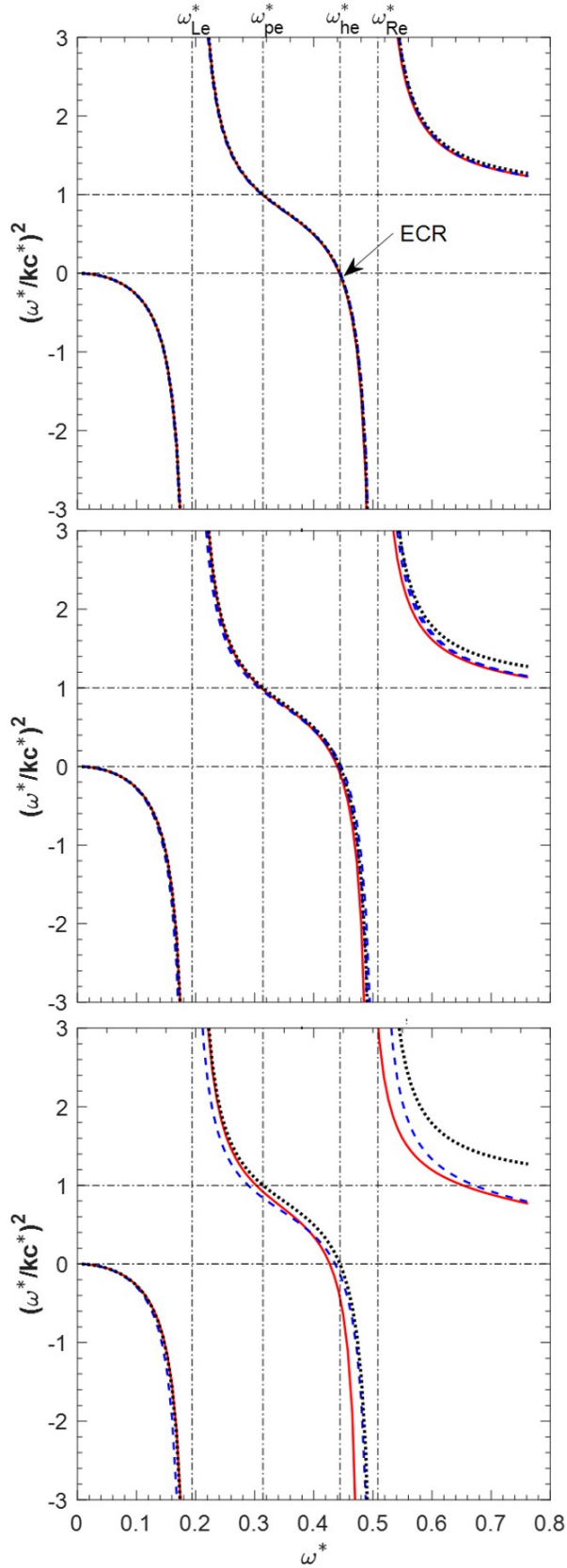


**Fig. C.14** Numerical dispersion relation for extraordinary waves. The dispersion relation can be calculated using the discrete Fourier transform (Eq. (C.60)). Red: EG-ECSIM, blue: ECSIM, black: theory. EG refers to the exact-gyro scheme proposed in subsection C.5.1. Top:  $T_m/40$ , center:  $T_m/20$ , bottom:  $T_m/10$ . In the high-frequency region ( $\omega^* > \omega_{Re}^*$ ), the EG scheme can suppress the dispersion error compared to that for the conventional ECSIM scheme.

### C.5.7 Demonstration of sub-cycle method

The proposed sub-cycle method (described in subsection C.5.1) was demonstrated. Unfortunately, there are no benchmark problems for ECR plasma sources. Instead, a very simply case is simulated. To check the validity of the numerical dispersion relation, the dimensions were  $\vec{E} = (E_x, E_y, 0)$ ,  $\vec{B} = (0, 0, B_{zm} + B_{zs})$ ,  $\vec{v} = (v_x, v_y, 0)$ , and  $\vec{x} = (x, 0, 0)$ . Here,  $B_{zs}$  is the static magnetic field and is given by  $B_z(x) = 2B_{ECR}(1 - \sin \pi x/L) - 2B_{min}(1 - 2 \sin \pi x/L)$ .  $B_{min} = 0.01$  T.  $B_{zm}$  is the variable of the magnetic field due to microwaves.  $E_y$  is the electric field of microwaves. The calculation domain is half the wavelength of microwaves. In this case, the frequency of microwaves is assumed to be  $\omega_m/2\pi = 4.25$  GHz. The calculation domain is thus about  $\lambda_m = 3.5$  cm. The resonance magnetic field  $B_{ECR}$  is about 0.15 T. The initial plasma density is given by satisfying  $\omega_{pe} = 0.5\omega_m$ . The initial electron temperature is assumed to be  $v_{th} = 0.01c$ . Time step is determined based on  $c\Delta t = \Delta x$ . The number of cells is 400. In this case, the grid size is approximately  $2.5\lambda_D$  to check the NDE scheme. The number of particles per cell is 100. The boundary condition is assumed to be the Mur boundary condition [178] at  $i = 0$  and a perfect electrical conductor (PEC) at  $i = N_x$ . The electric field of microwaves is excited at  $i = 1$  using soft injection. In this demonstration, for simplicity, the control of the electric field by absorption power is not performed [18].

The numerical proof is shown in Fig. C.15. If the sub-cycle method is mathematically correct, the explicit current density between macroscopic and particle interpolation must be exactly the same during a sub-cycle. The results indicate that even if statistical error is large, the two values are exactly the same within machine error. Therefore, the sub-cycle method is correct not only mathematically but also numerically. The demonstration of the sub-cycle method was performed using various numbers of sub-cycles  $L$ . The electric field with respect to the number of sub-cycle are shown in Fig. C.16. Here, three cases;  $L = 20, 40, 60$  are simulated and then the result shows after  $3 \times 10^3$  time steps. The results indicate that the distribution without the sub-cycle method is in good agreement with that with the sub-cycle method at  $L = 20, 40$ . Therefore, the proposed sub-cycle method is effective in practice. In this case, because the static magnetic field is about 4 to 5 orders of magnitude larger than the variable magnetic field, the approximation  $\bar{\alpha}_p^{n+k/L} \cong \bar{\alpha}_p^n \cong \bar{\alpha}_p^0$  is valid. However, for  $L = 80$  ( $dt = T_m/10$ ), the distribution is not in good agreement, especially for  $x/\lambda_m = 0 \sim 0.1$ . This result can be explained by the numerical dispersion relation shown in Fig. C.14. In other

words, the prediction of the time step may be effective. Note that this numerical dispersion relation cannot include the effect of thermal motion and boundary conditions, and may thus generate a difference between simulation and prediction.

The simulation time and numerical error versus the number of sub-cycles are shown in Fig. C.17. Here, the simulation time was normalized by the case without sub-cycles. The numerical error is defined as follows:

$$N_{sub, error} = \frac{1}{N_{cell}} \sum_{i=1}^{N_{cell}} \left( \frac{E_{y,w/o sub} - E_{y,w, sub}}{E_{y,w/o sub}} \right)^2 \quad (C.64)$$

where  $E_{y,w/o sub}$  and  $E_{y,w, sub}$  are the electric field without and with sub-cycles, respectively. Even if the number of sub-cycles is  $L = 40$ , the numerical error can be suppressed to be 15 %. Note that the evaluation of numerical error is based on the instantaneous values. It is expected that the error will be even smaller if time-averaged values are used. In this work, because the simulation was performed on a single processor, the simulation time saturated near  $L = 20$  and was about 10 times shorter than that without sub-cycles. This is because the simulation time of the particle velocity update and field solver increases with increasing number of sub-cycles. However, it is emphasized that the simulation time of the particle velocity update can be largely reduced by using parallel computing because the calculation is independent for each particle. Additionally, the field solver and the particle velocity update can be calculated separately. Therefore, with parallel computing, the simulation time can be further reduced for a given number of sub-cycles and will not saturate even for a large number of sub-cycles. In the current study, based on the tradeoff between numerical error and simulation time,  $L = 20 - 40$  is suitable for a single processor and  $L = 40 - 60$  is suitable for parallel computing.

The sub-cycle method is limited to NGP as the weight function. Several papers reported that the NGP function generates statistical noise that is larger than that for the cloud-in-cell function. This noise can increase finite grid instability [156, 157]. However, ECSIM has high robustness against finite grid instability [145]. Finally, to investigate the effect of the proposed numerical scheme, a simulation was performed with the NDE and EG schemes, respectively. It is noted that to achieve the steady state in an ECR plasma thruster, the simulation time requires  $10^4 \sim 10^6$  cycles. Therefore, the long cycle simulations are necessary.

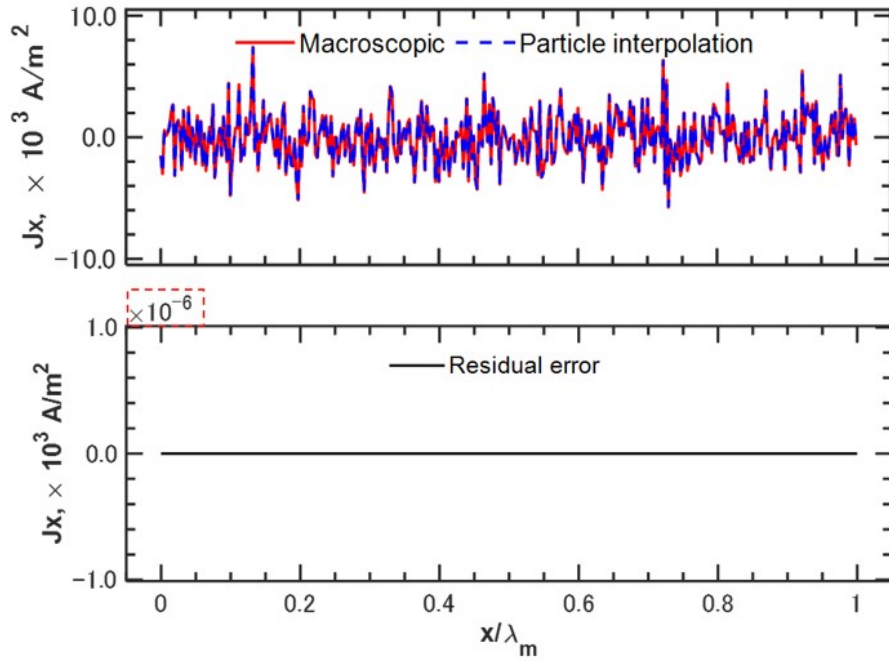


**Fig. C.15** Numerical proof of sub-cycle method. Residual error is the difference between macroscopic and particle interpolation. This figure shows that the explicit current densities calculated using macroscopic and particle interpolation are exactly the same during a sub-cycle.

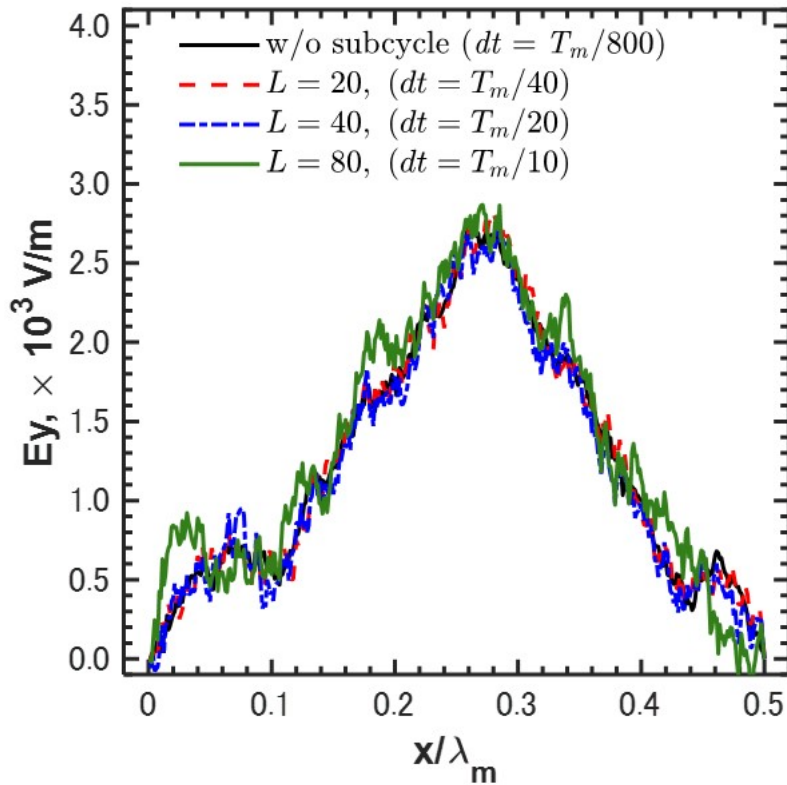


**Fig. C.16** Electric field with respect to the number of sub-cycle time step.  $L$  is the number of sub-cycles.

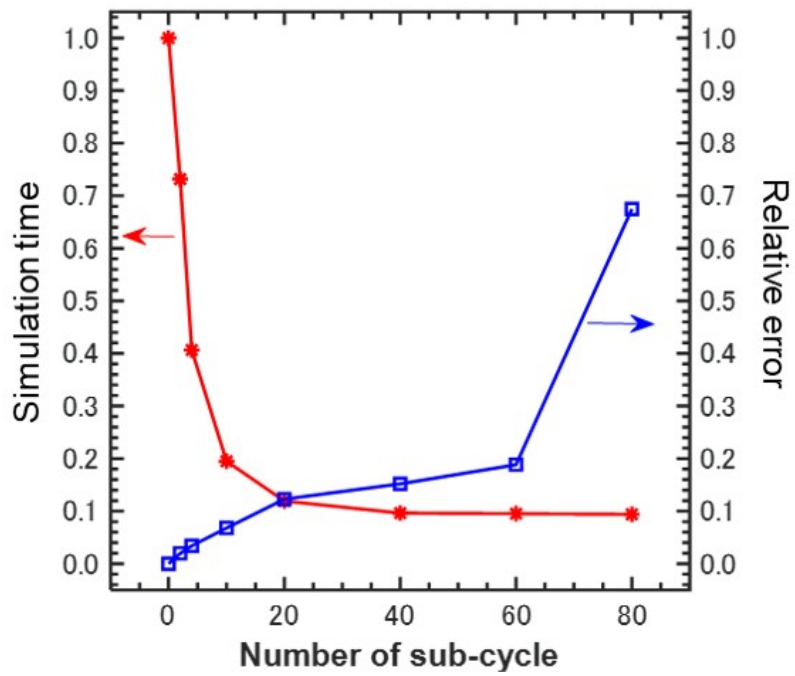


**Fig. C.17** Simulation time and numerical error versus number of sub-cycles. Note that the simulation was performed on a single processor. Here, the numerical error is that defined in Eq. (C.64) .

## C.6 Short conclusion

To establish the self-consistent numerical simulation model of microwave discharge ion thrusters, full-kinetic approach have been developed. Firstly, The explicit ES-full PIC simulation was developed. Then, following knowledge was obtained.

- Explicit Es full-PIC simulation

1. The plasma density in magnetic confined regions is ten times larger than that in other regions. The electron temperature in the confined regions is also larger than other regions and is the highest near the ECR layer, which is the fundamental characteristic of ECR plasma source and the results agree with the experimental results obtained by an electrostatic probe.
2. The trajectories of the electrons provided a insight in view of electron heating and confined. Electrons are confined by the two effects of the mirror magnetic field and the plasma sheath, indicating that the confinement effect depends on the electron energy, which leads to a superposition of two Maxwellian distributions.
3. The current percentage of ions and electrons is different at each wall. This is considered to be the result of diffusion against the magnetic field. The current percentage of ions is larger than that of electrons, where there is a parallel component of the magnetic field to the surface.
4. The trajectories of ions indicate that ions are weakly magnetized. As a result, ions have a drift velocity in the azimuthal direction and generate a roll torque around the thruster axis. However, the magnetic field makes ions are transported to the grid more efficiently. Therefore, whether or not ions are affected by the magnetic field is an important feature.

However, the ES full-PIC simulation cannot be captured by transition of microwave propagation, e.g, cut-off; thus, plasma mode-transition cannot be reproduced. In contrast, comparing ES-PIC simulation with EM-PIC simulation, simulation cost and numerical stability of EM-PIC simulation is more severe than that of ES-PIC simulation. To overcome this difficulty, the author focuses on the energy-conserving semi-implicit approach recently developed in filed of computational physics. Then, to apply to practical problem such as EP-devices, this thesis

provided fundamental research including the benchmark problem, macroscopic conservation, numerical dispersion relation. Detailed resells are described below.

- Implicit EM PIC simulation

1. Based on  $v_{th} \ll c$  (e.g., for LTPs), a sub-cycle method that maintains ECSIM was proposed. The proposed method is based on three assumptions, namely  $\vec{x}_p^{n+1/2+k/L} \cong \vec{x}_p^{n+1/2}$ ,  $\bar{\alpha}_p^{n+k/L}(\vec{x}_p^{n+1/2+k/L}) \cong \bar{\alpha}_p^n(\vec{x}_p^{n+1/2})$ , and the weight function is NGP. This method can avoid the calculation of particle interpolation during a sub-cycle, which reduces simulation time and enhances the efficiency of parallelization. We confirmed the correctness of the proposed method mathematically and numerically. The sub-cycle method was applied to an ECR plasma source. The results indicate that this method is very effective. In future work, long-term stability will be evaluated and parallel computing will be applied to multi-dimensional simulation.
2. To apply strongly magnetized plasma, the high-accuracy Boris solver proposed by Zenitani [158] was implemented in the ECSIM algorithm. This scheme is nonlinear on the magnetic field; however, this nonlinearity does not collapse the ECSIM solver because the solver is explicit on the magnetic field. In the ECR heating process, numerical damping can be greatly suppressed. It is possible to suppress errors in the high-frequency region, which indicates that the EG scheme is also superior to the conventional scheme in terms of the dispersion relation.
3. To make the proposed ECSIM easy to extend to many practical problems, the difficulty of code development must be reduced. In this paper, code validation using macroscopic conservation was proposed. The validation can be applied practical problems to evaluate the effect of grid size, time step, numerical scheme, and boundary conditions. The effects of the grid size and time step can be checked before a simulation by using the numerical dispersion relation.

## Appendix D

# Simulated ion extraction in the absence of ion extraction

### D.1 Objective

In gridded ion thrusters, high-voltage is applied to the grid system, e.g, screen and accelerator grids [1]. In such a situation, electric insulation is the one of the biggest burden in the experiment. Especially, to perform the probe measurement, it becomes more serious one. To overcome this problem, 'simulated experiment without ion extraction' was proposed by Brophy [179]. The method indicates that the plasma state of ion extraction is reproduced by decreasing the flow rate under without ion extraction; the method is based on the 0D-equation;  $n_n = n_{n0}(1 - \eta_u)$  [180]. Additionally, in numerical simulation, the plasma and neutral particles are often calculated independently [181]. In this method, DSMC simulation is performed without plasma and the plasma simulation uses the distribution of the neutral density obtained by DSMC simulation. The method is very effective to save the simulation cost, but the effect of ion extraction is not included. In this thesis, the author calls the simulation method 'decoupled numerical simulation'.

Though it is possible that these approaches do not include the non-0D effect (e.g., gas injection, ionization, ion recombination), which generates the difference from the plasma state in the presence of ion extraction. Thus, in this appendix, the validity of 'simulated ion extraction' and 'decoupled numerical simulation' will be discussed based on DSMC simulation described in chapter 3.

### D.1.1 Proposed methods to reproduce the neutral density under ion extraction

To reproduce ‘simulated experiment without ion extraction’ is that Eq. (D.11) matches Eq. (D.12). By integrating these equations over volume, following equations can be obtained.

$$\dot{M}_{out} = \dot{M}_{in} - \dot{M}_{in}\alpha_m\eta_u(1 - \eta_i), \quad (D.1)$$

$$\dot{M}_{out} = \dot{M}_{in}(1 - \alpha_m\eta_u). \quad (D.2)$$

Assuming that the velocity distribution function of neutral species is Maxwellian distribution at the grid. In addition, because it is difficult to predict the neutral bulk velocity  $U_n$  in advance,  $U_n = 0$  is employed. Under assumption of  $U_n = 0$ ,  $\dot{M}_{out}$  can be expressed as follows [22].

$$\dot{M}_{out} \approx \frac{A_{eff}v_{th}n_{n,ave}}{4}. \quad (D.3)$$

Here,  $v_{th}$  is thermal velocity,  $A_{eff}$  is the effective surface area transparent to neutral particles at the grid, and  $n_{n,ave}$  is the averaged neutral density over volume. From reference [122], the neutral density must be matched between with and without ion extraction.

$$n_{n,ave} = \frac{4\dot{M}_{in,w}(1 - \alpha_m\eta_u)}{v_{th}A_{eff,w}} = \frac{4\dot{M}_{in,w/o}(1 - \alpha_m\eta_u(1 - \eta_i))}{v_{th}A_{eff,w/o}}. \quad (D.4)$$

Here,  $v_{th}$  is assumed to be constant. The subscripts  $w$  and  $w/o$  show the states with and without ion extraction. Then, the author introduces the combination factor  $C$  as follows.

$$\dot{M}_{in,w/o} = C\dot{M}_{in,w}. \quad (D.5)$$

$$A_{eff,w/o} = C\frac{(1 - \alpha_m\eta_u(1 - \eta_i))}{1 - \alpha_m\eta_u}A_{eff,w}. \quad (D.6)$$

Based on Eqs (D.5) and (D.6), three choices: (A) Expansion of transparency, (B) Reduce gas, and (C) Combination of (A) and (B) are proposed. Firstly, the transparency at the grid is expanded to reproduce the neutral density with ion extraction. In particular, if the flow rate is the same ( $\dot{M}_{w/o} = \dot{M}_w$ ), the surface area can be calculated as follows.

$$A_{eff,w/o} = \frac{1 - \alpha_m\eta_u(1 - \eta_i)}{1 - \alpha_m\eta_u}A_{eff,w}. \quad (D.7)$$

In this paper, this case is called (A) Expansion of transparency. In this situation,  $\eta_i \approx 1$  may not be valid in case the transparency is expanded. Ideally, after predicting  $\eta_i$ ,  $A_{eff,w/o}$  should be determined. However, it is generally difficult to predict  $\eta_i$  in advance. Thus, the author proposes that  $A_{eff,w/o}$  is determined under  $\eta_i = 1$  as follows.

$$A_{eff,w/o} = \frac{1}{1 - \alpha_m \eta_u} A_{eff,w}. \quad (D.8)$$

The second choice is that  $\dot{M}_{w/o}$  is reduced to match the neutral density with ion extraction. In particular, if the same grid system is used ( $A_{eff,w/o} = A_{eff,w}$ ),  $\dot{m}_{w/o}$  can be calculated as follows.

$$\dot{M}_{w/o} = \frac{1 - \alpha_m \eta_u}{1 - \alpha_m \eta_u (1 - \eta_i)} \dot{M}_w. \quad (D.9)$$

In this situation, because SHAG is used,  $\eta_i \approx 1$  is valid as described in section 2.5.1.

$$\dot{M}_{w/o} \approx (1 - \alpha_m \eta_u) \dot{M}_w. \quad (D.10)$$

This case is called (B) Reduce gas.

Finally, the third choice is the combination of cases (A) and (B). Usually, to measure plasma parameters such as by a Langmuir probe, punched metal is used instead of the screen grid and accelerator grid [162, 161]. However, it can be difficult to reproduce the neutral density in a single kind of punched metal (grid). For instance, if  $\eta_u$  is drastically changed by the input flow rate, it is impossible to reproduce the neutral density for all values of the input flow rate. In this case, it is necessary to combine (A) and (B).

### D.1.2 Validity of ‘simulated experiment without ion extraction’ and ‘decoupled numerical simulation’

To reproduce the neutral density distribution under the condition without ion extraction, three methods: (A) Expansion of transparency, (B) Reduce gas, and (C) Combination of (A) and (B) were simulated. Simulation cases are summarized in Tab. D.1. In method (A), three cases: (a)  $\eta_i = 1.0$ , (b)  $\eta_i = 0.75$ , (c)  $\eta_i = 0.5$  were simulated. In case (d), method (B) was simulated. Finally, in method (C),  $\eta_i = 0.75$  is selected based on the simulation results of (a), and the combination factor (e)  $C = 0.9$ , (f)  $C = 0.8$  were simulated. As the simulation condition, the optimal flow rate was used, and the ionization rate was used in two cases (i)  $R = 0.0$  and (ii)  $R = 0.5$ , and was  $L_w = 18$  cm according to the simulation results with ion extraction.

Fig. D.1 and shows the simulation results for WG and DC injection. Then, the maximum, minimum, and average neutral density are summarized in Tab .D.2. For comparison, the neutral density distribution with ion extraction (same as Fig. 3.5-top (b)) is also shown.

In case (i) of WG injection (Fig. D.1-left), case (a), (b), and (c) are in good agreement for the “w ion extraction”. As shown in TABLE II, the average neutral density is only changed from  $2.4 \times 10^{19} \text{ m}^{-3}$  to  $2.2 \times 10^{19} \text{ m}^{-3}$  by reducing from  $\eta_i = 1.0$  to  $\eta_i = 0.5$ , which indicates that  $\eta_i$  is not very sensitive to the neutral density distribution. Case (d) cannot reproduce the “w ion extraction”. Additionally, in case (ii), (a), (b), and (c) are also better agreement with “w ion extraction” than (d). These results indicate that (A) Expansion of transparency is superior to (B) Reduce gas.

In DC injection, in both cases (i) and (ii) (Fig. D.2-right), case (a), (b), and (c) are also in better agreement with “w ion extraction” than (d). However, in DC injection,  $\eta_i$  is sensitive to the density distribution and the result of (b)  $\eta_i = 0.75$  is the best agreement. In both WG and DC injections, case (e) is in better agreement with “w ion extraction” than (f), which also indicates that it is better to be as close to (A) as possible.

Based on these simulation results (Fig. D.1 and Fig. D.2), the author recommends that transparency is expanded to reproduce Eq. (D.6) as much as possible and that the remaining discrepancy is removed by adjusting the flow rate. If it is difficult to make the punched metal, another alternative is that the accelerator grid is removed while the screen grid is maintained. Typically, the transparency of the accelerator and screen grid is 10% and 70% respectively. Thus, if  $\eta_u$  is 0.85, the transparency at the grid is  $10/(1-0.85) \approx 70\%$ , which indicates that

removing the accelerator grid can reproduce the state with ion extraction. Secondly, if  $\eta_u$  is varied in different thruster conditions, e.g., different flow rates and microwave power, the transparency at the grid  $A_{eff,w/o}$  should be adjusted by the maximum value of  $\eta_u$ . Last, the author also recommends that in decoupled numerical simulation, the input flow rate be the same as the state with ion extraction and that pre-DSMC simulation is performed to set the transparency  $A_{eff,w/o}$ , as shown in Eq. (D.6), by estimating  $\eta_u$ .

These recommendations can be explained from the continuity equation. From Fig. 3.1, in the presence of ion extraction, the continuity equation can be expressed as follows.

$$\vec{\nabla} \cdot (n_n \vec{U}_n) = \dot{M}_{in} f_{in}(\vec{x}_{in}) + \dot{M}_{in} \frac{\alpha_m \eta_u}{\eta_{ex}} [-f_{ioni}(\vec{x}_{ioni}) + (1 - \eta_{ex}) f_{re}(\vec{x}_{re})]. \quad (D.11)$$

In contrast, in the case without ion extraction, the continuity equation (D.11) is modified as follows.

$$\vec{\nabla} \cdot (n_n \vec{U}_n) = \dot{M}_{in} f_{in}(\vec{x}_{in}) + \dot{M}_{in} \frac{\alpha_m \eta_u}{\eta_{ex}} [-f_{ioni}(\vec{x}_{ioni}) + (1 - \eta_{ex}) f_{re}(\vec{x}_{re}) + \eta_i \eta_{ex} f_{re}^*(\vec{x}_{re})]. \quad (D.12)$$

By subtracting from Eq. (D.11) to (D.12) and considering Eq. (D.5), following equation can be obtained.

$$\begin{aligned} \vec{\nabla} \cdot (\delta \vec{\Gamma}) &= (1 - C) \dot{M}_{in} f_{in}(\vec{x}_{in}) - \frac{\alpha_m \eta_u}{\eta_{ex}} \delta \dot{M}_{ioni} \\ &+ \frac{\alpha_m \eta_u (1 - \eta_{ex})}{\eta_{ex}} \delta \dot{M}_{recom} - C \dot{M}_{in} \alpha_m \eta_u \eta_i f_{re}^*(\vec{x}_{re}). \end{aligned} \quad (D.13)$$

Here,  $\delta \vec{\Gamma} = n_{n,w} \vec{U}_{n,w} - n_{n,w/o} \vec{U}_{n,w/o}$ ,  $\delta \dot{M}_{ioni} = \dot{M}_{in} (f_{ioni,w} - C f_{ioni,w/o})$ ,  $\delta \dot{M}_{recom} = (1 - C) \dot{M}_{in}$ . We used  $\dot{M}_{in,w/o} = C \dot{M}_{in,w}$ . If  $C$  is close to 1, i.e., (A) Expansion of transparency can better reproduce the density distribution with ion extraction because the flow rate of gas injection  $\dot{M}_{in}$  is the same. In addition, because the second, third, fourth terms on the right-hand side (D.13) are proportional to  $\eta_u$ , the discrepancy of  $\vec{\nabla} \cdot (\delta \vec{\Gamma})$  becomes small when  $\eta_u$  is small.

Our recommendation can be applied to several kinds of ion thrusters. For instance, in the  $\mu 10$  ion thruster, the difference between WG and DC injection gives a density gradient inside the waveguide. Our recommended settings and parameters can reproduce this density gradient

to a reasonable degree. Additionally, in the case of DC discharge ion thrusters, gas injection is concentrated on the exit of the hollow cathode [182]. From the numerical simulation of Wirtz [182], the inhomogeneity of gas injection is expected to be very important because the ionization accounts for 50% of the ionization downstream of the hollow cathode. Thus, our recommendation is suitable for reproducing the ionization downstream of the hollow cathode.

Finally, the discrepancy of  $\eta_i$  is explained. Because the surface area  $A_{eff,w/o} = A_{eff,w}/(1 - \alpha_m \eta_u)$  is determined based on  $\eta_i = 1$  (Eq. (D.8)), case (a) ( $\eta_i = 1$ ) should be in the best agreement with ‘with ion extraction’. However, the simulation results show that (b)  $\eta_i = 0.75$  is in better agreement than (a)  $\eta_i = 1$ . This discrepancy is derived from the assumption of  $U_n \approx 0$ . As shown in Eq. (D.3),  $A_{eff,w/o}$  is determined based on  $U_n \approx 0$ . However, as shown in Fig. 3.6, the velocity distribution exists in the case with ion extraction. Because it is difficult to predict the velocity distribution in advance, it is also difficult to predict  $\eta_i$  accurately. However, because the neutral species at the grid has negative velocity,  $\eta_i$  should be  $\eta_i < 1$ . In our simulation cases, because  $\eta_i \approx 0.75$  is a good agreement, the collecting current should be 75% of ion beam current.  $\eta_i$  can be roughly adjusted by changing the negative bias voltage at the grid (punched metal) until ion saturation current [161].

**Table D.1** Summary of simulation cases to reproduce the neutral density distribution under the condition without ion extraction. (A) ~ (C) is explained in subsection D.1.1.

Case	Method	$\eta_i$
(a)	(A) Expansion of transparency	1.0
(b)	(A) Expansion of transparency	0.75
(a)	(A) Expansion of transparency	0.5
(d)	(B) Reduce gas	1.0
(e)	(C) Combination of (A) and (B) (C=0.9)	0.75
(f)	(C) Combination of (A) and (B) (C=0.8)	0.75

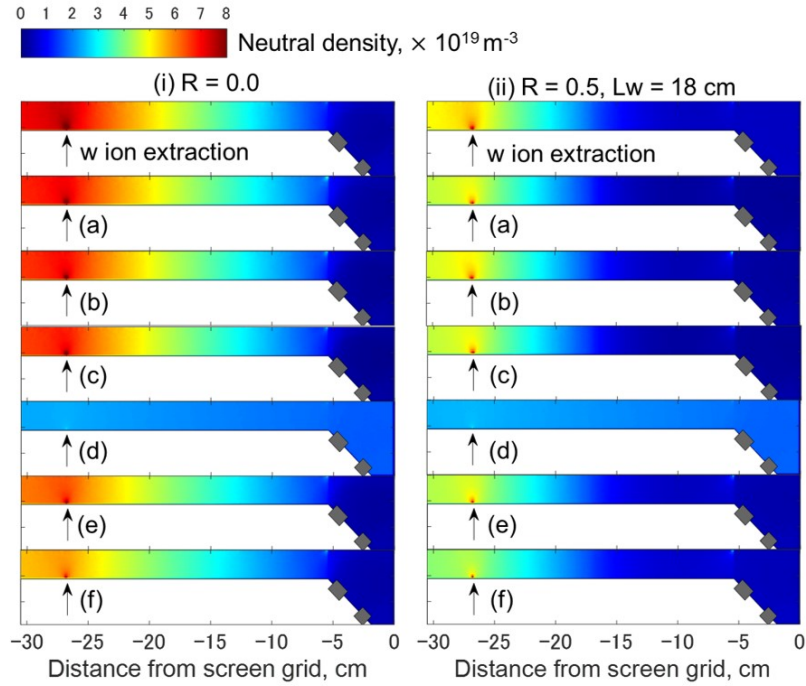


**Fig. D.1** Two-dimensional neutral density distribution in case of WG injection. The simulation cases are summarized in Tab D.2. For comparison, simulation results in the case with ion extraction (Fig. 3.5) are also shown.

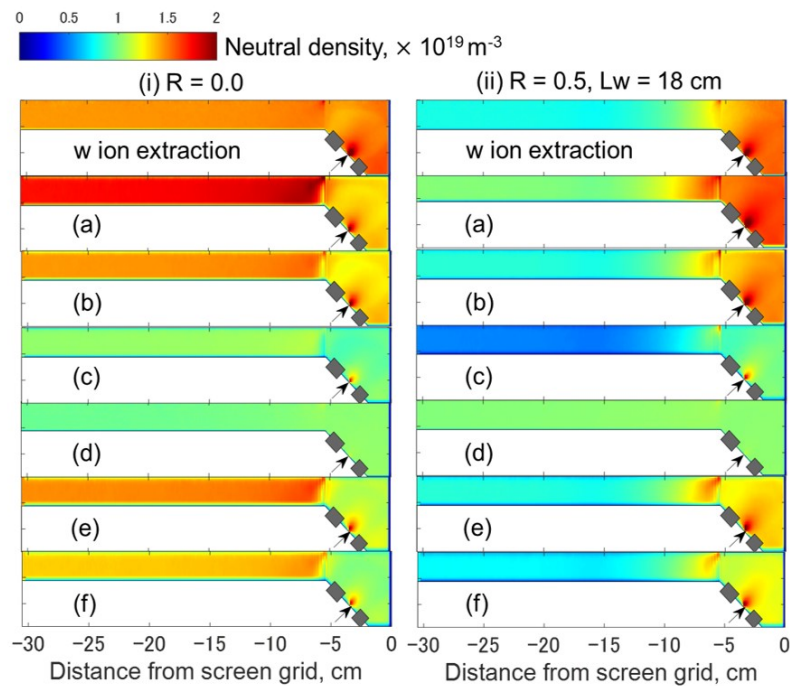


**Fig. D.2** Two-dimensional neutral density distribution in case of DC injection. The simulation cases are summarized in Tab. D.2. For comparison, simulation results in the case with ion extraction (Fig. 3.5) are also shown.

**Table D.2** Comparison of the maximum, minimum, average neutral densities for WG and DC injection. Results of this table are obtained from Fig. D.1 and D.2. The simulation cases are summarized in Table D.1.

	WG injection						DC injection					
	(i) $R = 0.0$			(ii) $R = 0.5, L_w = 18$ cm			(i) $R = 0.0$			(i) $R = 0.5, L_w = 18$ cm		
w ion	9.0	0.22	2.2	8.9	0.38	1.7	3.3	0.72	1.4	3.3	0.40	1.2
(a)	9.0	0.20	2.4	8.8	0.20	1.4	2.9	0.94	1.5	2.9	0.68	1.4
(b)	8.9	0.15	2.3	8.7	0.17	1.3	2.7	0.88	1.4	2.7	0.55	1.2
(c)	8.9	0.11	2.2	8.7	0.15	1.2	2.5	0.73	1.2	2.5	0.37	0.90
(d)	2.0	0.80	1.2	1.9	0.78	1.2	1.5	1.1	1.2	1.2	1.0	1.0
(e)	8.3	0.20	2.2	8.2	0.30	1.3	2.3	0.90	1.3	2.6	0.70	1.3
(f)	7.6	0.27	2.1	7.4	0.41	1.3	1.8	0.95	1.2	2.3	0.64	1.1

## D.2 Short conclusion

In this appendix, validity of ‘simulated experiment without ion extraction’ and ‘decoupled numerical simulation’, i.e., to reproduce the neutral density distribution under ion extraction in the absence of ion extraction, i.e., ‘simulated experiment without ion extraction’, was investigated by using DSMC simulation model.

To reproduce the neutral density distribution with ion extraction by using experimental conditions without ion extraction, there are three choices: (A) Expansion of transparency, (B) Reduce gas, and (C) Combination of (A) and (B). Based on the simulations of these three cases, case (A) is the best agreement. That is, the grid transparency is adjusted so that Eq.(D.8) is reproduced as much as possible and the rest difference is commented by adjusting the flow rate. This is because when the flow rate is the same, the inhomogeneity of gas injection is consistent with the case with ion extraction. If  $\eta_u$  is varied in different thruster conditions, the transparency is adjusted at the maximum value of  $\eta_u$ .

## REFERENCES

- [1] John R. Brophy. NASA's deep space 1 ion engine (plenary). *Review of Scientific Instruments*, 73(2 II):1071, 2002.
- [2] Marc D. Rayman, Thomas C. Fraschetti, Carol A. Raymond, and Christopher T. Russell. Dawn: A mission in development for exploration of main belt asteroids Vesta and Ceres. *Acta Astronautica*, 58(11):605–616, 2006.
- [3] Christoph Steiger, Elsa Montagnon, Andrea Accomazzo, and Paolo Ferri. BepiColombo mission to Mercury: First year of flight. *Acta Astronautica*, 170(January):472–479, 2020.
- [4] Vernon H. Chaplin, Dan M. Goebel, Rhodri A. Lewis, Francis Lockwood Estrin, and Peter N. Randall. Accelerator Grid Life Modeling of T6 Ion Thruster for BepiColombo. *Journal of Propulsion and Power*, 37(3):436–449, 2021.
- [5] Ralf Kukies Ranter Killinger, Michael Surauer, Angeo Tomasetto, and Leo van Holtz. ARTEMIS ORBIT RAISING INFLIGHT EXPERIENCE WITH ION PROPULSION. *Acta Astronautica*, 50(5):239–244, 2003.
- [6] Hitoshi Kuninaka, Kazutaka Nishiyama, Ikko Funaki, Yukio Shimizu, Tetsuya Yamada, and Jun'ichiro Kawaguchi. Assessment of plasma interactions and flight status of the HAYABUSA asteroid explorer propelled by microwave discharge ion engines. *IEEE Transactions on Plasma Science*, 34(5 II):2125–2132, 2006.
- [7] Kazutaka Nishiyama, Satoshi Hosoda, Ryudo Tsukizaki, and Hitoshi Kuninaka. In-flight operation of the Hayabusa2 ion engine system on its way to rendezvous with asteroid 162173 Ryugu. *Acta Astronautica*, 166(March 2019):69–77, 2020.
- [8] Hiroyuki Koizumi, Hiroki Kawahara, Kazuya Yaginuma, Jun Asakawa, Yuichi Nakagawa, Yusuke Nakamura, Shunichi Kojima, Toshihiro Matsuguma, Ryu Funase, Junichi

- Nakatsuka, et al. Initial flight operations of the miniature propulsion system installed on small space probe: Procyon. *Transactions of the Japan Society for Aeronautical and Space Sciences, Aerospace Technology Japan*, 14(ists30):Pb\_13–Pb\_22, 2016.
- [9] Ryudo Tsukizaki, Hiroyuki Koizumi, Satoshi Hosoda, Kazutaka Nishiyama, and Hitoshi Kuninaka. Improvement of the thrust force of the ecr ion thruster  $\mu 10$ . *Transactions of the Japan Society For Aeronautical and Space Sciences, Aerospace Technology Japan*, 8(ists27):Pb\_67–Pb\_72, 2010.
- [10] Ryudo Tsukizaki, Hiroyuki Koizumi, Kazutaka Nishiyama, and Hitoshi Kuninaka. Measurement of axial neutral density profiles in a microwave discharge ion thruster by laser absorption spectroscopy with optical fiber probes. *Review of Scientific Instruments*, 82(12), 2011.
- [11] Ryudo Tsukizaki, Toshiyuki Ise, Hiroyuki Koizumi, Hiroyoshi Togo, Kazutaka Nishiyama, and Hitoshi Kuninaka. Thrust Enhancement of a Microwave Ion Thruster. *Journal of Propulsion and Power*, 30(5):1383–1389, 2014.
- [12] Toshiyuki Ise, Ryudo Tsukizaki, Hiroyoshi Togo, Hiroyuki Koizumi, and Hitoshi Kuninaka. Electric field measurement in microwave discharge ion thruster with electro-optic probe. *Review of Scientific Instruments*, 83(12), 2012.
- [13] Priti, R. K. Gangwar, and R. Srivastava. Collisional-radiative model of xenon plasma with calculated electron-impact fine-structure excitation cross-sections. *Plasma Sources Science and Technology*, 28(2), 2019.
- [14] Rajesh Srivastava, A. D. Stauffer, and Lalita Sharma. Excitation of the metastable states of the noble gases. *Physical Review A - Atomic, Molecular, and Optical Physics*, 74(1):1–10, 2006.
- [15] D. Ton-That and M. R. Flannery. Cross sections for ionization of metastable rare-gas atoms ( $\text{Ne}^*$ ,  $\text{Ar}^*$ ,  $\text{Kr}^*$ ,  $\text{Xe}^*$ ) and of metastable  $\text{N}_2^*$ ,  $\text{CO}^*$  molecules by electron impact. *Physical Review A*, 15(2):517–526, 1977.
- [16] Y. Tani, R. Tsukizaki, D. Koda, K. Nishiyama, and H. Kuninaka. Performance improvement of the  $\mu 10$  microwave discharge ion thruster by expansion of the plasma production volume. *Acta Astronautica*, 157(July 2018):425–434, 2019.

- [17] Yoshitaka Tani, Yusuke Yamashita, Ryudo Tsukizaki, Kazutaka Nishiyama, and Hitoshi Kuninaka. Effect of discharge chamber geometry on ion loss in microwave discharge ion thruster. *Acta Astronautica*, 176(May):77–88, 2020.
- [18] Y. Yamashita, Y. Tani, R. Tsukizaki, D. Koda, and K. Nishiyama. Numerical investigation of plasma properties for the microwave discharge ion thruster  $\mu 10$  using PIC-MCC simulation. *Physics of Plasmas*, 26(7), 2019.
- [19] Ryudo Tsukizaki. *Plasma diagnostics of the microwave ion thruster utilizing optical fiber probes*. PhD thesis, The University of Tokyo, 2013.
- [20] Erich S. Weibel. Spontaneously growing transverse waves in a plasma due to an anisotropic velocity distribution. *Physical Review Letters*, 2(3):83–84, 1959.
- [21] Yuxi Chen and Gábor Tóth. Gauss ’ s Law satisfying Energy-Conserving Semi-Implicit Particle-in-Cell method. *Journal of Computational Physics*, 386:632–652, 2019.
- [22] Dan M Goebel and Ira Katz. *Fundamentals of electric propulsion: ion and Hall thrusters*, volume 1. John Wiley and Sons, 2008.
- [23] Howard Gray, Peter Smith, and David Fearn. Design and development of the uk-10 ion propulsion system. In *32nd Joint Propulsion Conference and Exhibit*, page 3084, 1996.
- [24] Rainer Killinger, Helmut Bassner, Johann Mueller, and Ralf Kukies. Rita ion propulsion for artemis lifetime test results. In *36th AIAA/ASME/SAE/ASEE Joint Propulsion Conference and Exhibit*, page 3273, 2000.
- [25] Kiyoshi Kinefuchi, Yoshio Nunome, Shinatora Cho, Ryudo Tsukizaki, and Tat Loon Chng. Two-photon absorption laser induced fluorescence with various laser intensities for density measurement of ground state neutral xenon. *Acta Astronautica*, 161(March):382–388, 2019.
- [26] Ikkoh Funaki, Hitoshi Kuninaka, Kyoichiro Toki, and Shin Satori. Plasma diagnostics and numerical modeling of a microwave ion engine. *34th AIAA/ASME/SAE/ASEE Joint Propulsion Conference Exhibit*, pages AIAA 98–3341, 1998.
- [27] Dan Lev, Roger M. Myers, Kristina M. Lemmer, Jonathan Kolbeck, Hiroyuki Koizumi, and Kurt Polzin. The technological and commercial expansion of electric propulsion. *Acta Astronautica*, 159(March):213–227, 2019.

- [28] E. Y. Choueiri. A Critical History of Electric Propulsion: The First 50 Years (1906-1956). *Journal of Propulsion and Power*, 20(2):193–203, 2004.
- [29] Stéphane Mazouffre. Electric propulsion for satellites and spacecraft: Established technologies and novel approaches. *Plasma Sources Science and Technology*, 25(3), 2016.
- [30] I. Levchenko, S. Xu, S. Mazouffre, D. Lev, D. Pedrini, D. Goebel, L. Garrigues, F. Taccogna, and K. Bazaka. Perspectives, frontiers, and new horizons for plasma-based space electric propulsion. *Physics of Plasmas*, 27(2), 2020.
- [31] Hitoshi Kuninaka and Shin Satori. Development and Demonstration of a Cathodeless Electron Cyclotron Resonance Ion Thruster. *Journal of Propulsion and Power*, 14(6):1022–1026, 1998.
- [32] H. Nishiyama, K. Hosoda, S. Usui, M. Tsukizaki, R. Hayashi, H. Shimizu, Y. Kuninaka. Feasibility Study on Performance Enhancement Options for the ECR Ion Thruster  $\mu 10$ . *TRANSACTIONS OF THE JAPAN SOCIETY FOR AERONAUTICAL AND SPACE SCIENCES, SPACE TECHNOLOGY JAPAN 2008*, 7(July):1–12, 2008.
- [33] Hiroyuki Koizumi and Hitoshi Kuninaka. Miniature Microwave Discharge Ion Thruster Driven by 1 Watt Microwave Power. *Journal of Propulsion and Power*, 26(3):601–604, 2010.
- [34] Kazutaka Nishiyama and Hitoshi Kuninaka. Microwave power absorption coefficient of an ECR xenon ion thruster. *Surface and Coatings Technology*, 202(22-23):5262–5265, 2008.
- [35] Hiroyuki Koizumi, Kimiya Komurasaki, Junichi Aoyama, and Koji Yamaguchi. Engineering model of the miniature ion propulsion system for the nano-satellite: Hodoyoshi-4. *Transactions of the Japan Society for Aeronautical and Space Sciences, Aerospace Technology Japan*, 12(ists29):Tb\_19–Tb\_24, 2014.
- [36] Kazutaka Nishiyama, T Hiroyuki, K Yasuhiro, and A Tomoko. Destiny+: technology demonstration and exploration of asteroid 3200 phaethon. In *68th Int. Astronaut. Congress*, 2017.
- [37] Igor D. Kaganovich, Andrei Smolyakov, Yevgeny Raitses, Eduardo Ahedo, Ioannis G. Mikellides, Benjamin Jorns, Francesco Taccogna, Renaud Gueroult, Sedina Tsikata,

- Anne Bourdon, Jean Pierre Boeuf, Michael Keidar, Andrew Tasman Powis, Mario Merino, Mark Cappelli, Kentaro Hara, Johan A. Carlsson, Nathaniel J. Fisch, Pascal Chabert, Irina Schweigert, Trevor Lafleur, Konstantin Matyash, Alexander V. Khrabrov, Rod W. Boswell, and Amnon Fruchtman. Physics of  $e \times B$  discharges relevant to plasma propulsion and similar technologies. *Physics of Plasmas*, 27(12), 2020.
- [38] Kentaro Hara. An overview of discharge plasma modeling for Hall effect thrusters. *Plasma Sources Science and Technology*, 28(4):44001, 2019.
- [39] Kazunori Takahashi. *Helicon-type radiofrequency plasma thrusters and magnetic plasma nozzles*, volume 3. Springer Singapore, 2019.
- [40] I. Adamovich, S. D. Baalrud, A. Bogaerts, P. J. Bruggeman, M. Cappelli, V. Colombo, U. Czarnetzki, U. Ebert, J. G. Eden, P. Favia, D. B. Graves, S. Hamaguchi, G. Hieftje, M. Hori, I. D. Kaganovich, U. Kortshagen, M. J. Kushner, N. J. Mason, S. Mazouffre, S. Mededovic Thagard, H. R. Metelmann, A. Mizuno, E. Moreau, A. B. Murphy, B. A. Niemira, G. S. Oehrlein, Z. Lj Petrovic, L. C. Pitchford, Y. K. Pu, S. Rauf, O. Sakai, S. Samukawa, S. Starikovskaia, J. Tennyson, K. Terashima, M. M. Turner, M. C.M. Van De Sanden, and A. Vardelle. The 2017 Plasma Roadmap: Low temperature plasma science and technology. *Journal of Physics D: Applied Physics*, 50(32), 2017.
- [41] Francis F Chen et al. *Introduction to plasma physics and controlled fusion*, volume 1. Springer, 1984.
- [42] A. Smolyakov, T. Zintel, L. Couedel, D. Sydorenko, A. Umnov, E. Sorokina, and N. Marusov. Anomalous Electron Transport in One-Dimensional Electron Cyclotron Drift Turbulence. *Plasma Physics Reports*, 46(5):496–505, 2020.
- [43] T. Charoy, T. Lafleur, A. Tavant, P. Chabert, and A. Bourdon. A comparison between kinetic theory and particle-in-cell simulations of anomalous electron transport in  $e \times B$  plasma discharges. *Physics of Plasmas*, 27(6), 2020.
- [44] Benjamin A. Jorns, Ioannis G. Mikellides, and Dan M. Goebel. Ion acoustic turbulence in a 100-A LaB6 hollow cathode. *Physical Review E - Statistical, Nonlinear, and Soft Matter Physics*, 90(6):1–10, 2014.

- [45] T. Lafleur, R. Martorelli, P. Chabert, and A. Bourdon. Anomalous electron transport in Hall-effect thrusters: Comparison between quasi-linear kinetic theory and particle-in-cell simulations. *Physics of Plasmas*, 25(6), 2018.
- [46] Ioannis G. Mikellides, Alejandro Lopez Ortega, Ira Katz, and Benjamin A. Jorns. Hall2De simulations with a first-principles electron transport model based on the electron cyclotron drift instability. *52nd AIAA/SAE/ASEE Joint Propulsion Conference, 2016*, pages 1–20, 2016.
- [47] Ioannis G. Mikellides and Alejandro Lopez Ortega. Growth of the modified two-stream instability in the plume of a magnetically shielded Hall thruster. *Physics of Plasmas*, 27(10), 2020.
- [48] Ioannis G. Mikellides and Alejandro Lopez Ortega. Growth of the lower hybrid drift instability in the plume of a magnetically shielded Hall thruster. *Journal of Applied Physics*, 129(19):193301, 2021.
- [49] Jean Pierre Boeuf. Tutorial: Physics and modeling of Hall thrusters. *Journal of Applied Physics*, 121(1), 2017.
- [50] Yoshinori Takao, Hiroyuki Koizumi, Kimiya Komurasaki, Koji Eriguchi, and Kouichi Ono. Three-dimensional particle-in-cell simulation of a miniature plasma source for a microwave discharge ion thruster. *Plasma Sources Science and Technology*, 23(6), 2014.
- [51] Yoshinori Takao, Koji Eriguchi, and Kouichi Ono. Effect of capacitive coupling in a miniature inductively coupled plasma source. *Journal of Applied Physics*, 112(9), 2012.
- [52] S. Barral, K. Makowski, Z. Peradzyński, N. Gascon, and M. Dudeck. Wall material effects in stationary plasma thrusters. II. Near-wall and in-wall conductivity. *Physics of Plasmas*, 10(10):4137–4152, 2003.
- [53] Yosuke Sato, Hiroyuki Koizumi, Masakatsu Nakano, and Yoshinori Takao. Electron loss mechanisms in a miniature microwave discharge water neutralizer. *Physics of Plasmas*, 27(6):063505, 2020.
- [54] T. Hori, M. Kogano, M. D. Bowden, K. Uchino, and K. Muraoka. A study of electron energy distributions in an inductively coupled plasma by laser Thomson scattering. *Journal of Applied Physics*, 83(4):1909–1916, 1998.

- [55] Benjamin Vincent, Sedina Tsikata, and Stéphane Mazouffre. Incoherent Thomson scattering measurements of electron properties in a conventional and magnetically-shielded Hall thruster. *Plasma Sources Science and Technology*, 29(3), 2020.
- [56] Michael A Lieberman and Alan J Lichtenberg. *Principles of plasma discharges and materials processing*. John Wiley and Sons, 2005.
- [57] Yuichi Nakagawa, Hiroyuki Koizumi, Yuki Naito, and Kimiya Komurasaki. Water and xenon ECR ion thruster - Comparison in global model and experiment. *Plasma Sources Science and Technology*, 29(10), 2020.
- [58] Vernon H. Chaplin, Benjamin A. Jorns, Alejandro Lopez Ortega, Ioannis G. Mikellides, Ryan W. Conversano, Robert B. Lobbia, and Richard R. Hofer. Laser-induced fluorescence measurements of acceleration zone scaling in the 12.5 kW HERMeS Hall thruster. *Journal of Applied Physics*, 124(18), 2018.
- [59] V. H. Chaplin, R. B. Lobbia, A. Lopez Ortega, I. G. Mikellides, R. R. Hofer, J. E. Polk, and A. J. Friss. Time-resolved ion velocity measurements in a high-power Hall thruster using laser-induced fluorescence with transfer function averaging. *Applied Physics Letters*, 116(23):234107, 2020.
- [60] W. A. Hargus and M. A. Cappelli. Laser-induced fluorescence measurements of velocity within a Hall discharge. *Applied Physics B: Lasers and Optics*, 72(8):961–969, 2001.
- [61] Stéphane Mazouffre. Laser-induced fluorescence diagnostics of the cross-field discharge of Hall thrusters. *Plasma Sources Science and Technology*, 22(1), 2013.
- [62] L. C. Pitchford, J. Kang, C. Punset, and J. P. Boeuf. Calculated characteristics of radio-frequency plasma display panel cells including the influence of xenon metastables. *Journal of Applied Physics*, 92(12):6990–6997, 2002.
- [63] Xi Ming Zhu and Yi Kang Pu. A simple collisional-radiative model for low-temperature argon discharges with pressure ranging from 1 Pa to atmospheric pressure: Kinetics of Paschen 1s and 2p levels. *Journal of Physics D: Applied Physics*, 43(1), 2010.
- [64] M. Walhout, A. Witte, and S. L. Rolston. Precision measurement of the metastable  $6s\ [3/2]2$  lifetime in xenon. *Physical Review Letters*, 72(18):2843–2846, 1994.

- [65] Ralchenko Yu. Reader J. Kramida, A. and NIST ASD Team. NIST Atomic Spectra Database (version 5.9). *Journal of Physics D: Applied Physics*, 2021.
- [66] J. Meunier, Ph Belenguer, and J. P. Boeuf. Numerical model of an AC plasma display panel cell in neon-xenon mixtures. *IEEE International Conference on Plasma Science*, 731(March 1995):126, 1994.
- [67] G. J.M. Hagelaar, K. Makasheva, L. Garrigues, and J. P. Boeuf. Modelling of a dipolar microwave plasma sustained by electron cyclotron resonance. *Journal of Physics D: Applied Physics*, 42(19), 2009.
- [68] Kentaro Hara, Michael J. Sekerak, Iain D. Boyd, and Alec D. Gallimore. Perturbation analysis of ionization oscillations in Hall effect thrusters. *Physics of Plasmas*, 21(12), 2014.
- [69] Yang Wang, Yan Fei Wang, Xi Ming Zhu, Oleg Zatsarinny, and Klaus Bartschat. A xenon collisional-radiative model applicable to electric propulsion devices: I. Calculations of electron-impact cross sections for xenon ions by the Dirac B-spline R-matrix method. *Plasma Sources Science and Technology*, 28(10), 2019.
- [70] Vernon H. Chaplin, Mary Konopliv, Timothy Simka, Lee K. Johnson, Robert B. Lobbia, and Richard E. Wirz. Insights from Collisional-Radiative Models of Neutral and Singly-Ionized Xenon in Hall Thrusters. pages 1–23, 2021.
- [71] Leanne C Pitchford, Luis L Alves, Klaus Bartschat, Stephen F Biagi, Marie-Claude Bordage, Igor Bray, Chris E Brion, Michael J Brunger, Laurence Campbell, Alise Chachereau, et al. Lxcat: An open-access, web-based platform for data needed for modeling low temperature plasmas. *Plasma Processes and Polymers*, 14(1-2):1600098, 2017.
- [72] Robert B. Lobbia and Brian E. Beal. Recommended practice for use of langmuir probes in electric propulsion testing. *Journal of Propulsion and Power*, 33(3):566–581, 2017.
- [73] T. Lagarde, Y. Arnal, A. Lacoste, and J. Pelletier. Determination of the EEDF by Langmuir probe diagnostics in a plasma excited at ECR above a multipolar magnetic field. *Plasma Sources Science and Technology*, 10(2):181–190, 2001.

- [74] Robert B. Lobbia and Alec D. Gallimore. Two-dimensional time-resolved breathing mode plasma fluctuation variation with hall thruster discharge settings. 2009.
- [75] J. P. Sheehan, Yevgeny Raitses, Noah Hershkowitz, and Michael McDonald. Recommended practice for use of emissive probes in electric propulsion testing. *Journal of Propulsion and Power*, 33(3):614–637, 2017.
- [76] Dan M. Goebel, Kristina K. Jameson, Ira Katz, and Ioannis G. Mikellides. Potential fluctuations and energetic ion production in hollow cathode discharges. *Physics of Plasmas*, 14(10), 2007.
- [77] G. Bousselin, N. Lemoine, J. Cavalier, S. Heuraux, and G. Bonhomme. Note: On the measurement of plasma potential fluctuations using emissive probes. *Review of Scientific Instruments*, 85(5):1–4, 2014.
- [78] G. Bousselin, N. Plihon, N. Lemoine, J. Cavalier, and S. Heuraux. How plasma parameters fluctuations influence emissive probe measurements. *Physics of Plasmas*, 22(5), 2015.
- [79] Daniel L. Brown, Mitchell L.R. Walker, James Szabo, Wensheng Huang, and John E. Foster. Recommended practice for use of faraday probes in electric propulsion testing. *Journal of Propulsion and Power*, 33(3):582–613, 2017.
- [80] George F. Karabadzhak, Yu Hui Chiu, and Rainer A. Dressler. Passive optical diagnostic of Xe propelled Hall thrusters. II. Collisional-radiative model. *Journal of Applied Physics*, 99(11), 2006.
- [81] S. S. Baghel, S. Gupta, R. K. Gangwar, and R. Srivastava. Diagnostics of low-temperature neon plasma through a fine-structure resolved collisional-radiative model. *Plasma Sources Science and Technology*, 28(11), 2019.
- [82] Juan Yang, Shigeru Yokota, Ryotaro Kaneko, and Kimiya Komurasaki. Diagnosing on plasma plume from xenon Hall thruster with collisional-radiative model. *Physics of Plasmas*, 17(10), 2010.
- [83] S. Mazouffre, R. Jousot, B. Vincent, and S. Tsikata. Discharge and plasma plume characterization of a 100 A-class LaB 6 hollow cathode . *Journal of Applied Physics*, 130(17):173301, 2021.

- [84] N. Yamamoto, K. Tomita, K. Sugita, T. Kurita, H. Nakashima, and K. Uchino. Measurement of xenon plasma properties in an ion thruster using laser Thomson scattering technique. *Review of Scientific Instruments*, 83(7), 2012.
- [85] M W Crofton, A G Hsu Schouten, J A Young, E J Beiting, K D Diamant, R L Corey, and J J Delgado. Neutral Xenon Density in the SPT-140 Near-Field Plume. *33rd International Electric Propulsion Conference*, (IEPC Paper 2013-399):1–41, 2013.
- [86] Christoph Eichhorn, Michael Winter, Monika Auweter-kurtz, and Stefan L. Multi-Photon Spectroscopy on Xenon for Application on Ion Thruster Plasma Parameter Investigations : Experiment and Theory. *30th International Electric Propulsion Conference*, pages 1–11, 2007.
- [87] Christoph Eichhorn, Stefan Löhle, Stefanos Fasoulas, Hans Leiter, Stephan Fritzsche, and Monika Auweter-Kurtz. Photon laser-induced fluorescence of neutral xenon in a thin xenon plasma. *Journal of Propulsion and Power*, 28(5):1116–1120, 2012.
- [88] Yusuke Yamashita, R. Tsukizaki, Kiyoshi Kinefuchi, D. Koda, Yoshitaka Tani, and Kazutaka Nishiyama. Neutral ground state particle density measurement of xenon plasma in microwave cathode by two-photon laser-induced fluorescence spectroscopy. *Vacuum*, 168(June):108846, 2019.
- [89] D. A. Carl. Axial radio frequency electric field intensity and ion density during low to high mode transition in argon electron cyclotron resonance discharges. *Journal of Vacuum Science Technology B: Microelectronics and Nanometer Structures*, 9(2):339, 1991.
- [90] Z. Y. Fan and N. Newman. Kinetic energy distribution of nitrogen ions in an electron cyclotron resonance plasma. *Journal of Vacuum Science Technology A: Vacuum, Surfaces, and Films*, 16(4):2132–2139, 1998.
- [91] S. H. Fu and Z. F. Ding. Characteristics of microwave ECR ion thruster powered with plate antenna in cross-magnetic field: Standing wave, skin effect, and mode transition. *Physics of Plasmas*, 28(3), 2021.
- [92] Juan LI, Shenghui FU, Yurou YANG, and Zhenfeng DING. On abnormal behaviors of

- ion beam extracted from electron cyclotron resonance ion thruster driven by rod antenna in cross magnetic field. *Plasma Science and Technology*, 23(8), 2021.
- [93] Mutumi Tuda and Kouichi Ono. New-type microwave plasma source excited by azimuthally symmetric surface waves with magnetic multicusp fields. *Journal of Vacuum Science and Technology A: Vacuum, Surfaces, and Films*, 16(5):2832–2839, 1998.
- [94] Mutumi Tuda, Kouichi Ono, Hiroki Ootera, Masaaki Tsuchihashi, Minoru Hanazaki, and Toshio Komemura. Large-diameter microwave plasma source excited by azimuthally symmetric surface waves. *Journal of Vacuum Science and Technology A: Vacuum, Surfaces, and Films*, 18(3):840–848, 2000.
- [95] U. Kortshagen, N. D. Gibson, and J. E. Lawler. On the E-H mode transition in RF inductive discharges. *Journal of Physics D: Applied Physics*, 29(5):1224–1236, 1996.
- [96] Min-Hyong Lee and Chin-Wook Chung. On the e to h and h to e transition mechanisms in inductively coupled plasma. *Physics of plasmas*, 13(6):063510, 2006.
- [97] Hyo-Chang Lee, Min-Hyong Lee, and Chin-Wook Chung. Effects of rf-bias power on plasma parameters in a low gas pressure inductively coupled plasma. *Applied Physics Letters*, 96(7):071501, 2010.
- [98] Shu-Xia Zhao, Xiang Xu, Xue-Chun Li, and You-Nian Wang. Fluid simulation of the e-h mode transition in inductively coupled plasma. *Journal of Applied Physics*, 105(8):083306, 2009.
- [99] Yusuke Yamashita, Ryudo Tsukizaki, Koda Daiki, Yoshitaka Tani, Ryo Shirakawa, Kana Hattori, and Kazutaka Nishiyama. Plasma hysteresis caused by high-voltage breakdown in gridded microwave discharge ion thruster  $\mu 10$ . *Acta Astronautica*, 185(May):179–187, 2021.
- [100] Yusuke Yamashita, Ryudo Tsukizaki, and Kazutaka Nishiyama. Investigation of plasma mode transition and hysteresis in electron cyclotron resonance ion thrusters. *Plasma Sources Science and Technology*, 30(9):095023, 2021.
- [101] Koizumi Hiroyuki Kuninaka Hitoshi YaMagiwa Yoshiki Sugita, Yuto and Makoto Matsui. Number Density Measurement of Neutral Particles in a Miniature Microwave Dis-

- charge Ion Thruster. *Transactions of the Japan Society for Aeronautical and Space Sciences, Aerospace Technology Japan*, 12(ists29):Tb31–Tb35, 2014.
- [102] Ioannis G. Mikellides and Ira Katz. Numerical simulations of Hall-effect plasma accelerators on a magnetic-field-aligned mesh. *Physical Review E - Statistical, Nonlinear, and Soft Matter Physics*, 86(4), 2012.
- [103] J. Cavalier, N. Lemoine, G. Bonhomme, S. Tsikata, C. Honoré, and D. Grésillon. Hall thruster plasma fluctuations identified as the  $E \times B$  electron drift instability: Modeling and fitting on experimental data. *Physics of Plasmas*, 20(8):082107, 2013.
- [104] Benjamin Jorns. Predictive, data-driven model for the anomalous electron collision frequency in a Hall effect thruster. *Plasma Sources Science and Technology*, 27(10), 2018.
- [105] Christine M. Greve, Manoranjan Majji, and Kentaro Hara. Real-time state estimation of low-frequency plasma oscillations in Hall effect thrusters. *Physics of Plasmas*, 28(9), 2021.
- [106] Graeme A Bird. Molecular gas dynamics and the direct simulation of gas flows. *Molecular gas dynamics and the direct simulation of gas flows*, 1994.
- [107] J. P. Verboncoeur. Particle simulation of plasmas: Review and advances. *Plasma Physics and Controlled Fusion*, 47(5 A), 2005.
- [108] J. W. Cuthbertson, W. D. Langer, and R. W. Motley. Reflection of low energy plasma ions from metal surfaces. *Journal of Nuclear Materials*, 196-198(C):113–128, 1992.
- [109] Yoshinori Nakayama. Rarefied propellant flow vector measurement within a vacuum chamber. *TRANSACTIONS OF THE JAPAN SOCIETY FOR AERONAUTICAL AND SPACE SCIENCES, AEROSPACE TECHNOLOGY JAPAN*, 18(5):174–179, 2020.
- [110] Masataka Iwamoto, Naoji Yamamoto, Taichi Morita, Hideki Nakashima, Kentaro Tomita, and Kiichiro Uchino. Rayleigh scattering measurement of neutral atom number density downstream of a hall thruster under cold flow conditions. *Transactions of the Japan Society for Aeronautical and Space Sciences*, 60(5):327–330, 2017.
- [111] Hiroki Takayanagi, Shun Kato, Takeharu Sakai, Masahito Mizuno, Keisuke Fujii, Kazuhisa Fujita, Makoto Matsui, and Yoshiki Yamagiwa. Translational temperature

- distribution measurements in high enthalpy flows by laser-induced fluorescence. *51st AIAA Aerospace Sciences Meeting including the New Horizons Forum and Aerospace Exposition 2013*, (January):3–5, 2013.
- [112] G. D. Stancu, F. Kaddouri, D. A. Lacoste, and C. O. Laux. Atmospheric pressure plasma diagnostics by OES, CRDS and TALIF. *Journal of Physics D: Applied Physics*, 43(12), 2010.
- [113] Christoph Eichhorn, Frank Scholze, Carsten Bundesmann, Daniel Spemann, Horst Neumann, and Hans Leiter. Two-Photon Laser-Induced Fluorescence in a Radiofrequency Ion Thruster Plume in Krypton. *Journal of Propulsion and Power*, 35(6):1175–1178, 2019.
- [114] Tad Wegner, Adam J. Friss, Ciprian Dumitrache, and Azer P. Yalin. Two-Photon Absorption Laser Induced Fluorescence (TALIF) of Ground State Neutral Xenon. *The 36th International Electric Propulsion Conference*, pages 1–7, 2019.
- [115] Xi Ming Zhu, Zhi Wen Cheng, Yi Kang Pu, and Uwe Czarnetzki. Escape factors for Paschen 2p-1s emission lines in low-temperature Ar, Kr, and Xe plasmas. *Journal of Physics D: Applied Physics*, 49(22), 2016.
- [116] Yusuke Yamashita, Yoshitaka Tani, Ryudo Tsukizaki, Daiki Koda, and Kazutaka Nishiyama. Characteristics of plasma and gas in microwave discharge ion thruster  $\mu 10$  using kinetic particle simulation. *TRANSACTIONS OF THE JAPAN SOCIETY FOR AERONAUTICAL AND SPACE SCIENCES, AEROSPACE TECHNOLOGY JAPAN*, 18(3):57–63, 2020.
- [117] Ryo Shirakawa, Yusuke Yamashita, Daiki Koda, Ryudo Tsukizaki, Yusuke Shimizu, Masahito Tagawa, and Kazutaka Nishiyama. Investigation and experimental simulation of performance deterioration of microwave discharge ion thruster  $\mu 10$  during space operation. *Acta Astronautica*, 2020.
- [118] John Michael Fife. *Hybrid-PIC modeling and electrostatic probe survey of Hall thrusters*. PhD thesis, Massachusetts Institute of Technology, 1998.
- [119] Nathaniel Selden, Natalia Gimelshein, Sergey Gimelshein, and Andrew Ketsdever. Anal-

- ysis of accommodation coefficients of noble gases on aluminum surface with an experimental/computational method. *Physics of Fluids*, 21(7), 2009.
- [120] Amit Agrawal and S. V. Prabhu. Survey on measurement of tangential momentum accommodation coefficient. *Journal of Vacuum Science Technology A: Vacuum, Surfaces, and Films*, 26(4):634–645, 2008.
- [121] Wayne M. Trott, Jaime N. Castaeda, John R. Torczynski, Michael A. Gallis, and Daniel J. Rader. An experimental assembly for precise measurement of thermal accommodation coefficients. *Review of Scientific Instruments*, 82(3), 2011.
- [122] J BROPHY and P WILBUR. Calculation of plasma properties in ion sources. *International Electric Propulsion Conference*, 24(9):1516–1523, 1985.
- [123] T Takayanagi, S Kato, M Mizuno, K Fujii, K Fujita, M Matsui, and Y Yamagiwa. Flow temperature measurement of arc wind tunnel with laser induced fluorescence. In *ISAS/JAXA Space Flight Dynamics Symposium*, 2013.
- [124] T Ida, M Ando, and H Toraya. Extended pseudo-voigt function for approximating the voigt profile. *Journal of Applied Crystallography*, 33(6):1311–1316, 2000.
- [125] Jay Grinstead, Barry Porter, and Enrique Carballo. Flow Property Measurements Using Laser-Induced Fluorescence in the NASA Ames Interaction Heating Facility Arc Jet. (January):1–11, 2011.
- [126] Makoto Matsui, Kimiya Komurasaki, Satoshi Ogawa, and Yoshihiro Arakawa. Influence of laser intensity on absorption line broadening in laser absorption spectroscopy. *Journal of Applied Physics*, 100(6):2–6, 2006.
- [127] Donald J. Santeler. New concepts in molecular gas flow. *Journal of Vacuum Science Technology A: Vacuum, Surfaces, and Films*, 4(3):338–343, 1986.
- [128] O. Chapurin, A. I. Smolyakov, G. Hagelaar, and Y. Raitses. On the mechanism of ionization oscillations in Hall thrusters. *Journal of Applied Physics*, 129(23):233307, 2021.
- [129] Rainer A. Dressler, Yu Hui Chiu, Oleg Zatsarinny, Klaus Bartschat, Rajesh Srivastava, and Lalita Sharma. Near-infrared collisional radiative model for Xe plasma electrostatic

- thrusters: The role of metastable atoms. *Journal of Physics D: Applied Physics*, 42(18), 2009.
- [130] A Barbet, N Sadeghi, and JC Pebay-Peyroula. Decay of metastable xenon atoms  $\text{xe}^*(3p2)$  in a xenon afterglow. *Journal of Physics B: Atomic and Molecular Physics*, 8(10):1776, 1975.
- [131] Meeker dc2021finite element method magnetics. <https://femm.info/wiki/HomePage>.
- [132] Giulio Coral, Ryudo Tsukizaki, Kazutaka Nishiyama, and Hitoshi Kuninaka. Microwave power absorption to high energy electrons in the ECR ion thruster. *Plasma Sources Science and Technology*, 27(9):095015, 2018.
- [133] Xi Ming Zhu, Yan Fei Wang, Yang Wang, Da Ren Yu, Oleg Zatsarinny, Klaus Bartschat, Tsanko Vaskov Tsankov, and Uwe Czarnetzki. A xenon collisional-radiative model applicable to electric propulsion devices: II. Kinetics of the 6s, 6p, and 5d states of atoms and ions in Hall thrusters. *Plasma Sources Science and Technology*, 28(10), 2019.
- [134] Yoshinori Takao, Naoki Kusaba, Koji Eriguchi, and Kouichi Ono. Two-dimensional particle-in-cell Monte Carlo simulation of a miniature inductively coupled plasma source. *Journal of Applied Physics*, 108(9), 2010.
- [135] S. Cruz y Cruz and R. Razo. Wave propagation in the presence of a dielectric slab: The paraxial approximation. *Journal of Physics: Conference Series*, 624(1), 2015.
- [136] Hitendra K. Malik. Density bunch formation by microwave in a plasma-filled cylindrical waveguide. *Epl*, 106(5), 2014.
- [137] Hiroyuki Koizumi and Hitoshi Kuninaka. Antenna design method for low power miniaturized microwave discharge ion engines. *Journal of the Japan Society for Aeronautical and Space Sciences*, 57(665):234–243, 2009.
- [138] Charles E. Garner, Marc D. Rayman, and John R. Brophy. In-flight operation of the dawn ion propulsion system through year one of cruise to ceres. *49th AIAA/ASME/SAE/ASEE Joint Propulsion Conference*, 1 PartF, 2013.
- [139] M. Nakano, K. Nakamura, Y. Naito, Y. Nakagawa, Y. Takao, and H. Koizumi. Computational design of a high-efficiency accelerator grid for a miniature ion thruster by full-aperture ion optics simulations. *AIP Advances*, 9(3), 2019.

- [140] Jan Egedal, Ari Le, and William Daughton. A review of pressure anisotropy caused by electron trapping in collisionless plasma, and its implications for magnetic reconnection. *Physics of Plasmas*, 20(6), 2013.
- [141] Benjamin A. Jorns. Two Equation Closure Model for Plasma Turbulence in a Hall Effect Thruster. *36th International Electric Propulsion Conference*, pages 1–12, 2019.
- [142] Alejandro Lopez Ortega, Benjamin A. Jorns, and Ioannis G. Mikellides. Hollow cathode simulations with a first-principles model of ion-acoustic anomalous resistivity. *Journal of Propulsion and Power*, 34(4):1026–1038, 2018.
- [143] Liang Wang, Ammar H. Hakim, A. Bhattacharjee, and K. Germaschewski. Comparison of multi-fluid moment models with particle-in-cell simulations of collisionless magnetic reconnection. *Physics of Plasmas*, 22(1), 2015.
- [144] Rodney J. Mason. Implicit moment particle simulation of plasmas. *Journal of Computational Physics*, 41(2):233–244, 1981.
- [145] Giovanni Lapenta. Exactly energy conserving semi-implicit particle in cell formulation. *Journal of Computational Physics*, 334:349–366, 2017.
- [146] G. Chen, L. Chacón, and D. C. Barnes. An energy- and charge-conserving, implicit, electrostatic particle-in-cell algorithm. *Journal of Computational Physics*, 230(18):7018–7036, 2011.
- [147] J. U. Brackbill. On energy and momentum conservation in particle-in-cell plasma simulation. *Journal of Computational Physics*, 317:405–427, 2016.
- [148] Charles K Birdsall and A Bruce Langdon. *Plasma physics via computer simulation*. CRC press, 2018.
- [149] Charles K. Birdsall and Dieter Fuss. Clouds-in-clouds, clouds-in-cells physics for many-body plasma Simulation. *Journal of Computational Physics*, 135(2):141–148, 1997.
- [150] P. W. Rambo. Finite-grid instability in quasineutral hybrid simulations, 1995.
- [151] G Chen, L Chacón, L Yin, B J Albright, D J Stark, and R F Bird. algorithm for the relativistic Vlasov-Maxwell equations. 407, 2020.

- [152] Valentin Pagès, Martin Campos, and A Pinto. A semi-implicit electromagnetic FEM-PIC scheme with exact energy and charge conservation Valentin Pagès , Martin Campos Pinto To cite this version : HAL Id : hal-02521069 exact energy and charge conservation. 2020.
- [153] Diego Gonzalez-herrero, Alfredo Micera, Elisabetta Boella, and Jaeyoung Park. ECsim-CYL : Energy Conserving Semi-Implicit particle in cell simulation in axially symmetric cylindrical coordinates. *Computer Physics Communications*, 236:153–163, 2019.
- [154] Shinatora Cho, Kimiya Komurasaki, and Yoshihiro Arakawa. Kinetic particle simulation of discharge and wall erosion of a Hall thruster. *Physics of Plasmas*, 20(6), 2013.
- [155] Shinatora Cho, Hiroki Watanabe, Kenichi Kubota, Shigeyasu Iihara, Kenji Fuchigami, Kazuo Uematsu, and Ikkoh Funaki. Study of electron transport in a Hall thruster by axial-radial fully kinetic particle simulation. *Physics of Plasmas*, 22(10), 2015.
- [156] B Godfrey. Numerical Cherenkov Instabilities in Electromagnetic Particle Codes. 504521:504–521, 1974.
- [157] Hong Qin, Shuangxi Zhang, Jianyuan Xiao, Jian Liu, Yajuan Sun, William M. Tang, and ARTICLES. Why is Boris algorithm so good ? 084503(July 2013), 2018.
- [158] Seiji Zenitani and Takayuki Umeda. On the Boris solver in particle-in-cell simulation. *Physics of Plasmas*, 25(11), 2018.
- [159] Yosuke Sato, Hiroyuki Koizumi, Masakatsu Nakano, and Yoshinori Takao. Electron extraction enhancement via the magnetic field in a miniature microwave discharge neutralizer. *Journal of Applied Physics*, 126(24), 2019.
- [160] Kengo Nakamura, Hiroyuki Koizumi, Masakatsu Nakano, and Yoshinori Takao. Effects of negative ions on discharge characteristics of water plasma source for a miniature microwave discharge ion thruster. *Physics of Plasmas*, 26(4):043508, 2019.
- [161] Kazutaka Nishiyama, Ryoichi Kukuchi, Hitoshi Kuninaka, and Haruki Takegahara. a High Current Compact Ecr Ion Source. *58th International Astronautical Congress*, pages IAC–06–C4.P.4.14, 2006.

- [162] Ikkoh Funaki, Hitoshi Kuninaka, and Kyoichiro Toki. Plasma Characterization of a 10-cm Diameter Microwave Discharge Ion Thruster. *Journal of Propulsion and Power*, 20(4):718–727, 2004.
- [163] Yusuke Yamashita, Ryudo Tsukizaki, Yuta Yamamoto, Daiki Koda, Kazutaka Nishiyama, and Hitoshi Kuninaka. Azimuthal ion drift of a gridded ion thruster. *Plasma Sources Science and Technology*, 27(10), 2018.
- [164] Kane S Yee. Numerical Solution of Initial Boundary Value Problems Involving Maxwell’s Equations in Isotropic Media. 1966.
- [165] T. Zh Esirkepov. Exact charge conservation scheme for Particle-in-Cell simulation with an arbitrary form-factor. *Computer Physics Communications*, 135(2):144–153, 2001.
- [166] James W. Eastwood. The virtual particle electromagnetic particle-mesh method. *Computer Physics Communications*, 64(2):252–266, 1991.
- [167] John Villasenor and Oscar Buneman. Rigorous charge conservation for local electromagnetic field solvers. *Computer Physics Communications*, 69(2-3):306–316, 1992.
- [168] T. Umeda, Y. Omura, T. Tominaga, and H. Matsumoto. A new charge conservation method in electromagnetic particle-in-cell simulations. *Computer Physics Communications*, 156(1):73–85, 2003.
- [169] A. Bruce Langdon. On enforcing Gauss’ law in electromagnetic particle-in-cell codes. *Computer Physics Communications*, 70(3):447–450, 1992.
- [170] J. P. Verboncoeur. Symmetric spline weighting for charge and current density in particle simulation. *Journal of Computational Physics*, 174(1):421–427, 2001.
- [171] Hiroshi Nakashima, Yoshiki Summura, Keisuke Kikura, and Yohei Miyake. Large Scale Manycore-Aware PIC Simulation with Efficient Particle Binning. *Proceedings - 2017 IEEE 31st International Parallel and Distributed Processing Symposium, IPDPS 2017*, pages 202–212, 2017.
- [172] Heiko Burau, Renée Widera, Wolfgang Hönig, Guido Juckeland, Alexander Debus, Thomas Kluge, Ulrich Schramm, Tomas E. Cowan, Roland Sauerbrey, and Michael

- Bussmann. PIconGPU: A fully relativistic particle-in-cell code for a GPU cluster. *IEEE Transactions on Plasma Science*, 38(10 PART 2):2831–2839, 2010.
- [173] Yohei Miyake and Hideyuki Usui. New electromagnetic particle simulation code for the analysis of spacecraft-plasma interactions. *Physics of Plasmas*, 16(6):1–11, 2009.
- [174] S. E. Parker and C. K. Birdsall. Numerical error in electron orbits with large  $\omega ce\Delta t$ . *Journal of Computational Physics*, 97(1):91–102, 1991.
- [175] Motohiko Tanaka. The macro-EM particle simulation method and a study of collisionless magnetic reconnection. *Computer Physics Communications*, 87(1-2):117–138, 1995.
- [176] Motohiko Tanaka. Macroscale implicit electromagnetic particle simulation of magnetized plasmas. *Journal of Computational Physics*, 79(1):209–226, 1988.
- [177] Xujing Wang, Xiao Bo Wang, and Peter R.C. Gascoyne. General expressions for dielectrophoretic force and electrorotational torque derived using the Maxwell stress tensor method. *Journal of Electrostatics*, 39(4):277–295, 1997.
- [178] Tengfei Liang, Qi Li, and Wenjing Ye. Performance evaluation of Maxwell and Cercignani-Lampis gas-wall interaction models in the modeling of thermally driven rarefied gas transport. *Physical Review E - Statistical, Nonlinear, and Soft Matter Physics*, 88(1):1–11, 2013.
- [179] John R. Brophy. Simulated ion thruster operation without beam extraction. *AIAA/DGLR/JSASS 21st International Electric Propulsion Conference, 1990*, 1990.
- [180] Ben Dankongkakul and Richard E. Wirz. Miniature ion thruster ring-cusp discharge performance and behavior. *Journal of Applied Physics*, 122(24), 2017.
- [181] S. L. Guo, X. L. Jin, L. Lei, X. Y. Zhang, and B. Li. Numerical investigation of plasma characteristics for an ion thruster discharge chamber. *Physics of Plasmas*, 28(1), 2021.
- [182] Richard Wirz and Ira Katz. Plasma processes of DC ion thruster discharge chambers. *41st AIAA/ASME/SAE/ASEE Joint Propulsion Conference and Exhibit*, 2005.